ADAPTIVE RETRACKING OF RADAR ALTIMETRY WAVEFORMS OVER HETEROGENEOUS INLAND WATERS

Andrew Marshall

B. Surveying (University of NSW)
M. Surveying Science (University of NSW)

A thesis submitted in fulfilment of the requirements for the Degree of Doctor of Philosophy

Faculty of Engineering and Built Environment
The University of Newcastle, Australia

September 2020

This research was supported by an Australian Government Research Training Program (RTP) Scholarship

DECLARATION

STATEMENT OF ORIGINALITY

I hereby certify that the work embodied in the thesis is my own work, conducted under normal supervision. The thesis contains no material which has been accepted, or is being examined, for the award of any other degree or diploma in any university or other tertiary institution and, to the best of my knowledge and belief, contains no material previously published or written by another person, except where due reference has been made. I give consent to the final version of my thesis being made available worldwide when deposited in the University's Digital Repository, subject to the provisions of the Copyright Act 1968 and any approved embargo.

Andrew Marshall

31 August 2020

ACKNOWLEDGMENT OF AUTHORSHIP

I hereby certify that the work embodied in this thesis contains published paper/s/scholarly work of which I am a joint author. I have included as part of the thesis a written declaration endorsed in writing by my supervisor, attesting to my contribution to the joint publication/s/scholarly work.

By signing below, I confirm that Andrew Marshall contributed as joint author to the paper entitled 'Image analysis for altimetry waveform selection over heterogeneous inland waters'.

Xiaoli Deng

31 August 2020

ACKNOWLEDGEMENTS

I express gratitude to my principal supervisor, A/Prof Xiaoli Deng, for her support and encouragement during the period of my PhD candidature at the University of Newcastle. Her patience in guiding my research is greatly appreciated.

I acknowledge the European Space Agency for allowing open access to Envisat, SARAL and Cryosat-2 altimetry data and for support with data download and format interpretation.

To my colleagues at Ok Tedi Mining who have supported my work over many years, I am deeply grateful. Environment Department managers including Marshall Lee, Jim Veness, Dr Michael Ridd and Jesse Pile, have unreservedly supported my endeavours and research activities, and for that I am indebted. The field teams that have worked alongside me on the Fly River floodplain have contributed tirelessly under what is typically extremely difficult conditions. In particular, I would like to thank Nicko Paulus who has selflessly assisted my work over the past two decades. Special thanks go to the OTML Hydrology Section for meeting frequent data requests over an extended period and supplying quality hydrologic data that have been the key to the validation analyses undertaken in this study.

My work on the Fly River has been undertaken in conjunction with a diverse scientific team and I thank them all for their support. In particular, I thank Dr Geoff Pickup and Dr Michael Ridd, who have consistently supported my work and given invaluable advice regarding this research and the resulting thesis.

I am indebted to Jim Veness for his proofreading of this manuscript. His contribution to the grammar and style of the document is greatly appreciated.

Finally, I would like to acknowledge the love and support of my family. My wife Vanessa; my children Joshua, Philip, Thomas and Sarah; and my parents Donald and Annette. My family have unreservedly supported my research and the submission of this thesis would not have been possible without them. Thank you and I love you all very much.

TABLE OF CONTENTS

LIST OF FIGURES

LIST OF TABLES

LIST OF ABBREVIATIONS

AGC	Automatic gain control
AGD66	Australian Geodetic Datum 1966
ALES	Adaptive Leading Edge Sub-waveform (retracker)
ALOS	Advanced Land Observing Satellite
AltiKa	Altimeter in Ka-band
ARM	Approximate river mile
ASAR	Advanced synthetic aperture radar
AVISO	Archiving Validation and Interpretation of Satellite Oceanographic Data
CNES	Centre National d'Etudes Spatiales (National Centre for Space Study)
COG	Centre of gravity
DAC	Dynamic atmosphere correction
DAHITI	Database for Hydrological Time Series of Inland Waters
DEM	Digital elevation model
DORIS	Doppler Orbitography and Radiopositioning Integrated by Satellite
DSM	Digital surface model
ECMWF	European Centre for Medium Weather Forecast
EGM96	Earth Gravitational Model 1996
EGM2008	Earth Gravitational Model 2008
Envisat	ENVIronmental SATellite
ERS-1	European Remote Sensing Satellite-1
ERS-2	European Remote Sensing Satellite-2
ESA	European Space Agency
ETM7	Enhanced Thematic Mapper (Landsat 7)
FAN	File Array Notation
GDR	Geophysical Data Record
GFO	Geosat Follow-on
GIM	Global ionospheric map
GNSS	Global Navigation Satellite System
GOCE	Gravity field and steady-state Ocean Circulation Explorer
GPS	Global Positioning System
GRACE	Gravity Recovery and Climate Experiment
GRRATS	Global River Radar Altimetry Time Series
HH	(SAR) horizontal transmit/horizontal receive

IDL	Interactive Data Language
IE	Individual echo
InSAR	Interferometric SAR
ITRF92	International Terrestrial Reference Frame 1992
L1B/L2	Level 1B and Level 2
JAXA	Japan Aerospace Exploration Agency
JPL	Jet Propulsion Laboratory
LEGOS	Laboratoire d'Etudes en Géophysique et Océanographie Spatiales
LEP	Leading-edge position
LRM	Low-resolution mode
LRR	Laser retro-reflector
MIR	Middle infra-red
MLE	Maximum likelihood estimator
MMSE	Minimum mean square estimator
MSL	Mean sea level
MWaPP	Multiple Waveform Persistent Peak (retracker)
MWR	Microwave radiometer
NASA	National Aeronautics and Space Administration
NDVI	Normalised Difference Vegetation Index
NDWI	Normalised Difference Water Index
NetCDF	Network Common Data Form
NIR	Near infrared
NM	Nautical mile
NPPR	Narrow Primary Peak Retracker
OCOG	Offset Centre of Gravity
OHD	Ok Tedi Height Datum
OLCI	Ocean and Land Colour Imager
OLI8	Operational Land Imager (Landsat 8)
OLTC	Altimeter Open Loop Tracking Command for Hydrology
OMG	Ok Tedi Map Grid
OSCAR	Observing Systems Capability Analysis and Review
OSTM	Ocean Surface Topography Mission
OSU	Ohio State University
OTML	Ok Tedi Mining Limited

PNG	Papua New Guinea
PNGMG94	PNG Map Grid 1994
PRF	Pulse repetition frequency
PVC	Polyvinyl chloride
RA-2	Radar Altimeter 2
RANSAC	RANdom SAmple Consensus
RMSE	Root mean square error
SAR	Synthetic aperture radar
SARAL	Satellite with ARgos and AltiKa
SD	Standard deviation
SGDR	Sensor and Geophysical Data Record
SIRAL	SAR Interferometric Radar Altimeter
SMASH	Small Altimetry Satellites for Hydrology
SRAL	Synthetic Aperture Radar Altimeter
SRTM	Shuttle Radar Topography Mission
SSB	Sea state bias
SSH	Sea surface height
SWH	Significant wave height
SWOT	Surface Water Ocean Topography Mission
TEC	Total electron content
TM5	Thematic Mapper (Landsat 5)
T/P	Topex/Poseidon
UCLA	University of California, Los Angeles
USGS	United States Geological Survey
UTM	Universal Transverse Mercator
VV	(SAR) vertical transmit/vertical receive
WATeR	Waveform Adaptive Threshold Retracker
WGS84	World Geodetic System 1984
WLS	Weighted least squares
WSE	Water surface elevation

LIST OF SYMBOLS

A	waveform amplitude (OCOG and Threshold Retracker)
d	along-track distance
d_1	waveform power difference between adjacent gates
d_2	waveform power difference for a separation of 2 gates
G_{LEP}	waveform gate of the leading-edge position
G_{REF}	altimeter reference tracking gate
G_{2m}	conversion factor from gate to metres
H	satellite altitude above the reference ellipsoid
H_i	satellite altitude at time i
h_i	height above reference ellipsoid at time i
h	height above reference ellipsoid
Δh_{dac}	dynamic atmosphere correction
Δh_{earth}	solid earth tide correction
Δh_{geoid}	geoid correction
Δh_{WSE}	total range and geophysical corrections for inland waters
Δh_{load}	ocean loading tide correction
Δh_{ocean}	ocean tide correction
Δh_{SSH}	total range and geophysical corrections for sea surfaces
Δh_{pole}	geocentric pole tide correction
N	geoid–ellipsoid separation
$P(t)$	the returned power waveform as a function of time
$P_{FS}(t)$	average flat surface response
P_i	waveform power at gate i
P_N	thermal noise
Pu	waveform amplitude of Brown–Hayne retracking model
q	Threshold Retracker amplitude percentage
$q_s(t)$	surface probability density of specular points
R	correlation coefficient
R_{earth}	spherical radius of the Earth
R_i	range to reflecting surface at time i
R_{corr}	corrected altimetric range
R_{obs}	observed altimetric range
R_{obs}'	observed slant range

ΔR	range error
$rNIR$	near infrared band reflectance
$rRed$	red band reflectance
ΔR_{dry}	dry tropospheric propagation delay
ΔR_{iono}	ionospheric propagation delay
ΔR_{ssb}	sea state bias
ΔR_{wet}	wet tropospheric propagation delay
S_{d1}	standard deviation for all power differences between adjacent gates
S_{d2}	standard deviation for all power differences for a separation of 2 gates
$S_r(t)$	radar point target response
T_h	Threshold Retracker threshold level at q%
W	waveform width (OCOG and Threshold Retracker)
β_1	thermal noise of β-parameter retracking
β_2	return signal amplitude of β-parameter retracking
β_3	midpoint of leading-edge ramp of β-parameter retracking
β_4	waveform rise time of β-parameter retracking
β_5	slope of trailing edge of β-parameter retracking
δ_{si}	along track distance between t_{i-1} and t_i
φ	latitude
λ	longitude
$\frac{\partial a}{\partial s}$	satellite altitude along track variation
γ	function of the antennae beam width
ξ	waveform trailing edge slope for the Brown–Hayne retracking model
σ_c	waveform rise time for the Brown–Hayne retracking model
σ^0	backscatter coefficient (sigma0)
σ_s	slope of the waveform leading edge for the Brown–Hayne retracking model
τ	waveform epoch/time delay for the Brown–Hayne retracking model

ABSTRACT

To manage the pressure that population growth, human impact and climate change is having on the allocation of, and access to, water there is an increasing need to monitor the world's water resources, independent of infrastructure and inter-government policies. Traditionally the realm of the hydrologist, this task has relied on the deployment of in-situ gauges and instruments. Recent focus has been on the capabilities of satellite-based technologies to augment the existing hydrology in-situ network with the aim of replacing it with a global water level monitoring tool for inland rivers, lakes and wetlands.

This research has focussed on the satellite altimetry coverage of the middle Fly River floodplain as well as Lake Murray—both located in the Western Province of Papua New Guinea. The Fly River floodplain is a mine-impacted environment and monitoring of water level change through the various floodplain and wetland entities is required into the future. More than for other similar environments throughout the world there will become an increasing need to support Fly River local communities with information regarding predicted changes to inundation that may have impacts on their communities and subsistence livelihood.

The current state-of-the-art satellite altimetry analysis methodologies over heterogeneous inland waters do not meet the accuracy and reliability requirements for water surface measurement. This is particularly relevant for the relatively small river and lake systems that contribute to a typical complex floodplain or wetland system. Methodologies developed in this study enable routine, accurate and reliable extraction of water surface elevations from nadir-looking pulse-limited radar altimeters over heterogeneous inland waters. This is achieved by deconstructing the shape and form of the recorded waveform and correlating that form against external inputs so that the environmental factors that have affected the shape and form of the waveform are understood and can be addressed. The external inputs comprise a range of supporting data, including information derived from satellite imagery as well as in-situ water level observations. A process of waveform footprint classification is developed with assessment of footprint inundation extent based on image analysis from both multi-spectral and synthetic aperture radar (SAR) imagery. The methodology is extended to include a full definition of the landform cover type as well as prediction capabilities for off-nadir calm water detection.

A significant advancement over conventional processes is that waveforms, and the associated water surface elevations, are assessed based on an analysis of the waveform and

adjacent waveforms as well as the nature of the altimetry footprint rather than solely on statistical agreement of the derived water surface elevation with that derived from adjacent waveforms. This facilitates the retention of water level estimates over relatively small water bodies, where multiple, statistically consistent, estimates would not be practical. The processes developed in this research offer a methodology for the extraction of reliable water surface estimates, in both a temporal and spatial context, over heterogeneous inland waters. An optimised adaptive threshold retracker, the Waveform Adaptive Threshold Retracker, is developed as part of this study with methodology and workflow detailed in the thesis. Methods for the accurate identification of waveforms impacted by hooking and other sources of contamination are developed, along with tools for the rectification of impacts and estimation of likely contamination magnitude.

Optimised waveform retracking using the adaptive retracking methodology and workflow is validated at Envisat Radar Altimeter 2 (RA-2) and Satellite with Argos and AltiKa (SARAL/AltiKa) crossings of the Fly River and achieved by comparison of the altimetric time series with in-situ gauge data. Validation is also undertaken for floodplain sites where verified virtual in-situ gauges have been established for validation of both Envisat RA-2 and SARAL/AltiKa-derived elevations. This comparison has been undertaken for the 10 years of Envisat RA-2 data acquisitions and the pre-drifting phase cycles of SARAL/AltiKa data. Elevation profiles from Envisat RA-2, SARAL/AltiKa and Cryosat-2 SAR Interferometer Radar Altimeter (SIRAL) altimeters have been derived across both the Fly River floodplain and Lake Murray and used to assess the proposed retracking methodologies for the derivation of floodplain gradients and differential elevations between various floodplain water bodies.

The methodologies developed offer potential for the reprocessing of a significant archive of data from nadir-looking pulse-limited radar altimeters as well as supporting analyses of data from currently operational altimeters into the future. The work undertaken in this study has facilitated tangible improvements in the quality and quantity of water level estimates across complex inland water environments.

CHAPTER 1: INTRODUCTION

1.1 Satellite radar altimetry: past, present and the future

Satellite altimetry was designed as a technique to measure sea surface height (SSH) with continuous and global coverage. The concept is relatively simple and comprises a nadir range from the satellite to the sea surface coupled with a precisely determined satellite position to determine the SSH. The need for a global observation system to better understand oceanic phenomena, as well as the impact of climate change on the global water balance, has been the impetus for continuing research and development. Although the measurement of sea level has been the primary task and research focus of satellite altimeters there has been increasing application of the technology for sea ice measurement (e.g. Laxon, 1994; Wingham et al., 2006; Connor et al., 2009; Yang et al., 2012; Zakharova et al., 2015), glaciological studies (e.g. Bamber, 1994; Davis, 1997; Legresy et al., 2005) and measurement of water levels over inland rivers and lakes (e.g. Benveniste and Berry, 2004; Frappart et al., 2005; Berry, 2006; Crétaux and Birkett, 2006; Cai and Wei, 2009; Calmant et al., 2009; Lu et al., 2009; Zhang, 2009; Crétaux et al., 2011; Santos Da Silva et al., 2012; Troitskaya et al., 2012; Zakharova et al., 2014; Schwatke et al., 2015b; Biancamaria et al., 2017; Gao et al., 2019; Coss et al., 2020).

The first satellite altimeter mission was Skylab in 1973, which was followed by Geos-3 in 1975. However, the first usable data were obtained from the short-lived Seasat mission in 1978 and Geosat in 1985 (AVISO+, 2019). Numerous successful missions have been undertaken since that time, primarily by the National Aeronautics and Space Administration (NASA), the European Space Agency (ESA), and the French Space Agency (Centre National d'Etudes Spatiales, or CNES) with lesser contributions from the United States (US) Navy, the Russian Ministry of Defence and, in recent years, the Indian and Chinese space agencies (Benveniste, 2011). The continuity and homogeneity of altimetric data along with an extended period of scientific collaboration have enabled a significant improvement in satellite altimetry accuracy and a significant increase in potential applications of the data (AVISO+, 2019). The combination of several satellites operating simultaneously further enhances the potential for high-precision altimetry and decreases the impact of spatial and temporal resolution deficiencies.

The historical development of satellite altimeters over the past 30 years is documented in Figure 1-1.

Satellite altimeters have evolved from pulse-limited nadir-looking altimeters to incorporate synthetic aperture radar (SAR) (Sentinel-3 and Cryosat-2) and have the potential in the future to utilise wide-swath altimetry technology from the Surface Water Ocean Topography (SWOT) mission. The use of Ka-band altimetry (Satellite with Argos and AltiKa [SARAL/AltiKa)]), altimetric interferometry, constellations of identical satellites, and advances in Global Navigation Satellite System (GNSS) altimetry are areas of current and future advancement (Rosmorduc et al., 2018).

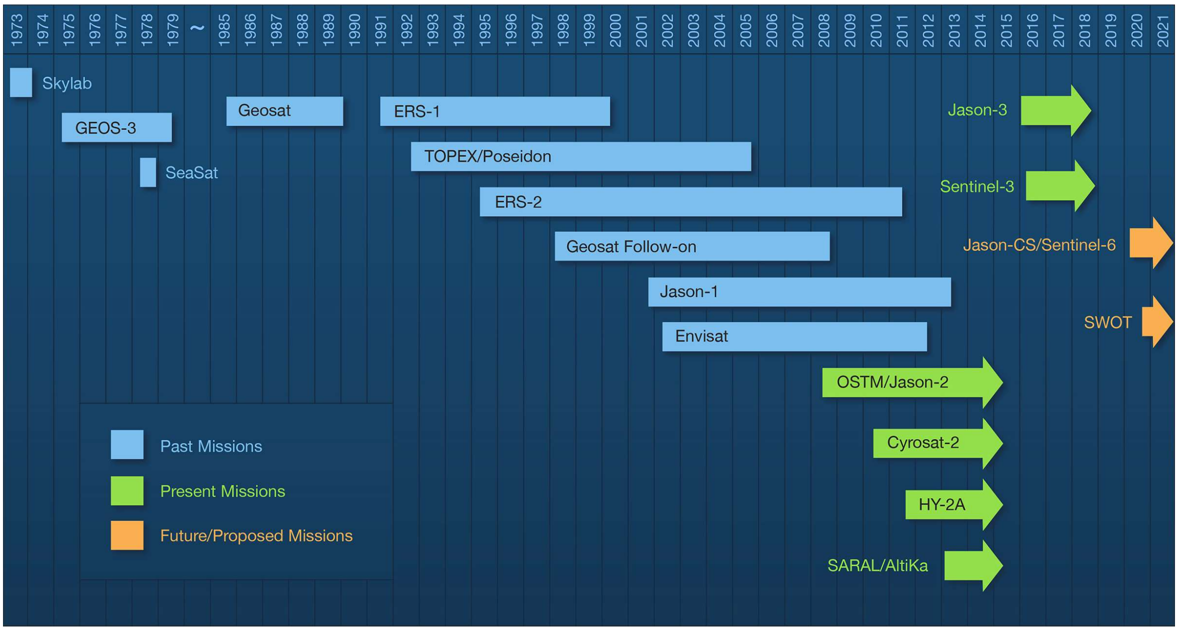

Figure 1-1 Satellite radar altimetry systems from Skylab in 1973 to the Jason-CS/Sentinel-6 satellites planned for 2020 and 2025 and the SWOT mission planned for 2021 (PODAAC, 2019).

Also over the past 30 years, significant improvements in orbit determination accuracy and satellite positioning capability have resulted in the derived altimetric position on the receiving surface being of sufficient quality that the assessment of oceanic processes is now feasible. These advances are due primarily to the incorporation of a dual-frequency Doppler tracking system—known as the Doppler Orbitography and Radiopositioning Integrated by Satellite (DORIS) system—for precise orbit determination; a laser retro-reflector (LRR) for range measurement calibration; and improvements in GNSS technology (Rosmorduc et al., 2018; AVISO+, 2019). Accuracy improvement in orbit determination since the Seasat and Geos-3 missions through to that achieved today is illustrated in Figure 1-2.

While the primary application of satellite altimetry is related to oceanic phenomena and the supply of continuous worldwide observations, it also relates to ocean circulation and currents, tides, mean sea level (MSL) change and oceanography (AVISO+, 2019). Satellite altimetry has been used in climatic research, particularly for the study of ocean–atmosphere coupled events such as El Niño, monsoons, the North Atlantic Oscillation and decadal oscillations (AVISO+, 2019).

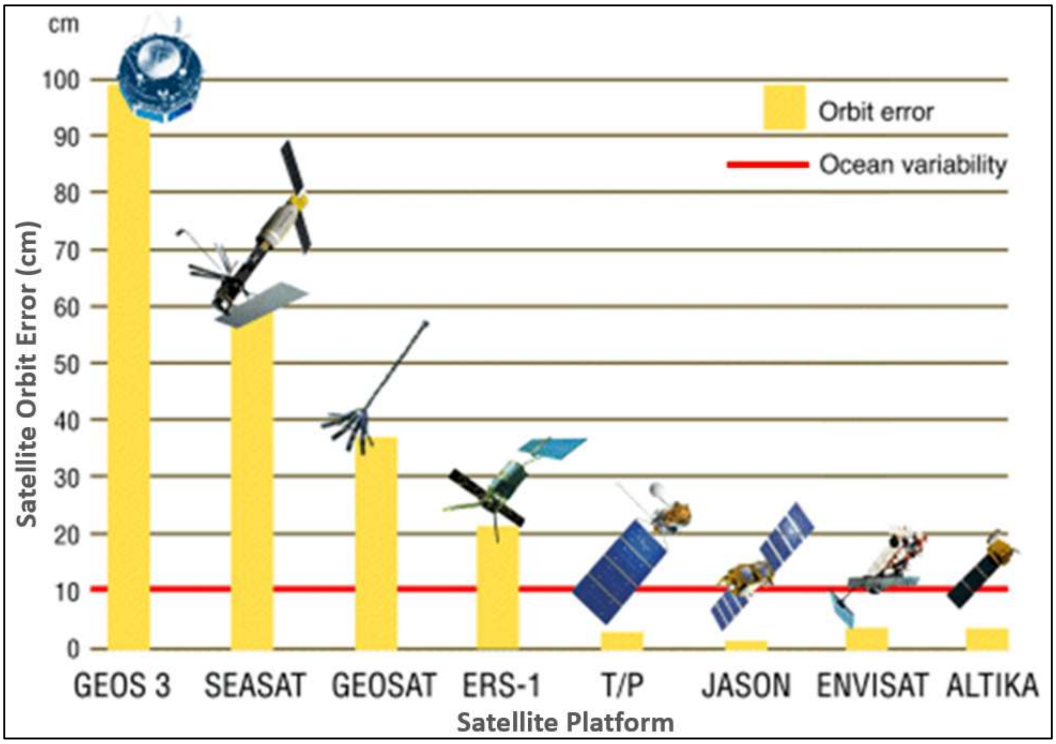

Figure 1-2 Improvements in orbit determination over the past 30 years (Rosmorduc et al., 2018).

Applications in the study of oceanic phenomena that have been difficult to assess within the coastal zone—where the ocean–land interface corrupts the altimetric radar return—have been reported over recent years (Gomez-Enri et al., 2010; Gommenginger et al., 2010). Of equal importance have been applications related to the cryosphere; particularly measurement over the continental ice sheets and sea ice to assess global climate change indices (Wingham et al., 2006; AVISO+, 2019). Secondary applications of satellite altimetry are found within the domain of geodesy, geophysics and hydrology (Benveniste and Berry, 2004; Berry et al., 2005a; Crétaux and Birkett, 2006).

The application area in this research is hydrological studies over continental waters, which involves measurement over lakes, rivers and wetland environments.

1.2 Measurement of inland water surface elevation from satellite altimetry

1.2.1 The evolution of satellite altimetry technology for inland water applications

The measurement of inland water surface elevation (WSE) from satellite altimetry and methodologies for analysis of altimetric data were driven by data captured during the Seasat mission, which allowed for an assessment of the echo derived from an inland water surface and for the derivation of WSE over some of the world's larger water bodies and lake systems (Berry, 2006; Tarpanelli and Benveniste, 2019). These investigations continued over the next two decades or so using data from the Geosat, European Remote Sensing Satellite-1 (ERS-1), Topex/Poseidon (T/P), European Remote Sensing Satellite-2 (ERS-2) and Jason-1 missions. Although some of the data captured during this period have been utilised for the measurement of inland WSE, significant deficiencies with the data have limited applicability to larger inland water bodies where the radar echo return mimics that of an ocean-like target. Data from Geosat were affected by a serious off-nadir pointing issue, ERS-1 by changing orbit configurations and ERS-2 by complex and unusable data formats (Berry, 2006). Designed primarily for the measurement of SSH over oceans, both T/P and Jason-1 have proven to have significant difficulties with maintaining lock on the reflecting surface as the satellite passes across a water body where the land on either side has varying topography and vegetation cover (Berry et al., 2005a; Berry, 2006; Frappart et al., 2006).

Despite significant limitations with the altimetry data captured during this initial period, several key advances were implemented in subsequent missions as a result of the evaluation of these data. The first of these was the incorporation of an 'ice mode' from the ERS-1 and ERS-2 series that allowed for improved performance compared with altimeters with only an 'ocean mode' capability (Benveniste and Berry, 2004). The second key modification to the altimeter was the implementation of methodologies to avoid the loss of surface lock that plagued the initial series of altimeters. The Envisat (ENVIronmental SATellite) Radar Altimeter 2 (RA-2) incorporated three range resolutions adapted to different reflecting surfaces and land topography. They were controlled autonomously by an on-board model-free retracker and permitted surface lock to be maintained (Resti et al., 1999; Benveniste et al., 2001), albeit with reduced derived WSE accuracy at the coarsest of the range resolutions, resulting in limited applicability for inland water applications in this mode (Berry, 2006). The SARAL/AltiKa (Steunou et al., 2015), Jason-2 (Dubey et al., 2015) and Cryosat-2 Synthetic Aperture Interferometric Radar Altimeter (SIRAL) (Wingham et al., 2006) satellite altimeters incorporate an on-board digital elevation model (DEM) that makes it possible to dynamically change the tracking window, allowing lock to be maintained on the reflecting surface even over steep, undulating or vegetated terrain. These developments have resulted in a significant improvement in the quality and quantity of altimetry data over inland waters.

Over the past decade, considerable effort has been made to better understand the complex echo return from inland water reflectors and to implement methodologies that allow for the water surface part of these waveforms to be isolated and retracked (Berry, 2006; Hwang et al., 2006).

The current series of satellite altimetry missions concentrate on SAR technology as utilised in both the Cryosat-2 (Wingham et al., 2006; Villadsen et al., 2016) and Sentinel-3 (ESA, 2020c; Gao et al., 2019) missions. This has significantly reduced contamination from land signals in the along-track direction (Villadsen et al., 2016; Gao et al., 2019). The emphasis of this thesis is on conventional nadir-looking pulse-limited radar altimeter missions and the development of methodologies to further improve the processing and analysis of the resulting data. Thus, other than to recognise the improvement in satellite altimetry capabilities with the advent of SAR technology, analysis of these data is not undertaken.

Future technological advances are proposed to address the spatial and temporal deficiencies (Tarpanelli and Benveniste, 2019) inherent in both nadir-looking pulse-limited radar altimeters and the SAR systems. The SWOT mission based on wide-swath SAR is planned for launch in 2021. The system is designed to undertake the first global survey of Earth's surface water along with measurement of how water bodies change on a temporal scale (Biancamaria et al., 2016). SMall Altimetry Satellites for Hydrology (SMASH) is a satellite altimetry technology that is complementary to the SWOT system and consists of a constellation of satellites that will provide data on daily water levels of rivers, lakes and inland water bodies to an accuracy of 10 cm (Verron et al., 2020).

1.2.2 Rationale for the measurement of inland water surface elevation

The current world population is 7.7 billion; with a growth rate of approximately 1% per annum this is projected to reach 10 billion by 2057 (United Nations Department of Economic and Social Affairs [UN-DESA], 2019). Population distribution is highly correlated with the location and availability of water, whether for human consumption, food resource management or transport, as human development prioritises regions of steady and continuous water supply. A growing world population will increase the need to monitor both the spatial extent and temporal change of freshwater occurrences to ensure that freshwater supply is available.

Climate change brings uncertainty to the issue of water supply and availability. In some locations, an increase in the frequency of flood events is likely, with the potential to cause loss of life, destruction of housing and farmland, and destruction or contamination of water supply. There is also potential for drought to affect water and food availability as well as health (United Nations Water [UN-Water], 2019).

Additionally, human impacts can have a significant effect on the availability and supply of water. Water supply through the Murray–Darling Basin in Australia is illustrative of upstream water allocations for farming and agriculture that have significant adverse effects on the water supply for human consumption and environmental flows downstream (Kirby et al., 2008). At the opposite extreme, raised river bed levels caused by riverine disposal of waste rock and tailings materials through mining at the headwaters of the Fly River catchment in Papua New Guinea (PNG) has had a significant impact on floodplain inundation levels, with inundation and environmental impacts forecast to continue rising well after mine closure (Pickup and Marshall, 2019).

To manage the pressure that population growth, human impact and climate change is having on the allocation of, and access to, water there is an increasing need to monitor the world's water resources, independent of infrastructure and inter-government policies (Frappart et al., 2006; Schwatke et al., 2015b; Villadsen et al., 2016). Traditionally the realm of the hydrologist, this task has been based on the deployment of in-situ gauges and instruments for the monitoring of WSE at discrete locations. Despite this requirement for an increase in hydrological effort, the number and spatial distribution of in-situ gauges have decreased over recent decades (Frappart et al., 2006). This reduction has prompted a focus on the capabilities of satellite-based technologies, primarily satellite altimetry, to augment the existing hydrology in-situ network and ultimately replace it with a global water level monitoring tool for inland rivers, lakes and wetlands with sufficient spatial and temporal coverage to meet current and forecasted hydrological demands (Santos da Silva et al., 2014; Biancamaria et al., 2016; Verron et al., 2020).

1.2.3 Current satellite altimetry capabilities for inland water surface elevation measurement

Satellite altimetry capabilities for inland water measurement have steadily improved over the past decade in line with improvements in altimeter technology as well as data processing methodologies. The main improvements have come from reprocessing of raw data using retracking algorithms permitting satellite-to-surface range definition—optimised for ocean surfaces—to now better reflect what is found through inland zones (Berry, 2006; Frappart et al., 2006; Santos da Silva et al., 2010). Retracking investigations have concentrated on the performance of the Ocean-1, Ice-1, Ice-2 and Sea Ice retrackers for various inland water applications, as detailed, for example, in Frappart et al. (2004), Berry et al. (2005a), Frappart et al. (2006), Santos da Silva et al. (2010), Maillard et al. (2015) and Schwatke et al. (2015a). The majority of the echoes that result from inland water reflectors do not conform to the Brown–Hayne model (Berry et al., 2005b; Freeman and Berry, 2006) and cannot be retracked using standard ocean retrackers such as the maximum likelihood estimator (MLE) and NASA β (Schwatke et al., 2015b). Significant effort has concentrated on the development of empirical retrackers that perform best for inland water applications. Such retrackers include the Improved Threshold Retracker (Hwang et al., 2006; Bao et al., 2008; Lee et al., 2008) and various sub-waveform retrackers (Yang et al., 2012; Passaro et al., 2014) that deconstruct the waveform, retaining only the nadir-reflected sub-waveform.

Significant effort has also been assigned towards what is recognised as the largest source of error for inland water altimetry. Specular reflectors within the altimetric footprint can lead to an off-nadir distortion termed hooking (Santos da Silva et al., 2010), which, if not detected, will result in an over-estimate of the satellite-to-nadir range and an incorrect WSE estimate. Various methodologies for correction of the hooking effect have been developed and implemented over the past decade (Santos da Silva et al., 2010; Maillard et al., 2015; Schwatke et al., 2015a; Boergens et al., 2016). The majority of these relate to nadir-looking pulse-limited radar altimeters as it is reported that the effect is significantly reduced in SAR altimetry because of the smaller altimeter footprint (Villadsen et al., 2016).

Over the past two decades, numerous altimetry applications over inland waters have been investigated and include studies of lakes (Crétaux and Birkett, 2006; Sarmiento and Khan, 2010; Crétaux et al., 2011; Abileah et al., 2014; Schwatke et al., 2015a; Sulistioadi et al., 2015), rivers (Frappart et al., 2006; Berry et al., 2005; Santos da Silva et al., 2010; Michailovsky et al., 2012; Jarihani et al., 2013; Schwatke et al., 2015a; Maillard et al., 2015; Boergens et al., 2016), wetlands (Smith and Berry, 2007; Khajeh et al., 2014; Zakharova et al., 2014; Dettmering et al., 2016) and flood forecasting (Biancamaria et al., 2011; Jarihani et al., 2013).

Accuracies—reported as the root mean square error (RMSE) based on comparisons with in-situ gauges—of WSEs derived from satellite altimetry systems over inland waters vary significantly. While a function of water body extent and the retracker used, there is relatively little variation between the various nadir-looking pulse-limited altimetry platforms. Over larger rivers and lakes, the reported accuracies approach those achieved in open water applications. For example, Ghosh et al. (2015) reports 1.5 cm from SARAL/AltiKa, Schwatke et al. (2015a) reports 3–5 cm for both Envisat RA-2 and SARAL/AltiKa, Nielsen et al. (2015) reports better than 8 cm for both Cryosat-2 SAR and Envisat RA-2 and Yi et al. (2013) reports 10–14 cm from Envisat RA-2. For studies undertaken over smaller rivers and lakes or complex wetlands, the reported accuracies depart significantly from those achievable in open water cases. Frappart et al. (2006) reports accuracies of 30 cm for rivers and 50 cm for wetlands. However, with careful data filtering and appropriate retracking, accuracies in the order of 30–70 cm (Santos da Silva et al., 2010; Kuo and Kao, 2011; Michailovsky et al., 2012; Dettmering et al., 2016) are achievable; accuracies exceeding 100 cm (Jarihani et al., 2013; Maillard et al., 2015; Zakharova et al., 2020) have been reported for some of the more complex environments. An understanding of distortions that affect the radar echo over inland water environments and the development of methodologies to identify and rectify these distortions will lead to significantly improved accuracies of the derived WSE, approaching those achieved over open water environments.

There has also been a series of global databases developed for inland WSE data that have been made available for public use; some of these are listed in Table 1-1.

Table 1-1 Global databases for inland WSE data derived from satellite altimetry

Database	Developer and web address
Hydroweb	Laboratoire d'Etudes en Géophysique et Océanographie Spatiales (LEGOS) http://www.legos.obs-mip.fr/soa/hydrologie/hydroweb/http://www.legos.obs-mip.fr/soa/hydrologie/hydroweb/ http://hydroweb.theia-land.fr/
River and Lake	ESA & De Montfort University http://altimetry.esa.int/riverlake/shared/main.html
Global Reservoir and Lake Monitor	Foreign Agricultural Service of the United States Department of Agriculture (USDA) http://www.pecad.fas.usda.gov/cropexplorer/global_reservoir/
Database for Hydrological Time Series over Inland Waters (DAHITI)	Deutsches Geodätisches Forschungsinstitut & Technische Universität München https://dahiti.dgfi.tum.de/en/
Altimeter Open Loop Tracking Command for Hydrology (OLTC)	ESA https://www.altimetry-hydro.eu/
Global River Radar Altimetry Time Series (GRRATS)	Ohio State University (OSU) and the University of California, Los Angeles (UCLA) as part of a NASA grant. https://podaac.jpl.nasa.gov/Pre-SWOT_Global_Storage_Change_Time_Series_Data
Copernicus Global Land Service	European Commission Joint Research Centre, European Commission. https://land.copernicus.eu/global/products/wl

A description of the processing methodologies for the first four databases can be found in Schwatke et al. (2015b). The OLTC and GRRATS datasets are recent additions. OLTC was developed for the ESA in 2018 and allows for inland water bodies to be defined by geographic location and to have WSE autonomously derived from the OLTC tables onboard the ESA Sentinel-3 Synthetic Aperture Radar Altimeter (SRAL). GRRATS was developed by OSU and UCLA as part of a NASA grant and uses Envisat and Ocean Surface Topography Mission (OSTM)/Jason-2 radar altimeter data covering the period 2002–16. The method runs unsupervised and is applied to all altimeter crossings of ocean-draining rivers with widths greater than 900 m (Coss et al., 2020).

The databases derive water level time series on a global basis for the larger inland rivers and lakes, with locations constrained by a combination of geographic coordinates and water mask. WSEs are extracted for each database using different retracking and estimation methodologies with results being included if statistical analysis of results determines the derived WSE to be valid (Berry, 2006).

1.3 Study domain

The study domain for this research is the Western Province of PNG and includes the middle Fly River floodplain as well as Lake Murray to the east. Figure 1-3 shows the study location adjacent to PNG's western border with Indonesia.

Figure 1-3 The study domain of the Fly River floodplain and Lake Murray, circled in red. The study area is located within the Western Province of PNG (ezilonMaps, 2009).

The Fly River drains an area of approximately 75,000 km^2 from the highlands of PNG and flows south into the Gulf of Papua (Pickup and Marshall, 2009). The river is considered one of the world’s major rivers, with the highest run-off per unit area of catchment and a mean discharge over 6,000 m^3 s^{-1} (Milton et al., 2005), although the discharge through the middle Fly study area is less, at around 2,200 m^3 s^{-1} (Day et al., 2008). The middle Fly floodplain is the region downstream from the junction with the Ok Tedi (DÁlbertis Junction) to the junction with the Strickland River (Everill Junction) as shown in Figure 1-4.

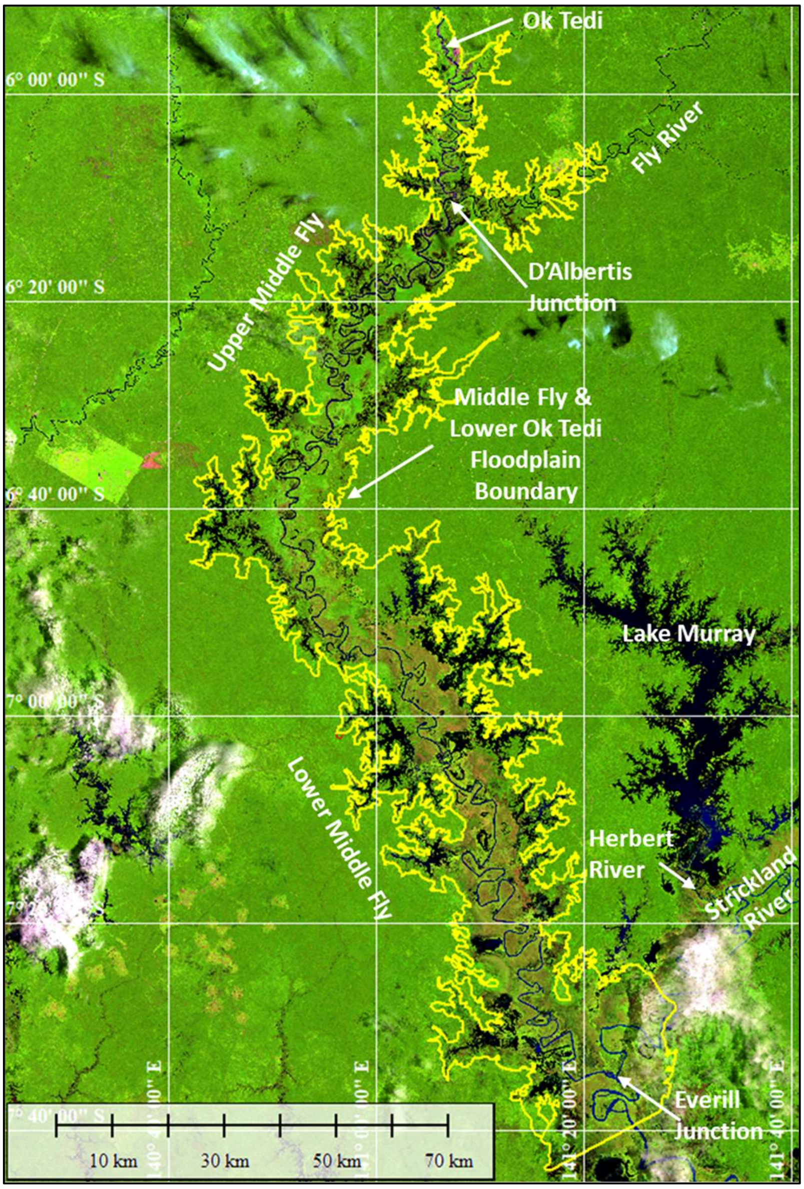

Figure 1-4 The Fly River floodplain and Lake Murray study domain. The background is a false colour Landsat TM5 image from February 2004.

The Fly River meanders for approximately 400 km through this region, which comprises extensive scroll-bar complexes, cut-offs and blocked-valley lakes (Pickup and Marshall, 2009). The region is characterised by a humid tropical climate with rainfall varying from 10 m a^{-1} in the upper reaches of the catchment down to approximately 5 m a^{-1} over the floodplain. Not only do rainfall rates, and consequently floodplain inundation levels, vary significantly between seasons but the region is also subject to periodic El Niño events (Pickup and Marshall, 2009) during which floodplain inundation drops significantly below average lows.

Inundation of the middle Fly River floodplain is influenced by upper catchment rainfall that impacts the spatial extent and depth of inundation. These factors directly control the diversity, density and extent of colonising floodplain vegetation. Figures 1-5 to 1-8 show the variability in floodplain vegetation type as well as inundation regime across the study area.

Figure 1-5 Lowland tropical rainforest colonises a large portion of the inundated floodplain through the upper-middle Fly reach The forest has been affected by an increase in inundation frequency and duration linked to upstream mining activities.

Figure 1-6 At the edge of the floodplain there is a rapid transition from an inundated zone colonised by aquatic grasses to a zone of lowland tropical rainforest established along a relatively low and flat region of higher ground.

Figure 1-7 A complex mix of floodplain forest and grass savannahs characterises the transition between upper- and lower-middle Fly in the northern half of the study area.

Figure 1-8 The lower reaches of the middle Fly floodplain show extensive zones of open water along with isolated zones of lowland tropical rainforest colonising the higher ground and aquatic grasses colonising shallow inundated areas.

Some of the blocked-valley lakes are permanently inundated and void of aquatic vegetation; however, the majority of the floodplain is characterised by a complex mix of environments ranging from clear open water through to inundated zones that are colonised by aquatic floodplain vegetation and, under a lower rainfall regime, a bare floodplain. The Fly River floodplain is predominantly inundated with average annual inundation rates of 30–50% through the upper reaches of the middle Fly, and approaching 90% through the lower reaches (Pickup and Marshall, 2009).

The middle Fly floodplain is divided into two major zones. The upper-middle Fly was originally a zone of lowland tropical rainforest coupled with isolated oxbows and blocked-valley lakes. Through mining impact, an increase in floodplain inundation rates since the early 1990s has resulted in vegetation dieback through the reach and an increase in off-river water body extent as well as inundation duration (Marshall, 1999).

The lower-middle Fly floodplain zone is usually inundated, with an average annual inundation frequency of 90%. The zone is colonised by grassland and aquatic vegetation as well as isolated islands that are elevated above the average inundation depth and colonised by lowland tropical rainforest. The floodplain is bordered by lowland tropical rainforest and there are numerous oxbows, blocked-valley lakes and other off-river water bodies scattered through the reach. Although the water level between all the floodplain entities would be relatively consistent at high Fly River water levels, there is a significant WSE difference during low flows because of differential drainage from the floodplain to the river. Mining impact has been less through this zone with the major change being an increase in overall floodplain inundation duration compared with the pre-mine state.

A transition zone links the impacted floodplain forest and the extensive grassland and aquatic regimes. Although there is significant variability in inundation extent and vegetation, the topography throughout the study area is relatively flat with elevation change from the floodplain through to the adjacent higher ground being generally less than 50 m. Figure 1-9 shows the floodplain digital surface model (DSM) generated from the Japan Aerospace Exploration Agency (JAXA) Advanced Land Observing Satellite (ALOS) between 2006 and 2011 (JAXA, 2011).

Lake Murray is PNG's largest lake and covers an area of approximately 64,700 ha; however, this can increase significantly during periods of high catchment rainfall. The lake is approximately 70 km long and 15 km wide and has a shoreline that is highly convoluted with many minor tributaries draining from the surrounding elevated ground (Osborne et al., 1987). The lake is located within a region of relatively flat terrain as shown in Figure 1-9 and its location relative to the Fly River floodplain as well as the Herbert and Strickland rivers is shown in Figure 1-4.

While Lake Murray drains via the Herbert River into the Strickland River to the south, there are periods where, at high river levels on the Strickland River, a reversal of flow back into Lake Murray is observed (Day et al., 2008). While the water body is predominantly devoid of vegetation through the central regions of the lake, there is some aquatic vegetation in the shallower zones of the tributaries to the lake.

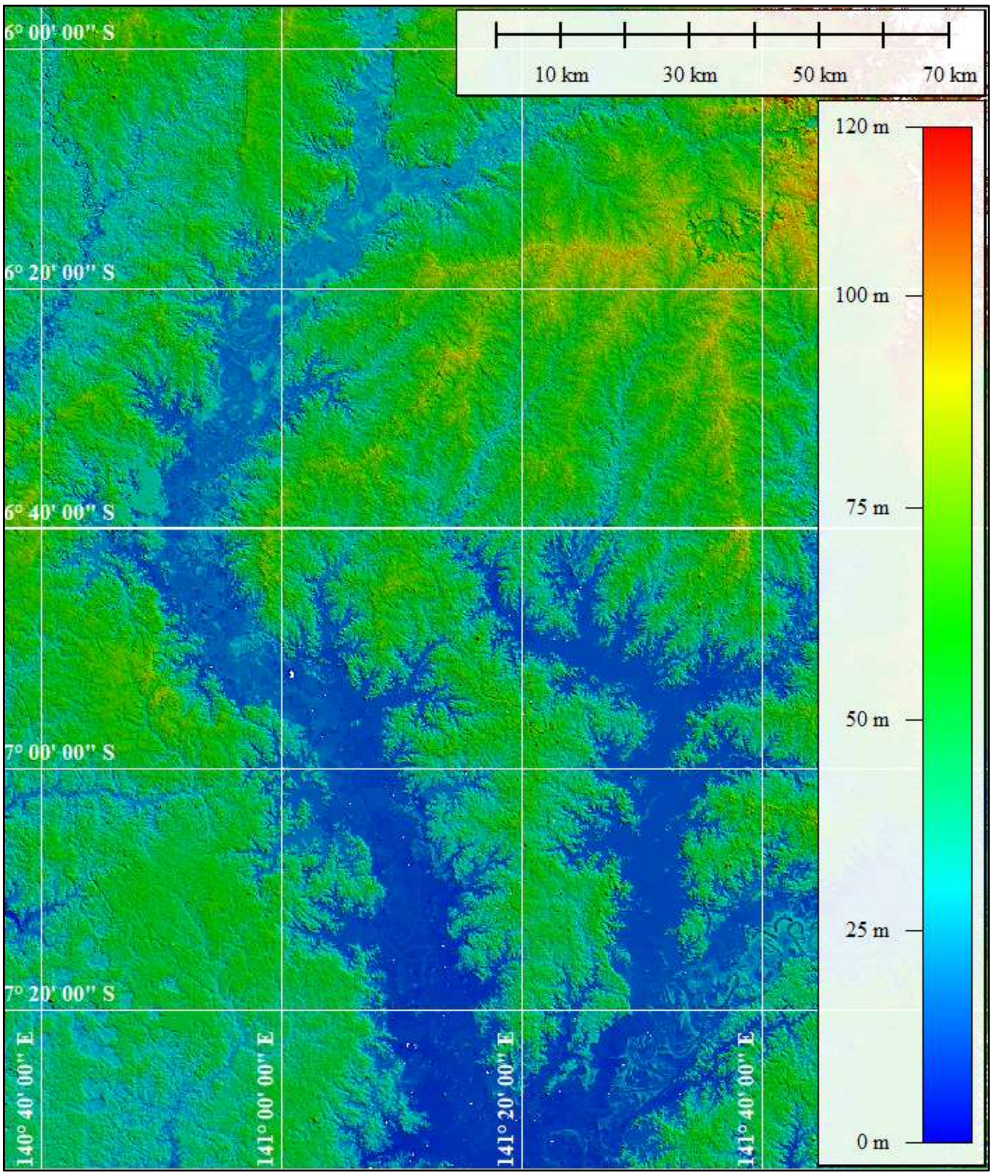

Figure 1-9 ALOS World 3D DSM of the middle Fly floodplain and Lake Murray showing elevation variations between the floodplain and the bordering higher ground to be less than 50 m.

1.4 Significance of the research

Section 1.2.2 highlighted the rationale for the monitoring and measurement of inland WSE. It also introduced the fact that the Fly River floodplain is an impacted environment where ongoing monitoring of water level change through the various floodplain and wetland entities is required as a result of increasing inundation associated with mining operations in the upper catchment of the river system (Pickup and Marshall, 2009; Pickup and Marshall, 2019). In addition to inundation increases, there are also predictions of increasing sedimentation that is likely to result in some water bodies becoming isolated from the main river while others maintain a connection. In such cases a riverine gauge will not be representative of water levels within the isolated water body. Figure 1-10 is an example showing a blocked lake that has become isolated from the Fly River to the extent that measured WSE from any riverine gauge will not be representative of water levels for water bodies in the southern portion of the image. Altimetry-derived WSE profiles would readily enable differentiation of the relative floodplain inundation levels for these water bodies.

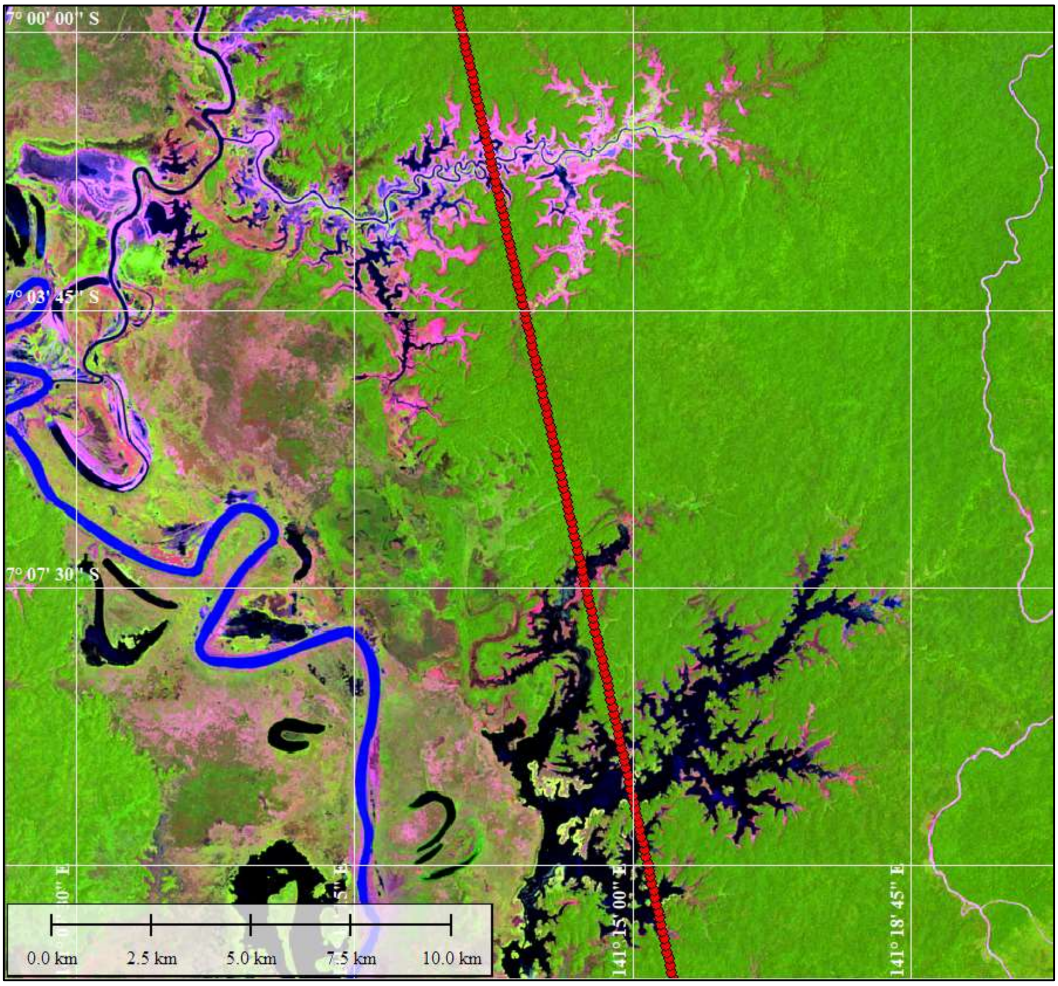

Figure 1-10 SARAL pass 0677 cycle 24 from 20 June 2015 overlayed on a Landsat ETM7 false colour image captured in October 2002 during an El Niño event. To the east of the Fly River are two major blocked-valley lakes. The northern lake has drained to the Fly River, as expected during an El Niño; however, the southern lake has a blocked tie channel so a riverine gauge would not be representative of changes in water body inundation for this location.

Floodplain, off-river water body and river water levels are likely to become increasingly varied throughout the system as the different floodplain entities become impacted. Along with environmental impact, there is a significant impact on the people living within the Fly River floodplain zone. Benefits of mining, such as improved health and education along with improved access to goods and services, meant that the population of the region increased from approximately 5,000 in the early days of mining (Swales, 2001) to approximately 30,000 by 1995 (Watling et al., 1995) and almost 80,000 by 2011 (PNG, 2013). The traditional landowners are hunters and gatherers who have been adversely impacted by floodplain inundation changes. The land is being converted from lowland tropical rainforest to impacted grassland or open water aquatic environments. The nearest viable land for hunting, gardening and food gathering increasingly is located at the edges of the floodplain on land elevated above the inundated floodplain.

Changing inundation regimes throughout the Fly River floodplain are likely to continue long after mining ceases (Pickup and Marshall, 2019) and, while there are currently a series of gauges on the Fly River for monitoring changing inundation, maintenance of these gauges is unlikely to continue past mine closure, currently estimated to be 2025 (OTML, 2020).

There will become an increasing need to support Fly River local communities with information regarding predicted changes to inundation that could lead to potential impacts on their communities and subsistence livelihood.

Future satellite altimetry missions are likely to utilise SAR technology, as is the case for the current Cryosat-2 (Wingham et al., 2006; Villadsen et al., 2016) and Sentinel-3 (Gao et al., 2019; ESA, 2020c) missions. Data from such platforms have significantly reduced contamination from land signals in the along-track direction (Villadsen et al., 2016; Gao et al., 2019). Issues that plague the processing of altimetry data acquired by conventional nadir-looking pulse-limited altimeters are significantly reduced in the altimeters based on SAR technology because of a greatly reduced footprint size. For calm water or over flat land the pulse-limited altimeter footprint is approximately 2 km. However, it will increase in size significantly up to 18 km for rough waters or where there is significant topographic and vegetation variation (Rosmorduc et al., 2018), while the SAR footprint is typically a fraction of this. For pulse-limited nadir-looking altimeters contamination from surrounding topography and vegetation as well as the hooking effect of multiple specular reflectors within the footprint means that the extraction of reliable data over inland water zones is a complex multi-task process for which, in some cases, there is no current solution and there is little option but to omit such measurements from the processing sequence.

While the advent of SAR technology is likely to solve many of the problems encountered in processing altimetry data over inland waters into the future, there are considerable unsolved problems with the 20+ years of altimetry data from the ERS-1, ERS-2, Envisat, Jason-1, Jason-2, SARAL, Cryosat-2 and HY-2A satellites, although only HY-2A Level-2 data products are currently available (Observing Systems Capability Analysis and Review [OSCAR], 2020). These data would offer a valuable baseline of floodplain WSE time series over multiple floodplain water bodies if the issues associated with waveform contamination, particularly hooking, could be identified and rectified.

The primary aim of this research is to investigate the micro-scale aspects of nadir-looking pulse-limited altimetry waveforms such that accurate WSE time series can be routinely extracted for passes over complex wetlands as well as over smaller rivers and lakes, covering the full middle Fly inundation range.

1.5 Research objectives

The derivation of WSE from satellite altimetry can be considered a mature science, particularly for the case of nadir-looking pulse-limited radar altimeters. The history of research dates back nearly half a century to the Seasat era for ocean investigations and at least 20 years for investigations over inland waters. The work undertaken by researchers during this period has resulted in a significant understanding of the processes that affect the radar echo and the resulting waveform recorded by the satellite altimeter. Such research has facilitated the development of methodologies for the analysis and creation of altimetry-derived WSE time series. While an understanding of the significant issues associated with the contamination of the altimeter return echo by the receiving environment—particularly over inland waters—has also been developed, it has resulted in limited use of satellite altimetry for investigations over inland waters, with application predominantly restricted to time series analysis for the larger river and lake systems where echo contamination is relatively low. In these cases, the derived water surface time series rely primarily on multiple, statistically consistent, water surface definitions for the validation process.

The current state-of-the-art satellite altimetry analysis methodologies over heterogeneous inland waters do not meet the accuracy and reliability requirements for water surface measurement over relatively small river and lake systems, particularly where WSE estimates are required both temporally and spatially. This project aims to develop methodologies that enable routine as well as accurate and reliable extraction of WSE from nadir-looking pulse-limited radar altimeters over heterogeneous inland waters. This is achieved by deconstructing the shape and form of the recorded waveform and correlating that form against external inputs so that the input factors that have affected the shape and form of the waveform are understood and can be addressed. The external inputs comprise a range of supporting data, including satellite imagery and in-situ water level observations, but also rely on knowledge of the receiving environment. Micro-scale assessments of the waveform structure facilitate a rigorous assessment of the shape of the waveform and how it represents the receiving environment.

These external inputs become a fundamental control in the selection of appropriate pre-processing and retracking methodologies so that there is an expectation that the derived WSE estimate is both accurate and represents the identified nadir-receiving environment. Of equal importance is that the process facilitates the discarding of waveforms that do not meet quality criteria or match expected echo return profiles. This retracking process is to be undertaken robustly and autonomously and to incorporate statistical verification and rigorous outlier detection.

The significant advancement over conventional processes is that waveforms and the associated WSE are retained based on an understanding of the waveform itself in conjunction with the waveform's statistical relationship to adjacent waveforms. This facilitates the retention of water level estimates over relatively small water bodies where multiple, statistically consistent, WSE estimates would not be practical. The processes developed in this research offer a methodology for the extraction of reliable WSE estimates, in both a temporal and spatial context, over heterogeneous inland waters. The methodologies developed offer potential for the reprocessing of a significant archive of nadir-looking pulse-limited radar altimeters as well as supporting analyses of the data from currently operational altimeters into the future.

Based on the discussions in Section 1.2 and 1.4, research objectives have been developed to address the current limitations of altimetry WSEs derived over heterogeneous inland waters to facilitate developments that will permit future inundation monitoring for these locations to be met by satellite altimetry. These objectives are:

a) To investigate the types of altimetry waveforms that result in different altimetry footprint types using data from Envisat RA-2 as the primary data source. Footprint variability will include open water, the water–land interface, cleared land and vegetated land environments, as well as a combination of these. Altimetric waveform structure for various inundation levels will also be assessed. Results from the Envisat RA-2 investigations will be verified for consistency against returns from SARAL/AltiKa and Cryosat-2 SIRAL waveforms.

b) To investigate the current suite of altimetry waveform retrackers with an emphasis on those that have both been effectively used over inland water environments and developed specifically to facilitate retracking of waveforms that deviate from the typical Brown–Hayne ocean model form. Where practical it is intended to optimise the retrackers to facilitate improved and more robust processing of complex and multi-peaked waveforms typical of heterogeneous inland waters.

c) To develop methodologies that will facilitate the automated extraction of an altimetry footprint classification so that the nadir-receiving environment for each waveform can be accurately defined. The process will be based on remote sensing and image analysis techniques using a suite of radiometric and SAR imagery covering the range of expected inundation states. Ancillary information from the altimetry Sensor and Geophysical Data Record (SGDR) will also be utilised.

d) To investigate the impact of off-nadir distortion on the altimetry waveform and estimate the extent and magnitude of the effect for various altimetry footprints and inundation ranges. This will be developed from the Envisat RA-2 SGDR datasets but will be supported using both SARAL/AltiKa and Cryosat-2 SIRAL data. The analysis will utilise ancillary information from the altimetry SGDR data, such as the magnitude of backscatter coefficient and waveform shape characteristics. It will also include information from the altimetry footprint classification process where confirmation of land-to-water hooking and water-to-water hooking can be identified.

e) To develop a process that facilitates the identification of whether a waveform is impacted by hooking, particularly for complex wetland environments, where there are likely to be numerous reflectors within each altimetry footprint. If the hooking effect can be unambiguously removed, then methodologies to facilitate this will be developed. For cases where the hooking source cannot be accurately identified then the waveform can be confidently omitted from the waveform sequence so that the WSE profile is not contaminated.

f) To prepare water level time series for select passes over the Fly River floodplain and over Lake Murray to demonstrate the impact of the proposed processing methodologies with an emphasis on improvement relative to existing methodologies. Validation of derived altimetry WSE is proposed against a series of in-situ gauges as well as internally via statistical consistency.

1.6 Thesis outline

This thesis consists of eight chapters. Chapter 1 presents an introduction to the research project. It includes a brief description as well as a history of satellite radar altimetry; a more detailed introduction of satellite altimetry measurement capabilities over inland waters; and a rationale for why this capability is required. Further, it documents the current state-of-the-art for satellite altimetry monitoring and measurement for inland waters. The chapter also introduces the study domain for the research: the Fly River floodplain and Lake Murray located within the Western Province of PNG. The chapter concludes with a review of the significance of the research and details of the project objectives.

In Chapter 2 the details of the nadir-looking pulse-limited radar altimeters utilised in the research are introduced and the technical specifications of the instruments are detailed. The chapter includes a summary of the principles of satellite radar altimetry and details the range and geophysical corrections to be applied in processing. The chapter concludes with a review of the satellite altimetry data types and formats used in the analyses.

The location and availability of in-situ river level data within the Fly River study domain are documented in Chapter 3. This chapter includes details of the fieldwork program undertaken to establish in-situ floodplain water level gauges and the derivation of floodplain virtual gauges to facilitate longer-term analysis at these sites.

In Chapter 4 the process of altimetry footprint classification is developed. A classification methodology assessing footprint inundation extent, based on image analysis using both multi-spectral and SAR imagery, is presented along with the results of the classification process. The methodology is extended to include a full definition of landform cover type as well as prediction capabilities for identifying off-nadir calm water locations.

Chapter 5 introduces the principle of waveform retracking and details the range of retrackers that are available based on both model fitting and empirical methodologies. Detailed reviews are undertaken for retrackers suited to inland water applications. The chapter brings together the key developments of this research project. Sub-waveform identification and selection methodologies, optimised for complex inland waters, have been developed in this study as an improvement on the Improved Threshold Retracker. An adaptive altimetry threshold retracking process developed in this study—the Waveform Adaptive Threshold Retracker (WATeR)—is detailed in this chapter. The final section of the chapter documents the software developed to facilitate the required analysis.

Chapter 6 details the dominant waveform distortions that are likely for inland water targets. The discussion focusses on the hooking effect, which is recognised as the largest source of uncertainty for satellite radar altimetry over inland waters, and details its impact on the accuracy of the derived altimetric WSE sequence This chapter introduces existing methodologies for the correction of the hooking effect and analyses specific contexts in which these corrections can be applied. Forms of the hooking effect are introduced with land to water for both single and multiple specular reflectors, as well as hooking over water bodies with variable calm and rough water zones. Methods for the accurate identification of waveforms impacted by hooking are developed. Tools for the rectification of the impact, identification of the likely specular reflector location and, in cases where rectification is not possible, estimation of the likely magnitude of the distortion so the deletion of the waveform can be undertaken if required, are also developed.

Distortions associated with waveform averaging and waveform saturation are also reviewed in Chapter 6. Waveform saturation predominantly affects SARAL/AltiKa and occurs when significant specular reflectors exist within the altimetry footprint. The impact of this saturation on the derived altimetric WSE profiles is assessed and methods for the identification of waveforms to be omitted from the WSE sequence are developed. The impact of waveform averaging on the derived altimetric WSE profiles is reviewed.

In Chapter 7 the WATeR adaptive retracking methodology is utilised for the creation of temporal and spatial altimetric waveform sequences over a range of diverse locations on the Fly River, within the Fly River floodplain and over Lake Murray. Validation of the derived altimetry data is undertaken by direct comparison with virtual in-situ river gauge data and virtual floodplain gauge data. In addition, statistical analyses are undertaken to assess the internal consistency of the derived data. Comparison of WATeR WSE time series is undertaken between data extracted from global databases, specifically Theia Hydroweb and ESA River and Lake, in order to assess performance of the retracking process relative to published alternatives.

Chapter 8 summarises the thesis with an emphasis on the main developments and achievements of the research. The chapter reviews the processes required to optimise altimetry waveform retracking over heterogeneous inland waters, documents limitations of the proposed methodologies, and introduces recommendations for future research. The study results are summarised for floodplain, lake and river time series data as well as for WSE profiles covering the full extent of the floodplain.

CHAPTER 2: SATELLITE ALTIMETRY

2.1 Satellite altimeters

In this research project, the performance of three nadir-looking pulse-limited radar altimeters has been evaluated. The majority of the work has been undertaken using data from Envisat RA-2, but additional investigation based on data from SARAL/AltiKa and the Cryosat-2 SIRAL low-resolution mode (LRM) altimeter has also been undertaken. Pulse-compression deramping techniques and the general principles of pulse-limited altimetry are described in Chelton et al. (2001) and the performance parameters for each satellite are detailed in Table 2-1.

Table 2-1 Satellite altimeter performance parameters for Envisat RA-2, SARAL/AltiKa and Cryosat-2 SIRAL (Resti et al., 1999; Bouzinac, 2010; Soussi, 2011; Quartly and Passaro, 2014; Steunou et al., 2015; Schwatke et al., 2015a; Bronner et al., 2016)

	Envisat RA-2	SARAL/AltiKa	Cryosat-2 SIRAL
Altimeter	RA-2 dual-frequency, pulse-limited nadir-looking radar	AltiKa single-frequency, pulse-limited nadir-looking radar	SIRAL single frequency pulse-limited nadir-looking altimeter (LRM mode)
Mean orbit altitude	~800 km	~800 km	~700 km
Orbit inclination	98.5°	98.5°	92°
Repeat period	35 days	35 days	369 days
Equatorial ground track spacing	~80 km	~80 km	~7.5 km
Altimeter band	13.575 GHz (Ku-band)	35.75 GHz (Ka-band)	13.575 GHz
Pulse bandwidth	320, 80, 20 MHz	500 MHz	350 MHz
Pulse duration	20 µs	110 µs	44.8 µs
Antenna diameter	1.2 m	1.0 m	1.2 m & 1.1 m (side-by-side)
Antenna beamwidth (3 Db)	1.29°	0.61°	1.06° (along track) 1.1992° (across track)
Vertical resolution	0.47 m	0.31 m	0.469 m
Pulse repetition frequency (PRF)	1.8 kHz	3.8 kHz	1.97 kHz
Echo averaging	18 Hz	40 Hz	20 Hz
Number of individual echoes (IEs) for each averaged echo	100	96	91
Samples per echo	128	128	128
Ionospheric correction	Smoothed dual-frequency (to cycle 64) then Jet Propulsion Laboratory (JPL) global ionospheric map (GIM)	JPL GIM	JPL GIM
Wet tropospheric correction	Microwave radiometer (MWR)	Model (European Centre for Medium Weather Forecast (ECMWF))	Model (ECMWF)
Dry tropospheric correction	Model (ECMWF)	Model (ECMWF)	Model (Meteo France)

2.1.1 Envisat RA-2

The Envisat mission was launched on 1 March 2002 by the ESA, tasked with continuing the altimetric observations of ERS-1 and ERS-2. The altimetry payload comprised a dual-frequency, nadir-looking pulse-limited RA-2 instrument operating in Ku and S bands for the measurement of satellite-to-surface range, a dual-frequency nadir-viewing MWR for the determination of the tropospheric delay, a dual-frequency DORIS system for precise orbit determination and a LRR for range measurement calibration (Benveniste et al., 2001). The dual-frequency nature of the RA-2 instrument enabled the correction of range errors induced by the ionosphere (Resti et al., 1999) through to cycle 64 when S-band failed and the correction was model based from that time (Bosch et al., 2014). Figure 2-1 shows the Envisat satellite configuration, detailing the instrument payload including the RA-2 altimeter.

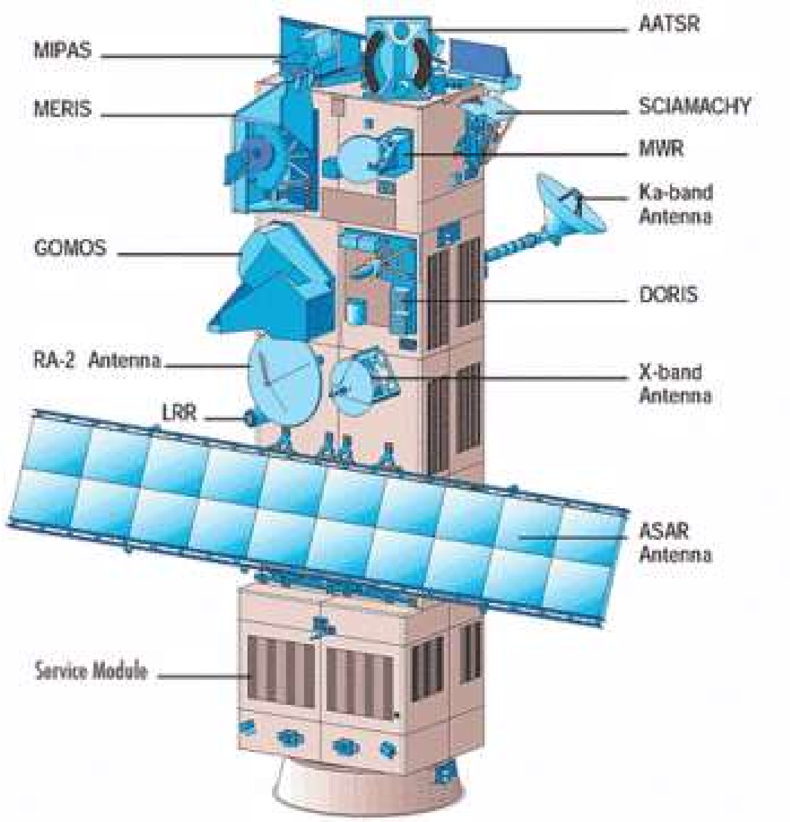

Figure 2-1 A schematic diagram of the Envisat satellite detailing the instrument payload including the RA-2 altimeter (AVISO+, 2020).

The Envisat RA-2 altimeter used linearly frequency-modulated pulses (chirps) to achieve high range resolution but at low power demands and this was based on a full-deramp technique. The altimeter utilised a model-free tracker whereby transmission bandwidth was able to vary between 320, 80 and 20 MHz to enable autonomous uninterrupted tracking of the reflecting surface (Resti et al., 1999). Envisat RA-2 operated with a PRF of 1800 Hz from which averaged waveforms were generated at 18 Hz (Benveniste et al., 2001). At the

320-MHz transmission bandwidth, the waveform comprised 128 samples with a tracking range gate of 0.47 m (Roca et al., 2009).

The reference ellipsoid for Envisat is the World Geodetic System 1984 (WGS84), which is defined by an equatorial radius of 6378137 m and a flattening coefficient of 1/298.2572236 (Soussi, 2011), with SSH derived using the Earth Gravitational Model 1996 (EGM96) geoid (ESA, 2014). Envisat operated in a sun-synchronous orbit at an approximate altitude of 800 km and with a repeat period of 35 days (Benveniste et al., 2001) and remained in its original orbit until it moved into a new lower repetitive orbit on 22 October 2010 (AVISO+, 2012). The mission ended on 8 April 2012 (Blarel et al., 2015) when communication with the satellite was lost.

2.1.2 SARAL/AltiKa

The SARAL mission was launched on 25 February 2013 in an orbit consistent with Envisat. The altimetry payload consisted of a mono-frequency, nadir-looking pulse-limited radar altimeter (AltiKa) operating in Ka-band, a dual-frequency MWR for the determination of the tropospheric delay, a dual-frequency DORIS system for precise orbit determination and an LRR array for range measurement calibration. Although the mono-frequency altimeter is unable to determine the ionospheric delay, the magnitude of the delay is considered very low in Ka-band (Steunou et al., 2015; Bronner et al., 2016) and the correction is based on the JPL GIM (Bosch et al., 2014). Figure 2-2 shows the SARAL satellite configuration with the instrument payload including the AltiKa altimeter.

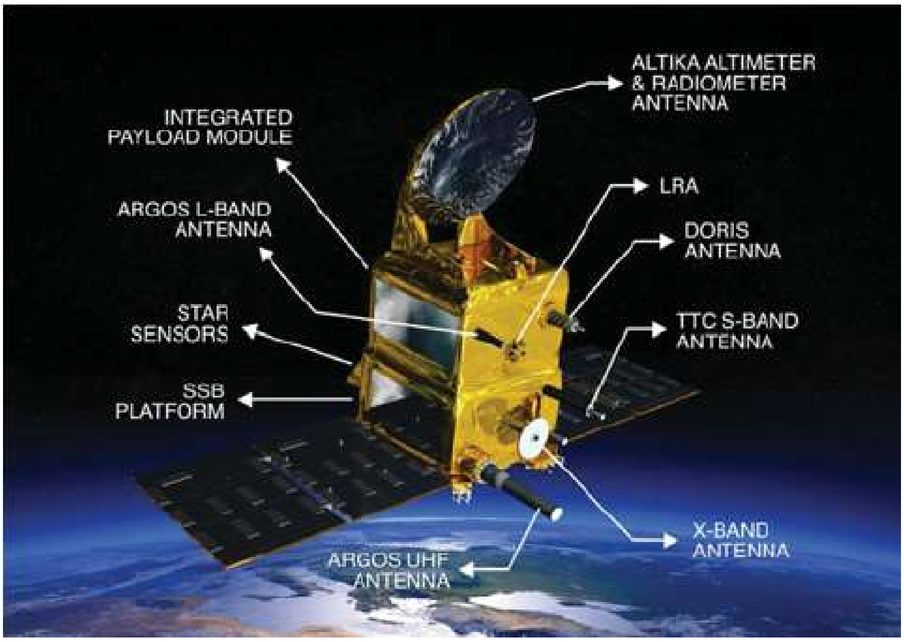

Figure 2-2 The SARAL satellite showing the instrument payload including the AltiKa altimeter (Verron et al., 2015).

SARAL/AltiKa operates with the full-deramp technique for pulse compression, which allows for high range resolution to be achieved with lower transmission power and telemetry data rate. As with RA-2, this is achieved via the transmission of a chirp pulse as the active signal (Steunou et al., 2015).

The main disadvantage of Ka-band altimetry relates to its high sensitivity to atmospheric liquid water, with significant attenuation rates of the pulse under light rain or cloudy conditions. In comparison, the Ku-band pulse is impacted only under significantly heavier rainfall conditions (Steunou et al., 2015; Tournadre et al., 2015; Verron et al., 2015; Zhang and Sandwell, 2017). Tournadre et al. (2009) report significant waveform distortion in cases of cloud/rain variability within the altimeter footprint which leads to erroneous geophysical parameter estimates. However Verron et al. (2018) and Bonnefond et al. (2018) report little practical impact of rain on the availability and quality of the Ka-band altimetric data and, despite uncertainty around the impact of rain attenuation on the determination of the backscatter coefficient (Bronner et al., 2016), the quality exceeds pre-mission targets (Verron et al., 2018).

The SARAL/AltiKa PRF is 3540–3780 Hz with averaged waveforms generated at 40 Hz for transmission via telemetry to the ground. With a 500-MHz transmission bandwidth, the waveform echo is comprised of 128 samples with a tracking range gate of 0.31 m (Zhang and Sandwell, 2017). SARAL/AltiKa can operate in an autonomous tracking mode as well as a Diode/DEM tracking mode, with the latter using an on-board DEM to perform range tracking to minimise tracking losses (Steunou et al., 2015).

SARAL's reference ellipsoid is the T/P ellipsoid, which is defined by an equatorial radius of 6378136.3 m and a flattening coefficient of 1/298.257 (Bronner et al., 2016), and is the same ellipsoid as used for the T/P, Jason-1 and Jason-2 missions. The geoid is defined using the EGM96 geopotential (Bronner et al., 2016). SARAL operates in a sun-synchronous orbit at an altitude of approximately 800 km and with a repeat period of 35 days (Bronner et al., 2016). As a result of technical problems, from July 2016, SARAL was put into a drifting orbit whereby the repetitive ground tracks were no longer maintained (Guinle et al., 2016; Dibarboure et al., 2018; AVISO+, 2019; Verron et al., 2020). Although the cycle duration, number of passes and availability of altimetry data products have remained relatively unchanged, the fact that SARAL moved into a drifting orbit has meant that acquired data are not suitable for some hydrological monitoring applications, specifically the estimation of WSE time series at virtual stations, from the date of the change to a drifting phase. As such the data used in this study consist of the first 34 cycles of SARAL/AltiKa data, dating from April 2013 to June 2016. Some studies have used acquisitions from the SARAL drifting phase but mainly for applications not requiring spatially repetitive data, such as mesoscale meteorological assessments (Dibarboure et al., 2018; Verron et al., 2020).

Where the SARAL/AltiKa altimeter passes over surfaces of highly variable scattering and there are specular reflectors within the altimetric footprint, it is likely that the waveform will saturate (Verron et al., 2018) at a maximum count of 1250. This is consistent with the finding of Zakharova et al. (2015) that saturation of the SARAL/AltiKa waveform occurred over high reflectance surfaces such as ice leads and polynyas. This occurrence can be explained by the antennae gain control loop within SARAL/AltiKa, which is optimised for ocean returns and is not sufficiently rapid to follow the high backscatter shifts that occur leading into a zone of high reflectance. The waveform then saturates the power recording window (Zakharova et al., 2015). The occurrence of waveform saturation, and the impact of the saturation on derived WSE, is not widely reported and there are cases where it would be expected to be a significant issue but has not been documented. This is the case, for example, in Verron et al. (2020) where studies over expansive flat, smooth specular reflectors were undertaken with no documented waveform saturation. In some studies, for example Ghosh et al. (2015), although the occurrence of saturation distortion has not been documented its impact is effectively confirmed as any waveform with a peak count exceeding 1250 is deleted from the waveform sequence.

SARAL/AltiKa waveform saturation has been reported in the study area of this research. Figure 2-3 is an example of a SARAL pass transiting over the Fly River and adjacent floodplain with evidence of saturation within select waveforms. Saturated waveforms are evident at water sites, returning the maximum 1250 counts, and at inundated vegetation sites where the waveform also saturates at the maximum 1250 counts. These are sites where waveform saturation is expected as they are locations of high variable scattering with specular reflectors within the altimetric footprint (Verron et al., 2018).

The practical implication of this saturation is a flat-top appearance for the waveform with the extent of saturation typically affecting one to two gates but with occurrences where a larger number of gates are affected. The impact of saturation on the derived altimetric WSE profile and methodologies for detection are discussed in Chapter 4 with rectification methodologies proposed for future research. Unless the retracking of saturated waveforms can be undertaken successfully, the use of SARAL/AltiKa over heterogeneous inland waters will be severely limited. The occurrence of unsaturated quasi-specular waveforms is likely to be significantly reduced and any WSE time series or profiles will be determined primarily from sub-waveforms extracted from multi-peaked returns.

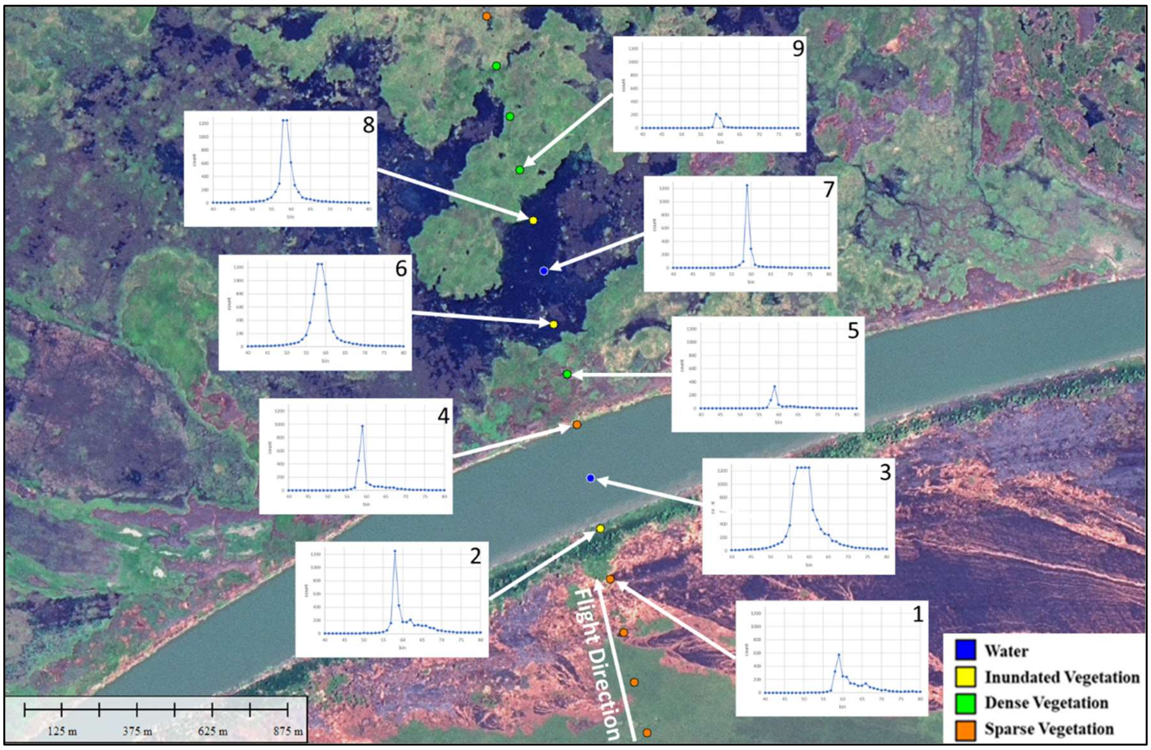

Figure 2-3 The waveform sequence without automatic gain control (AGC) correction from SARAL pass 0677 cycle 24 at 7.578ºS 141.340ºE. Footprint classifications are based on the methodology developed in Chapter 4. Saturated SARAL/AltiKa waveforms are evident at water sites (waveforms 3, 6, 7 and 8), returning the maximum 1250 counts, and at inundated vegetation sites (waveform 3) where the waveform also saturates at the maximum 1250 counts. These sites are locations where specular reflectors at nadir are expected. The background image is a SPOT7 true colour image captured in September 2015.

2.1.3 Cryosat-2 SIRAL

Cryosat-2 was launched on 8 April 2010 with the primary aim of monitoring the thickness of the Earth's land and sea ice surfaces. However, it has also been used successfully for hydrological analysis (e.g. Mayer et al., 2014; Villadsen et al., 2014; Schneider et al., 2017). Cryosat-2 operates in a low Earth orbit at an altitude of approximately 700 km. The orbit is not sun-synchronous (Bouzinac, 2010) and is near polar (+88º of latitude) with a repeat period of 369 days (Wingham et al., 2006). The reduced temporal coverage makes the extraction of meaningful hydrologic time series impractical, but its 30-day sub-cycle provides approximately monthly coverages of the Earth's surface. The limitation relating to the low repeat frequency of the orbit is offset by an increase in spatial coverage related to the satellite's drifting orbit. The reference ellipsoid for Cryosat-2 is WGS84, which is the same as the reference frame used by ERS-1, ERS-2 and Envisat, with SSH and WSE derived using the EGM96 geoid (Bouzinac, 2010).

The altimetry payload is comprised of a SIRAL, a dual-frequency DORIS system for precise orbit determination and a LRR for range calibration (Bouzinac, 2010). The SAR altimeter operates in three measurement modes as a function of a geographical mode mask (Wingham et al., 2006). In LRM mode the altimeter operates like a traditional nadir-looking pulse-limited radar altimeter, while in the other two modes—SAR and interferometric SAR (InSAR)—the altimeter utilises SAR processing (Villadsen et al., 2014). While neither of the SAR measurement modes is available over the Fly River study area, the technical specifications of the defined altimeter are for LRM mode as this mode was used for all analyses in the project.

Cryosat-2 SIRAL employs full-deramp pulse compression and, in LRM mode, operates at a PRF of 1971 Hz from which 20-Hz averaged waveforms are derived. A 350-MHz bandwidth chirp is transmitted although this measurement bandwidth and is reduced to 320 MHz, resulting in 128 samples per echo with a tracking range gate of 0.4684 m (Wingham et al., 2006; Bouzinac, 2010).

Figure 2-4 shows the Cryosat-2 instrument payload including the dual SIRAL antenna configuration.

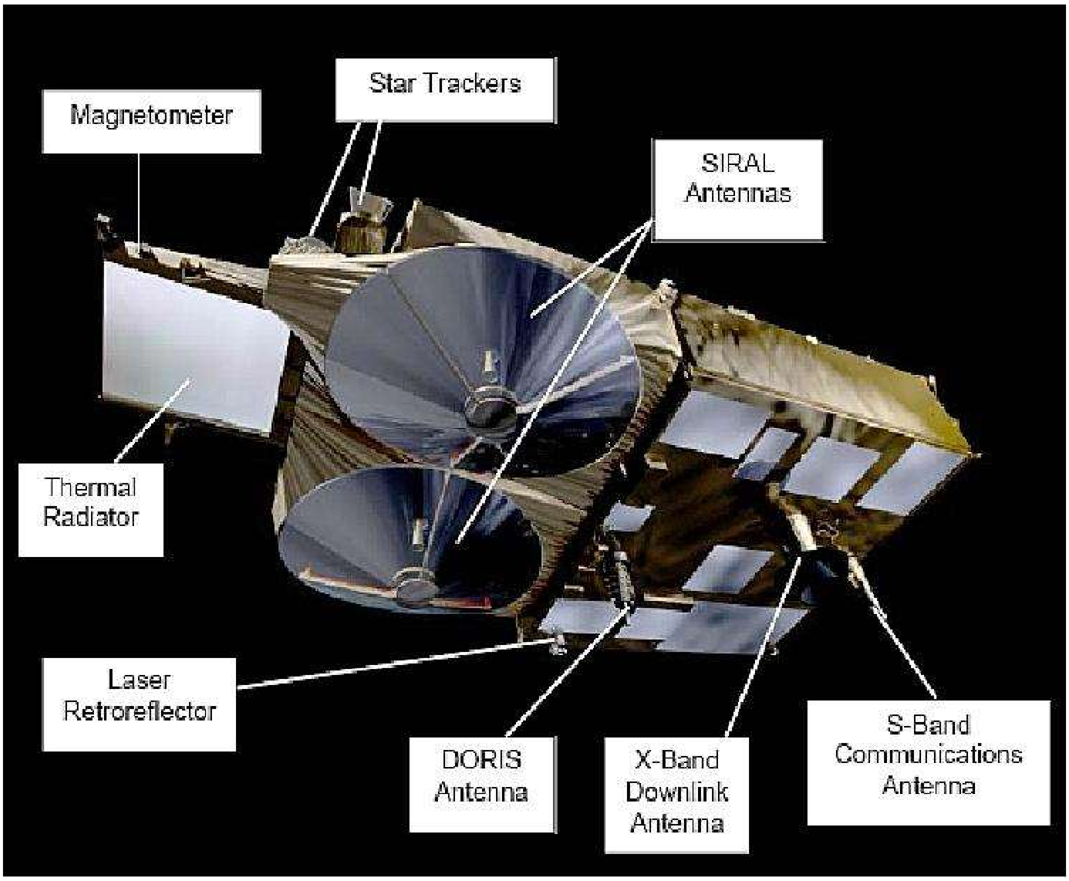

Figure 2-4 The Cryosat-2 satellite with the instrument payload including the dual SIRAL antenna configuration (ESA, 2020a).

2.2 Satellite altimetry—basic principle

In its basic form satellite altimetry involves the measurement of the distance from a satellite to a nadir target and the positioning of that target using the known satellite location. A radar pulse transmitted by the satellite altimeter is reflected from the water or land beneath the satellite and the echo is received back at the altimeter. The return signal is maintained within a fixed-length analysis window that is continuously adjusted to maintain the leading edge of the return signal, which is nominally the nadir return, tied to a nominal tracking point within the window (Vignudelli et al., 2019). Relative to the on-board tracking of the return signal, the round-trip travel time of the radar pulse from the satellite to surface is measured and used to derive the range from the satellite to the target surface.

Figure 2-5 depicts the principle of satellite altimetry-derived observations along with a definition of reference surfaces, measurements and required corrections.

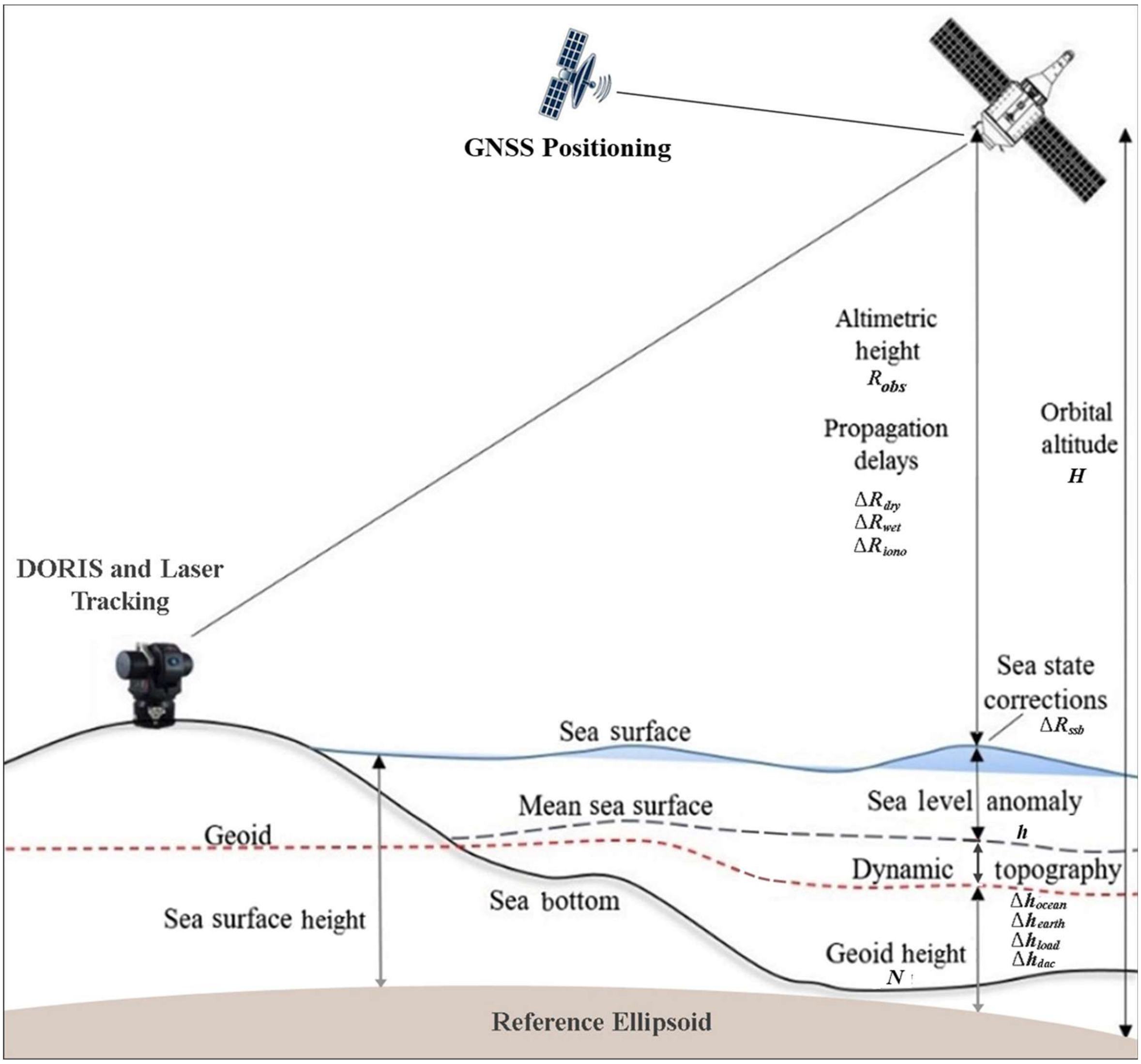

Figure 2-5 The principle of satellite radar altimetry with the definition of reference surfaces, measurements and required corrections; modified from Abazu et al. (2017).

As the satellite is located with respect to a geodetic reference ellipsoid, the elevation of the target can be determined by subtracting the satellite-to-surface range from the known satellite altitude. In addition to the position and elevation of the target reflector, further analysis of the radar waveform characteristics allows for determination of variables such as surface roughness, wave height and wind speed.

To achieve an accurate estimate of water level height at the nadir target, corrections to the measured altimeter range are required. These corrections relate to the way that the radar pulse behaves in the atmosphere and to the corrections required for sea state and geophysical phenomena.

In the following description of the range and geophysical corrections, the notation used by Fu and Cazenave (2000) is predominantly adopted and the typical corrections applied for inland water applications are listed in Table 2-2.

Table 2-2 Range and geophysical corrections applied to the measured satellite altimetry range. Corrections are added to the measured range, which is subtracted from the satellite altitude to give a surface elevation.

Correction	**Symbol**	**Comment**
Range correction		
Dry tropospheric correction	ΔR_{dry}	
Wet tropospheric correction	ΔR_{wet}	
Ionospheric correction	ΔR_{iono}	
Sea state bias	ΔR_{ssb}	Not applied over inland waters
Geophysical correction		
Geoid correction	N	
Ocean tide correction	Δh_{ocean}	Not applied over inland water
Solid Earth tide correction	Δh_{earth}	
Ocean loading tide correction	Δh_{load}	
Geocentric pole tide correction	Δh_{pole}	
Dynamic atmosphere correction	Δh_{dac}	Not applied over inland waters

Range corrections are required to correct for the interaction between the radar signal and the atmosphere and include impacts through both the troposphere and ionosphere. An additional range correction—relevant to ocean returns—relates to sea state bias (SSB), which is the bias of the altimeter range measurement towards the trough of a wave. The correction can only effectively be derived from Brown–Hayne waveforms (Andersen and Scharroo, 2011) and is not relevant for the majority of inland water applications. Application of range corrections enables the height at the reflecting surface to be accurately defined with respect to the satellite reference ellipsoid. Geophysical corrections relate to temporally varying geophysical phenomena that affect the derived target elevation. Application of geophysical corrections enables height determination with respect to the Earth's equipotential surface, which is effectively a dynamic water level height.

2.2.1 Range corrections

Range corrections relate to the changes made to the radar pulse speed as it passes through the atmosphere, and to the scattering surface of the radar pulse. The corrections that are made through the atmosphere are the dry tropospheric correction (ΔR_{dry}), the wet tropospheric correction (ΔR_{wet}) and the ionospheric correction (ΔR_{iono}). The dry tropospheric correction is the largest and ranges from 1.7 to 2.5 m (Gao et al., 2019). The correction is largest in the sub-tropics and is largely unaffected by proximity to land (Andersen and Scharroo, 2011). The dry tropospheric correction is determined from operational weather models.

The wet tropospheric correction relates to the amount of water vapour in the troposphere. It ranges from 0 to 50 cm (Rosmorduc et al., 2018; Gao et al., 2019), with the maximum impact being in hot, wet environments and minimum impact in cold, dry environments. The correction can be determined from either on-board MWRs, which effectively provide a direct measure of the wet tropospheric correction or weather model predictions. The wet tropospheric correction is affected by proximity to land however, simultaneous radiometric measurements typically fail over land and through the coastal zone making a humidity retrieval method for determining the correction unsuitable. For these locations, the wet tropospheric correction is usually derived from meteorological model outputs (Desportes et al., 2007; Rosmorduc et al., 2018).

The ionospheric correction is required because of the refraction of electromagnetic waves as they propagate through the atmosphere in the presence of free electrons and ions. As the ionospheric correction is inversely proportional to the square of the radar frequency (Andersen and Scharroo, 2011), the difference in total travel time at two different frequencies can be used as an estimate of the total electron content (TEC) from which ΔR_{iono} can be derived. As an alternative to the determination of the ionospheric correction by differencing at two significantly different frequencies, climatic models using the systematic behaviour in the temporal and spatial variation of TEC, along with parameters such as solar flux and sunspot activity, enable estimation of TEC at any global location. The magnitude of the ionospheric correction ranges from 6 to 12 cm (Gao et al., 2019).

The scattering of the radar signal by the reflecting surface is non-Gaussian (Andersen and Scharroo, 2011) as there are more wave troughs and these reflect more of the radar signal back to the satellite. This results in an over-estimate of the range to the mean sea surface and a biasing of the estimated sea surface elevation to be lower than actual. The SSB correction (ΔR_{ssb}) is a function of wind and wave conditions. Parameters required for the determination of ΔR_{ssb} can only be derived from Brown–Hayne ocean waveforms and so the correction term is generally not applied for either the coastal zone or inland water bodies.

The corrected range (R_{corr}) is derived from the observed range (R_{obs}) as follows:

$$R_{corr} = R_{obs} + \Delta R_{dry} + \Delta R_{wet} + \Delta R_{iono} + \Delta R_{ssb} \qquad 2\text{-}1$$

and the height (h) of the water body above the reference ellipsoid is given by:

$$h = H - R_{corr} \qquad 2\text{-}2$$

where H is the altitude of the satellite altimeter with respect to the same reference ellipsoid.

2.2.2 Geophysical corrections

Geophysical corrections account for the impact on the water surface height resulting from the time-variant ocean, Earth and pole tides as well as dynamic atmospheric pressure loading. The largest geophysical correction is the geoid correction (N), which relates the geoid (the Earth's equipotential surface) to the satellite reference ellipsoid. This correction is not temporally variable but varies spatially as a function of spatially distributed density heterogeneity within the Earth's crust. The correction has a range of –105 m to +85 m (Andersen and Scharroo, 2011) and is derived from various global gravity data sources. While the accuracy of determination of N is important for the determination of mean SSH and associated oceanographic variables, particularly for global studies, it has less relevance for inland water studies where water bodies have a relatively small spatial extent and where the geoidal correction will be cancelled out in the differencing process when comparing altimetric and in-situ data as long as both data are referenced to a consistent geoid model.

Of the geophysical corrections, tidal correction is the main contributor to temporal SSH variability. Ocean tides (Δh_{ocean}) account for the largest portion of the geophysical correction but the correction also includes solid Earth tides(Δh_{earth}), ocean loading tides (Δh_{load}) and geocentric pole tides (Δh_{pole}). Ocean tides result from the gravitational forces of the Sun and Moon and can be readily modelled. As this correction only applies to altimetric measurements over the open ocean and coastal zones it is not incorporated for studies over inland waters.

The solid Earth tide (Δh_{earth}) is the response of the solid Earth towards the gravitational effects of the Sun and Moon. The magnitude of these geophysical effects is –30 to +30 cm (Gao et al., 2019) and can be determined with high accuracy. The ocean loading tide (Δh_{load}) relates to the displacement of the ocean bed as a result of the loading of the water column above and has a magnitude of –2 to +2 cm (Gao et al., 2019). The pole tide correction results from variability in the Earth's rotational axis with respect to the actual geographic pole. This variability induces a centrifugal force change that produces a change to water level height at the same frequency (Andersen and Scharroo, 2011). The magnitude of the Δh_{pole} correction is estimated to be in the range –2 to +2 cm (Gao et al., 2019).

The correction to SSH because of temporal variation in the atmospheric pressure loading is the dynamic atmosphere correction (DAC) (Δh_{dac}). This is also known as the inverse barometer correction, as the sea level rises when pressure is low and falls when pressure is high. The correction is within the range of –10 to +10 cm and is derived from global atmospheric pressure models (Andersen and Scharroo, 2011). The correction is generally not applicable to inland water applications of satellite altimetry.

The sum of the geophysical corrections for the ocean surface is given by Equation 2-3 and for inland waters by Equation 2-4:

$$\Delta h_{SSH} = N + \Delta h_{ocean} + \Delta h_{earth} + \Delta h_{load} + \Delta h_{pole} + \Delta h_{DAC} \qquad 2\text{-}3$$

$$\Delta h_{WSE} = N + \Delta h_{earth} + \Delta h_{load} + \Delta h_{pole} \qquad 2\text{-}4$$

2.2.3 Dynamic sea surface height and water surface elevation

The combination of range and geophysical corrections enables the dynamic SSH (for ocean applications) or dynamic WSE (for inland water applications) to be determined. The SSH is derived as follows:

$$SSH = H - R_{corr} - \Delta h_{SSH} \qquad 2\text{-}5$$

For inland applications the WSE becomes:

$$WSE = H - R_{corr} - \Delta h_{WSE} \qquad 2\text{-}6$$

where the corrected range (R_{corr}) is defined by Equation 2-1.

2.3 Altimetry data

The altimetry data used in this research project are the SGDR data product for Envisat RA-2 (SGDR V2.1), SARAL/AltiKa (SGDR-T) and Cryosat-2 SIRAL (Baseline-C LRM L1B and L2). The (near) real-time product contains preliminary orbit and meteorological data while the precise Geophysical Data Record (GDR) and SGDR records, typically available 30 days after capture, incorporate precise meteorological predictions and precise instrument calibrations and orbit solutions (Soussi, 2011). Details of the data, data formats and conventions are contained in the product manuals for the various satellites; these user manuals and product guides have been utilised in the development of software solutions for analysis of the data. For Envisat RA-2, the *Envisat Altimetry Level 2 User Manual* (Soussi, 2011) and the *RA2/MWR Products User Guide* (ESA, 2014) have been used. The *SARAL/AltiKa Products Handbook* (Bronner et al., 2016) has been used for SARAL/AltiKa investigations and the *Cryosat-2 Product Handbook* (Bouzinac, 2010) and *Cryosat L1B and L2 Products Specifications* (Mantovani, 2015a; Mantovani, 2015b) have been utilised for Cryosat-2 SIRAL investigations.

While there is slight variation in data and delivery formats, the SGDR records for all three satellite platforms show relative consistency and uniformity of content and data structure. The Level 2 geophysical data used in this research consist of time-invariant data (e.g. range and geophysical corrections) at 1 Hz as well as time-dependent data (e.g. time tagging, geolocation, orbit altitude, output from retrackers and waveforms) at the echo averaging frequency (Soussi, 2011).

The geophysical data are converted to geophysical units in the waveform retracking process with the geophysical parameters extracted including parameters for range, wind speed, SWH and backscatter coefficient. These are bundled with additional parameters including time tagging, geolocation, orbital altitude (Soussi, 2011), range and geophysical corrections and the waveform record in the SGDR data record. To retrieve the geophysical parameters over all types of surface (ocean, ice, sea ice, land), four specialised retrackers are continuously run in parallel. The operation of these retrackers is covered in detail in Chapter 5, including the Ocean Retracker (based on a modification of the Hayne model), Ice-1 (an empirical retracker based on the Offset Centre of Gravity [OCOG] methodology), Ice-2 (a Brown model retracking algorithm optimised for ocean echoes) and Sea Ice (a threshold-based empirical retracker optimised for specular returns) (Soussi, 2011; Snaith, 2011).

Echo averaging for Envisat RA-2, SARAL/AltiKa and Cryosat-2 SIRAL is undertaken at 18 Hz, 40 Hz and 20 Hz respectively. Based on the pulse repetition frequencies listed in Table 2-1 the number of IEs used in each averaged waveform is 100, 96 and 91 for Envisat RA-2, SARAL/AltiKa and Cryosat-2 SIRAL respectively. While all averaged echoes are transmitted from the satellite to ground-based receiving stations, only select bursts of IEs are recorded (Roca et al., 2007; Berry et al., 2012).

The SGDR product used in this research is the same as the precise GDR product; however, it also incorporates the averaged altimeter waveforms at the echo averaging frequency of the satellite. While the waveforms associated with the IEs are stored in the SGDR as well, no IE bursts were transmitted for the Fly River study area.

CHAPTER 3: FIELDWORK AND IN-SITU DATA

The study area for this research is in the Western Province of PNG, which features an extensive floodplain and complex wetland along with lake systems of various sizes. This research focusses on satellite altimetry waveforms and retracking methodologies leading to accurate WSE determination over a variety of inland water bodies. An important study component relates to the availability of quality in-situ data for validation. Existing data sets, collected in part by Ok Tedi Mining Limited (OTML), consist of extensive archives of survey and spatial data in the form of vegetation maps, satellite imagery and aerial imagery as well as, more importantly, an established geodetic network and WSE records covering the 200 km north–south extent of the study area. As historical floodplain water level data do not exist, the purpose of the fieldwork program associated with this research is to provide data to facilitate the generation of virtual floodplain water level gauges specifically for altimetry WSE validation.

3.1 Geodetic datums

The geodetic datum used in the Western Province of PNG for all operations approximates the Australian Geodetic Datum 1966 (AGD66) and has been used for all spatial activities by OTML since early exploration undertaken in the 1970s. The Universal Transverse Mercator (UTM) projection of this datum is the Ok Tedi Map Grid (OMG). Papua New Guinea's geodetic datum is PNG94 and was established on 1 January 1994 along with a UTM projection, PNG Map Grid 1994 (PNGMG94). PNG94 is essentially a snapshot of the dynamic International Terrestrial Reference Frame 1992 (ITRF92) at epoch 1994.0 (Stanaway, 2008).

PNG is in a tectonically active region with the major activity being related to the colliding of the Australian and Pacific plates, although there are several smaller microplates. Tectonic velocities can be in the order of 2 m every 10 years (Stanaway, 2008) and even greater when considering the impact of deformation from earthquakes. Understanding of the relationship between static geodetic systems (OMG and PNG94) and dynamic systems is necessary to ensure accuracy in the processing of dynamic system positions (WGS84 for Envisat and Cryosat-2 and the T/P ellipsoid for SARAL) supplied with the satellite altimetry data.

The geodetic network used in this research is a three-dimensional network comprising position and elevation covering the full extent of the Fly River floodplain. Position is defined with respect to both OMG and PNGMG94 and then converted to WGS84 for comparison with altimetry data. Several height datums are in use throughout the Western Province, each based on a different geoid model for the conversion of ellipsoidal height to MSL. These height datums include MSL (Kiunga), MSL (PNG08) (Stanaway, 2012) and the Ok Tedi Height Datum (OHD), among which elevation varies by several metres. As the majority of available historical data are referenced to OHD, it is this datum as well as WGS84 ellipsoidal height, that are used as the height references for all derived WSEs in this study.

The conversion of WGS84 ellipsoidal heights to OHD geoidal heights is undertaken via application of the PNG (Kearsley) geoid model (Stanaway, 2012), which was specifically developed for use throughout OTML operations in 1996 and comprises geoid–ellipsoid separations (N) on a 0.1° grid. When comparing elevations obtained directly from the satellite altimetry SGDR data record—where the EGM96 geoid model is used for the definition of WSE—with the OHD elevation measurements there will be an elevation offset related directly to the difference between the two geoid models. This offset will vary as a function of spatial location in line with the variation in the geoid model N. All altimetry data derived in this study use the PNG (Kearsely) geoid model N for estimation of WSE, achieved by application of the PNG (Kearsely) model N instead of the supplied EGM96 value from the altimetry SGDR record. For altimetry WSE data, based on EGM96 and sourced from global databases such as Hydroweb or River & Lake, the ellipsoidal height is derived by extracting the supplied EGM96 N, from which an OHD WSE is then calculated for comparison with in-situ data and the results of this study as required.

3.2 In-situ river level gauges

To validate the satellite altimetry-derived river and floodplain WSEs, OTML's historical data from its seven river level gauges are used (OTML, 1963–2020) with the data for all gauges referenced to OHD. The study primarily uses WSE data from the Kiunga, Kuambit, Manda and Obo gauges. In mid-2004 the gauge at the Manda site (FLY16) was relocated approximately 14 km downstream to Manda Village and established as FLY17. To enable continuity of analysis the water level relationship between the two sites was determined at the time of relocation. The seven in-situ gauges are listed in Table 3-1, showing station identity (ID), geographic location, period of operation and approximate river mile (ARM)[1] location.

[1] ARM (approximate river mile) is the unit of measurement on the Fly River and relates to the distance in nautical miles (nm) from the Fly River delta.

Table 3-1 OTML river gauging stations located on the lower Ok Tedi and Fly rivers.

Site location	Station ID	Latitude (WGS84)	Longitude (WGS84)	Period of operation	ARM
Konkonda	TED25	5°58'54.61"S	141°09'36.01"E	01/1984–	-
Kiunga	FLY05	6°07'29.77"S	141°17'50.10"E	03/1968–	458
Kuambit	FLY10	6°11'10.80"S	141°06'30.00"E	01/1984–06/2004	435
Manda	FLY16	7°01'39.86"S	141°03'57.42"E	05/1993–08/2004	307
Manda Village	FLY17	7°05'23.94"S	141°06'31.80"E	10/2004–	299
Obo	FLY15	7°35'17.61"S	141°19'27.96"E	03/1987–	215
Kuima	FLY26	7°45'12.19"S	141°34'54.90"E	05/2003–	180

Figure 3-1 shows the location of the in-situ gauge sites within the study area. The sites cover most of the lower-middle Fly floodplain where the majority of research is undertaken.

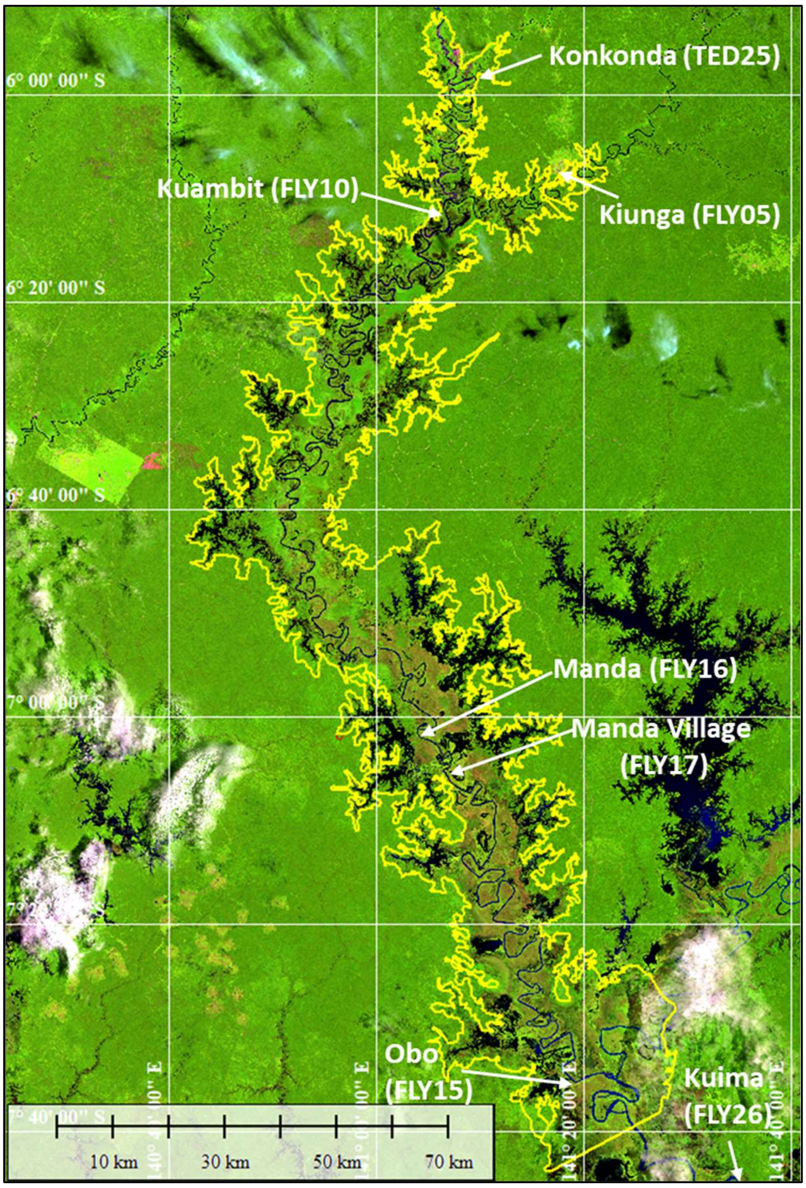

Figure 3-1 Locations of the OTML river gauging sites on the lower Ok Tedi and Fly rivers in PNG. The primary river level gauges used are Kiunga (FLY05), Manda (FLY16 and FLY17) and Obo (FLY15). The background image is a false colour extract from Landsat TM5 acquired during a period of moderate floodplain inundation in February 2004.

Figure 3-2 shows an extract from the water level records for Kiunga (FLY05), Kuambit (FLY10), Manda (FLY16 and FLY17) and Obo (FLY15) presenting daily average river level with respect to OHD. There is high correlation between the records of Manda (FLY 16 and FLY17) and Obo (FLY15) with a consistent pattern of WSE evident at both sites. This is despite a significant spatial separation of approximately 150 river kilometres. The Kiunga (FLY05) and Kuambit (FLY10) records demonstrate higher frequency variability than downstream sites as the river stage through this area is supplemented less by floodplain discharge.

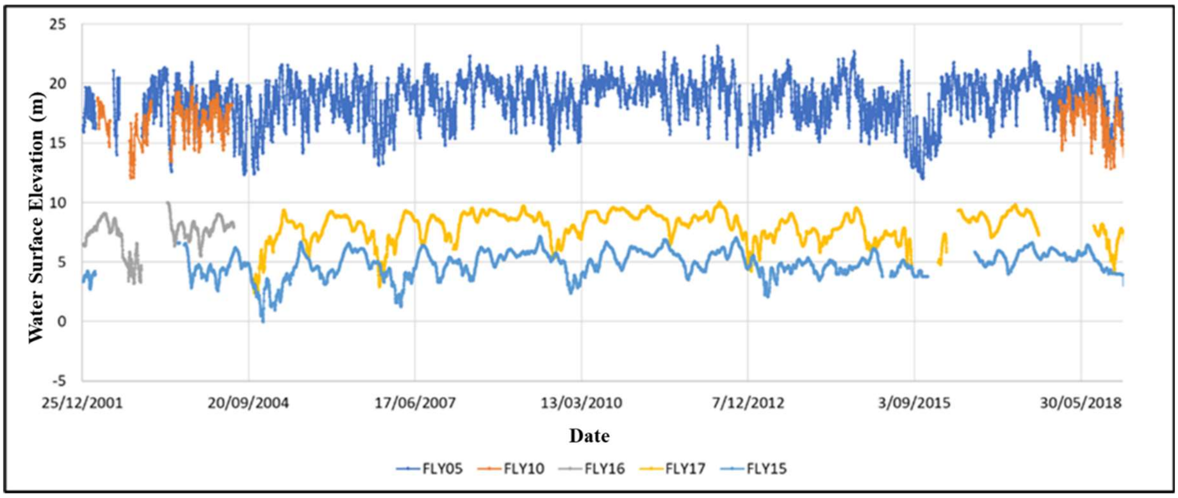

Figure 3-2 River level records for Kiunga (FLY05), Manda (FLY16 & FLY17) and Obo (FLY15) referenced to OHD.

In the upper reaches of the floodplain, water levels vary rapidly as a function of upper catchment rainfall and floods from both the Ok Tedi and upper Fly rivers. As the water moves downstream the short-term variability disappears with changes to the water level being on the scale of weeks to months (Pickup and Marshall, 2009). When the river level is low there is typically an inflow from the floodplain; conversely, when river levels are high the water flow is onto the floodplain. These inflows and outflows tend to dampen the short-term river level changes that are evident through the upper reaches and are primarily caused by attenuation of the flood waves by exchange of water between the river and the floodplain through creeks, tie channels and levee breaches in the lower half of the floodplain. The river level range is relatively stable throughout the middle Fly; however, there is a greater observed range in the upper reaches than in the lower reaches because of the significant water exchange with the floodplain in the downstream zone.

Floodplain inundation rates vary throughout the middle Fly floodplain and tend to increase with increasing downstream distance. Floodplain inundation frequency at Kiunga is reported to be approximately 15% in an average year but can increase to 30% with wetter than average conditions (Marshall, 1999). The average frequency of inundation at Manda is 65% and at Obo, 70%. Inundation frequency increases to approximately 95% under wetter than average or La Niña conditions (Marshall, 1999).

A deficiency with the in-situ gauge network relates to data availability at low river levels, particularly at extreme low river levels as observed under El Niño conditions. Under these conditions the river level dropped below the sensor orifice at most of the OTML in-situ gauge sites, resulting in data voids for these periods. This deficiency limits validation of derived altimetric WSEs under similar conditions.

3.3 In-situ floodplain water level gauges

Despite OTML having multiple river level gauges covering the Ok Tedi and Fly rivers, neither it nor other private, commercial or government agencies maintain any in-situ gauges that directly measure water level on the floodplain. While the interaction of water between the main stem and the floodplain is recognised and approximate relationships for different flow conditions have been estimated, there are no records that accurately document the relative levels between the river and the floodplain under different flow conditions. This was seen as a serious limitation for this research project that might lead to incomplete data analysis, particularly regarding validation and interpretation of the impact of floodplain complexity on the derived altimetry WSE estimates. While validation of the altimetry record for passes over the main stem of the Fly River in relative proximity to the river gauge locations would be possible, it would not be possible to accurately undertake any floodplain water level validation.

During the planning phase for this project, it was decided that virtual gauges within the floodplain would need to be established based on the existing river level gauges located on the Fly River. It was recognised, however, that the relationship between the main stem gauge and the floodplain gauge would not necessarily be linear and would need to be defined prior to validation of the altimetry retracking process. While data records for sites on the main stem pre-date the Envisat, SARAL and Cryosat-2 missions (Table 3-1) there are no floodplain water level records available. The fieldwork program undertaken in July 2011 was designed to establish a relationship between main stem water levels and floodplain water levels for two selected sites on the floodplain. These relationships would then be applied to the main stem data record, resulting in a long-term virtual floodplain WSE record suitable for validation. The sites selected were at Kemea Lagoon and Vataiva Lake, detailed in

Sections 3.3.1 and 3.3.2 respectively. The location of the sites with respect to the Manda (FLY17) and Obo (FLY15) gauges, along with the Envisat and SARAL ascending pass 0677, are shown in Figure 3-3.

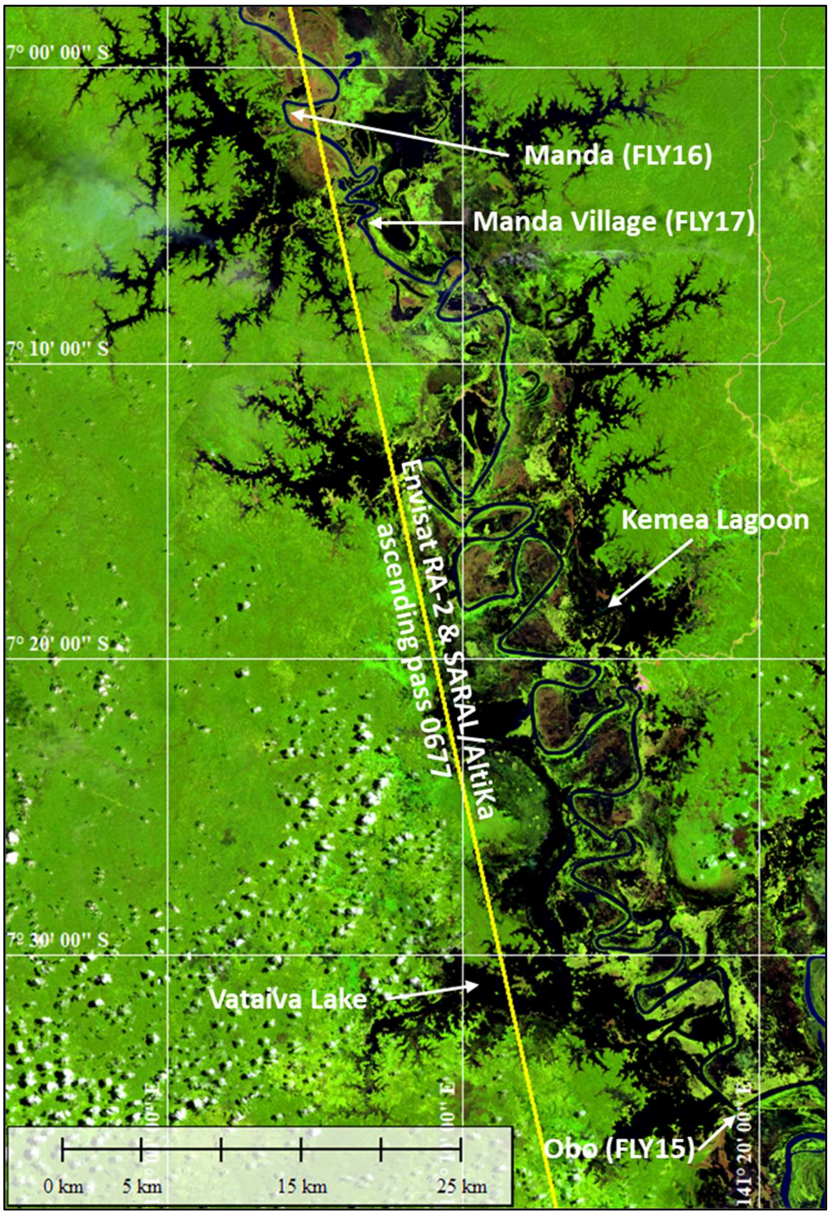

Figure 3-3 The locations of the Manda (FLY17) and Obo (FLY15) river level gauges relative the Kemea Lagoon and Vataiva Lake floodplain sites. The location of Envisat and SARAL ascending pass 0677 is shown against a Landsat ETM7 false colour image acquired on 9 December 2000 at high floodplain inundation.

While the main altimetry input for the project was to be from Envisat RA-2 it was recognised that data from additional altimetry sensors would ensure that research initiatives were not platform-specific. Jason-1 was excluded due to recognised problems with the on-board tracking window that limited the recovery of accurate WSEs (Berry et al., 2007b) and, while Jason-2 was shown not have the same tracking issues as Jason-1 (Desai et al., 2015; Dubey et al., 2015; Kuo and Kao, 2011), it was considered that altimeters using the same orbit would facilitate a more direct comparison of performance. The final array of satellites and associated altimeters used in the project were Envisat RA-2 and SARAL/AltiKa, with Cryosat-2 SIRAL also utilised due to the potential to target specific inland water zones as a function of the Cryosat-2 drifting orbit. The Vataiva Lake location was significant as it was located in relatively close proximity to the Obo gauge and on ascending pass 0677 of the Envisat and SARAL satellites. As Envisat moved into a new orbit in October 2010 and SARAL was not launched until April 2013, no direct validation has been undertaken from the logged floodplain WSEs; however, the creation of a virtual floodplain WSE gauge has been undertaken and this facilitated validation of Envisat RA-2 and SARAL/AltiKa altimetric data acquired between 2002 and 2016.

In-situ gauges were established at Kemea Lagoon on 14 July 2011 and Vataiva Lake on 16 July 2011. All work was undertaken with the aid of OTML's Environment Department during a scheduled monitoring program undertaken on the river. The sites were selected based on the following constraints and requirements:

a) relative proximity to existing altimetry theoretical tracks
b) ease of access and logistical considerations
c) the likelihood that the gauges would remain for approximately 12 months without vandalism or destruction due to environmental factors
d) approval from the local landowners regarding access to their land
e) sites that would remain inundated even under low flow conditions.

The gauges used at both sites were the Solinst Levelogger Gold pressure sensors, which consist of a data logger, a pressure transducer and a temperature sensor in a self-contained stainless steel housing. The sensors offer a battery life of 10 years and the capability to record water levels every minute at depths up to 20 m with accuracy of ±1 cm. A third sensor was deployed to measure barometric pressure and to compensate for the impact of atmospheric pressure fluctuations on the water level record. A single logger was deployed to correct the pressure readings from both the Kemea Lagoon and Vataiva Lake sensors and was established at the OTML gauging site at Obo.

The Levelogger sensors were secured in a polyvinyl chloride (PVC) pipe housing fixed to a steel star picket and secured into the bed of the floodplain at depths of approximately 2.5 m and 2.1 m at Kemea Lagoon and Vataiva Lake respectively. While there was a preference to install the loggers in deeper floodplain waters this was not practical as there was a risk that the loggers would not be readily recovered after a 12-month deployment if established in these more isolated locations.

Static GPS surveys were undertaken between reference sites located within the Fly River geodetic network and both Kemea Lagoon and Vataiva Lake floodplain gauge sites. The GPS equipment used was the Leica System 1200+ dual-frequency GNSS system logging both GPS and Glonass data. All data analyses were undertaken using the Leica GeoOffice software. The purpose of these surveys was to establish the WSE at the in-situ sites so that the floodplain gauge data could be converted to a datum consistent with that of the river gauge sites. Geoidal elevations with respect to OHD were derived through application of the PNG (Kearsley) geoid model N to the adjusted ellipsoidal elevations. Observations were undertaken at the start and end of the 12-month deployment so that the stability of the sensor for the period of logging could be determined. The difference in derived WSEs between the two surveys was less than 1 cm for both sites. Figures 3-4–3-9 document the process of sensor deployment and retrieval at the Kemea Lagoon and Vataiva Lake sites.

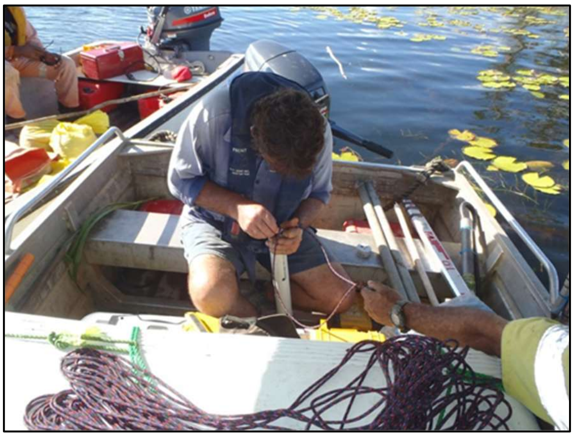

Figure 3-4 Securing the water level logger and protective PVC housing to a star picket before deployment. A retrieval line was secured to a tree in case retrieval based on site coordinates failed.

Figure 3-5 Final configuration of the water level recorder, PVC protective housing and star picket at the Kemea Lagoon site.

Figure 3-6 Geodetic surveys designed to transfer water level from the Obo Station reference site. Leica system 1200+ GNSS receivers were used with orthometric heights derived from the PNG (Kearsley) geoid model.

Figure 3-7 Retrieval of the water level logger at Kemea Lagoon after a 12-month deployment.

Figure 3-8 Obo Station hydrology gauging station with the barometric logger deployed in the site hut. The Obo Station Permanent Survey Mark was used as the OHD reference for the floodplain gauges.

Figure 3-9 Vataiva Lake geodetic survey with direct measurement of WSE required because of the lack of dry ground in the vicinity of the site.

3.3.1 Kemea Lagoon

Kemea Lagoon is in the lower-middle Fly floodplain approximately 4 km from the eastern bank of the Fly River at ARM260; however, the lake is connected to the floodplain via breaches and tie channels at ARM265 and ARM249. The site is in a part of the floodplain that is permanently inundated except during periods of extreme low catchment rainfall that result in low flow conditions in the Fly River. Figures 3-10 and 3-11 show the site at median inundation levels and Figure 3-12 shows the site location within the Fly River floodplain.

Figure 3-10 Kemea Lagoon is located on the eastern floodplain of the Fly River in a zone of permanent inundation except in periods of drought.

Figure 3-11 Kemea Lagoon floodplain location with sensor deployment at a depth of approximately 2.5 m.

The logger was deployed from 14 July 2011 to 16 June 2012 with water level and temperature logged at 30-minute intervals. The water level record for the floodplain was downloaded, corrected for atmospheric fluctuations and transformed into OHD for analysis and comparison with both altimetry and other in-situ gauge data.

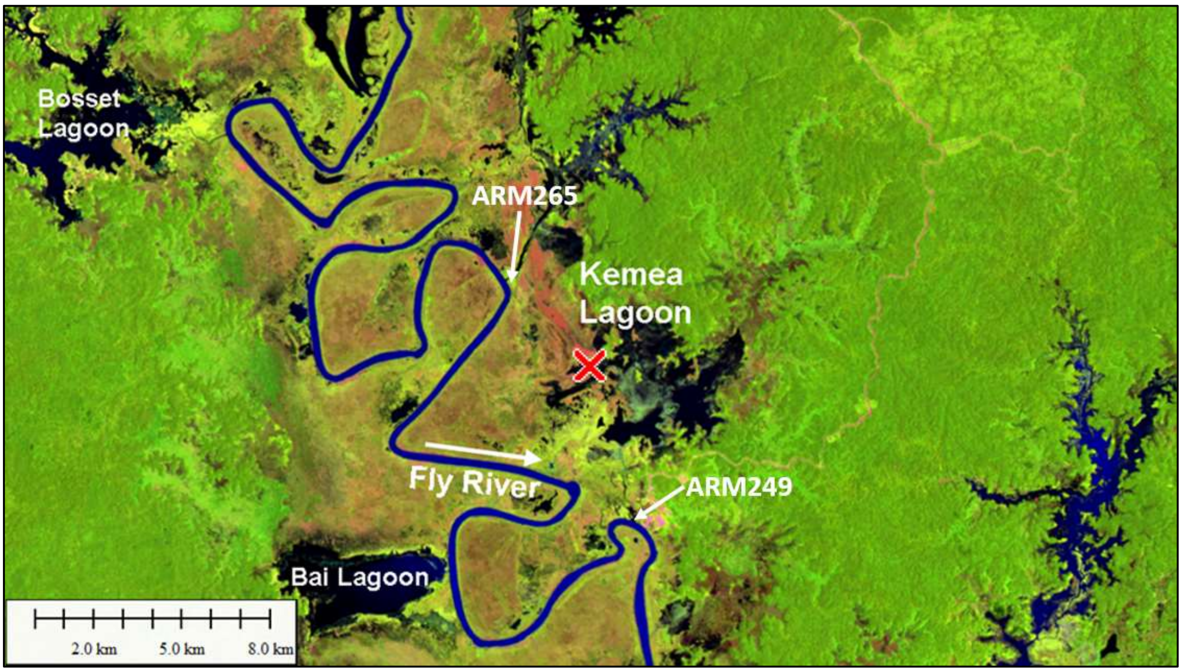

Figure 3-12 The Kemea Lagoon logger site at latitude 7.3022ºS and longitude 141.2411ºE on the east bank floodplain of the Fly River. The lake is connected to the floodplain via breaches and tie channels at ARM265 and ARM249.

Figure 3-13 shows the measured floodplain water level record for the period of deployment along with the WSE record for the Manda (FLY17) gauge. While there is an overall trend agreement between the two records, the offset between high and low river levels differs, being approximately 2.1 m at low flow and decreasing to approximately 1.5 m at high flow.

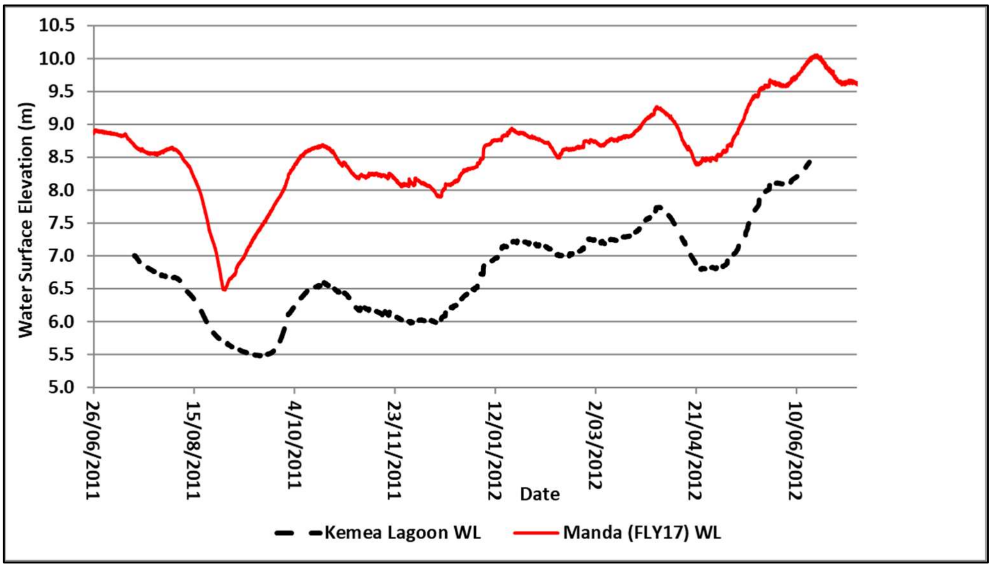

Figure 3-13 Manda (FLY17) river level and Kemea Lagoon WSE records for the period of deployment of the floodplain logger (2011–12). The Manda gauge is located approximately 40 nm upstream of Kemea Lagoon.

The FLY17 river level record requires correction for the downstream gradient as well as the application of a temporal offset to account for the delay in inundation between the main stem and the floodplain site. An assessment of the floodplain geomorphology shows that, at low river level, the lake discharges to the river at ARM249; at high river level, when the floodplain is inundated, the zone is controlled by the prevailing river level at ARM265. The floodplain WSE is therefore consistent with a FLY17 river level corrected via ARM265 at high flow and via ARM249 at low flow. The observed flow paths between the river and floodplain for the Kemea Lagoon site are illustrated in Figure 3-14.

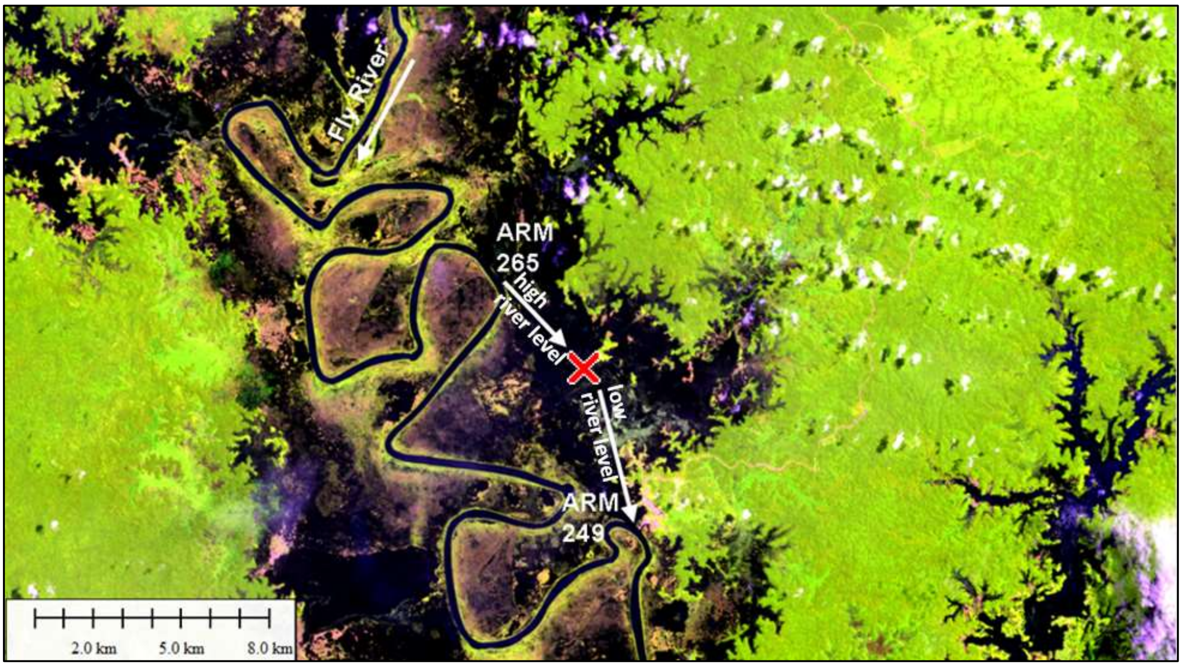

Figure 3-14 The floodplain WSE dynamics at Kemea Lagoon for varying Fly River stage heights. The predominant flow direction under high flow conditions is via a connection to ARM265, and under low flow conditions via ARM249. The background is a false colour image from Landsat TM5 acquired during a period of high floodplain inundation in March 2009.

The relationship between the FLY17 in-situ gauge WSE and the Kemea Lagoon-recorded WSE has been derived for floodplain infilling at FLY17 WSEs between 7.8 and 8.5 m and for floodplain discharge at FLY17 WSEs above 8.5 m. The relationship between the two gauges is shown in Figure 3-15 with a correlation coefficient (R) derived for both median and high flow cases. The results show a moderate correlation ($R = 0.88$) between the two sites for median water level and a higher correlation ($R = 0.98$) at higher river levels. The RMSE of the difference between the derived and measured water levels for Kemea Lagoon was 8 cm for the median and high flow cases but significantly greater than this across the full inundation range. At river levels below 7.8 m, there is a time delay in response that converts into WSE uncertainty of approximately 0.2–0.3 m. As there is a poor correlation between the observed river level at FLY17 and the WSE at Kemea Lagoon during periods of low inundation, no virtual record has been derived for these conditions.

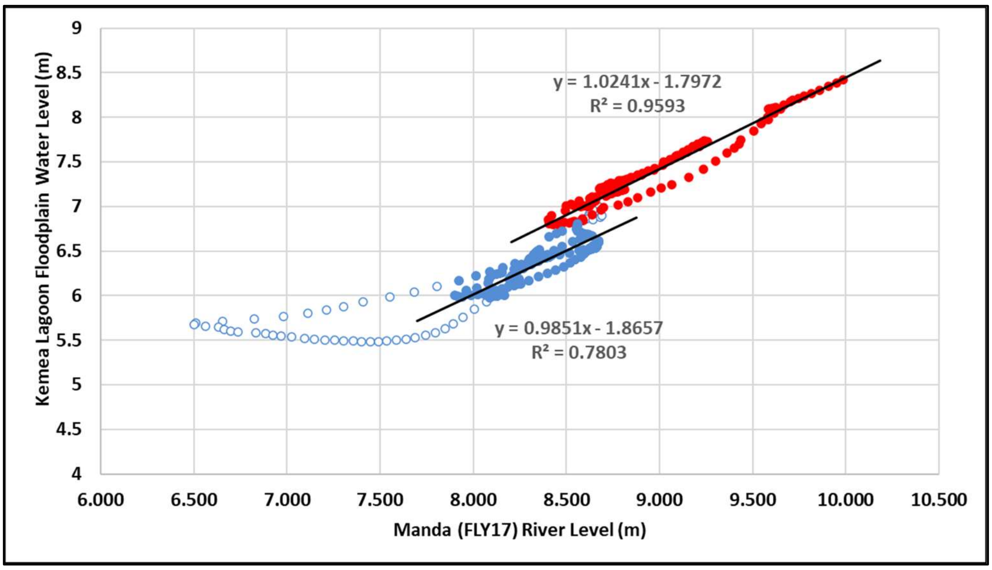

Figure 3-15 The relationship between the FLY17 river level and Kemea Lagoon WSE. There is a moderate correlation ($R = 0.88$) between the two sites at median river level and relatively high correlation ($R = 0.98$) at higher river levels.

The results for the virtual gauge derived for the Kemea Lagoon site are shown in Figure 3-16 and are based on connection to the floodplain via ARM265 at high river level and via ARM249 at low river level.

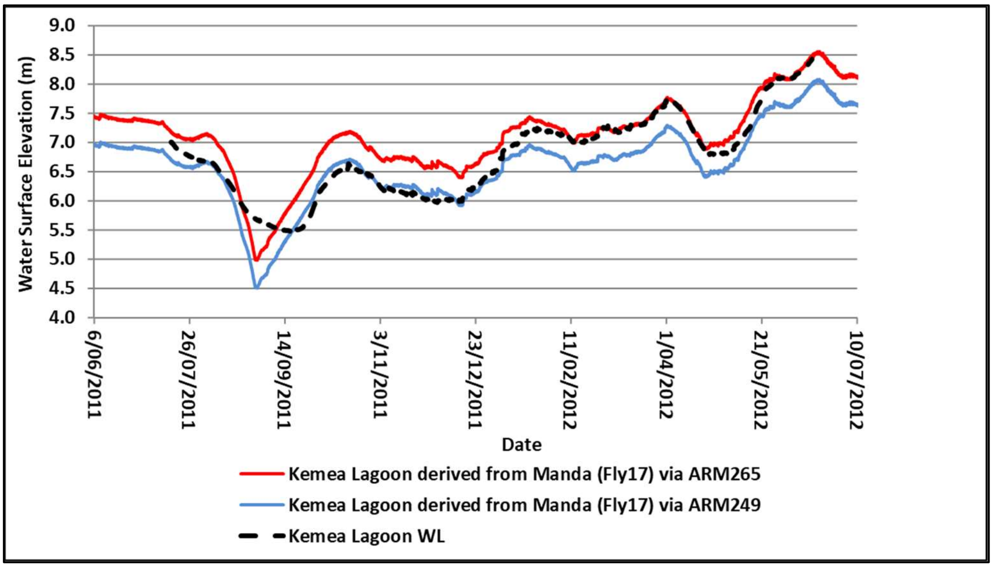

Figure 3-16 The Kemea Lagoon observed water level record and the two derived records based on FLY17 data with floodplain connections via ARM265 for high river levels and via ARM249 at low river level.

The Kemea Lagoon virtual water level record is a useful approximation of floodplain water level at river levels above the lower quartile but is complicated by the floodplain dynamics that influence the site. The virtual record at the lower quartile cannot be used for altimetric validation because of the poor correlation between the main stem gauge record and the floodplain record. At median-to-high levels, the accuracy of the record at Kemea Lagoon is estimated to be satisfactory for validation, subject to the virtual record being applied with knowledge of floodplain dynamics and processes that contribute to floodplain WSE change.

3.3.2 Vataiva Lake

Vataiva Lake is located in the lower-middle Fly floodplain, approximately 9 km from the western bank of the Fly River at ARM228. The site is in the part of the floodplain that is permanently inundated, except during periods of extreme low catchment rainfall that result in low flow conditions in the Fly River. Figures 3-17 and 3-18 show the site at median inundation levels and Figure 3-19 shows the location of the site within the Fly River floodplain.

Figure 3-17 Vataiva Lake located on the western floodplain of the Fly River, approximately 9 km from the Fly River.

Figure 3-18 The Vataiva Lake site with logger deployment at a depth of approximately 2.1 m.

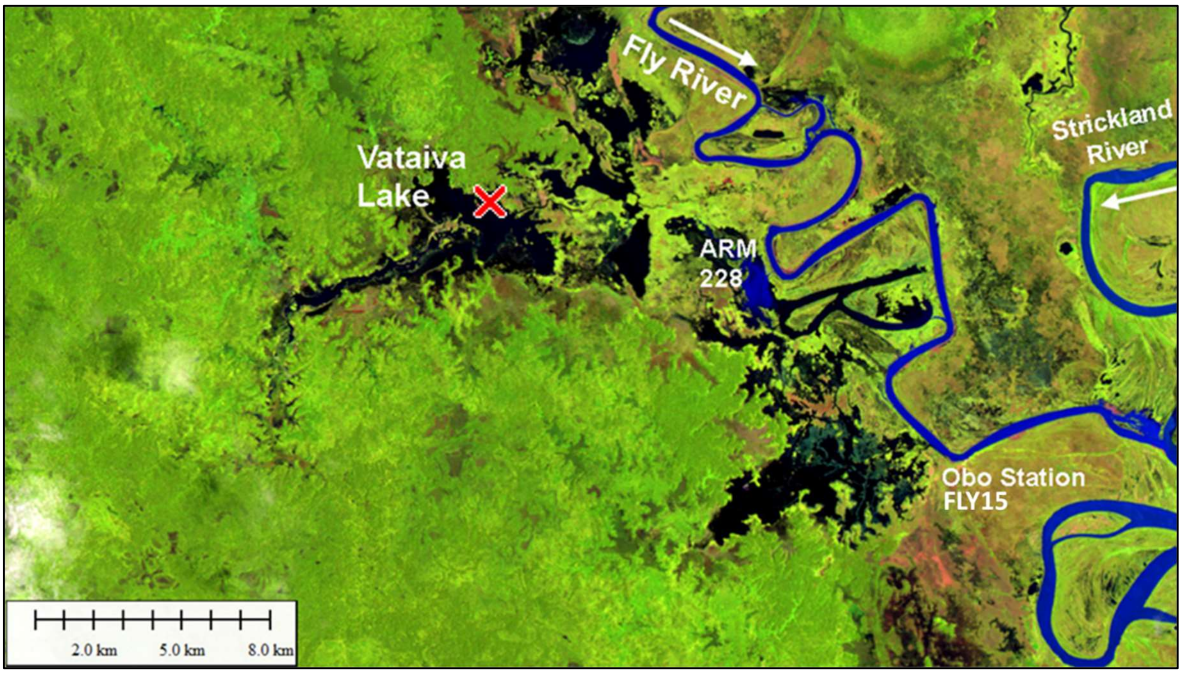

Figure 3-19 The Vataiva Lake logger site at latitude 7.5103ºS and longitude 141.1803ºE on the west bank floodplain of the Fly River.

The water level recorder at Kemea Lagoon was deployed over the same period as the Vataiva Lake logger and the data recording duration, applied corrections and output format were the same as those for the Vataiva Lake logger.

Figure 3-20 shows the Vataiva Lake WSE record for the period of deployment along with the river level record for the Obo (FLY15) gauge. There is a good correlation between the two records with a relatively systematic offset of approximately 0.4 m, which is predominantly a function of the river gradient between the ARM228 and the Obo gauge site along with a temporal offset to account for the delay in water level between the floodplain site and the main stem.

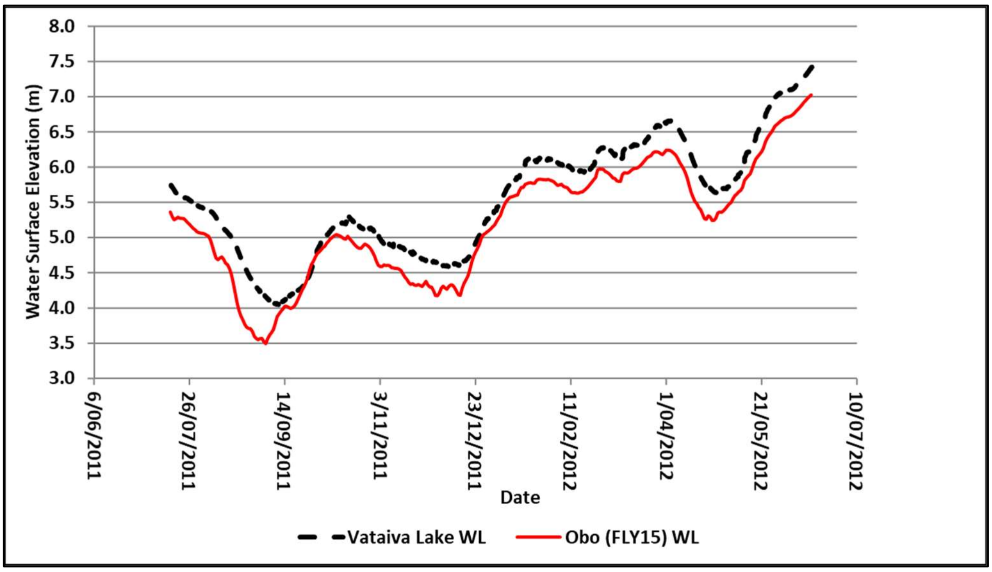

Figure 3-20 Obo (FLY15) and Vataiva Lake water level records for the period of July 2011 to June 2012. The Obo river level gauging site is located approximately 10 nm downstream of the Vataiva Lake site.

The relationship between the FLY15 gauge and the Vataiva Lake WSE is shown in Figure 3-21 and this plot confirms the high correlation ($R = 0.99$) between the WSE records of the two sites. The RMSE for the difference between the measured and derived water levels at Vataiva Lake was 13.7 cm over the full inundation range and 7.8 cm over the median-to-high range. At very low water levels, there is a temporal response delay, which converts into an elevation uncertainty of approximately 0.2–0.3 m.

A corrected gauge for the floodplain water levels at Vataiva Lake was created so that direct comparison with the altimetric WSE record could be undertaken for the period 2002–16. Unlike the Kemea Lagoon site, the majority of water exchange between river and floodplain for the Vataiva Lake site occurs in the vicinity of ARM228, as evident in the relatively uniform correlation between Vataiva Lake WSE and FLY15 river levels for the full range of inundation conditions.

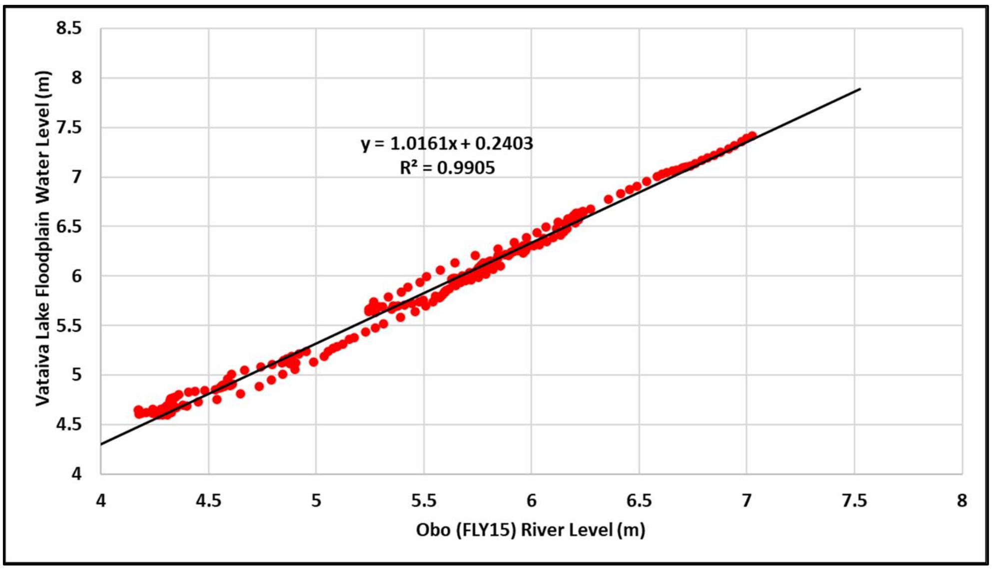

Figure 3-21 The relationship between the Obo (FLY15) river level and Vataiva Lake WSEs showing high correlation ($R = 0.99$) between WSEs over the majority of the inundation range. This relationship facilitates the creation of a virtual gauge at Vataiva Lake for the verification of Envisat RA-2 and SARAL/AltiKa altimetric WSEs.

The result of the comparison between the Vataiva Lake WSE record and the water level derived from FLY15 in-situ gauge river level record is shown in Figure 3-22.

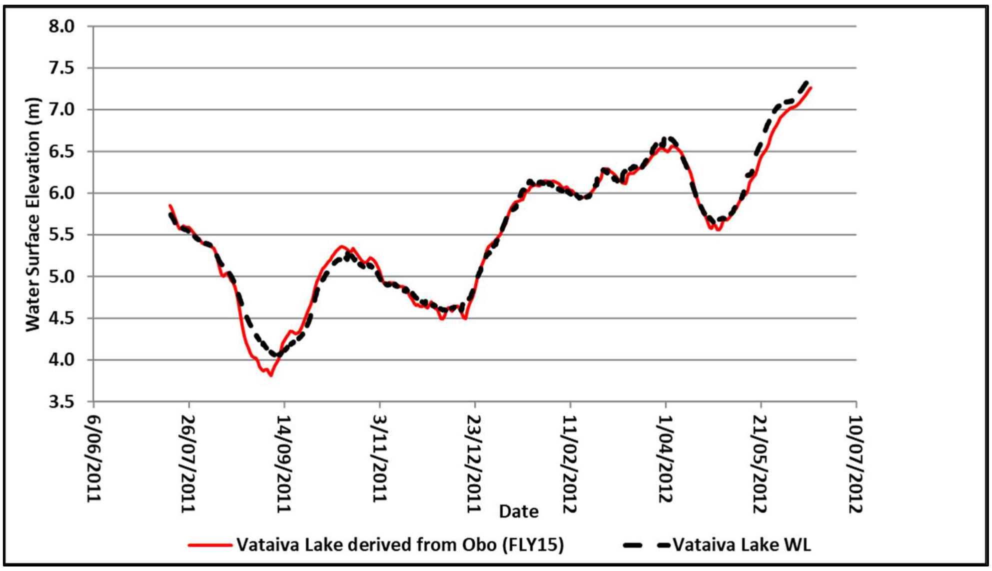

Figure 3-22 Vataiva Lake and the virtual ARM228 WSE gauge for the period of deployment. The corrected record correlates well with the observed floodplain water level at medium-to-high inundation levels; however, there is a minor unresolved latency evident at very low floodplain inundation levels.

Based on the above results, the virtual gauge at Vataiva Lake can be used for the majority of the altimetric WSE validation and additional hydrological studies through the whole of the floodplain inundation range, although with reduced accuracy at very low water levels. Improvements to the Vataiva Lake virtual gauge would require additional investigation to assess the relationship between the main stem WSE and the floodplain WSE for low inundation conditions and as a function of whether the floodplain was filling or discharging.

3.4 Summary

An extensive in-situ hydrologic network exists on the Fly River and has been maintained by OTML over the past three to four decades. These data form an integral part of the validation undertaken in this study. A deficiency with the in-situ gauge network, however, relates to data availability at low river level, specifically at extreme low river levels as observed under El Niño conditions. Under such conditions the river level has dropped below the orifice of the sensor at all sites and this resulted in data voids during these periods. This limits the validation of derived altimetric WSEs under similar conditions.

The rationale for quantitatively assessing the relationship between floodplain WSEs and main stem river levels is to determine the potential for using virtual floodplain WSE records, derived from riverine gauges, to validate satellite altimetry-derived WSEs across the floodplain. The above results confirm that virtual WSE records derived from in-situ gauges can be used for floodplain altimetric WSE assessments subject to an understanding of floodplain hydrological interactions.

Although the in-situ river gauge data can be corrected to approximate floodplain WSE, the complexity of the system means that any validation needs to be undertaken with a solid understanding of the hydrological processes to be effective. Floodplain complexity relates to the extent of levee breaches, tie channels and creeks that facilitate the exchange of water between the river and the floodplain as well as the extent of open water and vegetation within the floodplain itself. A significant additional complexity is the response of the floodplain water as a function of flow levels in the main stem. Based on the data from Kemea Lagoon and Vataiva Lake, these complexities mean that, while surrogate water level records can be used for some hydrologic studies, validation in the more complex hydrological zones will require data from in-situ floodplain WSE recorders.

The in-situ floodplain records for Kemea Lagoon and Vataiva Lake allow for an understanding of the relationship between floodplain and river water levels. For this research project the Vataiva Lake site, in particular, is of importance because of its proximity to Envisat and SARAL ascending pass 0677 and because of its high correlation with WSE on the main stem. The results from the establishment of the virtual gauge at this site indicate that data validation can be undertaken over the full period of Envisat RA-2 data acquisition as well as for SARAL/AltiKa data acquisitions prior to the move to a drifting phase.

CHAPTER 4: ALTIMETRY FOOTPRINT LANDFORM CLASSIFICATION

4.1 Introduction

The primary application of satellite radar altimetry is the measurement of SSH over open ocean. Of late, there has been an increased emphasis on the measurement of SSH in the coastal zone and WSE over inland waters. In these zones, radar altimetry returns are often contaminated by adjacent land topography and vegetation cover. Many inland water bodies vary in extent, both spatially and temporally, and recent studies have been limited to regions that are large, temporally invariant and permanently inundated. In many of these studies water extent masks and geographic limits have been used to isolate waveforms that should be considered for retracking (Berry, 2006; Frappart et al., 2006; Becker et al., 2014; Villadsen et al., 2016). At these sites, it is assumed that all waveforms within the fixed mask bounds relate to a reflection from an inundated surface and there is little scope to omit individual waveforms from analysis if the nature of the reflecting surface changes.

The largest source of error for inland water altimetry results from specular reflectors within the altimeter echo footprint that can lead to an off-nadir distortion termed hooking (Santos da Silva et al., 2010). If not detected and removed, this distortion will result in an over-estimate of the estimated satellite-to-nadir range leading to an incorrect WSE estimate. In the case of a single off-nadir reflector—evident, for example, in cases of one calm water target surrounded by exposed land or vegetation—the resulting water surface profile exhibits a signature hyperbolic shape (Frappart et al., 2006; Santos da Silva et al., 2010; Maillard et al., 2015; Boergens et al., 2016). This occurs because the altimeter has hooked into the bright target as it approaches and then passes over the target. The resulting WSEs are derived from the off-nadir range to the bright target, which results in a hyperbolic shape for the derived WSE. In the case of a complex wetland, however, it is likely that the hooking reflector changes as the echo footprint moves across the terrain and passes over a myriad of potential reflectors. In this case, the typical hyperbolic shape does not always form, and the derived WSE profile appears contaminated by random noise without any uniform water surface defined. The ability to classify the altimetric echo footprint allows for the existence of any off-nadir distortion to be identified and for the location of any off-nadir reflectors that may exist to be determined. An understanding of these characteristics facilitates implementation of methods to either correct for the distortion or exclude the waveform from further calculations. In Marshall and Deng (2016), the importance of off-nadir distortion was understated; however, the methodology developed in that study has been effectively incorporated into the processes developed in this thesis associated with identification and management of the hooking effect.

This section introduces satellite image analysis methodologies that aid the automated selection of waveforms with an inundated nadir footprint within heterogeneous inland waters. Altimetry waveforms identified as being contaminated by land topography or vegetation cover are assessed for sub-waveform peaks that relate to a nadir water return. If such a sub-waveform is not identified, then, despite having waveform structure that potentially facilitates further analysis, the waveform is omitted so that there is no contamination of the final WSE time series. The waveform selection methodologies introduced in this thesis are most suited to regions where there is a complex mix of landform and inundated zones, such as exists in large floodplains and complex wetlands. For these areas the altimetry footprint classification approach is used in conjunction with altimetry waveform variables (e.g. shape and backscatter coefficient) to determine waveform returns, or the portion of a complex waveform, derived from nadir water surfaces. While the methods developed offer significant benefits for altimetry retracking over heterogeneous inland waters—where the topography is more variable—as well as single well-defined water bodies or where larger water bodies are evident, a classical waveform analysis approach along with the use of inundation masks is likely to offer a more robust and simpler solution.

4.2 The rationale for altimetry footprint classification

While some waveform shapes suggest a water surface origin, shape alone does not offer a robust method for determining the nature of the reflecting surface, particularly for flat floodplain and complex wetland environments. For large inland water bodies, it is possible to create water masks that delineate the spatial extent (Smith and Berry, 2007; Sulistioadi et al., 2015; Villadsen et al., 2016) since extent varies little even with significant differences in catchment rainfall. Methodologies have been proposed using waveform analysis with selection based on shape conformance (Tourian, 2012; Sulistioadi et al., 2015) and use of the backscatter coefficient as a measure of inundation extent (Rosmorduc et al., 2018). Such methodologies, however, do not account for high-power specular returns that may result from extensive flat features such as beds of inundated aquatic vegetation and exposed mud banks. In this study, a method is proposed based on image analysis that facilitates the accurate and automated classification of the nadir waveform reflecting surface and enables the extraction of those waveforms that represent a return from a water surface. The process developed builds on the results published in Marshall and Deng (2016). Methodologies for the selection of waveforms over water using satellite imagery have been proposed (Baup et al., 2014; Sulistioadi et al., 2015), but these methods are limited to the definition of geographic extent masks derived from the imagery. In this study, 30-m resolution Landsat multispectral imagery and Envisat advanced synthetic aperture radar (ASAR) imagery are used for waveform classification and to illustrate the methodology. The Landsat imagery used is a combination of Landsat 5 Thematic Mapper (TM5), Landsat 7 Enhanced Thematic Mapper (ETM7) and Landsat 8 Operational Land Imager (OLI8) cloud-free imagery, with the ETM7 data being restricted to acquisitions before the failure of the scan line corrector. The ASAR imagery used is a composite false colour image derived from the horizontal transmit/horizontal receive (HH) and vertical transmit/vertical receive (VV) polarisations.

The proposed method is flexible and a range of input image types could be used, although the assessment criteria for each would differ as a function of radiometry type. Multispectral imagery offers the advantage of multiple bands including bands in the infra-red spectrum, which allows identification of vegetation and water within the scene. ASAR imagery is not affected by cloud cover and allows direct identification of water in a scene by assessing radar return intensity. While this could result in a larger image archive than that for multispectral acquisitions, the lack of global coverage would limit use. Although aerial photography could be used it would be limited to interpretation from the visible spectrum and there would need to be a more qualitative assessment of water and vegetation footprints.

Classifications with the highest accuracy will be achieved in cases where the image and the altimetry data are temporally coincident. As the acquisition time between data points increases, the potential for errors in inundation classification will also increase unless other image selection strategies are employed.

4.3 Study area and data

The study area for these investigations is the middle Fly floodplain as defined in Figure 1-4. The inundation range across the study area can be as high as 15 m between drought and flood conditions and there is a maximum river level rate of change of approximately 2 m per day in the upper reaches and approximately half that through the lower reaches (OTML, 1963–2020). While the rate of change in water level across the floodplain will not be as high as that in the main stem, the magnitude of change is still significant on a weekly timescale. If altimetry acquisition occurs during a period of rapid water level change the classification imagery would need to be acquired within several days to give an accurate assessment of the state of the altimetry footprint. To minimise the potential for errors stemming from not acquiring the image within this time, an archive of images is used with an image referenced to a floodplain inundation range rather than being referenced to a specific time. Initial retracking enables the extraction of an approximate floodplain WSE that facilitates the selection of imagery from the archive that best represents the inundation state at the time of altimetry acquisition. While there will be some minor spatial variation in aquatic vegetation extent between acquisition dates, the location and extent of floodplain forest, the spatial extent of the floodplain and the location of geomorphological elements are relatively stable as the Fly River does not experience rapid lateral migration (Pickup and Marshall, 2009). Periodic updating of the image archive, with cloud-free imagery as it becomes available, is undertaken to manage longer-term changes. This process means that the inundation state can be accurately derived from an image kernel extracted at the altimetry footprint irrespective of temporal offset between the classification image and the altimetric acquisition.

The altimetry waveforms used in this section are from the Envisat RA-2 altimeter, but the methodology is not dependent on waveform type or structure and the classification methodology is readily applied to data from other radar altimeters. The classification process has been automated with little processing time penalty added to the retracking task. Inputs consist of the archive of classification imagery, the altimetry waveform SGDR data and the geographic bounds of the study area.

In this section, altimetry cycles representing extreme conditions—a predominantly wet period in March 2009 and a predominantly dry period in October 2002—are used to assess the proposed methodology. Figure 4-1 shows the portion of the Fly River floodplain used in this study along with an example of the floodplain conditions and resulting altimeter waveforms for the wet March 2009 period. In Figure 4-2 the Envisat RA-2 18-Hz waveforms for the 2009 case are shown. For this period, most waveform returns are moderate- to high-power quasi-specular returns with no evidence of any significant hooking effect.

In Figure 4-3 the Envisat RA-2 18-Hz waveforms for the dry 2002 case are shown. There are quasi-specular returns of moderate to high power but there is also evidence of low-power and multi-peaked returns. While most of the higher-power quasi-specular returns are from inundated zones, there is evidence of quasi-specular returns from both bare and vegetated nadir altimetry footprints as well. This is illustrated in Figure 4-4, which shows the waveforms from the northern end of the study area for the dry 2002 example.

Figure 4-1 Envisat RA-2 waveforms for pass 0677 cycle 077 (26 March 2009) over the Fly River floodplain between latitude 7.0794°S and 6.8052°S. The background is a false colour image from Landsat TM5 acquired on 29 March 2009.

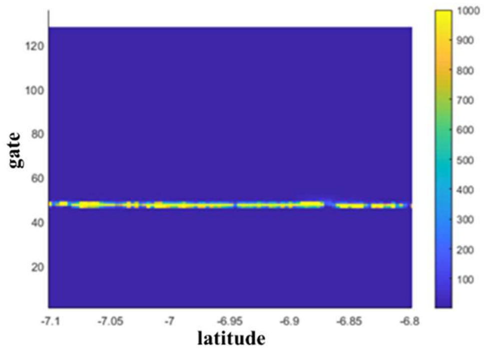

Figure 4-2 Envisat RA-2 waveforms for pass 0677 cycle 077 (26 March 2009) between 7.0794°S and 6.8052°S. Floodplain inundation levels were high at the time of the altimeter pass. (Waveform power has been stretched to the range 0–1000). Most waveforms are moderate- to high-power quasi-specular returns and there is no evidence of any significant hooking in the waveform sequence.

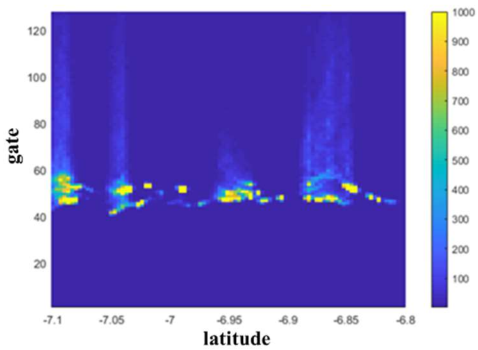

Figure 4-3 Envisat RA-2 waveforms for pass 0677 cycle 010 (24 October 2002) between 7.0794°S and 6.8052°S. (Waveform power has been stretched to the range 0–1000 to emphasise the structure of the lower-power returns). Floodplain inundation levels were low at the time of the altimeter pass.

In Figure 4-4, the dominant waveform shape is quasi-specular, typical of a calm water return (quasi-specular with relatively high maximum power and backscatter coefficient) despite being located over bare land. The potential for nadir returns from exposed mudflats (cf. Figures 4-5 and 4-6 from Lake Daviumbu, located immediately west of Obo) or for off-nadir distortion due to hooking into adjacent water bodies requires further investigation that is assisted by the developments presented in this section. Based on the high power of waveforms 72 and 73, compared with the power of the other waveforms in this sequence, it is likely that the altimeter has hooked to the Agu River through this portion of the pass.

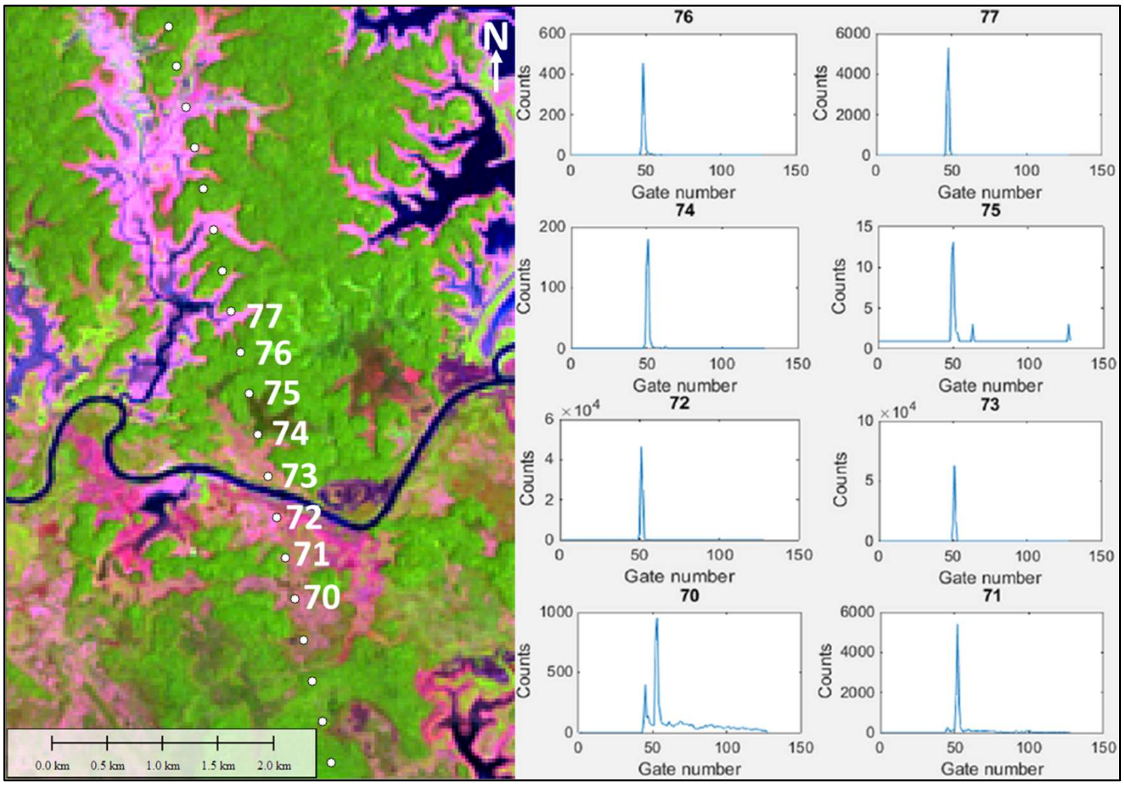

Figure 4-4 Envisat RA-2 waveforms (right panel) for pass 0677 cycle 010 (left panel) acquired on 24 October 2002 at the northern end of the study area. The existence of moderate- to high-power quasi-specular returns indicates the potential for a hooking event; however, the return may also be nadir returns from the exposed mudflats at locations 70–73. The background is a false colour image from Landsat ETM7 acquired on 28 October 2002.

Figure 4-5 Lake Daviumbu, (located in the south-west of the Fly River floodplain) during a high inundation period in July 2011.

Figure 4-6 The exposed mudflats of Lake Daviumbu during the 2015 El Niño.

Although waveforms 72 and 73 are likely associated with an Agu River return, the remaining waveforms would be incorrectly retained and processed in a manner consistent with a return from a nadir floodplain water body unless additional waveform selection methods were employed. The exclusion of these data from the final WSE sequence would rely heavily on statistical outlier detection methodologies; however, this is not practical in cases where the floodplain is relatively dry and numerous echo contamination sources limit the quantity of valid data for comparison.

All waveforms captured over water surfaces on the Fly River floodplain are likely to be contaminated in part by surrounding vegetation and variable topography and this suggests that a robust waveform classification and identification method are required.

4.4 Image analysis methodology

The methodologies proposed are flexible with a range of potential image inputs possible, although the assessment criteria for each will differ as a function of radiometry type.

4.4.1 Landsat multispectral imagery—classification methodology and results

Landsat sensors record reflected and emitted energy from Earth in various wavelengths of the electromagnetic spectrum (United States Geological Survey [USGS], 2020). The reflectance characteristics of the Landsat sensor are well documented and can be used to discriminate vegetation, soil and water within a scene based on analysis of the relative reflectance in different band combinations.

The near infrared (NIR) (0.76–0.90 µm) and middle infrared (MIR) (1.55–1.75 µm) bands of the Landsat sensor exhibit low reflectance over water bodies (both clear and turbid) and high reflectance over vegetation, varying as a function of density and health of the vegetation. For this study, the relative intensity of the NIR band (reflected NIR intensity scaled in the range 0–255) is used as the primary measure of inundation extent over the altimetry footprint. The Normalised Difference Vegetation Index (NDVI) is used to quantify the density of plant growth (Weier and Herring, 2015) and is calculated from the red (*rRed*) and NIR (*rNIR*) reflectance as:

$$NDVI = \frac{(rNIR - rRed)}{(rNIR + rRed)} \qquad \text{4-1}$$

The NDVI ratio (–1.0 to +1.0) is used as an indicator of vegetation extent once inundation status has been determined. The Normalised Difference Water Index (NDWI) (McFeeters,

1996) is not used because it leads to classification inconsistencies between turbid, clear and tannin-containing water.

An image kernel is captured at the nadir of each altimetry waveform location from a Landsat false-colour MIR, NIR and visible red image. The image kernel size used in this study is a 5 × 5-pixel patch, equivalent to 150 × 150-m ground coverage, which allows for an off-nadir assessment of inundation as well as of surrounding vegetation and land surface conditions. For a more targeted assessment, the kernel size would be reduced so that the footprint information came only from the altimetry nadir image pixel. If land surface conditions further from nadir were contaminating the waveform the kernel size would be increased. In this study, the altimetry footprint is classified as inundated if the average NIR intensity is less than an empirically derived threshold level of 100, and the zone is classified as vegetated if the NDVI ratio is > –0.1. Both threshold levels are derived empirically for the 5 × 5-pixel patch by comparison of the average NIR intensity and NDVI ratio for select sites, which are compared against in-situ assessments of inundation state and vegetation cover. Locations selected for the assessment consist of inundated, bare and vegetated sites. From these assessments, threshold levels that allow for discrimination between the land surface types are derived.

The extracted image kernels for a small section of the middle Fly floodplain are shown as examples of the image analysis process in Figures 4-7 and 4-8. The latitude range for the waveforms is 7.0376°S to 7.0141°S.

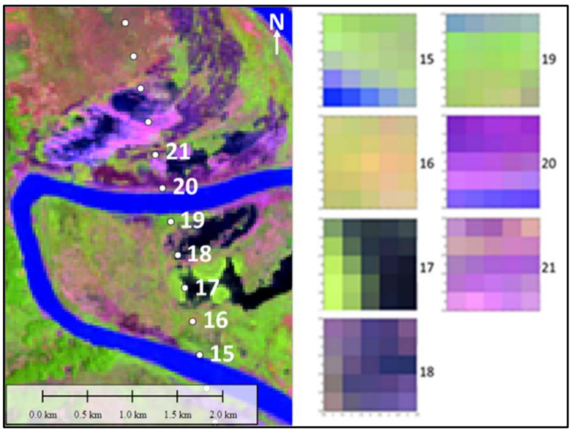

Figure 4-7 Image kernel extract locations (left panel) from Landsat ETM7 (28 October 2002) with associated image kernel extracts in the right panel. Envisat RA-2 waveform locations are from 24 October 2002. Returns 15, 17, 18, 19 and 20 show some degree of water within the captured image kernel, while return 16 represents a vegetated dry floodplain and return 21 a bare dry floodplain.

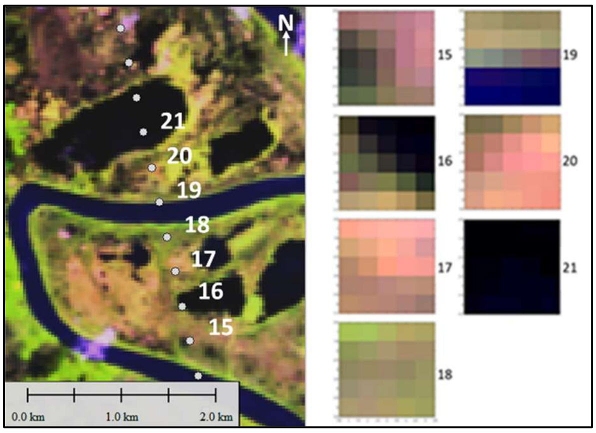

Figure 4-8 Envisat RA-2 waveform locations are from 26 March 2009. Image kernel extract locations from Landsat TM5 (29 March 2009) with associated image kernel extracts are in the right panel. Waveform 21 footprint is inundated while returns 16 and 19 are from an inundated floodplain with partial vegetation cover.

The sub-plots referenced by the along-track waveform numbers are the 5 × 5-pixel image kernels within the altimetry footprint and consist of the reflected intensity scaled in the range 0–255. Figures 4-9 and 4-10 show the NIR intensity and NDVI results for the 84 waveforms across the floodplain for the 2002 dry floodplain and 2009 wet floodplain respectively.

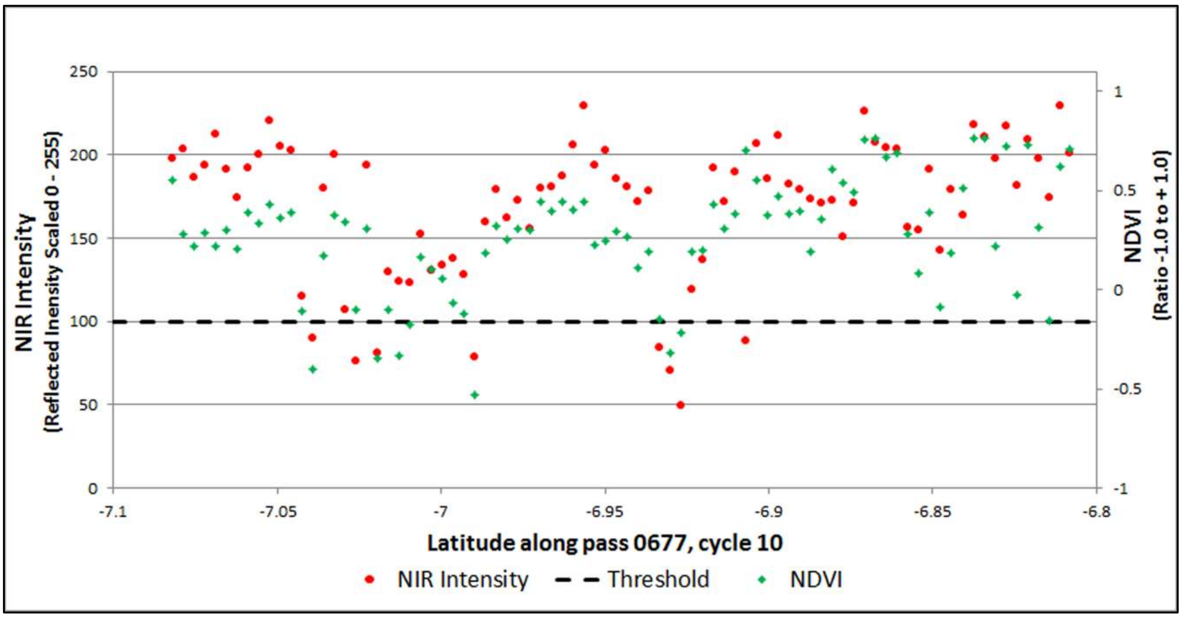

Figure 4-9 NIR intensity and NDVI extracted from Landsat ETM7 (28 October 2002) for Envisat pass 0677 cycle 10 altimetry footprint classification. The dashed line defines the threshold for NIR intensity, 100 on the left axis, and for NDVI, –0.1 on the right axis. NIR less than the defined threshold indicates inundation and NDVI greater than the defined threshold indicates vegetation.

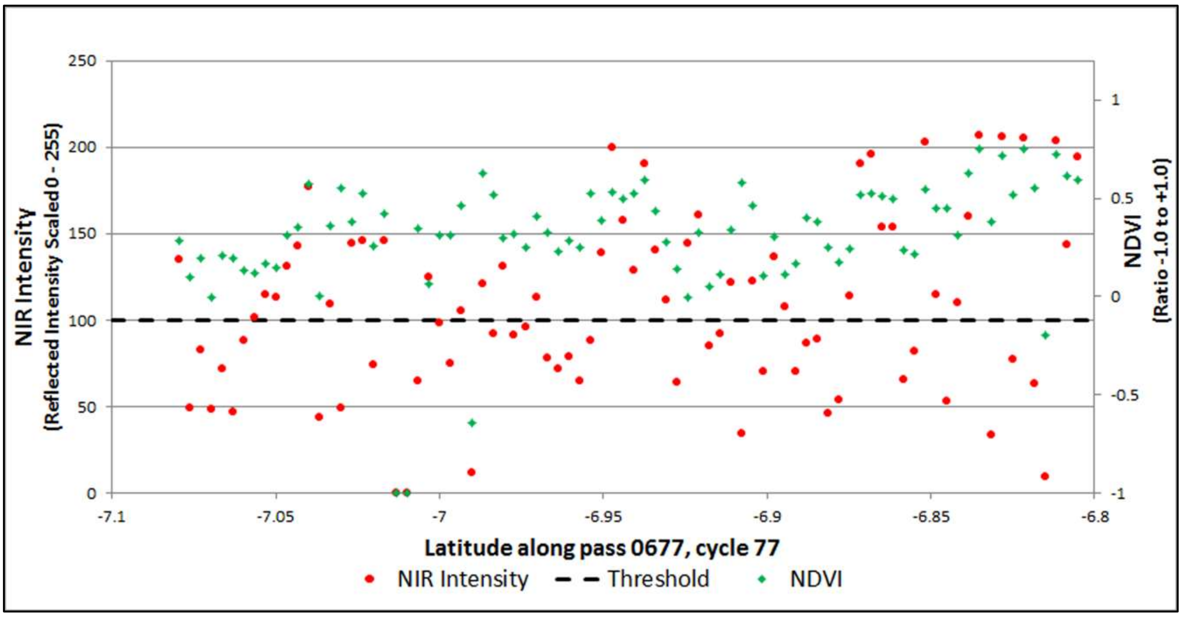

Figure 4-10 NIR intensity and NDVI extracted from Landsat TM5 (29 March 2009) for Envisat pass 0677 cycle 77 altimetry footprint classification. The dashed line defines the threshold for NIR intensity, 100 on the left axis, and for NDVI, 0.1 on the right axis. NIR less than the defined threshold indicates inundation and NDVI greater than the defined threshold indicates vegetation.

In the example of the dry floodplain (October 2002, Figure 4-9) only six waveforms are identified as being reflected from a surface that is both inundated and vegetation free. In the example of the inundated floodplain (March 2009,Figure 4-10) 40 locations are classified as inundated. Most of these locations contain some degree of vegetation cover with only four being classified as free of vegetation.

For each altimetry footprint, ground truthing was undertaken as part of a program of classification using robust remote sensing methodologies along with an in-situ assessment in July 2011. This involved measurement of inundation state and vegetation cover type at each altimetry footprint location for validation of the process. The in-situ results are used to calibrate the remote sensing process developed using a Landsat TM5 image captured on 4 April 2011 under similar inundation conditions to the in-situ assessment. The calibrated remote sensing process is then applied to the results derived from the October 2002 and March 2009 images.

Using the image analysis classification process developed in this section, 95% of sites were correctly classified for inundation extent using the NIR intensity measure while 93% of sites were correctly classified with respect to vegetation cover for the 2002 inundated floodplain. The 2009 epoch is at the upper quartile of floodplain inundation levels, with little exposed landform across the floodplain but with extensive vegetation colonisation over most of the inundated zones. The image analysis classification process, using the NIR threshold exceedance measure, successfully classified 92% of waveforms for inundation extent and all sites were correctly assessed for vegetation extent using the NDVI ratio.

Waveform classifications are also undertaken using the classical approach of analysis based on an assessment of the shape and maximum return power. Noisy and non-specular waveforms are excluded, as are specular waveforms of low maximum power. While the approach does not allow for determination of the exact nature of the altimetry footprint, this can be inferred from waveform shape. However, the method does not account for the significant risk of hooking and the fact that a specular return may not originate from nadir.

The results from the classical waveform classification approach are compared with the ground truthing results for an assessment of classification reliability. For the 2002 dry floodplain example, the classification accuracy was 81%, with 15 of the 84 waveforms assessed as having an inundated footprint despite being overexposed mudflats. For the 2009 inundated floodplain example, the classification accuracy was 65% with 29 of 84 waveforms showing a false positive for inundation. These false positives are likely to have been due to an extensive cover of aquatic vegetation or a hooking effect, which would need to have corrections applied for any derived water levels to be valid.

Figures 4-11 and 4-12 show the results of the altimetry footprint classification, using the results from the image analysis methodology developed in this section, for the two periods detailed in this study. Waveforms assessed to originate from an inundated nadir and those that originate from an inundated and vegetated nadir are identified.

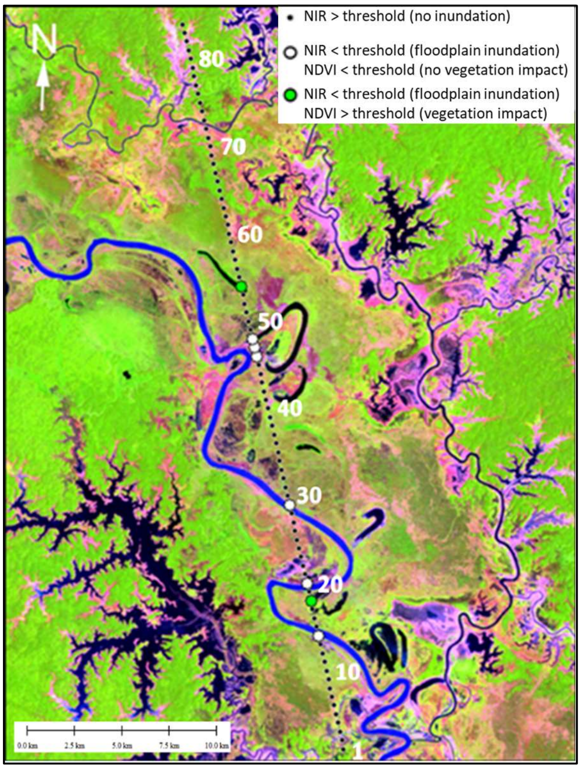

Figure 4-11 Results of the Envisat RA-2 18-Hz waveform inundation classification (pass 0677, cycle 10) from the Landsat ETM7 image acquired 28 October 2002. Waveforms over open water (white marker) and over water with partial vegetation cover (green marker) are identified

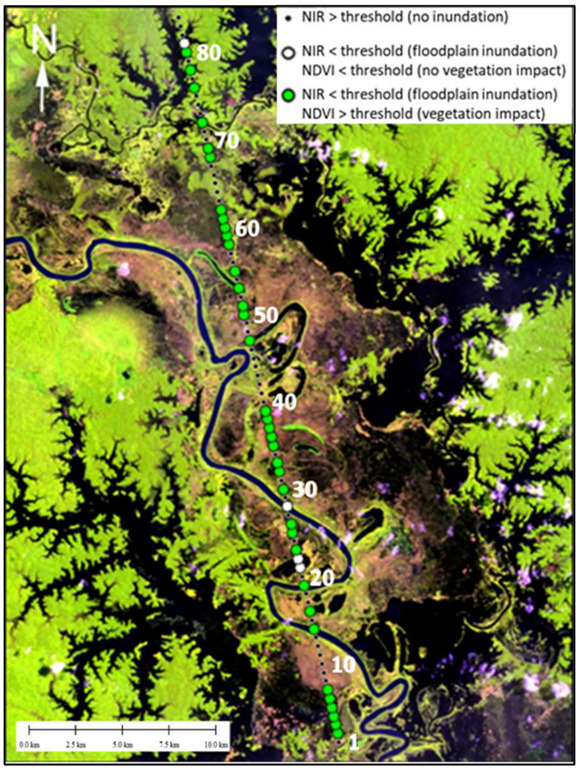

Figure 4-12 Results of the Envisat RA-2 18-Hz waveform inundation classification (pass 0677, cycle 77) from the Landsat TM5 image acquired 29 March 2009. Waveforms over open water (white marker) and over water with partial vegetation cover (green marker) are identified.

Based on these results it is proposed that an initial classification be undertaken using NIR intensity and that waveforms below the NIR intensity threshold be flagged for retracking. The NDVI should be calculated for those waveforms below the NIR intensity threshold and the extent of vegetation cover estimated.

The classification methodology detailed above can be extended to facilitate the extraction of additional information regarding the altimetry footprint so that the waveform shape can be rigorously interpreted and any derived WSE more accurately assessed. This classification is undertaken using multi-spectral imagery, as detailed above, and is extended to allow for estimation of the nature of the altimetry footprint, not only an assessment of the inundation extent at nadir. This is of particular importance for assessing zones of inundated vegetation or bare ground that are candidate locations for off-nadir hooking. The methodology relies on defining the relationship between radiometric response in a multispectral image and the composition of the actual altimetry footprint. Accurately geo-referenced imagery with appropriate calibration and consistent balancing is required for this to be extended across a range of images covering an extended temporal range. For Landsat imagery, a false colour composite scene is formed using MIR (1.57–1.65 µm), NIR (0.85–0.88 µm) and red bands (0.64–0.67 µm) (USGS, 2020). For four-band multispectral imagery, the NIR band along with red and green bands is used, although classification criteria will vary slightly from that developed in this section. The footprint categories and image bands used for the analysis can vary as a function of the application and the type of imagery available for interpretation.

To illustrate the analysis methodology, classifications are undertaken using the same October 2002 and March 2009 Landsat scenes introduced above. The altimetry footprint classes that are defined are open water, inundated vegetation, dense vegetation, sparse vegetation (grassland/open forest), bare ground and inundated bare ground. Cut-off levels for each band are determined by empirical comparison of the radiometric response and ground-truthing records, with the radiometric response values for each altimetry footprint classification class defined in Table 4-1.

Table 4-1 Footprint classification criteria adopted for the Landsat ETM7 and TM5 images in Figures 4-13 and 4-14. MIR, NIR and red bands are used along with NDVI. Cut-off levels for each band are determined by empirical comparison of the radiometric response and ground-truthing records.

Footprint category	Class	NIR – MIR	NDVI	NIR
Open water	1	<40	<0.15	<50
Dense vegetation (forest)	3	>50	>0.15	>120
Inundated forest	2	>50	>0.15	<120
Sparse vegetation (grass/open forest)	4	<50	>0.15	>120
Inundated sparse vegetation	2	<50	>0.15	<120
Bare ground	5	<0	<0.15	>120
Inundated bare ground	6	<0	<0.15	<120

Classification results for Envisat RA-2 pass 0677, cycle 10 acquired 24 October 2002 and for Envisat RA-2 pass 0677, cycle 77 acquired 29 March 2009 are shown in Figures 4-13 and 4-14.

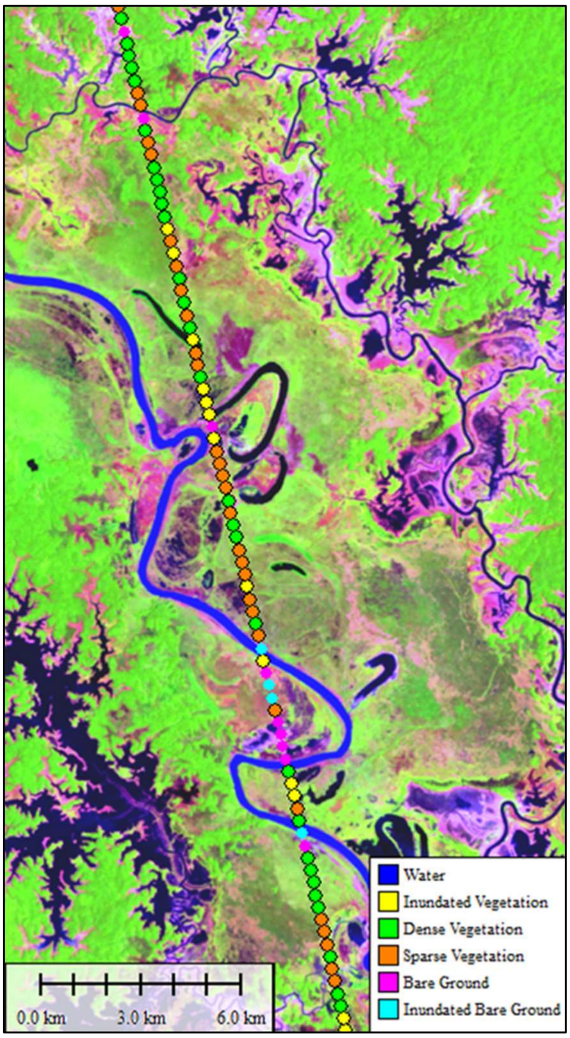

Figure 4-13 Results of the Envisat RA-2 18-Hz altimetry footprint classification for pass 0677, cycle 10 derived from the Landsat ETM7 image acquired 28 October 2002. Waveform locations are identified by the markers on the waveform track with classification identified by colour.

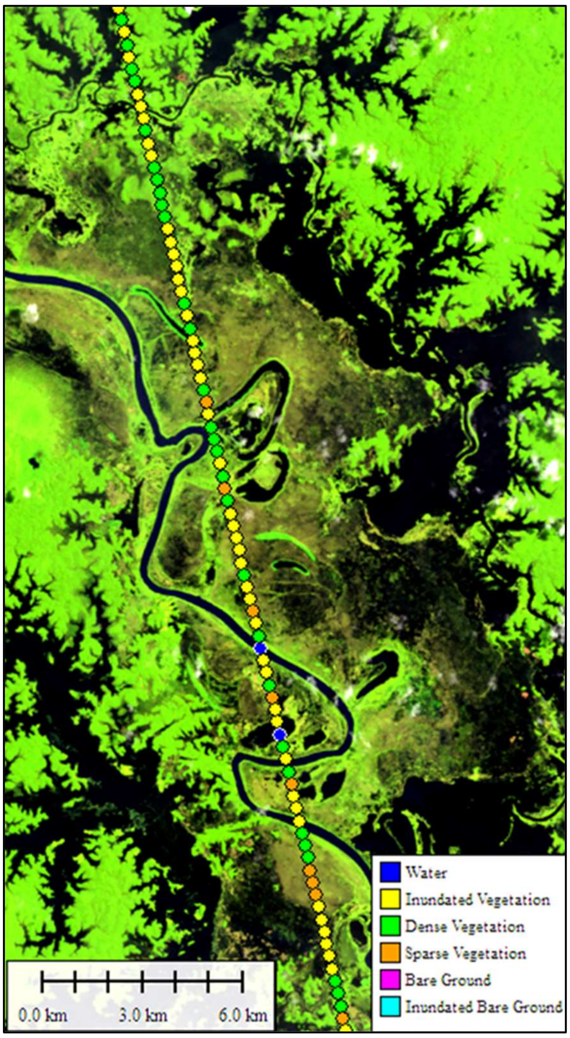

Figure 4-14 Results of the Envisat RA-2 18-Hz altimetry footprint classification for pass 0677, cycle 77 derived from the Landsat TM5 image acquired 29 March 2009. Waveform locations are identified by the markers on the waveform track with classification identified by colour.

It is evident from Figures 4-13 and 4-14 that the classification methodology not only detects zones of open water but identifies zones of inundated vegetation and inundated bare ground, from which quasi-specular altimetric waveforms would originate and that are potential candidate specular reflectors for waveform hooking. In this study, the footprint classification classes used are given in Table 4-1 and are used in the formulation of the optimised waveform retracker developed in Chapter 5.

4.4.2 Envisat ASAR imagery—classification methodology and results

The Envisat ASAR was one of nine instruments included in the Envisat satellite payload. The instrument operated at C-band in five modes, which allowed for a range of coverages and polarisations (Snaith, 2011). In alternating polarisation mode, two simultaneous images were acquired over a swath of 100 km and at a 30-m resolution.

While Envisat ASAR imagery is acquired at the same time as the altimetry acquisition from the RA-2 sensor it is an off-nadir acquisition. As such, the ASAR data acquired at the time of the altimetric acquisition do not cover the nadir track of the satellite. The temporal offset, however, will be relatively small as ASAR coverages are available from adjacent passes within the repeat cycle so the need to select suitable imagery from an inundation referenced catalogue is not critical. For this study, a single Envisat ASAR image is used to check suitability for water body detection and assessing the extent of vegetation colonisation of each altimetry footprint. As water surface on a radar image is represented by a low-intensity return signal (Liebe et al., 2008) this condition is used in differentiating water from vegetation and other landform features. A composite false colour image in HH and VV polarisations, represented as red (HH), green (VV) and blue (HH/VV), is used in the study with Envisat RA-2 18-Hz waveforms for pass 0677, cycle 36 acquired on 21 April 2005. Data are acquired during a period of average floodplain inundation. In a manner similar to that used for Landsat image processing, a 5 × 5-pixel image kernel is captured for each altimetry footprint with the example of a sequence of seven waveforms shown in Figure 4-15.

The HH polarisation is reported as optimal for classification of flooded areas, while VV polarisations offer better discrimination of forest and open grasslands (Henry et al., 2003). An empirically derived intensity cut-off threshold of 100 is used for both HH and VV polarisations. The results show a high correlation between these polarisations; however, subtle differences in intensity at the 100 threshold level facilitate an assessment of vegetation cover. For the HH polarisation data, 96% of inundated sites were identified correctly while for the VV polarisation 80% of inundated zones were correctly detected. The remaining 20% related to inundated sites colonised by floodplain vegetation. When classifying the nature of the altimetry footprints this dual polarisation assessment offers potential for detecting inundated zones and identifying locations that are colonised by sparse aquatic vegetation.

The primary classification of the altimetry waveforms using Envisat ASAR imagery is based on the HH polarisation, with an inundated floodplain indicated for sites with intensity below the threshold level of 100. The VV polarisation is used as a secondary process for vegetation discrimination over inundated zones to estimate vegetation extent. Figure 4-16 shows the results of the analysis of waveforms detailed in this study using ASAR imagery with identification of those waveforms determined to be over inundated zones. Waveforms acquired over inundated vegetation are also identified.

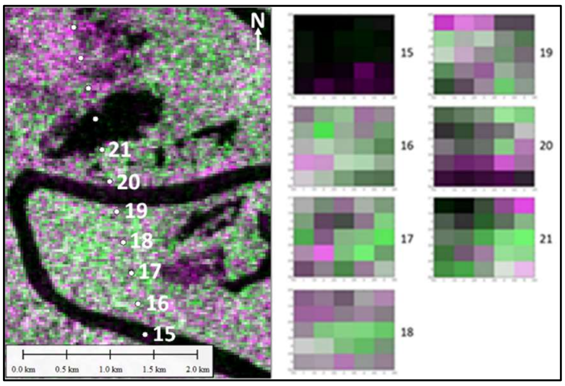

Figure 4-15 Image kernel extract locations (left panel) from Envisat ASAR (4 April 2005) with associated image kernel extracts in the right panel. The return for waveform 15 is located within the Fly River main channel, with the remaining returns being from an inundated but partially vegetated floodplain.

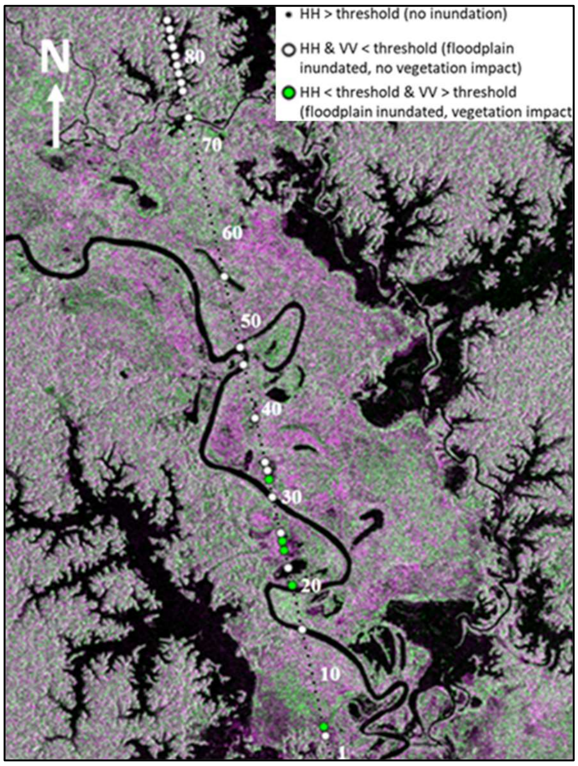

Figure 4-16 Results of the Envisat RA-2 18-Hz waveform classification (pass 0677, cycle 36) from the Envisat ASAR image acquired 4 April 2005. Waveforms over open water (white marker) and over water with partial vegetation cover (green marker) are identified.

4.5 Calm water prediction using image analysis

The water surface measurements derived from satellite altimetry can be severely contaminated by hooking distortions resulting from specular reflectors within the altimetry footprint. The distortion is arguably the largest single error source for nadir-looking pulse-limited altimeters (Calmant et al., 2009; Rosmorduc et al., 2018). There is no information inherent in a single waveform that identifies the leading-edge reflector although the location can be derived from a sequence of waveforms if a hooking hyperbola artefact is evident in the waveform echo sequence. For many applications over inland waters, particularly large floodplains and heterogeneous landforms, such an artefact does not exist as the bright source location varies as the satellite passes. In this section, a method is developed to estimate the location of the nearest calm water source relative to the satellite nadir location. This potential hooking location could be used as a target for a derived WSE estimate by using the slant range to the location in the processing phase. Alternatively, the range to the predicted location could be used to assist with the selection of the correct sub-waveform representing the nadir return or to assess waveform status where hooking is predicted from footprint classification, but where waveform shape is atypical.

The methodology developed in Section 4.4 is extended here to enable the prediction of the closest calm water location to the satellite nadir location. For this study, a calm water location is likely to be one comprising inundated vegetation, whether that be aquatic vegetation colonising an inland water body or an inundated sparse floodplain forest zone. It is also likely that calm water zones are evident at the interface between land and water where significant wind impacts are mitigated. The search process used is based on the Spiral of Theodorus (Gautschi, 2010), which is constructed from a series of right-angled triangles placed adjacent side to hypotenuse. The spiral starts with a triangle with sides of length i with the node formed between the adjacent sides and the hypotenuse located at the nadir point and with the sides oriented in cardinal directions. The hypotenuse of triangle one is $i\sqrt{2}$ and this becomes the base of the next triangle, which has sides of length i and $i\sqrt{2}$; and hypotenuse $i\sqrt{3}$. This process continues to the nth triangle where the sides are of length i and $i\sqrt{n}$. The starting direction for the search is arbitrary and can be altered if required as the construction process will result in a spiral irrespective of initial orientation. The construction methodology for the Spiral of Theodorus is depicted in Figure 4-17.

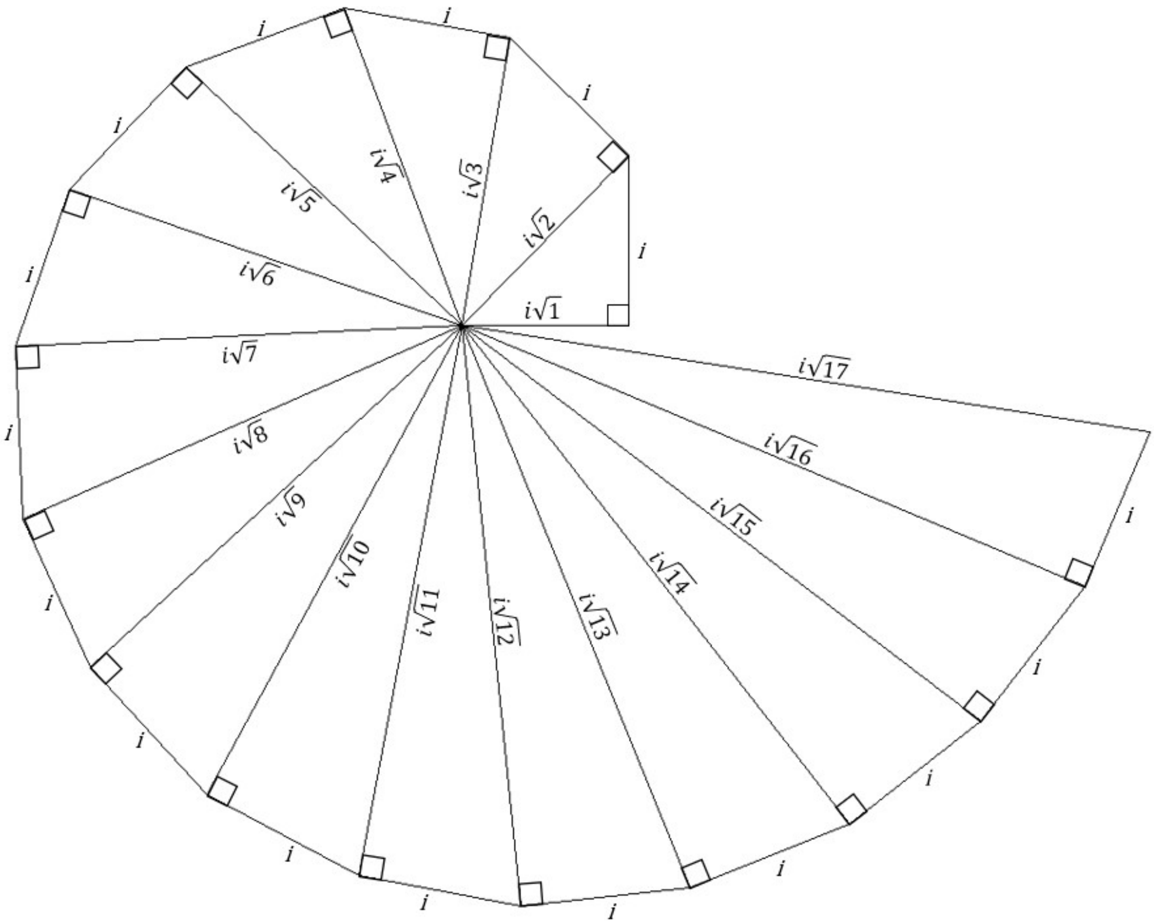

Figure 4-17 The methodology for the construction of a Spiral of Theodorus commencing with a right-angled triangle with legs of length i and ending at the nth triangle with leg lengths of i and $i\sqrt{n}$. The spacing of the spiral nodes and the separation of the spirals is governed by the scaling factor i.

The spacing between the spiral nodes and the separation of the spirals is governed by scaling factor *i*. A scaling factor of 30 results in a resolution comparable to standard Landsat imagery and this would accurately detect the closest calm water location, although there would be some computational time penalty if numerous searches were undertaken. In this study, a scaling factor of 100 is adopted, which gives a node spacing of 100 m and a spiral separation of approximately three times the node spacing. This is compatible with the image kernel resolution adopted for use in the footprint classification process detailed in Section 4.4. The search scaling factor can be arbitrarily varied, however, as a function of the balance between additional computing time versus the spatial resolution of the search.

In the case of water transitions the aim is to detect the closest potential calm water location and this is likely to be at the land–water interface where wind effects on surface water are reduced and the potential for specular reflectors (which cause hooking) is enhanced. Figure 4-18 shows an altimetry sequence over Lake Murray from Envisat RA-2 in descending pass 004 cycle 113 captured on 21 March 2012 with the Spiral of Theodorus calm water prediction shown.

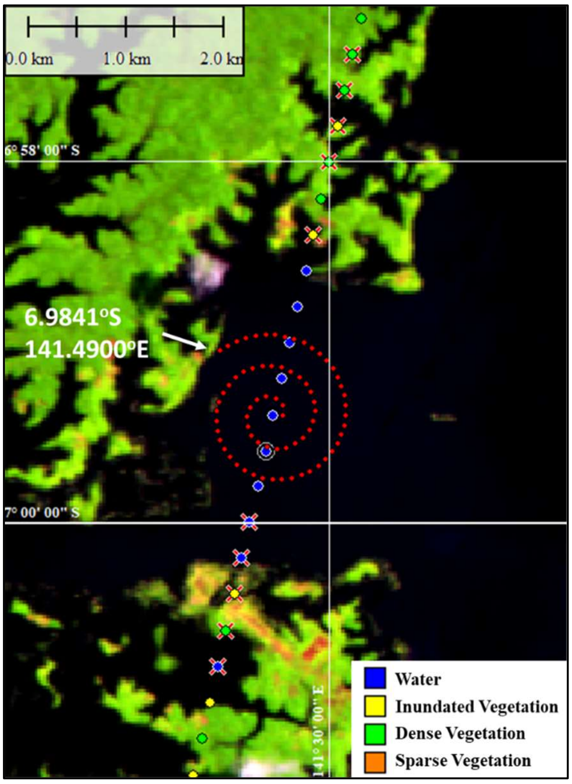

Figure 4-18 Altimetry sequence over Lake Murray from Envisat RA-2 in descending pass 004 cycle 113 captured on 21 March 2012 with a false colour image background captured by Landsat TM5 in April 2011. Specular waveforms are shown with a red cross and the predicted closest calm water site is identified using a Spiral of Theodorus search.

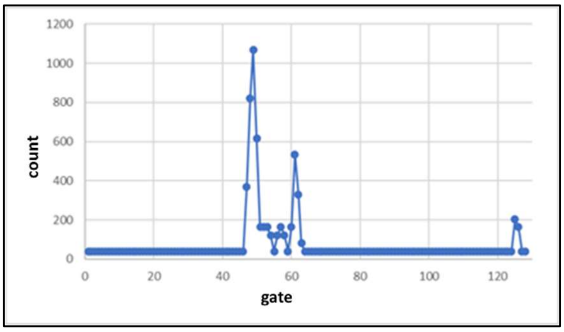

Figure 4-19 The multi-peaked waveform acquired at the origin for the calm water search of Figure 4-18. Based on WSE estimates calculated for quasi-specular returns leading into and out of the lake crossing, it was determined that this waveform did not contain a peak relating to a nadir reflection and that all peaks were from off-nadir reflectors.

A scaling factor of 100 is used to predict the closest calm water location for the multi-peaked waveform of Figure 4-19 with likely hooking to a reflector identified at a distance of approximately 885 m and bearing of 320° as shown in Figure 4-18.

Quasi-specular waveforms derived from inundated altimetry footprints leading into and out of the lake crossing are retracked and the WSE elevations estimated. The average WSE for these locations was determined to be 13.604. This is used to confirm that the waveform of Figure 4-19 did not contain a peak relating to a nadir reflection and that all peaks are related to off-nadir reflectors. The first peak is extracted as a sub-waveform and retracked with a resulting WSE of 13.042. The corrected satellite-to-surface range is hypothesised to be a slant range to the identified calm water reflector at a distance of 885 m and a correction for an equivalent nadir range is derived on this basis. A correction of 0.506 m is applied to the nadir WSE to give a WSE at the identified calm water location of 13.548, which is consistent with the WSE estimates leading into and out of the lake crossing.

In the case of land–water transitions, the location of the closest calm water site assists with the processing methodology adopted for specular waveforms originating from a non-water nadir footprint and for input into the sub-waveform selection process from a multi-peaked waveform if deriving a water level estimate for an off-nadir location. Figure 4-20 shows an altimetry pass leading into the upper reaches of Lake Murray acquired from Cryosat-2 SIRAL (LRM) on 7 March 2011 with a false colour image background captured by Landsat TM5 in April 2011.

At the location of the first specular waveform in the ascending pass, a prediction using the Spiral of Theodorus principle is undertaken to determine the closest zone of inundated vegetation to the altimetry nadir location. This is done as the altimetry nadir location was assessed as being not inundated dense vegetation and thus that hooking had occurred. The process identified a zone of inundated vegetation approximately 800 m ahead on the altimeter track. Figure 4-21 is for the same pass, but the required target is a calm open water site (at the scale of the image kernel being used in the image analysis) and this was identified approximately 3.5 km to the south-west. However, this location is an unlikely potential hooking location as it would be expected that preceding echoes in the sequence, which were closer to the predicted target, would have also been subject to the hooking distortion and had similar waveform shape characteristics.

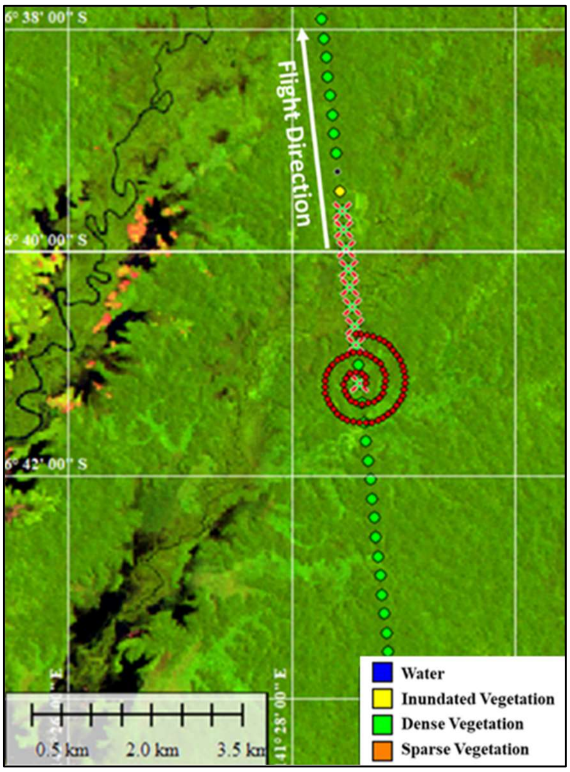

Figure 4-20 Altimetry sequence leading into the upper reaches of Lake Murray for a Cryosat-2 SIRAL (LRM) ascending pass captured on 7 March 2011 with a false colour image background captured by Landsat TM5 in April 2011. Specular waveforms are shown with a red cross and the predicted closest zone of inundated vegetation is identified, in this case along track.

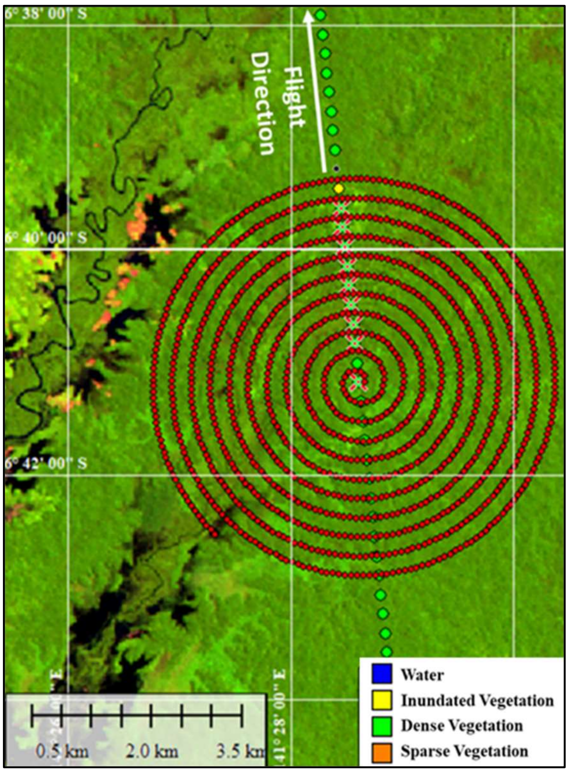

Figure 4-21 Altimetry sequence leading into the upper reaches of Lake Murray for a Cryosat-2 SIRAL (LRM) ascending pass captured on 7 March 2011 with a false colour image background captured by Landsat TM5 in April 2011. Specular waveforms are shown with a red cross and the predicted closest open water site is located.

While the calm water prediction process is not aimed at unambiguously identifying the hooking location for inland water satellite altimetry waveforms, it does offer an additional tool that can be used in an autonomous and adaptive retracking process to improve the quality and reliability of altimetry water level time series and WSE profiles across extensive floodplain and wetland environments.

4.6 Summary

Recent studies using altimetry data over inland waters have been generally restricted to the large river or lake systems where there is little or no contamination from surrounding landform and where extent masks or geographic limits offer a means of waveform selection from water body targets. A flexible method for the accurate and automated assessment of the inundation status of an altimetry footprint and assessment of the extent of vegetation cover has been developed in this study. The methodology utilises remote sensing techniques to identify waveforms reflected from a water surface. At the defined threshold levels, the method accurately identified ~90% of inundated sites along altimeter ground tracks and correctly selected waveforms reflected from water surfaces. This represents a significant improvement over the approach using classical waveform shape analysis.

The proposed altimetry footprint classification methodologies are not suited for all applications. For analyses conducted over large water bodies or in situations of variable topography, the classical approach of waveform shape analysis along with the use of accurate inundation masks would be both simpler and more robust, particularly if there is little topographic or hydrological variability within the area of the altimeter footprint. For large flat floodplains and their associated river systems, the proposed image analysis methodology does, however, offer a significant improvement in the accuracy of selection of inundated sites and offers potential for incorporation into an adaptive retracking process that manages the analysis as a function of both altimetry waveform structure and nature of the nadir altimetry footprint. There is also potential for improvement through learning strategies to aid the selection process and for optimised retracking of the waveforms assessed as being over water.

While the classification of the nadir footprint of an altimetry echo can be successfully and robustly undertaken, there will be cases where nadir is not the actual reflector for which the altimetric range is derived. Hooking can result in an off-nadir slant range estimate that, if left unidentified and not rectified, will result in errors in the derived WSE. In conjunction with other measures, including waveform shape and backscatter coefficient magnitude, the classification of the waveform nadir footprint can be used to assist in the treatment of any identified off-nadir distortion robustly and autonomously. It can also be used in the identification of off-nadir calm water reflectors using lateral and along-track searches to identify potential hooking sources.

CHAPTER 5: WAVEFORM RETRACKING

The satellite altimetry echo from open ocean reflectors varies little in shape and conforms to microwave scattering at nadir theory (Gommenginger et al., 2010) and this facilitates global and continuous measurements of SSH and other oceanic and geophysical parameters. Early developments focussing on microwave scattering theory were advanced by Brown (1977) and refined by Hayne (1980) with their work leading to what is known as the Brown–Hayne model. Wingham et al. (1986) reports the ocean-like return as being one from a horizontal homogeneous rough surface; the Brown–Hayne model represents the theoretical shape of an echo from such a surface (Gommenginger et al., 2010).

Waveform retracking is used extensively for ocean applications where the return time for the mid-power point of the waveform leading edge corresponds to the range between the satellite and a relatively flat average sea surface. For land and ice applications, topographic features are typically smaller than the altimeter footprint, so the reflected waveform can contain contributions from numerous reflecting surfaces (Nuth et al., 2002).

Through the coastal zone and across inland waters the altimetry echo does not generally conform to the theoretical shape defined by the Brown–Hayne model. Wingham et al. (1986) noted that if the Brown–Hayne model retracking algorithm is implemented over non-ocean targets, the derived range will be incorrect because the algorithm will attempt to fit a Brown–Hayne return template to a return shape that does not conform to the model structure. Early attempts to analyse inland water echoes were restricted to large water bodies, such as those found in the Great Lakes and in the lower reaches of the Amazon River (Berry et al., 2005a), where the altimetry echo replicated an ocean-like return. However, this was not possible for echoes over smaller water bodies as distortions to the echo return resulted in them being rejected by the Brown–Hayne model algorithm.

The presence of non-water targets within the altimeter footprint will introduce artefacts into the received waveforms with this signal contamination resulting in inaccurate range estimates (Vignudelli et al., 2019). An objective for the processing of data captured over inland waters has been to provide altimetric measurement over the range of inland water reflectors with retrieval frequency and accuracy rivalling that achieved over open oceans. To achieve this aim it was necessary to deviate from using physically based model retrackers (e.g. the Brown–Hayne model) and develop retrackers based on empirical observation and practical experience (Wingham et al., 1986; Gommenginger et al., 2010). The first class of empirical retrackers developed was based on fitting empirical functional forms with the second class being based on the statistical properties of the echo.

This chapter introduces physically based retrackers and model function-fitting empirical retrackers (Section 5.1), details statistical empirical retrackers (Section 5.2) and documents the WATeR altimetry retracking process developed in this study (Section 5.3.2).

5.1 Physical and empirical model fitting retrackers

5.1.1 Brown–Hayne ocean model

The Brown–Hayne model is based on the theory that the altimetry echo that results from open ocean reflectors conforms to the theoretical knowledge of microwave scattering at nadir. For a rough scattering surface, the waveform $W(t)$ is given by a convolution of three terms as defined by Brown (1977) and Hayne (1980):

$$W(t) = P_{FS}(t) * q_s(t) * S_r(t) \qquad \text{5-1}$$

where $P_{FS}(t)$ is the average flat surface response, $q_s(t)$ the surface probability density of specular points and $S_r(t)$ the radar point target response (Brown, 1977; Hayne, 1980).

Gommenginger et al. (2010) comment that despite the relatively small number of theoretical models for retracking ocean waveforms, there are numerous versions that differ as a function of number and type of parameter to be retrieved. Examples of the various mathematical representations of the theoretical model are detailed in Brown (1977), Hayne (1980), Amarouche et al. (2004), Deng and Featherstone (2006), Gommenginger et al. (2010) and others. The general form of the model remains relatively constant and is a function of time, pointing angle and antenna beamwidth (Hayne, 1980).

Figure 5-1 shows the typical Brown–Hayne waveform shape. The model parameters used to define the shape are shown in Equation 5-2 (Passaro et al., 2014; Peng and Deng, 2018), which defines the time series of the mean power waveform $P(t)$ measured by the altimeter. In Figure 5-1:

- P_N is the thermal noise
- P_u is the signal amplitude (which contributes towards normalised backscatter),
- τ is the time measured at the satellite such that $t = t_0$ corresponds to the nadir range
- σ_c is the rise time of the leading edge
- ξ is the trailing edge slope (correlated to off-nadir mispointing angle).

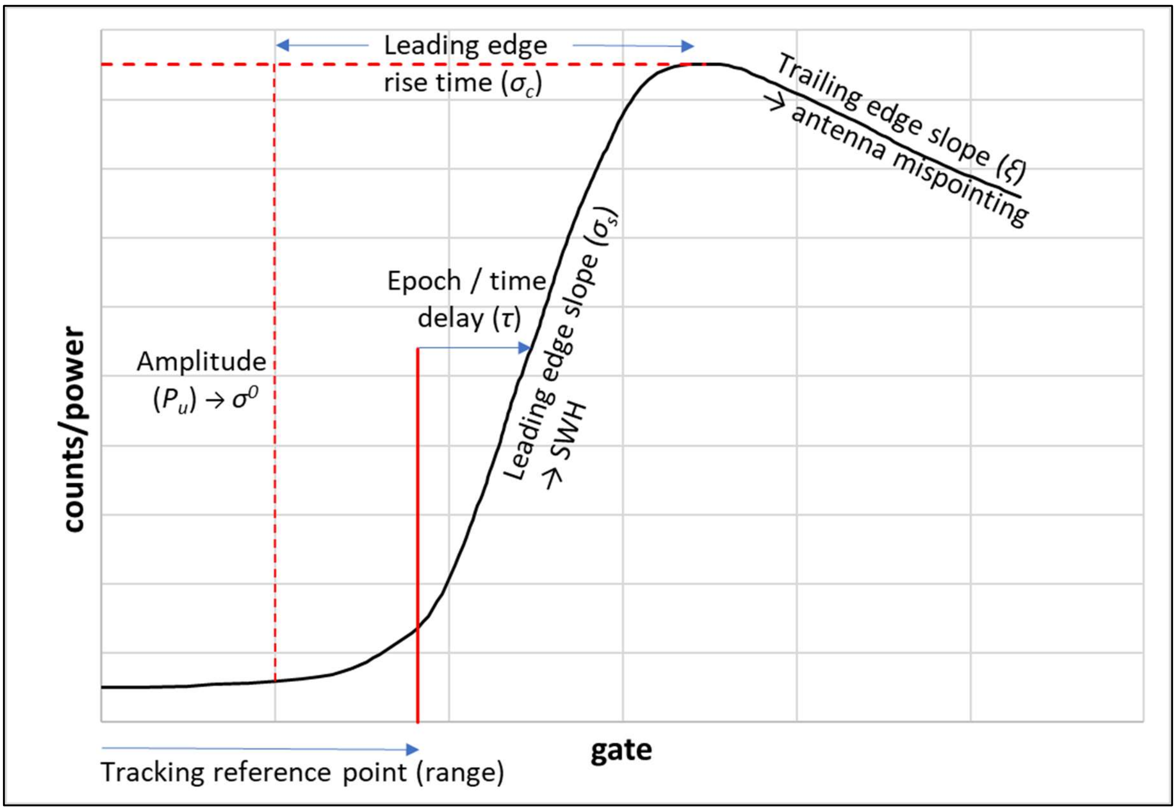

Figure 5-1 Brown–Hayne ocean waveform shape and Brown–Hayne model shape parameters, adapted from Gommenginger et al. (2010) and Passaro et al. (2014). P_u can be converted into the backscatter coefficient (σ^0) using instrument calibrations and significant wave height (SWH) is derived from σ_s. τ is the time measured at the satellite such that $t = t_0$ corresponds to the arrival time of the half power point of the radar return.

The practical derivation of the time series of the returned power waveform $P(t)$, as defined in Equation 5-1, is achieved using Equation 5-2 (Passaro et al., 2014; Peng and Deng, 2018):

$$P(t) = a_\xi P_u \frac{[1 + \text{erf}\,(u)]}{2} \exp(-v) + P_N \qquad \text{5-2}$$

where

$$a_\xi = exp\left(\frac{-4sin^2\xi}{\gamma}\right) \quad \gamma = sin^2(\theta_0)\frac{1}{2\ln(2)}$$

$$u = \frac{t - \tau - c_\xi\sigma_c^2}{\sqrt{2}\sigma_c} \quad v = c_\xi\left(t - \tau - \frac{1}{2}c_\xi\sigma_c^2\right)$$

$$erf(x) = 2\frac{2}{\sqrt{\pi}}\int_0^x e^{-t^2}dt$$

$$c_\xi = b_\xi a \quad b_\xi = cos(2\xi) - \frac{sin^2(2\xi)}{\gamma} \quad a = \frac{4c}{\gamma h\left(1 + \frac{H}{R_{earth}}\right)}$$

$$\sigma_c^2 = \sigma_p^2 + \sigma_s^2 \quad \sigma_s = \frac{SWH}{2c}$$

and:

- $R_{earth} \approx 6371000$ m is the mean radius of the Earth
- H is the satellite altitude above the reference ellipsoid
- γ is a function of the antennae beam width parameter θ_0 (Brown, 1977)
- c is the speed of light
- θ_0 is the antenna beam width
- σ_s is the slope of the leading edge (related to the SWH)
- σ_p is the radar point target response.

Equation 5-2 is fitted to the measured waveform to estimate five parameters: P_N, P_u, τ, σ_c and ξ, typically using weighted least squares (WLS) and unweighted least squares (UWLS) (Deng and Featherstone, 2006), a MLE (Gommenginger et al., 2010) or a minimum mean square estimator (MMSE) (Gommenginger et al., 2010; Passaro et al., 2014). The Brown–Hayne model forms the basis for the Ice-2 retracker implemented as an on-board satellite retracker in most altimetry missions since Envisat RA-2 (Rosmorduc et al., 2018).

5.1.2 Physical model variants

Gommenginger et al. (2010) note that there are a limited number of theoretical models that define ocean waveforms and none that effectively describe waveform returns over inland waters. In the case of ocean waveforms, despite the limited number of theoretical models, there are numerous variants and application methodologies, primarily as a function of the parameters incorporated in models. For example, while the National Oceanography Centre Southampton Non-linear Ocean Retracker was developed to account for the non-linearity of ocean waves, it is derived primarily from the original Brown–Hayne theoretic ocean waveform definition. Other model variants focus on the correlation between pairs of parameters—for example, trailing edge slope and backscatter coefficient (Amarouche et al., 2004; Deng and Featherstone, 2006)—and define estimation methodologies that facilitate the accurate extraction of both parameters.

5.1.3 β-Parameter empirical model retracker

The β-Parameter retracker is an empirical model retracking algorithm that was developed for the analysis of Seasat altimetry waveforms by Martin et al. (1983). Because of the complex topography over the continental ice sheets and the slow response of the Seasat on-board tracker, the initial pulse return of the altimeter waveform frequently departed from the tracking location. The β-Parameter retracker was developed to facilitate retracking of these waveforms. The algorithm was designed to compute the difference between the leading edge of the waveform and the tracking point and to correct the measured range from satellite to reflecting surface (Martin et al., 1983). The algorithm fitted a five-parameter function to single ramp waveforms and a nine-parameter function to double ramp waveforms. Figure 5-2 shows the functional elements in the five-parameter β-Parameter retracker, where β_1 is the thermal noise, β_2 is the return signal amplitude, β_3 is the midpoint of the leading-edge ramp, β_4 is the waveform rise-time and β_5 is the slope of the trailing edge (Martin et al., 1983; Gommenginger et al., 2010).

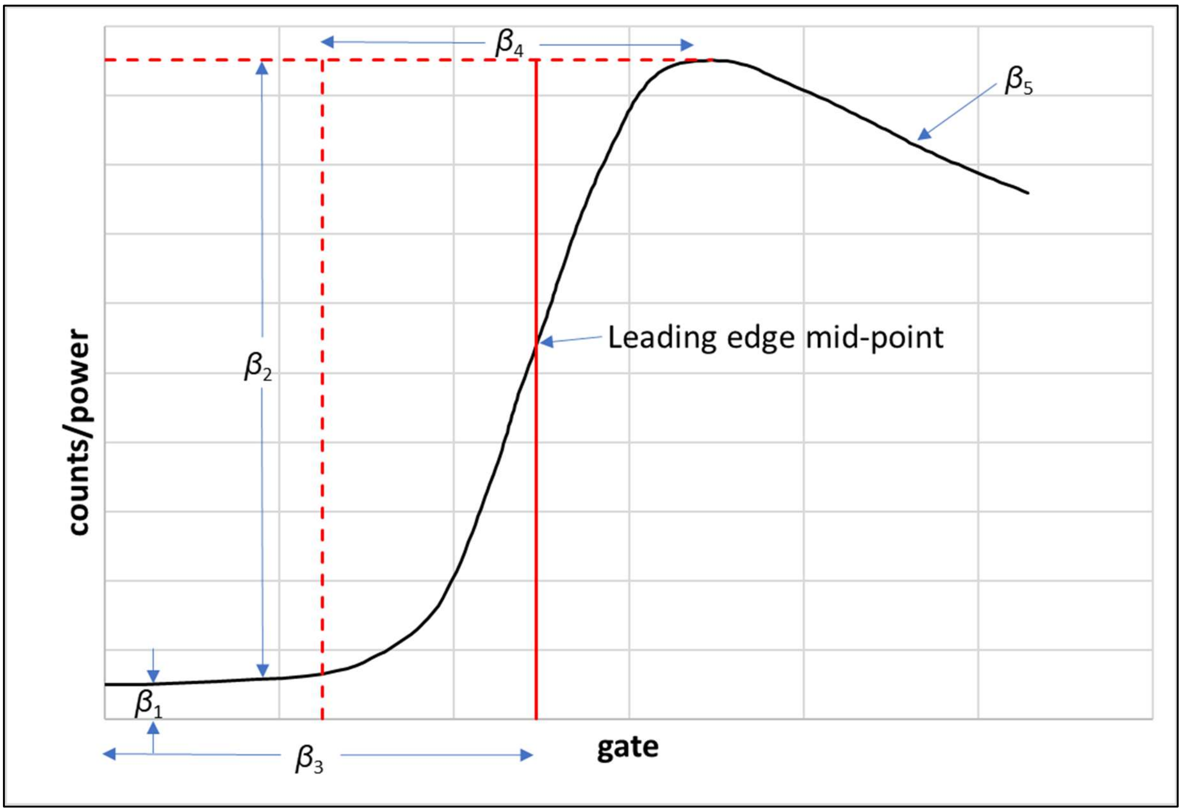

Figure 5-2 β-Parameter (single ramp) retracking algorithm functional elements. Parameters β_2–β_5 are repeated for the second ramp in the nine-parameter version.

The β-Parameter retracker algorithm can be expressed in the following manner (Deng and Featherstone, 2006):

$$y(t) = \beta_1 + \sum_{i=1}^{n} \beta_{2i}\,(1 + \beta_{5i}\,Q_i)P(\frac{t - \beta_{3i}}{\beta_{4i}}) \tag{5-3}$$

with

$$Q_i = \begin{cases} 0\; for\; t < \beta_{3i} + 0.5\beta_{4i} \\ t - (\beta_{3i} + 0.5\beta_{4i})\; for\; t \geq \beta_{3i} + 0.5\beta_{4i} \end{cases}$$

$$P(x) = \int_{-\infty}^{x} \frac{1}{\sqrt{2\pi}} \exp\left(\frac{-q^2}{2}\right) dq$$

where $n = 1$ for the single ramp five-parameter version and $n = 2$ for the nine-parameter double ramp version.

The empirical β-Parameter retracker replicates the shape defined by the Brown–Hayne model ocean-like waveform although the β parameters that are defined are part of a functional fit and do not necessarily relate to physical properties (Gommenginger et al., 2010).

Wingham et al. (1986) recognised that the fitting of an ocean-like waveform model to echoes from surfaces that are not ocean-like was not practical because of the complex and varied nature of waveform shapes returned from these surfaces. Hwang et al. (2006) found that the β-Parameter retracker had a limited success rate for complex waveforms due to convergence failure.

Because of the inherent ocean-like form of the β-Parameter retracking algorithm, it is not utilised in the analyses undertaken during this study although it is recognised that it has application in the retracking of waveforms with a fast decaying trailing edge (Deng and Featherstone, 2006) as is evident for some inland water reflectors.

5.1.4 Model fitting methodologies

A significant component of the model fit retracking process is the methodology by which the selected model is fitted to the altimeter waveform. The accuracy of the derived parameters in a particular range is dependent on the fitting methodology selected. The main methods used are based on the statistical fitting of the theoretical model return power to the measured return power. The statistical fitting process returns the minimum variance unbiased estimation of the parameters (Deng and Featherstone, 2006; Gommenginger et al., 2010) with the main methods including the MLE as well as both WLS and UWLS estimators.

5.2 Empirical statistical retrackers

5.2.1 Offset Centre of Gravity Retracker

The OCOG algorithm was developed by Wingham et al. (1986). It is based only on the statistics of the waveform samples and will give a solution for every sample, unlike physically based least squares retrackers, where the solution may not converge (Hwang et al., 2006). Wingham et al. (1986) reasoned that the fitting of a model ocean-like return shape to returns typically seen over non-ocean surfaces was inappropriate and that an alternative retracking algorithm was required to provide robust tracking over topographic terrain. A primary aim in developing the OCOG algorithm was to reduce the effects of the waveform noise (Davis, 1997) typical of waveforms over inland water reflectors that are contaminated by land, topography or vegetation.

The OCOG algorithm is based on a rectangle centred at the centre of gravity (COG) of the waveform with amplitude (A) and width (W) shown in Figure 5-3.

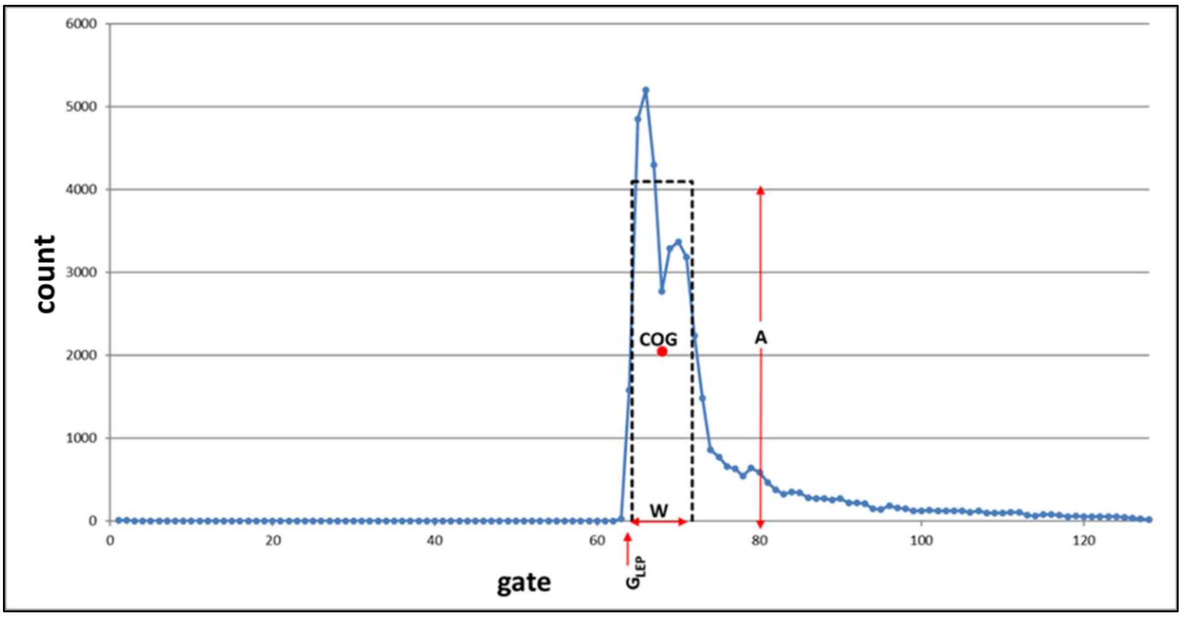

Figure 5-3 OCOG pulse shape parameters; pulse amplitude (A) and pulse width (W). The centre of gravity (COG) and leading-edge position gate (G_{LEP}) are also identified.

The parameters for the OCOG algorithm can be computed as:

$$A = \sqrt{\frac{\sum_{i=n_1+1}^{n-n_2} P_i^4(t)}{\sum_{i=n_1+1}^{n-n_2} P_i^2(t)}} \tag{5-4}$$

$$W = \frac{\left(\sum_{i=n_1+1}^{n-n_2} P_i^2(t)\right)^2}{\sum_{i=n_1+1}^{n-n_2} P_i^4(t)} \tag{5-5}$$

where $P_i(t)$ is the waveform power at gate i, with the summation being undertaken for the total number of samples n excluding the first n_1 and last n_2 samples.

Samples are excluded at the start and end of the waveform to eliminate noise (Hwang et al., 2006) and aliasing effects (Gommenginger et al., 2010) from the analysis. The number excluded varies as a function of sensor and the extent of aliasing. This is typically $n_1 = n_2 = 5$ but may be greater if significant aliasing exists.

The location of the waveform gate relating to the COG is given by:

$$COG = \frac{\sum_{i=n_1+1}^{n-n_2} iP_i^2(t)}{\sum_{i=n_1+1}^{n-n_2} P_i^2\,(t)} \tag{5-6}$$

and the gate relating to the leading-edge position (G_{LEP}) is defined as:

$$G_{LEP} = COG - \frac{W}{2} \tag{5-7}$$

The range correction (ΔR) is derived from:

$$\Delta R_{RET} = (G_{LEP} - G_{REF})G_{2m} \tag{5-8}$$

where ΔR_{RET} is the retracking range correction, G_{REF} is the satellite altimeter reference tracking gate and G_{2m} is the effective gate width in metres (Davis, 1997).

While the OCOG Retracker is recognised as robust, it is of limited use as the derived range correction is not related to any physical aspect of the reflecting surface but to the statistical spread and amplitude of the altimetry echo (Hwang et al., 2006; Deng et al., 2002). Figures 5-4 and 5-5 illustrate this limitation of the OCOG Retracker. While the leading-edge position (LEP) is in the correct location for a specular return, the LEP for the specular return coupled with a decaying trailing edge is shifted away from the actual leading edge as a result of a COG bias caused by the long decaying trailing edge of the waveform.

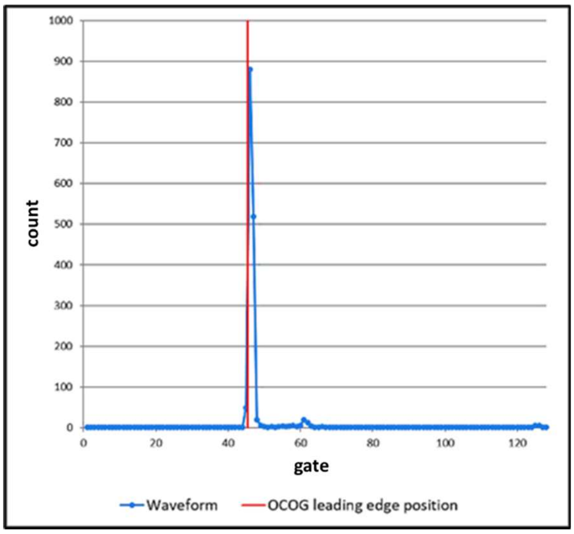

Figure 5-4 A typical Envisat RA-2 quasi-specular waveform with the OCOG-defined LEP correctly located on the leading edge.

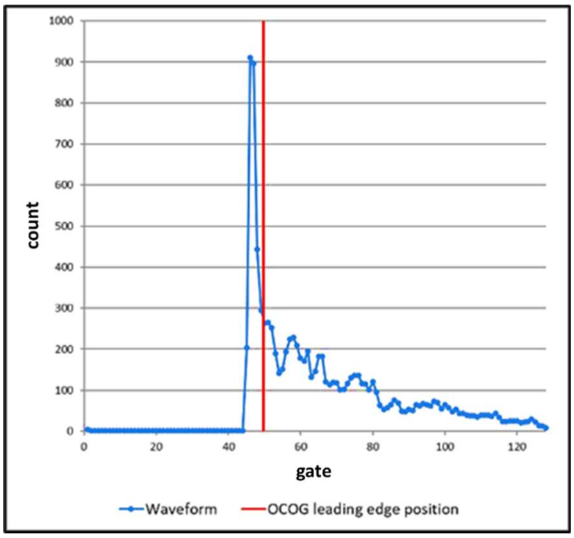

Figure 5-5 An Envisat RA-2 flat-patch waveform with a decaying trailing edge. The OCOG-defined LEP position is offset from the actual leading edge because of the bias induced by the location of the waveform COG.

The OCOG Retracker forms the basis of the Ice-1 retracker implemented as an on-board satellite retracker in most altimetry missions since Envisat RA-2 (Rosmorduc et al., 2018).

5.2.2 Threshold Retracker

The Threshold Retracker was developed by Davis (1997) to overcome the deficiency in the OCOG Retracker that led to the derived range correction often not being located with respect to the actual leading edge of the waveform. The algorithm was developed to measure changes in continental ice elevation with the significant benefit of producing consistent elevation measurements (Davis, 1997). The Threshold Retracker identifies the position on the leading edge of the waveform relative to the first range gate to exceed a percentage of the maximum waveform amplitude above the thermal noise bias. The retracking gate estimate is determined by linear interpolation between adjacent samples on the leading edge (Deng and Featherstone, 2006). The selected threshold percentage of the maximum waveform amplitude is critical as it has a direct influence on the derived satellite-to-reflecting-surface range (Deng and Featherstone, 2006). The percentage adopted is selected as a function of validation by in-situ data or from a priori knowledge of the reflecting surface. A threshold level of 10% is effectively a first-return retracker; a threshold level of 50% has been suggested for waveforms dominated by surface scattering; and 10–20% for those dominated by volume scattering (Davis, 1997; Gommenginger et al., 2010). For analyses undertaken in this study utilising the Threshold Retracker, threshold levels of 25%, 50% and 75% are calculated and the 25% threshold level selected for all analyses as the solution consistently gives the best fit with the in-situ gauge WSE record.

The Threshold Retracker algorithm detailed in the form of Equations 5-9 to 5-11 is adapted from (Gommenginger et al., 2010). The thermal noise is calculated from the first five gates, following the n_1 excluded gates that are contaminated by noise and aliasing, as follows:

$$P_N = \frac{1}{5}\sum_{i=n_1+1}^{i=n_1+5} P_i \tag{5-9}$$

where P_N is the averaged value of the power of the first five non-aliased gates starting from gate n_1+1. The threshold level is then calculated as:

$$T_h = P_N + q\,(A - P_N) \tag{5-10}$$

where T_h is the threshold level at q% of the difference between the OCOG amplitude (A), defined in the OCOG calculations of Equation 5-4, and the thermal noise level P_N. The value of q is relatively arbitrary and is generally determined by empirical means via comparison of the derived altimetry WSEs with an in-situ record and adopting the threshold yielding the best result. Linear interpolation between the gates adjacent to threshold T_h gives the location of the LEP from which the range correction is calculated.

G_{LEP} is the location of the LEP relative to the waveform gates and is derived from Equation 5-11:

$$G_{LEP} = G_{k-1} + \frac{T_h - P_{k-1}}{P_k - P_{k-1}} \qquad \text{5-11}$$

where k is the first gate exceeding the threshold level T_h and P_k is the power at the kth gate. The range correction (ΔR_{RET}) is then derived using Equation 5-8.

While the threshold retracker is not based on a physical model it does represent an empirical analysis of the altimetric echo where the statistical properties of the waveform are assessed and related to a known physical property; that is, the retracking correction referenced to the leading edge of the waveform, which is nominally the nadir water reflector.

In the example shown in Figure 5-5, the performance of the OCOG Retracker is shown to have calculated a retracking correction shifted from the leading edge of the waveform because of a COG bias. In Figure 5-6 the retracking correction is determined using the Threshold Retracker with 25% threshold and the location of the LEP can be seen to be correctly located on the actual leading edge of the waveform.

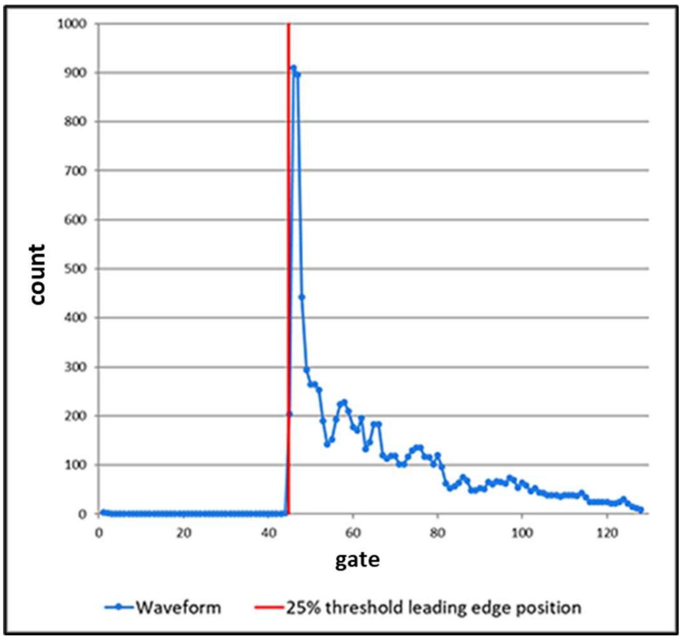

Figure 5-6 An Envisat RA-2 flat-patch waveform with a decaying trailing edge. The 25% Threshold Retracker-defined LEP position is correctly located on the actual leading edge of the waveform.

However, for complex and multi-peaked waveforms, the Threshold Retracker will not necessarily determine the correct ranging gate. In Figure 5-7 the LEP at a 25% threshold level is located on the first peak; for the same waveform but at a 50% threshold in Figure 5-8, the LEP is located on the leading edge of the second peak. If the first peak is the nadir water reflector, then the result from the 50% threshold calculation will be incorrect.

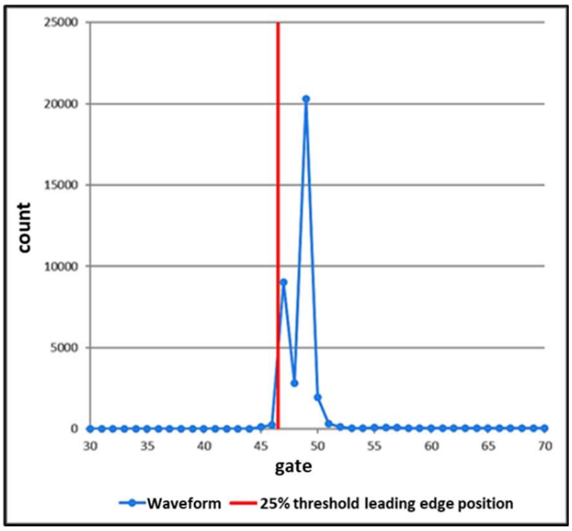

Figure 5-7 A multi-peaked waveform with the 25% Threshold Retracker defining the LEP position on the leading edge of the first peak. While the first peak is the likely nadir return it is not the maximum return which is likely to be from an off-nadir specular reflector.

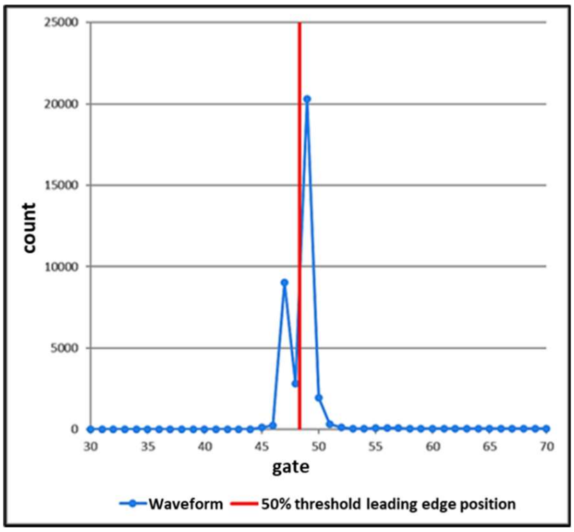

Figure 5-8 A multi-peaked waveform with the 50% Threshold Retracker defining the LEP position on the leading edge of the second peak. It is necessary to select a threshold level that is likely to use the nadir return for WSE estimation over the range of typical waveform shapes expected n the study area.

The switch from a 25% to a 50% threshold resulted in a 0.87-m range difference as it effectively shifted the LEP by two gates. There are likely two dominant surface reflectors within the altimetry echo footprint and, in this example, the threshold retracker will select different reflectors as a function of threshold level applied.

In this basic form the Threshold Retracker cannot consistently manage range corrections from complex and multi-peaked waveforms. This deficiency is addressed in the revised form of the retracker; the Improved Threshold Retracker.

The Threshold Retracker is used primarily for to process altimetric data over inland waters where returns vary between quasi-specular returns from calm water reflectors to complex and multi-peaked returns from echoes contaminated by topography and vegetation. The Threshold Retracker forms the basis of the Sea Ice retracker implemented as an on-board satellite retracker in most altimetry missions since Envisat RA-2 (Rosmorduc et al., 2018).

5.2.3 Improved Threshold Retracker

The Improved Threshold Retracker is a modification of the Threshold Retracker detailed in Section 5.2.2. It facilitates the retracking of complex multi-peaked waveforms by predicting the peak that relates to the nadir water body and effectively trimming the waveform of secondary peaks leading into and from the selected peak. It then utilises conventional retracking, as detailed in Section 5.2.2, to derive the LEP as well as the corresponding retracked range and water level estimate linked to the sub-waveform. The methodology was developed by Hwang et al. (2006) who found that the standard threshold retracking worked well if there was only a single ramp in the waveform. For waveforms with more than one ramp, the selected retracking gate was biased towards the leading edge of the first ramp and this may not have related to the ocean return. In the Improved Threshold Retracker one or more sub-waveforms and retracking gates are determined from within the measured waveforms and the leading edge—as well as the corresponding retracked range and SSH (or WSE)—is determined. Based on the methodology of Hwang et al. (2006), the SSH of the sub-waveforms is compared with SSH estimates leading into the coastal zone where waveforms are not contaminated by land, vegetation or topography and conform more to the theoretical Brown–Hayne model shape. The sub-waveform SSH with the closest fit to the uncontaminated SSH is selected as being valid and the corresponding sub-waveform assigned as being related to the altimeter nadir return.

Methods to aid the selection of the correct sub-waveform have been proposed by Bao et al. (2008) and Lee et al. (2008). Both methods utilise the analysis of the power difference between waveform gates as proposed by Hwang et al. (2006) and both aim to select a single sub-waveform that is most likely to be related to the nadir return from the water surface below the altimeter. In Bao et al. (2008), the start and end gates of the sub-waveform determined to be the nadir return are derived based on the slope and magnitude of the power differences. A retracking correction is then derived from this sub-waveform using the OCOG method defined in Section 5.2.1. Over oceans where sea ice can lead to returns that deviate from the classical Brown–Hayne model shape, Yang et al. (2012) proposed use of the Improved Threshold Retracker with selection of the nadir leading edge by matching with a reference sub-waveform.

In Lee et al. (2008) the complex waveforms over land are analysed. The power differences between waveforms are derived and the noise level along with the maximum value of the leading edge of the land waveforms are extracted. This allows for any bump before the leading edge to be avoided along with any spike after the leading edge. Although the Improved Threshold Retracker implemented by Lee et al. (2008) does not use external data for the selection of the appropriate sub-waveform it does use Shuttle Radar Topography Mission (SRTM) DEM as well as other geodetic observations from GPS, the Gravity Recovery and Climate Experiment (GRACE) and tide gauges for validation.

Using the improved threshold retracking process results in multiple sub-waveforms being identified within a single multi-peaked waveform. Comparison with external data allows the most likely sub-waveform to be selected based on the agreement of the derived water level height with an external a priori input. This methodology is most applicable in the coastal zone using SSH estimates from the more ocean-like waveforms immediately outside the coastal zone. Such estimates are not readily available through most inland water targets where water bodies are generally relatively small. Off-nadir distortion, land contamination and the limited number of waveforms means that the statistical properties of the waveforms along with external inputs such as topography, in-situ gauges and nature of the nadir reflecting surface need to be incorporated to correctly select the sub-waveform relating to the nadir return.

The sub-waveform identification process developed by Hwang et al. (2006), with significant contributions from Bao et al. (2008) and Yang et al. (2012), is modified in this study so that the derived sub-waveforms better represent the reflecting surface without contamination from adjacent sub-waveforms. Hwang et al. (2006), Jinyun et al. (2010) and Gommenginger et al. (2010) adopt a process where the selected sub-waveform extends four gates either side of the selected peak. Bao et al. (2008) and Yang et al. (2012) allow for some variability in defining sub-waveform extent; however, the focus is on peak detection and not sub-waveform lateral extent. In this study, the sub-waveform is defined to extend from troughs either side of the selected peak as opposed to a fixed extent about the selected peak. This facilitates a variable sub-waveform width and a mechanism that ensures that the extracted sub-waveform is not contaminated by neighbouring reflectors.

The sub-waveform identification process is designed to extract all statistically significant peaks within a waveform. While there is likely to be at least one major peak, there is also likely to be minor peaks that, while statistically significant, are not related to the dominant reflectors within the altimetry footprint. A development undertaken in this study is to incorporate functionality into the sub-waveform identification process that allows for sub-waveforms to be classed as major or minor as a function of significance within the overall waveform. To determine the class of the sub-waveform the power difference for a separation of two gates (d_2^i) and the power difference at adjacent gates(d_1^i) are compared to empirical threshold levels ε_1 and ε_2 respectively. Logical expressions are used to define the sub-waveform significance, with the sub-waveform classed as major if $d_1^i > \varepsilon_2 \; AND \; d_2^i > \varepsilon_1$ and classed as minor if $d_1^i > \varepsilon_2 \; OR \; d_2^i > \varepsilon_1$. This facilitates the ready removal of bumps preceding the first major peak that could bias retracking at low threshold values, as identified by Lee et al. (2008). The classification of sub-waveform significance also allows for prioritisation of sub-waveforms in the process of identifying the sub-waveform derived from the nadir reflector.

While Hwang et al. (2006) set the empirical threshold values ε_1 and ε_2 to 8 and 2 respectively for Geosat data, Fenoglio-Marc et al. (2010) use values derived from the standard deviation of the power differences with $\varepsilon_1 = 0.2S_{d2}$ and $\varepsilon_2 = 0.2S_{d1}$, where d_2^i is the power difference for a separation of two gates and d_1^i, the power difference at adjacent gates. S_{d2} is the standard deviation for all power differences for a separation of two gates and S_{d1} is the standard deviation of all power differences at adjacent gates:

$$d_2^i = \frac{1}{2}(P_{i+2} - P_i) \qquad 5\text{-}12$$

$$d_1^i = P_{i+1} - P_i \qquad 5\text{-}13$$

$$S_{d2} = \sqrt{\frac{(N-2)\sum_{i=n1}^{N-2}\left(d_2^i\right)^2 - \left(\sum_{i=n1}^{N-2} d_2^i\right)^2}{(N-2)(N-3)}} \qquad 5\text{-}14$$

$$S_{d1} = \sqrt{\frac{(N-1)\sum_{i=n1}^{N-1}\left(d_1^i\right)^2 - \left(\sum_{i=n1}^{N-1} d_1^i\right)^2}{(N-1)(N-2)}} \qquad 5\text{-}15$$

where n_1 is the number of gates affected by aliasing at the start of the waveform and n_2 is the number of gates affected by aliasing at the end. N is the total number of waveform gates less n_1 and n_2 (from Fenoglio-Marc et al. (2010) and Gommenginger et al. [2010]).

A flowchart of the waveform selection process, incorporating the developments undertaken in this study, is shown in Figure 5-9.

To illustrate the functionality of the sub-waveform identification and extraction process, a complex multi-peaked Envisat RA-2 waveform is selected with statistically significant sub-waveforms identified. Figure 5-10 shows the multi-peaked waveform with peaks identified using the methodology defined in Figure 5-9.

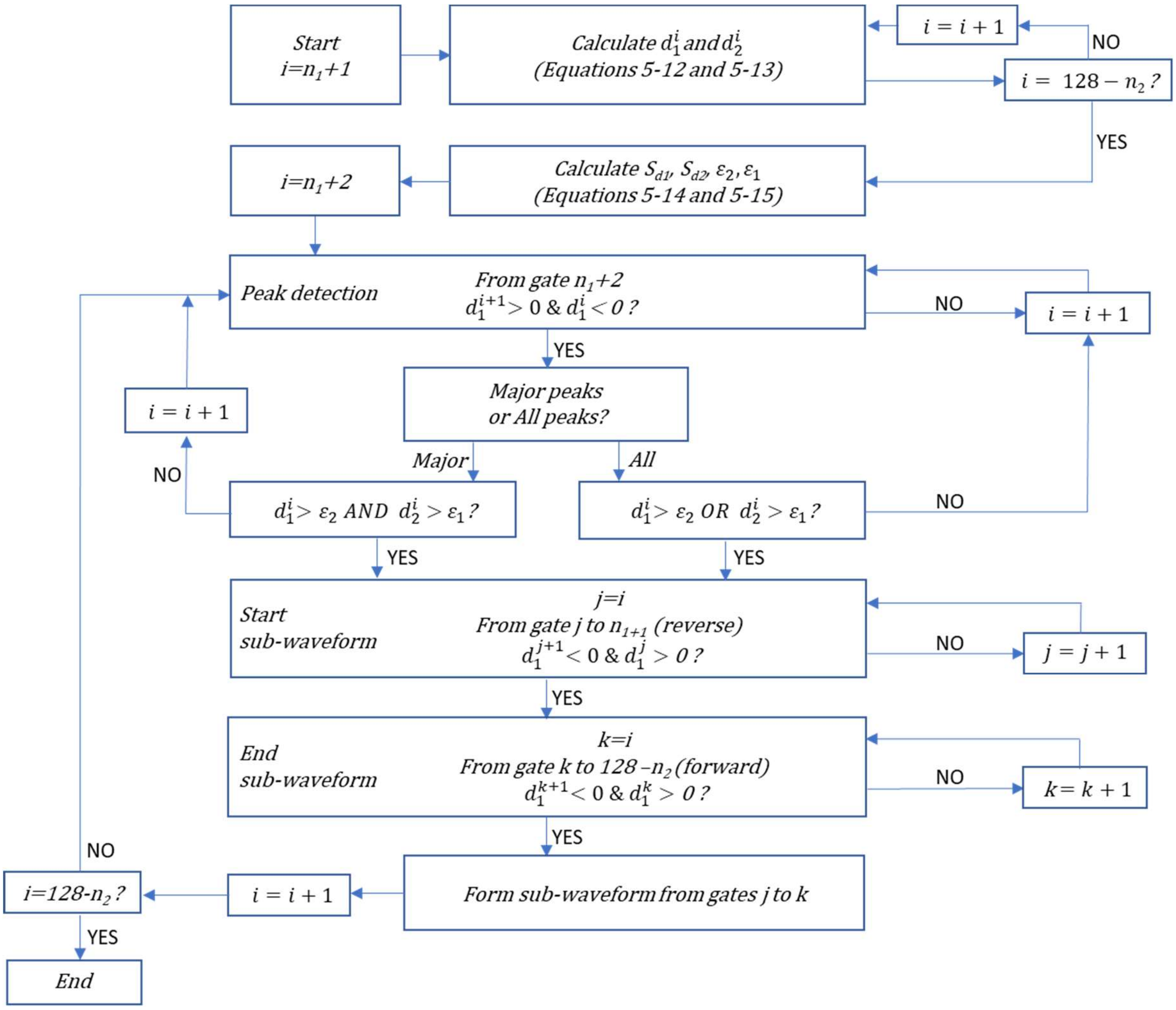

Figure 5-9 Flowchart of the sub-waveform selection methodology developed by Hwang et al. (2006), with significant contributions from Bao et al. (2008) and Yang et al. (2012). Advances developed in this study related to the sub-waveform extent and classification of sub-waveform peak significance, are incorporated into the workflow. Parameters ε_2 and ε_2 are empirical threshold values, calculated as $0.2S_{d2}$ and $0.2S_{d1}$ respectively.

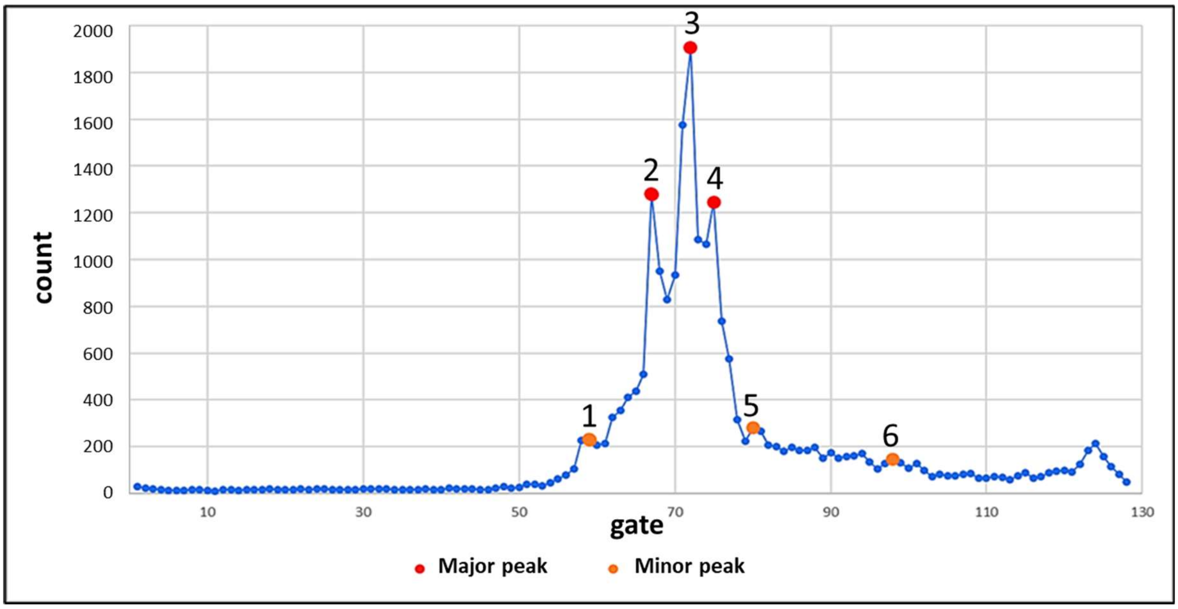

Figure 5-10 A multi-peaked waveform captured over the Fly River floodplain from Envisat RA-2 in March 2012. Six statistically valid peaks are identified of which three are identified as major peaks. Peaks were identified using the sub-waveform identification methodology detailed in Figure 5-9.

Figure 5-11 shows the results from the sub-waveform identification and extraction process using the methodology defined in Figure 5-9. Six statistically valid peaks are identified of which three are identified as major peaks.

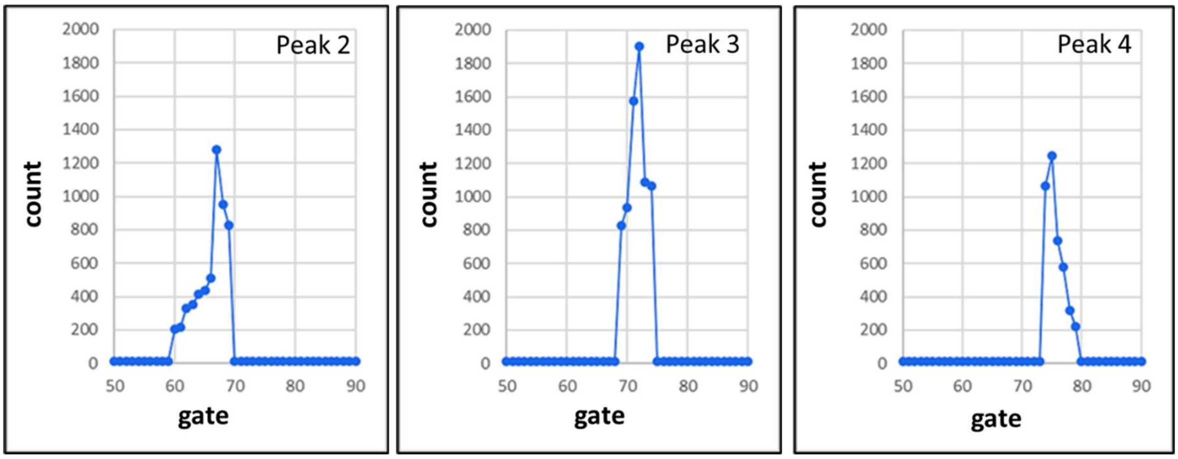

Figure 5-11 Sub-waveform extracts of the major peaks identified in Figure 5-10. These sub-waveforms are retracked using the Improved Threshold Retracker with outputs of WSE that can be assessed against a reference for the selection of the valid nadir reflection.

Each sub-waveform is retracked and the derived WSE compared with that derived from a neighbouring quasi-specular return determined to originate from a calm water source, which is assumed to be a valid WSE. The results for the derived WSE from each sub-waveform as well as the reference waveform are tabulated in Table 5-1. The comparison shows that the third major peak (peak 4) is the likely nadir water reflector.

Table 5-1 WSEs derived from the sub-waveforms identified in Figures 5-10 and 5-11 compared with the water level estimate derived from a neighbouring quasi-specular waveform. The comparison (values in red) indicates that the third major peak (peak 4) is the likely nadir reflector.

Waveform type	Peak number	Peak class	Derived WSE (m)
Multi-peaked	1	Minor	41.627
"	2	Major	38.568
"	3	Major	35.258
"	4	Major	33.017
"	5	Minor	30.667
"	6	Minor	22.698
Specular	1	Reference	33.096

5.3 Optimised retrackers

5.3.1 Current status

While significant research continues into developing new retracking methodologies for satellite radar altimetry waveforms, the focus has shifted to optimising existing retrackers to more accurately extract meaningful geophysical parameters from waveforms that previously would have been considered corrupt and consequently discarded (Passaro et al., 2014). The common link for the majority of this effort relates to the identification and rectification of the hooking effect within the waveform as well as ensuring that the correct peak within a multi-peaked waveform is correctly identified and extracted as a sub-waveform.

Switching between retrackers has been proposed as a method of managing changing waveform shapes over inland waters and through the coastal zone. An evaluation of waveform shape would determine which retracker was applied. For example, a typical ocean waveform would be retracked using the Brown–Hayne ocean model retracker but if the waveform shape transitioned to a quasi-specular return the Threshold Retracker would be activated. This methodology would be problematic in implementation and require the accurate quantification of biases between the retrackers to avoid stepping in the derived WSE profile (Passaro et al., 2014).

The preferred alternative is to implement a single retracker but to optimise performance for the variety of waveform shapes expected. An example developed for waveform analysis through the inland water zone is the Multiple Waveform Persistent Peak (MWaPP) retracker (Villadsen et al., 2016), which is based on the Improved Threshold Retracker (Section 5.2.3) but assesses adjacent waveforms to determine the best sub-waveform for retracking. Persistent peaks can be identified through a waveform sequence that is likely to represent the water body of interest. An alternative retracker proposed by (Villadsen et al., 2016) is the Narrow Primary Peak Retracker (NPPR), which uses the Improved Threshold Retracker with the sub-waveform selection methodology based on the evolution of the power in the reflected waveform with no assessment of neighbouring waveforms.

Developed for coastal zone studies, the Adaptive Leading Edge Sub-waveform (ALES) retracker (Passaro et al., 2014) was designed to manage the difficulties in transitioning from the ocean to the coastal zone; however, Quartly and Passaro (2014) found that ALES was also suited for application across narrow inland water bodies. The retracker is based on the

Brown–Hayne functional model but allows for the extraction of sub-waveforms where the trailing edge is affected by spurious returns but a distinct leading edge is still evident.

Idris and Deng (2012) propose a waveform retracking method for the quasi-specular and multi-peaked waveforms that predominate within the coastal zone and that are not retracked accurately using the Brown–Hayne model. Sub-waveforms are extracted that are based on returns from the water surface and these are then retracked using the Brown–Hayne model.

Peaky waveforms that are found within the coastal zone have been successfully retracked by Peng and Deng (2018) whereby the peak location within the waveform is identified and retracking occurs via a WLS process with downsizing of the weighting of the gates containing the identified peak. This facilitates the use of the Brown–Hayne model for retracking without needing to add a peak function.

Because of the significant variability in waveform shapes originating within the coastal zone and over inland waters, the development of a waveform retracker that suits all applications is not practical and likely not feasible. Instead the focus has been to optimise and modify the way that existing retrackers are used for the various receiving environments. While they are generally similar, there are also significant differences between the typical waveform returns from the coastal zone and larger inland water bodies compared with those acquired over complex wetland and floodplain environments. In the coastal zone and over larger inland water bodies, waveform shapes often still have an underlying Brown–Hayne model shape; however, they are contaminated by peaks within the trailing edge that represent landform or specular reflectors within the altimetry footprint. The adaptive retracking process fundamentally detects and extracts the peak so that the underlying Brown–Hayne model-shape waveform can be retracked. Over complex wetland environments the dominant return is quasi-specular; however, multi-peaked waveforms that typically do not have an underlying Brown–Hayne model shape are also common. The adaptive retracking process in these cases is to determine which waveforms comprise a nadir signature and to extract WSE using an empirical retracker based on this assessment.

Adaptive measures must focus on generating methods that are flexible and allow a range of waveform shapes to be successfully retracked. In optimising an existing retracker, the aim is to improve both the quality and reliability of the derived WSEs and, at the same time, to increase the proportion of waveforms that are successfully retracked that may have previously been discarded.

As part of this study, an adaptive waveform retracker has been developed with a particular focus on extracting reliable WSE estimates from complex wetland and floodplain environments. The retracker is based on the Improved Threshold Retracker developed by (Hwang et al., 2006) with significant advances in retracking methodology that facilitate the extraction of reliable WSE estimates in a semi-autonomous process.

5.3.2 Optimised retrackers developed in this study

5.3.2.1 Sub-waveform selection methodology optimised for inland waters

There has been considerable research into processes for identifying and extracting statistically significant sub-waveforms from a multi-peaked altimetry return as detailed in Section 5.2.3. There has been less research on the selection of the sub-waveform relating to the nadir return, particularly for inland water applications. In the coastal zone, a SSH derived from a waveform conforming to the Brown–Hayne model shape is derived (Passaro et al., 2014) as an a priori estimate and used for selection of the nadir return peak in a contaminated waveform.

Over inland waters the process of sub-waveform selection involves comparison with in-situ reference or use of analytical methods to extract the waveform relating to the nadir return (e.g. Lee et al., 2008; Villadsen et al., 2016). For the larger river and lake systems, which dominate inland water altimetry studies, the sub-waveform selection process can be based on coastal zone methodologies; however, in many cases, multi-peaked waveforms are simply discarded with retracking limited to waveforms with standard shapes, such as quasi-specular or Brown–Hayne model shapes (e.g. Sulistioadi et al., 2015). For complex wetlands and floodplain environments, water bodies can be relatively small and WSEs can differ between the various water bodies. To facilitate the autonomous selection of the sub-waveform relating to the nadir return for these environments, a robust and flexible method has been developed as part of this study.

The process of peak prediction, and subsequent extraction of a sub-waveform based on this peak, is dependent on the relationship between calm water and a quasi-specular waveform. In this study, it is hypothesised that if the nadir is determined to be a calm water target (i.e. determined to have an open water or inundated vegetation altimetry footprint and an associated high backscatter coefficient) and if the recorded waveform is quasi-specular in shape, then the altimetry waveform originates from nadir. Quasi-specular waveforms neighbouring the subject multi-peaked waveform are used in the selection of the nadir return sub-waveform. The WSE derived from these quasi-specular waveforms, determined to originate from a calm water source, are used to estimate the LEP required for a matching water level within the subject multi-peaked return. The predicted peak associated with the nadir return is then the next in the gate sequence greater than the LEP.

For each sub-waveform within the multi-peaked waveform the derived WSE, excluding any retracking correction (h_{raw})is derived using Equation 2-6. The predicted water level (h_{pred}) is the retracked WSE of the closest waveform to the subject waveform that has a nadir calm water footprint and is quasi-specular. The required retracking correction ΔR_{RET} is then determined from:

$$\Delta R_{RET} = h_{raw} - h_{pred} \tag{5-16}$$

The first gate greater than the LEP is calculated as:

$$G_{LEP} = INT\left(\frac{\Delta R_{RET}}{G_{2m}} + G_{REF}\right) + 1 \tag{5-17}$$

where G_{REF} is the satellite altimeter reference tracking gate and G_{2m} is the effective gate width in metres. The sub-waveform extracted will be formed around the next peak in the sequence with a gate greater than G_{LEP}.

In the sub-waveform selection methodology shown in Figure 5-12, the procedure associated with the selection of the sub-waveform associated with the nadir return is detailed. The process is optimised for complex wetland and floodplain environments with classification of the altimetry footprint to assist with the definition of calm water sites and to control the search extent, by limiting searches for the reference WSE to the same water body as the multi-peaked return. If the size of the water body is relatively small, then there may be no reference WSE to assist with sub-waveform selection. In such cases both the first and maximum major peaks are used with both derived WSEs assessed in a final review. Over inland waters it has been found that some complex waveforms do not contain a nadir return peak as all peaks within the waveform are associated with off-nadir reflectors. In this case, the selection process will identify that a peak does not exist at a gate location greater than the predicted G_{LEP} location so the first and maximum major peaks are both included with derived WSEs assessed to determine if they form part of a hooking hyperbola that can be used for subsequent nadir WSE estimation.

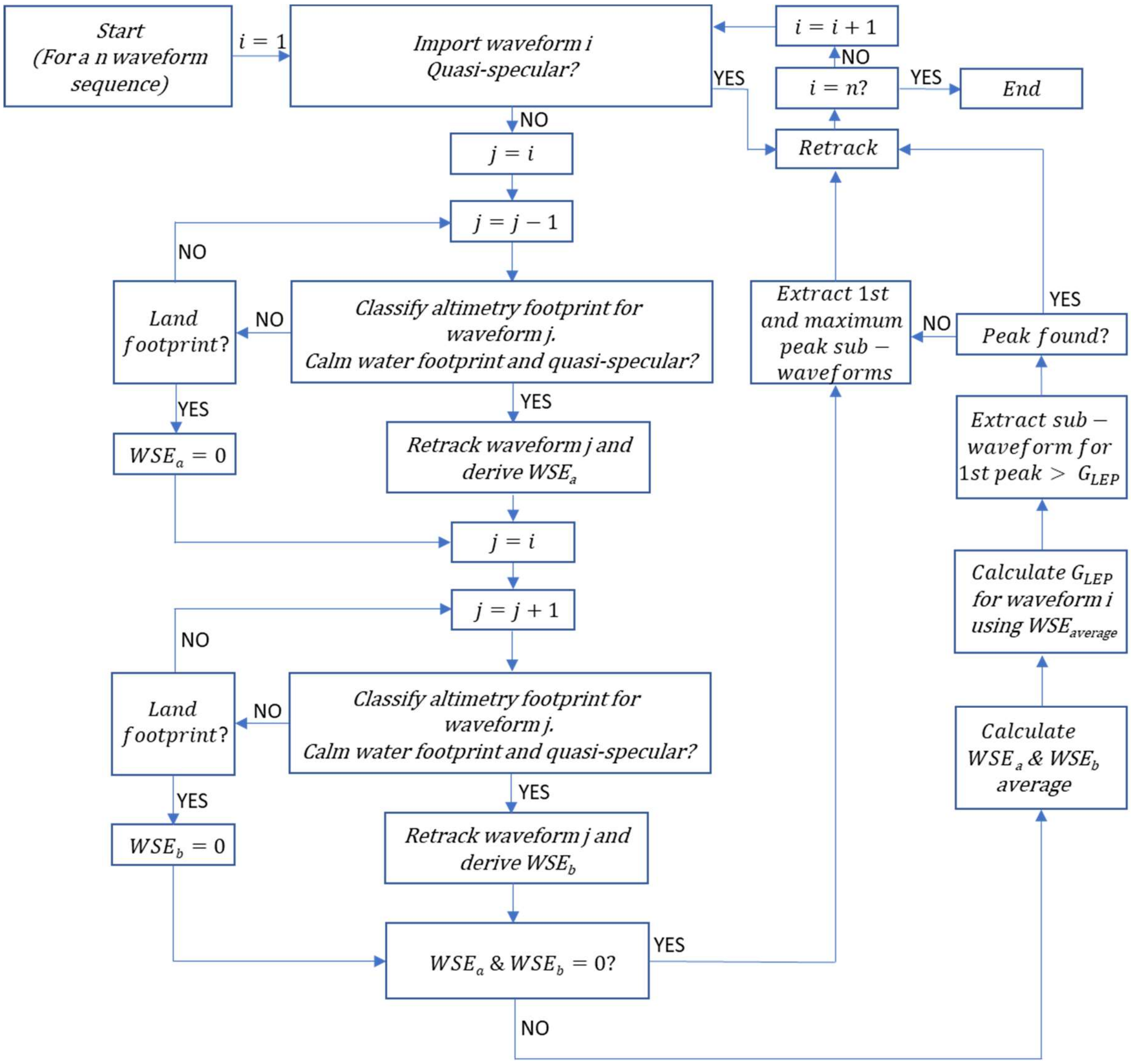

Figure 5-12 The sub-waveform selection methodology developed as part of this study. The process selects a sub-waveform corresponding to a nadir return as defined by a WSE derived from a neighbouring quasi-specular waveform originating from a calm water source. Where there is no candidate reference waveform or where hooking is identified, the first and maximum major peaks are the sub-waveforms extracted for retracking.

5.3.2.2 Waveform Adaptive Threshold Retracker (WATeR)

The study domain for this research contains a significant range of water body types and forms within the one wetland environment. To complicate this further, the variation extends to a temporal scale as the inundation extent of the wetland changes over time. This variation cannot be managed effectively by existing waveform retrackers and although existing solutions are satisfactory for some conditions and regions, they do not work accurately for all cases nor are they reliable across the entire wetland for all inundation conditions.

In this study, an adaptive retracker based on the Improved Threshold Retracker detailed in Section 5.2.3 has been developed. The Waveform Adaptive Threshold Retracker (WATeR) has been developed to optimise the semi-autonomous extraction of accurate water level time series from a variety of inland water targets. While incorporating the basic functionality of the Improved Threshold Retracker, WATeR utilises a range of ancillary information regarding waveform shape as well as external inputs such as the altimetry footprint classification to guide the retracking process. In the manner of an expert system, following selection of processing criteria options, WATeR undertakes the remainder of the retracking process in a predominantly autonomous manner. The retracker performs an initial pass of all waveforms in the sequence and, for each waveform, determines the retracked WSE using the standard Threshold Retracker as well as extracting a range of parameters related to waveform shape and structure. These parameters are then incorporated in a second pass that retracks the waveform based on either the full waveform or a sub-waveform as a function of predictions undertaken following the first iteration. Waveforms are automatically removed from the retracking process if they do not meet select conformance criteria. Some waveforms will retain a residual error from unresolved distortions and, if detected, these are flagged for rectification in a secondary process.

The proposed retracking process constitutes a deconstruction of the altimetry waveform and a micro-scale analysis of the impact of the receiving environment on the waveform structure. While aiming for an autonomous process, some facets require intervention as a secondary process; for example, outlier detection and resolution of unresolved hooking distortions.

The full analysis methodology developed for the WATeR altimetry retracking process is detailed in the flow charts of Figures 5-13–5-16. Iteration one (Figure 5-13) is the pre-processing pass where initial nadir WSE estimates, waveform shape characteristics and the nadir footprint classification are extracted for use in the second iteration.

The second iteration of the WATeR optimised retracker commences with an assessment of whether hooking is evident within the altimetric WSE profile generated in iteration one. If hooking hyperbola exist then the WSE corresponding to the apex of the hyperbola, along with the associated φ and λ of the apex, are extracted. The waveforms used in this process are flagged for exclusion in the individual waveform retracking phase undertaken in iteration two.

While the retracking process is primarily automated it is recognised that derived WSEs will require assessment in secondary processes. To facilitate this, retracking status flags along with the derived altimetric WSEs are output. The flags are based on parameters such as waveform shape, magnitude of the backscatter coefficient, nadir landform classification and extent of waveform distortions such as hooking and saturation. These flags do not relate directly to waveform quality but are designed to facilitate the selection of retracking options through the WATeR workflow and are defined in Table 5-2.

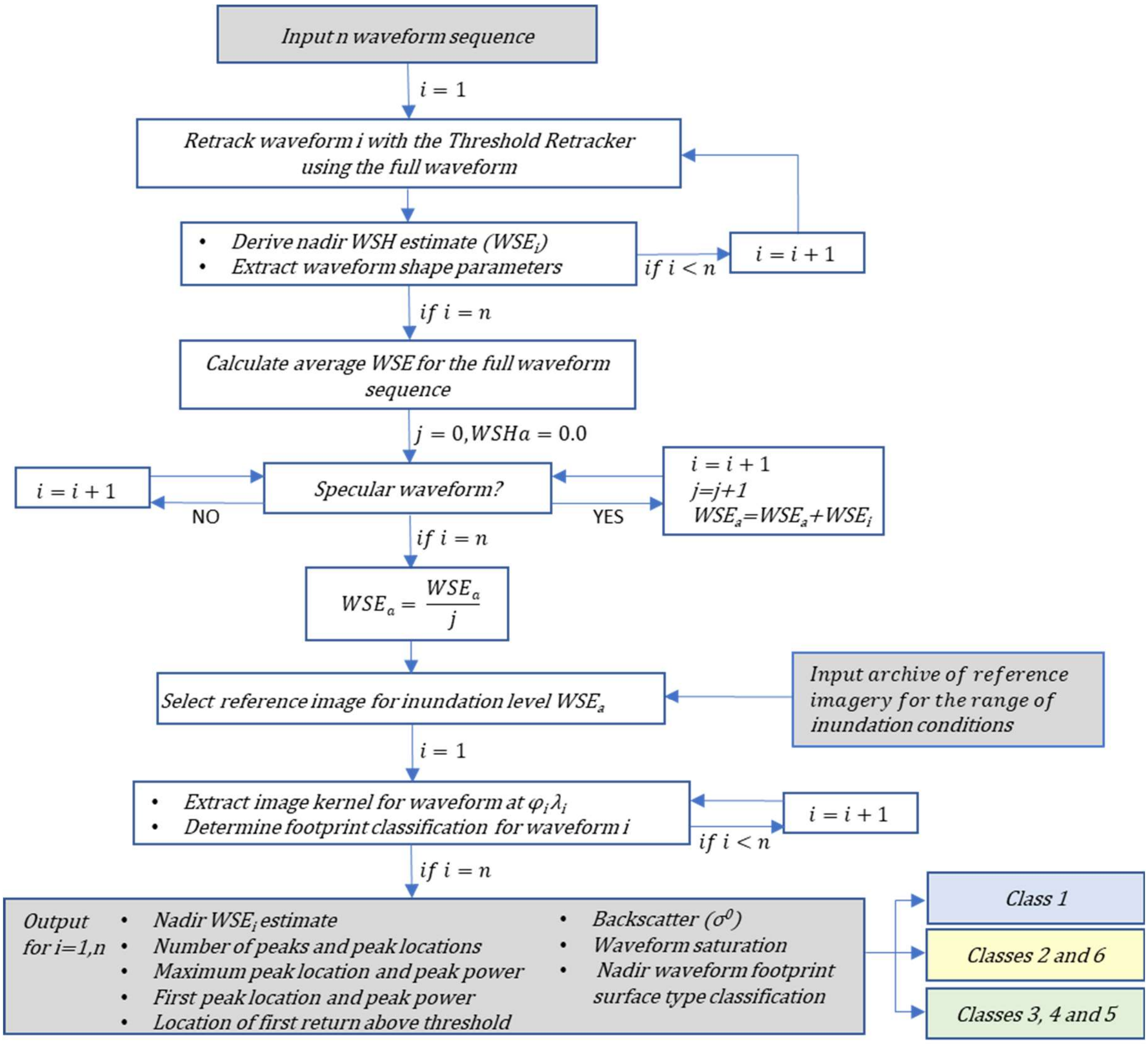

Figure 5-13 The WATeR workflow for the pre-processing phase where initial nadir WSE estimates, waveform shape and the nadir footprint classification are extracted. The second iteration process (cf. Figures 5-14–5-16) uses different processes as a function of inundation extent and altimetry footprint class types as defined in Table 5-2.

The quality flags generated in the retracking workflows are necessary for guiding the retracking process and in the archiving of data for use in any secondary process including outlier detection, statistical analysis and hooking distortion rectification, with different processes activated as a function of the state of the flags. Flag1 relates to the shape and nadir surface classification of the derived WSE estimate and is loosely correlated with the expected quality of the derived WSE. For example, a quasi-specular waveform from a water nadir footprint, where flag1 is set to 1, is expected to be of higher quality than a multi-peaked waveform over an inundated nadir footprint, where flag1 is set to 3, as it is recognised that there is likely to be some level of contamination within this return. Flag2 relates to the extent of waveform saturation, with the magnitude of the flag corresponding to the number of saturated gates within the waveform peak. Flag1 settings greater than 100 and flag2 settings are purely for tracking archived or deleted waveforms.

Table 5-2 WSE status flags derived as part of the WATeR optimised retracker analysis process. Flag1 relates to the shape and nadir surface classification of the derived WSE estimate and flag2 relates to the waveform saturation with flag value being the number of gates affected in the saturated peak.

Retracking flag1	Waveform shape	Backscatter coefficient	Nadir classification	Additional inputs	WSE location	Comments
1	Quasi-specular	> 35	Inundated	Nil	Nadir	
2	Quasi-specular	< 35	Inundated	Adjacent calm water WSE for verification	Nadir	
3	Multi-peaked	n/a	Inundated	PredictPeak input using a priori calm water WSE	Nadir	
4	Quasi-specular	n/a	Inundated	CalmWater Distance	Off-nadir	Hooking rectification.
5	Multi-peaked	n/a	Inundated	PredictPeak & CalmWater Distance	Off-nadir	Hooking rectification.
6	All	n/a	Dry vegetated or bare ground	CalmWater Distance	Off-nadir	Hooking rectification.
100	Multi-peaked	n/a	Dry vegetated or bare ground	PredictPeak & CalmWater Distance	none	Deleted waveform (no predicted water return)
101	All	n/a	All	flag2 > 1	n/a	Deleted waveform (saturation)
200	All	n/a	All	Altimetric WSE profile	Off-nadir	The waveform is used in hooking rectification derived from a hooking hyperbola.

The flow charts (Figures 5-14–5-16) reference subroutines PredictPeak and CalmWaterDistance. PredictPeak is a routine that determines the probable water return peak within a multi-peak waveform, as detailed in Sections 5.2.3 and 5.3.2.1, while CalmWaterDistance outputs the bearing and distance to the nearest likely calm water location based on the methodology developed in Section 4.5, along with parameters such as waveform specularity and backscatter coefficient magnitude, from which an assessment of the surface roughness of the echo return location is derived. These data are critical to the effective operation of the WATeR optimised retracker as they direct the processing methodology adopted for each specific waveform.

In cases where the nadir footprint is not smooth—consisting of either exposed land or a rough water surface—and there is a dominant off-nadir specular reflector that results in hooking, the nadir return may be a low power echo return and relatively insignificant compared with the return from the specular reflector. In some cases, it will be of such a low magnitude that it resides with the threshold noise making it undetectable. If this occurs the predicted gate for the nadir water return will be at a gate preceding the location of the first return above the threshold and it can be concluded that there is no nadir water return for the subject waveform. If the location of the predicted nadir footprint precedes the first waveform return above the threshold, then a 'gateslip' has occurred. The gateslip magnitude is the numeric difference between the predicted gate and the gate at the first return above threshold. In WATeR, if this parameter is returned as a negative integer, there is no sub-waveform to be extracted and the waveform is omitted. It is also possible that the predicted gate for the nadir water return is greater than the last identified waveform peak. In this case, the parameter 'lastgate' is derived and is the difference between the predicted gate and the last peak gate in the waveform. If lastgate is returned as positive, then the waveform is omitted from the processing sequence.

The backscatter coefficient offers valuable information relating to surface roughness, which guides decisions regarding retracking options, particularly where hooking is suspected. It is used extensively in the WATeR retracking workflow, in conjunction with the altimetric footprint classification, to direct hooking-related investigations. A high backscatter coefficient indicates a return from a specular surface while a low backscatter coefficient relates to a return from a surface of increased roughness. For altimeters used in this study, highly specular reflectors (e.g. calm water bodies) have a backscatter coefficient exceeding 50 while a single digit backscatter estimate is expected for surfaces of significant roughness (e.g. exposed vegetated land). Through open water zones, where wind has increased surface roughness, the backscatter coefficient typically lies in the mid-range.

Figure 5-14 details the WATeR processing workflow for the case where the waveform nadir footprint is predicted to be open water (class 1). Figure 5-15 is for the case of the footprint classification being inundated vegetation or inundated bare ground (classes 2 and 6), while Figure 5-16 is the case for a dry floodplain (classes 3, 4 and 5).

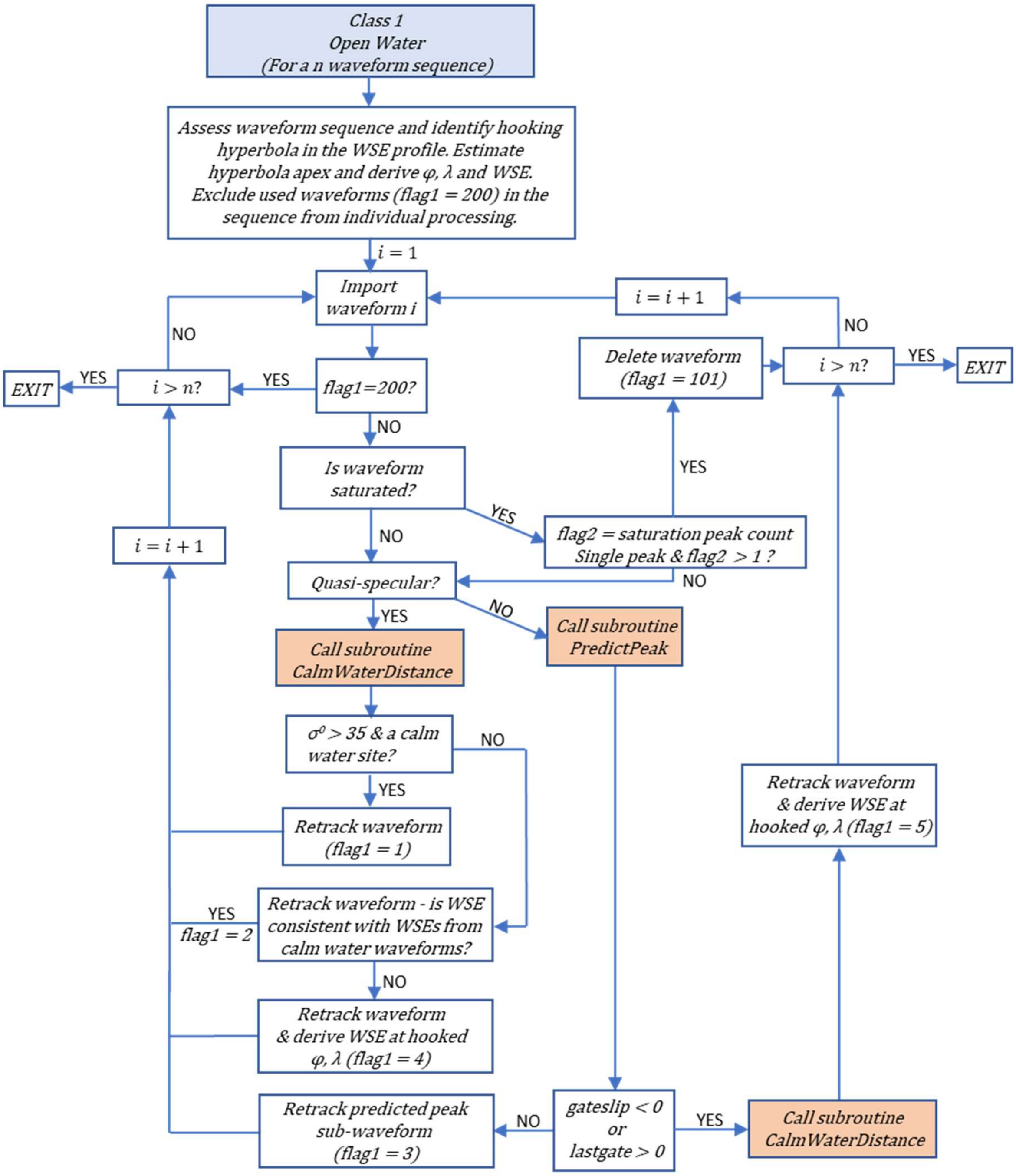

Figure 5-14 WATeR workflow for the second iteration in the retracking process for an open water footprint classification.

The workflows for the open water and inundated floodplain cases are similar except in the case of quasi-specular returns over open water, where verification of hooking is undertaken if the waveform location is not within a predicted calm water region. In cases where the nadir footprint is not smooth—consisting of either exposed land or a rough water surface—and there is a dominant off-nadir specular reflector that results in a hooking distortion, the nadir return will be a low-power echo return and relatively insignificant compared with the return from the specular reflector.

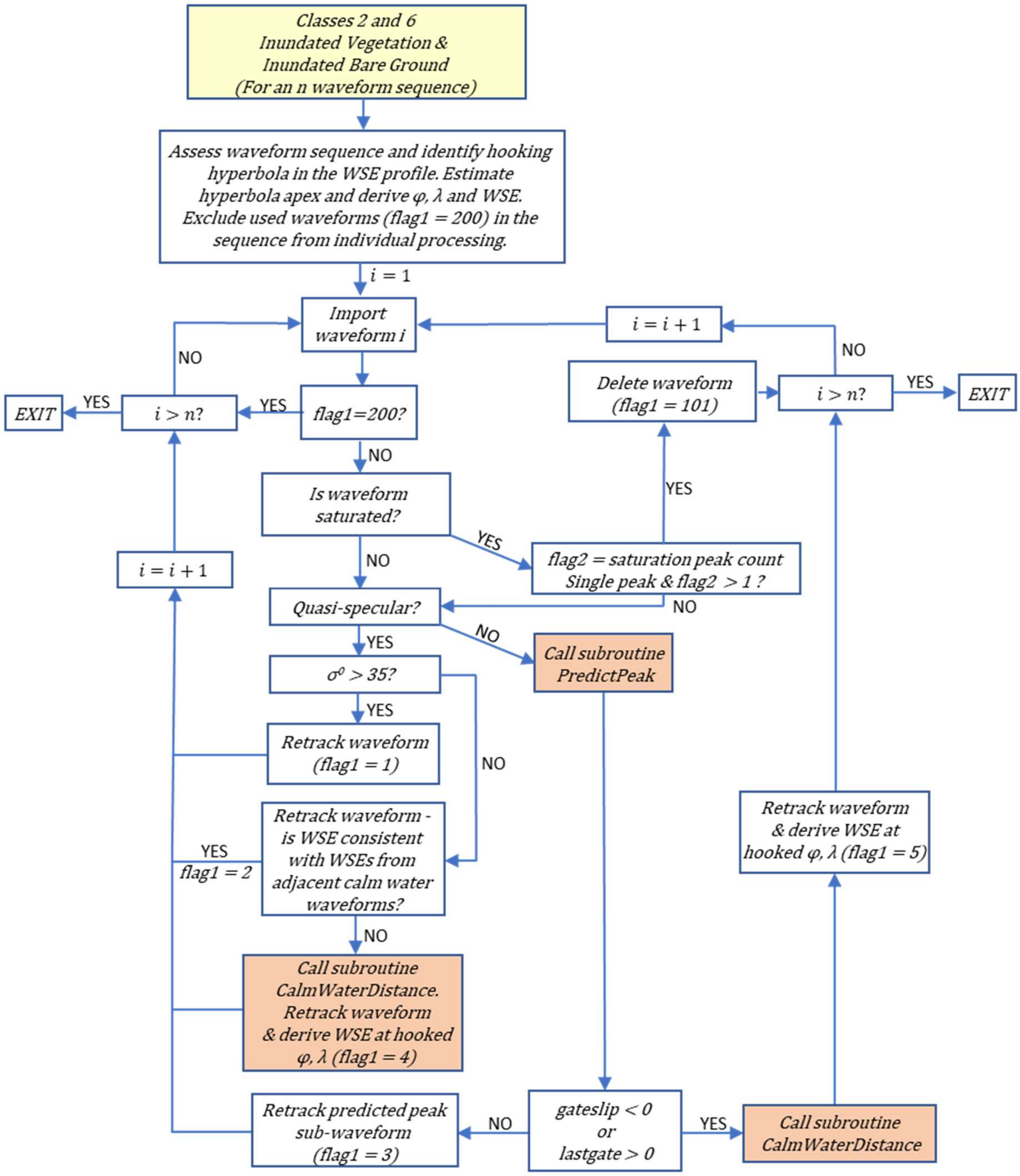

Figure 5-15 WATeR workflow for the second iteration in the retracking process for inundated vegetation or inundated land footprint classification.

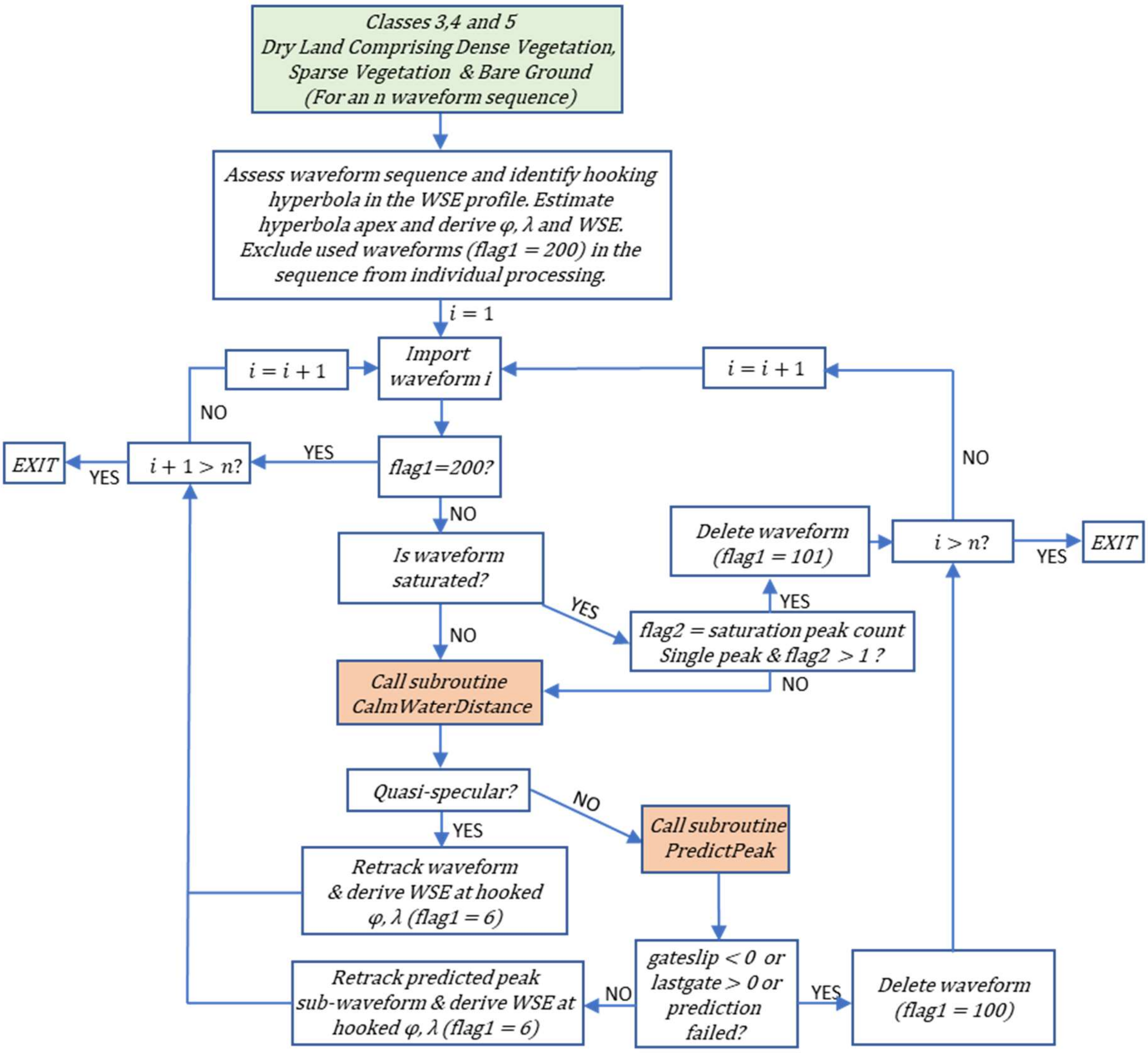

Figure 5-16 WATeR workflow for the second iteration in the retracking process for a footprint classification comprising dense vegetation, sparse vegetation or bare ground.

Examples of the WATeR altimetry retracking process applied across a wide range of wetland and complex floodplain zones are presented in Chapter 7. Extensive validation accompanies the altimetric analyses to quantify the quality of the data outputs and to demonstrate the potential for use of the retracker as an effective retracking tool over heterogeneous inland waters.

5.3.2.3 WATeR software development

To effectively investigate the properties of altimetric waveforms captured over heterogeneous inland waters it has been necessary to develop software that facilitates these investigations. The first software developed was undertaken using the Interactive Data Language (IDL) to read the Envisat RA-2 SGDR data record and to extract required parameters into an ASCII format for the latitude and longitude bounds of the study area. The required data from the Network Common Data Form (NetCDF) SARAL/AltiKa data record were extracted using a batch file process based on the File Array Notation (FAN) NetCDF command library (Davies, 2020) as well as a formatting program developed using Fortran 95. For Cryosat-2 SIRAL, Matlab software was developed to extract the required parameters from the SGDR record.

The comprehensive waveform retracking program WATeR was developed in Fortran 95, designed for analysing waveforms captured over inland water targets. The software is comprised of approximately 2,500 lines of software code that facilitates the following wide range of processing and research options:

a) data input from the ASCII SGDR record
b) extrapolation of 1-Hz records to the echo averaging frequency (Envisat RA-2 18 Hz, SARAL/AltiKa 40 Hz, Cryosat-2 SIRAL 20 Hz)
c) correlation of the altimetry record with an in-situ river level record and extraction of the river level record for calibration and verification of the derived altimetry profile
d) extraction of satellite imagery consistent with the predicted inundation frequency at the time of the altimetry pass
e) identification of saturated waveforms
f) AGC correction
g) determination of waveform characteristics
    i) maximum power
    ii) the number of peaks (specularity measure)
    iii) location and power of the first peak
    iv) location and power of maximum peak
    v) location of the first gate to exceed the noise threshold
    vi) the number of gates impacted in a saturated waveform
    vii) predicted threshold frequency to achieve in-situ water level
h) for non-specular waveforms, determination of gate of predicted nadir water return
i) selection of retracking methodology
    i) Offset Centre of Gravity Retracker
    ii) Threshold Retracker (set threshold levels)
    iii) Improved Threshold Retracker
        - first peak
        - last peak
        - maximum power peak
        - predicted peak

j) calculation of gateslip and lastgate for non-specular waveforms
k) output of results for all waveforms located between the latitude and longitude bounds of the study area.

Additional software was developed in Fortran 95 to facilitate the analysis of the retracked data with an emphasis on a statistical review of the retracked WSEs incorporating a robust outlier detection component.

Software programs were developed within Matlab to assist with research in optimising waveform retracking over inland waters. Software was developed to aid in the visualisation of the waveform sequence and comprised output in the form of individual waveform plots as well as plots of overall waveform sequences. Additional software was developed to allow for the inclusion of ancillary data (alongside in-situ water level records) in the retracking process so that the analysis and classification process for each waveform could be undertaken more accurately. The developed software scans a multispectral or SAR satellite image captured under similar inundation conditions to that of the altimetry pass. At the nadir location of the altimetry footprint an image kernel is extracted and an assessment of inundation conditions as well as land cover type is derived. This input allows for decisions regarding the probability of the return being a nadir return from an inundated target and provides valuable input into the identification and possible rectification of off-nadir distortion. An additional facet of the software is the feature whereby the potential locations of off-nadir specular reflectors are identified to facilitate the correction of off-nadir distortion.

5.4 Summary

In this chapter, the process of waveform retracking is detailed and the evolution of development of waveform retrackers is documented. Focus is primarily on retrackers that are applicable to non-ocean returns where the resulting satellite altimetry echo varies in shape and does not conform to microwave scattering at nadir theory. The Threshold Retracker developed by Davis (1997) is reviewed in detail as are the various permutations that have used the threshold retracking process (Hwang et al., 2006; Bao et al., 2008; Lee et al., 2008; Yang et al., 2012; Villadsen et al., 2016).

Methods for the identification and selection of the sub-waveform relating to the nadir return within a multi-peaked waveform, optimised for complex wetland and floodplain environments, have been developed as part of this study. Sub-waveform identification builds on the methodology derived by Hwang et al. (2006), Bao et al. (2008) and Lee et al. (2008) with additional functionality incorporated to accurately define sub-waveform lateral extent and to classify the identified sub-waveforms on the basis of significance. An autonomous sub-waveform selection methodology has been developed using derived WSE estimates from neighbouring quasi-specular returns derived from a calm water footprint to assist with the definition of the sub-waveform relating to the nadir return in the multi-peaked waveform. These processes maximise the number and quality of waveforms that are available for retracking, which is of considerable importance when deriving WSE over small rivers and inland water bodies.

An adaptive retracking process has been developed as part of this study and is detailed in this chapter. The WATeR has been designed to optimise the autonomous extraction of accurate WSE time series from a variety of inland water targets. While incorporating the basic functionality of the Improved Threshold Retracker, WATeR utilises a range of ancillary information regarding waveform shape as well as external inputs such as altimetry footprint classification to guide the retracking process. In the manner of an expert system, following selection of processing criteria options, WATeR will undertake the remainder of the retracking process in a predominantly autonomous manner. Statistical analyses, including outlier detection within the WSE time series, as well as hooking rectification are undertaken as secondary processes.

The retracker performs an initial pass of all waveforms in the sequence and, for each waveform, determines the retracked WSE using the standard Threshold Retracker and extracts a range of parameters related to waveform shape and structure. These parameters are then incorporated in a second pass that retracks the waveform based on either the full waveform or a sub-waveform as a function of predictions undertaken in the first pass. The sub-waveform selection methodologies proposed by Hwang et al. (2006), Bao et al. (2008) and Lee et al. (2008) are enhanced in this study. An a priori estimate of the WSE is derived from adjacent quasi-specular waveforms that have been identified as having an inundated nadir footprint and this WSE is used to select a sub-waveform for use in the Improved Threshold Retracker. Different retracking processes have been developed for the various nadir footprint classifications as these classes control the methods used to identify and rectify hooking distortion, the sub-waveform retracking method that is utilised and the process flow that is adopted for each waveform. The proposed retracking process constitutes a deconstruction of the altimetry waveform and a micro-scale analysis of the impact of the receiving environment on the waveform structure.

While the WATeR altimetry retracking process adds computational complexity to the retracking task, the benefit is a significant improvement in the understanding of any contamination that may have affected the waveform along with an estimate of the associated magnitude of any distortion in the derived WSE. The process has the potential to improve the overall accuracy of the derived WSE time series as a result of this understanding.

CHAPTER 6: WAVEFORM DISTORTIONS

Over inland water regions a wide range of external factors can lead to contamination of the altimetry return echo resulting in a recorded waveform that contains artefacts and spurious returns. Such external factors include topography (Benveniste and Berry, 2004; Berry et al., 2005), particularly in cases where the topography changes abruptly (Maillard et al., 2015). A wide range of echo shapes is observed within a waveform sequence whenever there is evidence of any type of land contamination (Benveniste and Berry, 2004; Schwatke et al., 2015b). This contamination can manifest as complex multi-peaked waveforms. Retracking processes such as the Improved Threshold Retracker (as detailed in Section 5.2.3) can facilitate accurate processing of these waveforms, particularly if a priori water level approximations are available so that the relevant water return peak can readily be isolated for processing.

For altimeters pre-dating ERS-1 operating only in ‘ocean mode’, there had been a significant paucity of data from inland targets, with altimeters maintaining lock only over limited areas of land (Benveniste and Berry, 2004; Berry et al., 2005a). This was rectified, in part, with the inclusion of an ‘ice mode’ in ERS-1 and subsequent platforms (Benveniste and Berry, 2004). Among the more recent altimetry missions, the performance of Jason-1 in particular over inland water targets is considered poor with a significant loss of data (Berry, 2006).

Hooking has been recognised as one of the most significant and problematic distortions that can affect the altimetric echo (Benveniste and Berry, 2004; Berry, 2006); while predominantly observed over inland waters, it will also occur within the ocean coastal zone. The impact of hooking, along with methodologies for identification and rectification of hooking distortion focussed on altimetric acquisitions within complex wetland and floodplain environments, is addressed in the following sections.

Waveform saturation occurs when the power of the return pulse exceeds the dynamic range of the receiver, resulting in distortions to the waveform (Bouzinac, 2010). This is typically a result of specular reflectors located within the altimetric footprint through a zone of highly variable scattering (Verron et al., 2018). Such distortion is regularly observed in SARAL/AltiKa waveforms where the pass is located over wetlands or other calm water bodies, with saturation of the waveform at a count of 1250. Despite being reported as possible for Cryosat-2 SIRAL (Bouzinac, 2010) waveform saturation has not been observed in the data used in this study nor has it been observed in Envisat RA-2 data. The saturated waveform may be complicated with a hooking component if the specular reflector is not at nadir, making the contamination difficult to rectify. Methods for identification of saturation, estimates of impact on the derived altimetry WSE profile and evaluation of potential rectification processes are investigated in the following sections. The impact of rain and cloud within the footprint of the SARAL/Altika footprint is known to attenuation the altimetry waveform leading to erroneous geophysical parameter estimates (Tournadre et al., 2009). This effect, coupled with hooking and saturation, increases the analysis complexity of the SARAL/Altika waveforms.

6.1 Hooking

The size of the radar altimeter footprint for conventional pulse-limited altimeters varies as a function of surface roughness (wave height for ocean applications; topographic variation and vegetation cover for inland water applications), satellite altitude, antenna beamwidth and pulse duration (Chelton et al., 2001). The smaller antenna beamwidth of SARAL/AltiKa leads to a smaller footprint (~8 km) than that of Envisat RA-2 and Cryosat-2 SIRAL (~9–15 km) for average surface roughness (Schwatke et al., 2015a). For calm seas or flat land, the altimeter footprint will narrow to approximately 2 km; however, it will significantly increase in size (up to 18 km) for a very rough sea state or where there is significant topographic and vegetation variation (Rosmorduc et al., 2018).

The reflected waveform contains contributions from a multitude of sources within the footprint (Nuth et al., 2002); some originating from exposed water bodies and others from vegetation communities, man-made structures or exposed topographic features. For inland applications, this typically creates a complex echo with portions originating from many varying heights (Rosmorduc et al., 2018). Where the radar-reflective surface becomes heterogeneous at the scale of the altimeter footprint, the location of the origin of the echo may become ambiguous and, as a function of the relative reflectivity within the footprint, may not be from the nadir location (Connor et al., 2009). The heterogeneity of the reflective surface is estimated to be the most significant contributor towards elevation uncertainty in terms of magnitude (Calmant et al., 2009; Rosmorduc et al., 2018) with a significant residual off-nadir distortion contaminating derived WSE unless it is identified and extracted.

Hooking describes the condition whereby the satellite on-board tracking system is dominated by off-nadir specular reflectors within the altimeter footprint (Villadsen et al., 2016). This will typically occur when the reflectance (i.e. backscatter and power magnitude) at nadir is lower than the off-nadir specular reflector. As the on-board tracker is locked onto the brighter off-nadir target within the footprint, the derived range is a slant range and, when applied at nadir, leads to an under-estimate of the surface height. This process is termed hooking; also referred to as snagging (Nuth et al., 2002; Connor et al., 2009; Villadsen et al., 2016) or off-nadir distortion (Frappart et al., 2006; Santos da Silva et al., 2010). If this process continues over subsequent waveforms, the resulting altimeter-derived height profile will appear as a downward-turning hyperbolic feature. These features are artefacts within the height profile and require identification and extraction from the data (Frappart et al., 2006).

6.1.1 Existing methodologies for the correction of the hooking distortion

There is evidence of hooking in most of the conventional nadir-looking pulse-limited altimeters dating back to Seasat. Wingham et al. (1986) reported changes in Seasat waveform pulse shape from quasi-specular to that associated with a diffuse reflector, as the specular reflector return followed a hyperbolic path through the range window. Hyperbolic features were observed from the ERS-1 altimeter (Wingham et al., 1993; Nuth et al., 2002) over ice and ice flows but were regarded as discontinuities in the surface topography. Methodologies—specifically Kirchhoff migration, a process developed by reflection seismologists—were employed to refocus energy within the hyperbolic feature (Nuth et al., 2002). However, the process was only partially successful because of the existence of 'out-of-plane' reflectors that confused the results.

During the development of the Rivers & Lakes database, Benveniste and Berry (2004) observed the existence of hooking within the ERS-1 and Envisat RA-2 data sets and noted that the most serious limitation of the data was the existence of bright components within the echo resulting from still pools. This was emphasised again in a summary paper covering retracked elevations from ERS-1, ERS-2, Envisat, T/P and Jason-1 (Berry, 2006). The existence of multiple specular targets within complex sequences was identified.

In ocean applications, reflectors located above the sea surface were noted to produce a characteristic hyperbolic shape within the waveform sequence (Tournadre, 2007; Gomez-Enri et al., 2010; Quartly, 2010). These reflectors were identified as being ships, lighthouses, beacons or small islands. Typically, there was only a single such reflector in each waveform sequence and methods were introduced to enable estimation of the signal strength and then removal of the feature before conventional waveform retracking (Quartly, 2010).

Initial methodologies for the identification and correction of the hooking distortion focussed on the identification of an upward-turning hyperbolic feature within the waveform sequence itself (Wingham et al., 1993; Nuth et al., 2002). However, this proved to be both complex and computationally difficult with derived water level profiles that were not significantly superior to results before correction. Subsequent methodologies have focussed on identification and correction within the altimeter-derived height profile with hooking to a single off-nadir specular reflector characterised by a downward-turning hyperbolic feature within the WSE profile (Frappart et al., 2006; Santos da Silva et al., 2010; Maillard et al., 2015; Boergens et al., 2016).

For inland water applications early investigations were undertaken by Frappart et al. (2006). Once hyperbolic features were identified in a waveform sequence a correction term was calculated based on integrating the energy over the feature and refocussing the sum at the apex. The migration technique proposed was applied to the derived altimetric ranges rather than to the altimeter waveform data as implemented by Nuth et al. (2002). Frappart et al. (2006) referred to this as migration with the principle of the process shown in Figure 6-1 and the height error estimated as:

$$\Delta h = h' - h = h\left(\sqrt{1+\left(\frac{d}{h}\right)^2} - 1\right) \approx \frac{d^2}{2h}\,; d \ll h \tag{6-1}$$

where:

- ΔR is the range error
- R_{obs} is nadir range to the water body at the apex of the hooking hyperbola
- R_{obs}' is the measured slant range
- d is the along-track distance between the satellite nadir and the target.

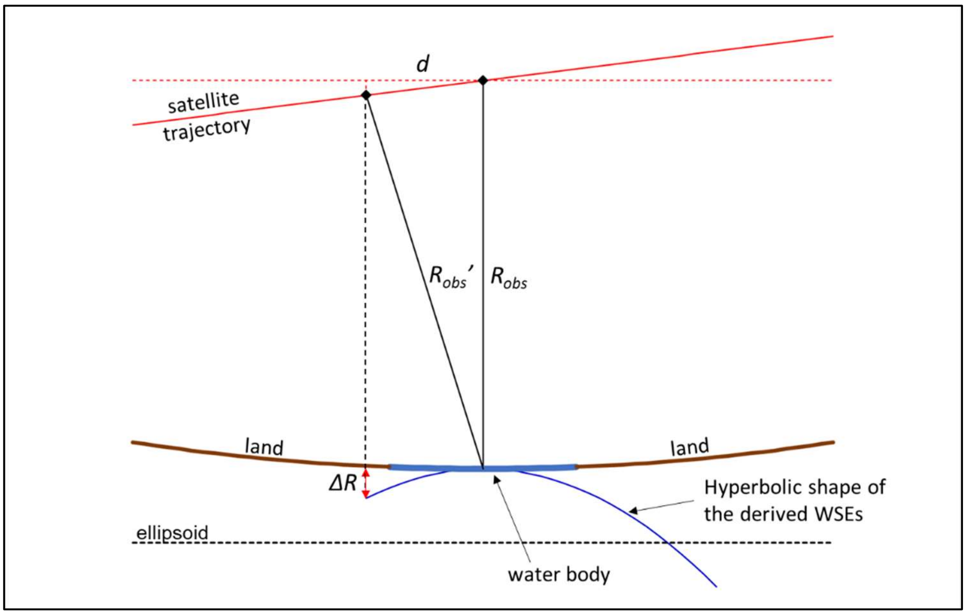

Figure 6-1 The principle of migration, adapted from Frappart et al. (2006).

This methodology was adapted by Calmant et al. (2009) to assist with the retracking of data from ERS-1, ERS-2, T/P, Jason, Geosat Follow-on (GFO) and Envisat missions.

The principle and mathematical formulation of the off-nadir correction, applicable specifically to inland water applications, was developed by Santos da Silva et al. (2010) and has been reproduced in similar forms including by Tourian et al. (2009) and Boergens et al. (2016). The correction is based on the principle that off-nadir ranges acquired as a result of a hooking event lead to a hyperbolic shape of the derived along-track heights (Boergens et al., 2016). This can be approximated by a parabola as the satellite altitude is typically much greater than the distance to the hooking point from nadir, which, in turn, is much greater than the height error (Quartly, 2010). The correction procedure detailed in Santos da Silva et al. (2010) uses a migration technique whereby the derived heights are integrated over the parabolic feature to yield a single WSE estimate at the apex of the parabolic feature in a manner similar to that of Frappart et al. (2006). The principle of the off-nadir distortion as developed by Santos da Silva et al. (2010) is illustrated in Figure 6-2.

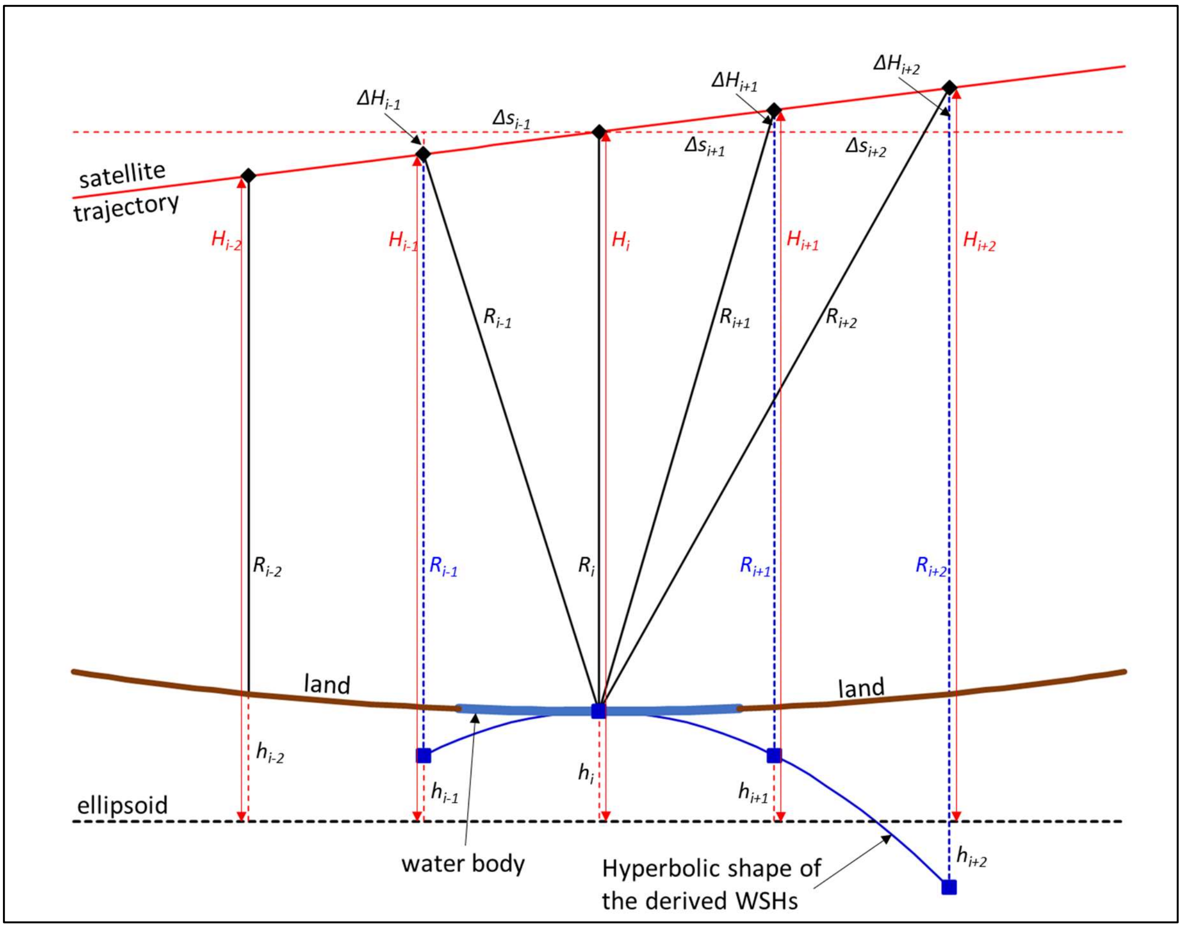

Figure 6-2 Schematic diagram showing the off-nadir distortion in along-track height profiles resulting from a hooking sequence caused by the altimeter locking onto a specular reflector within the radar footprint as it passes over an inland water body. The vertical blue dashed lines show the effect of the hooked range to the off-nadir reflector on the derived WSE. The hyperbolic shape of the WSE profile is shown as a solid blue curve.

At time t_i:

- H_i is the satellite altitude
- ΔH_i is the change in satellite altitude between times t_i and t_{i-1}
- Δs_i is the distance that the satellite has travelled between times t_i and t_{i-1}
- R_i is the range to the reflecting surface
- h_i is the derived ellipsoidal height of the reflecting surface.

The derived ellipsoidal height at time t_i is given by:

$$h_i = H_i - R \qquad (6\text{-}2)$$

For the example shown in Figure 6-2, this results in a WSE estimate free of off-nadir distortion at times t_{i-2} and t_i. While the estimate at time t_{i-2} is derived over land and is likely to be relatively inaccurate as a result of the expected contaminated waveform, it is not contaminated by off-nadir distortion. The estimate at time t_i represents a nadir estimate of WSE over the inland water body. In this schematic diagram, the impact of any geophysical or atmospheric corrections is neglected.

At times t_{i-1}, t_{i+1} and t_{i+2} the measurement is not a nadir range but is a slant range measured towards a bright source within the calm water zone of the lake or river. When the range is applied to Equation 6-2 a characteristic hyperbolic shape is evident in the derived along-track heights (cf. the solid blue line in Figure 6-2).

The measured range for the off-nadir acquisition at time t_{i+1} is given in Equation 6-3. At other times through the sequence where off-nadir distortion is evident the respective variables at that time are simply inserted into the correction equations:

$$R_{i+1} = \sqrt{\Delta s_{i+1}^2 + (R_i - \Delta H_{i+1})^2} \qquad (6\text{-}3)$$

and

$$\Delta H_{i+1} = \frac{\partial H}{\partial s} \Delta s_{i+1} \qquad (6\text{-}4)$$

where $\frac{\partial H}{\partial s}$ is the altitude variation of the satellite along its orbital trajectory.

Consistent with Equation 6-2:

$$h_{i+1} = H_{i+1} - R_{i+1} \qquad (6\text{-}5)$$

With substitution, h_{i+1} is expressed as a function of Δs_i in Equation 6-6 as:

$$h_{i+1} = H_i - \Delta H_{i+1} - R_i \sqrt{\left(1 - \frac{\Delta H_{i+1}}{R_i}\right)^2 + \frac{\Delta s_{i+1}^2}{R_i^2}} \tag{6-6}$$

Following the simplification process detailed in Santos da Silva et al. (2010) and Boergens et al. (2016) the quadratic relationship between h_i and δs_{i-1} can be defined as:

$$h_{i+1} = h_i - \Delta s_{i+1}^2 \left(\frac{1}{2R_i}\right)\left(1 + \left(\frac{\partial H}{\partial s}\right)^2\right) \tag{6-7}$$

The term $\frac{\partial H}{\partial s}$ is a second-order correction that is generally neglected (Boergens et al., 2016) as the distortion is estimated to be less than the typical accuracy of altimetry-derived inland water WSEs. This accuracy is reported to be at the decimetre level so second-order terms would need to be incorporated if pursuing higher-accuracy water level estimates.

The formulation of the off-nadir distortion correction is based on the assumptions that there is a single specular reflector and that this reflector is common at all echoes that contribute to the definition of the hyperbolic profile. While this is likely for land–water–land transitions where the land zones are predominantly dry, it will not be the case for the majority of water–water transitions or where there are multiple specular reflectors over inundated or partially inundated land. In the case of a heterogeneous wetland environment, there are likely to be numerous specular reflectors within each satellite footprint. Consequently, there will be changing hooking conditions within each pass so that the characteristic parabolic shape typically induced by a single specular reflector across the scene does not exist. In these cases, the derived WSE will appear to contain increased random noise with little evidence that this is related to variable hooking distortions. For these environments, alternative methods need to be implemented to extract the impact of the hooking distortion and to extract enough WSE estimates of acceptable quality across the wetland environment.

In the formulation of these corrections, while it is assumed that the hooking distortion is primarily evident in an along-track direction, this cannot be determined using the information within the acquired waveform sequence as the distortion is essentially a scalar quantity with no associated directional properties. A satellite track that passes obliquely over a river is likely to have any hooking occurring in a direction towards the most dominant specular reflector, which may not be located on-track. Boergens et al. (2016) show that if the orientation of the satellite track relative to the reflective off-track water body as well as the slope of the river system can be determined from ancillary data, the above correction processes can still be used but this is subject to the application of a simple trigonometric correction that adjusts the along-track distance ΔS_{i+1} to the off-track separation. The corrected distance from the nadir is given by $\Delta S'_{i+1}$:

$$\Delta S'_{i+1} = \Delta S_{i+1} \cos \beta \qquad 6\text{-}8$$

where β is the angle between the altimetry track and the direction to the water body.

The geometry is illustrated in Figure 6-3. With the application of the correction over meandering river systems, where the satellite track could pass over the main stem on several occasions, multiple hooking events that cannot be readily separated may be evident (Maillard et al., 2015). This will create significant difficulty in correcting for the off-nadir distortion.

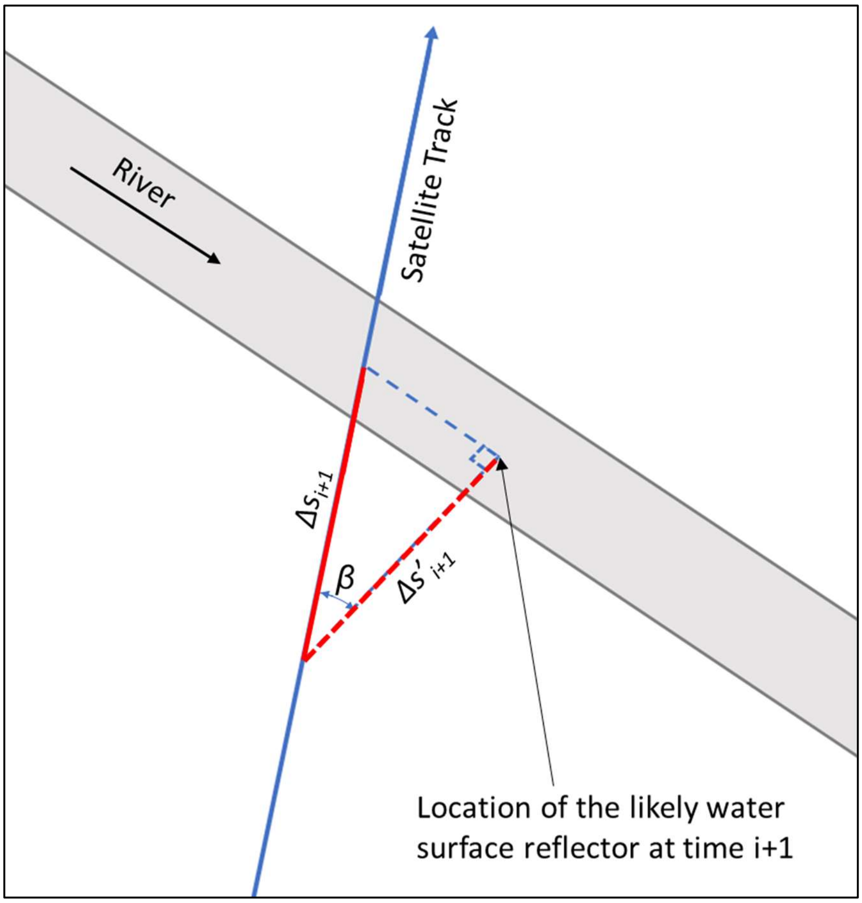

Figure 6-3 Schematic diagram showing the corrected distance to the likely off-track water surface reflector. β is the angle between the altimetry track and the direction to the water body The distance $\Delta S'_{i+1}$ is used in Equations 6-3, 6-4, 6-6 and 6-7 replacing ΔS_{i+1}.

More recent developments have focussed on methodologies for identifying hyperbolic features within a waveform sequence and automatically fitting curves to these features in a semi-autonomous manner. Maillard et al. (2015) developed a processing method whereby accurate a priori inputs, including location, width and shape of the river, are incorporated with a pattern recognition process to fit curves to the hooking hyperbola within a waveform sequence. The developed curve is inverted based on the Santos da Silva et al. (2010) methodology to give an estimate of river WSE. Boergens et al. (2016) developed an autonomous method that derives reliable water level time series over small rivers where there is evidence of the hooking effect. The method utilises a waveform retracker to improve the data along the hooking hyperbola, employs the iterative RANdom SAmple Consensus (RANSAC) algorithm to detect measurements affected by hooking and, once the measurements are identified, extracts water level estimates.

All the methodologies detailed in this section require a well-defined hyperbolic feature within the waveform sequence to identify that hooking is occurring and once identified, to facilitate the correction of the derived WSE. Initial investigations by researchers concentrated on large river and lake systems where there was usually only a single specular reflector leading into and out of the water zone (e.g. Frappart et al. [2006]; Santos da Silva et al. [2010]; Maillard et al. [2015]; Boergens et al. [2016]). In such cases, the reflectors would generally be located in the calm water zones close to the shore or bank. This would generally give rise to a limited number of hooking hyperbolae within the waveform sequence, all of which would cover multiple waveform echoes and would be readily identifiable within the sequence. While recent investigations and rectification methodologies have been implemented over smaller river and lake systems, they are not in highly heterogeneous environments and typically consist of a single dominant reflector within the altimeter footprint.

For highly heterogeneous environments there will typically be multiple specular reflectors within each altimetry footprint, all of which contribute towards a waveform shape that is complex and extensively contaminated. If no hooking hyperbolae are evident within the waveform sequence and the waveform structure conforms to selection criteria (i.e. the degree of specularity, maximum power, magnitude of the backscatter coefficient), it is likely that the waveform will be retracked and included in the altimetric WSE profile subject to statistical outlier assessment. Berry (2006) highlights the fact that statistical methods are required to assess the probability of derived heights being valid and that candidate inland water targets are therefore restricted to the larger water bodies where multiple height estimates can be extracted.

6.1.2 Forms of the hooking distortion

While hooking is conceptually a simple phenomenon and its impact on the derived altimetric WSE profile is understood, it is often difficult to identify and typically difficult to rectify accurately. A major challenge in using altimetry over inland waters relates to the handling of different reflections within the footprint (Schwatke et al., 2015b). It is accepted that single-peak quasi-specular waveforms represent a nadir calm water response from smaller rivers and lakes while multi-peaked and more complex waveforms are a result of land contamination of the radar echo. The challenge in correcting for the hooking distortion is that neither of the above assumptions is correct in all situations. In this research, there are examples of quasi-specular waveforms originating over land in transition to a water body where the echo is dominated by an off-nadir specular reflector with no evidence of any significant nadir return. There are also examples of multi-peaked waveforms over a water body where the peaks represent the various dominant reflectors within the radar altimetry footprint. In the case of multiple specular reflectors or single specular reflectors that change as the satellite transitions to a heterogeneous environment, the waveform itself and the derived altimetric WSE profile do not necessarily give information as to whether hooking has occurred and, if it has, do not give the location of the specular reflector to allow for rectification. Desai et al. (2015) documents the change in waveform shape during land–water and water–land transitions as the waveform shape changes from complex multi-peaked to quasi-specular and vice versa. This change is related to the extent of hooking and the extent to which calm water occurs within the echo footprint.

In this research, the waveforms acquired from nadir-looking pulse-limited altimeters are deconstructed in an attempt to identify if hooking has occurred and, where possible, to correct for the distortion. The majority of hooking correction methodologies focus on the distortion induced during the transition of an altimetry satellite from land to water or vice versa (Schwatke et al., 2015a; Boergens et al., 2016) as this is generally the easiest form to identify and the location of the off-nadir specular reflector can be identified with moderate accuracy. Transitions across a water body can also yield waveforms that are contaminated by hooking if there is varying surface roughness across the water body, which is typically induced by varying wind conditions and associated surface waves with water surfaces at the edge of the water body being significantly calmer, and therefore more reflective, than water towards the centre. While hooking distortion occurs during a water transition (Santos da Silva et al., 2010; Boergens et al., 2016) it is difficult to identify and correct with existing correction methodology. For water transitions, the current methodology requires the water body to be relatively large with multiple echoes representing the water surface. For this reason, most earlier studies were restricted to larger water bodies, where waveform echo structure, including the presence of a leading edge and significant power within the waveform, is used to select candidate waveforms and statistical methods are used to assess the probability of waveforms being valid (Berry, 2006).

6.1.2.1 Land–water transitions

Hooking that occurs during passes from land to water or water to land is typically the easiest to identify and rectify. The bright source that instigates the hooking will usually be located along the edge of a water body in calm water zones unaffected by wind. A hyperbolic shape will be evident in the waveform sequence with the correct water level being at the apex of the downward-looking hyperbola. The scenario becomes more complex for an inundated floodplain where multiple bright sources may exist as there could be multiple complex and mixed hyperbolae or, in the case where the off-nadir specular reflector changes for each waveform, where there may be no hyperbolic shape but a more random scatter within the waveform sequence and the derived altimetric profile. The following cases illustrate the land–water hooking process. The first case involves a single specular reflector typical of a dry floodplain where it is likely that there will only be one or two calm water sources within the altimeter footprint. The second case is for an inundated floodplain where multiple calm water sources exist within the footprint and hooking will likely occur to several different targets as the satellite passes. In this case, a systematic hooking hyperbola within the altimetric profile is unlikely and the derived WSE profile will appear to have relatively high random variation in WSE related to changes in the hooking source.

6.1.2.1.1 Land–water transitions for a single specular reflector

Figure 6-4 shows the SARAL ascending pass 0677 cycle 24 over the Fly River floodplain during the El Niño of 2015. The Fly River is the only significant water body within the altimetry footprint leading into the crossing of the altimetry track with the river.

Figure 6-5 depicts the ascending satellite track with the waveform sequence leading into the river crossing at 7.6505ºS 141.3564ºE. A secondary reflector becomes evident in the first waveform after the inundated vegetation zone. The peak created by this secondary reflector becomes more dominant as the satellite moves towards the river and becomes the only significant reflector approximately 1 km from the river. The location of this second peak through the waveform sequence forms the upturned hyperbolic feature that is evident in Figure 6-6. A large portion of the normally inundated wetland is dry.

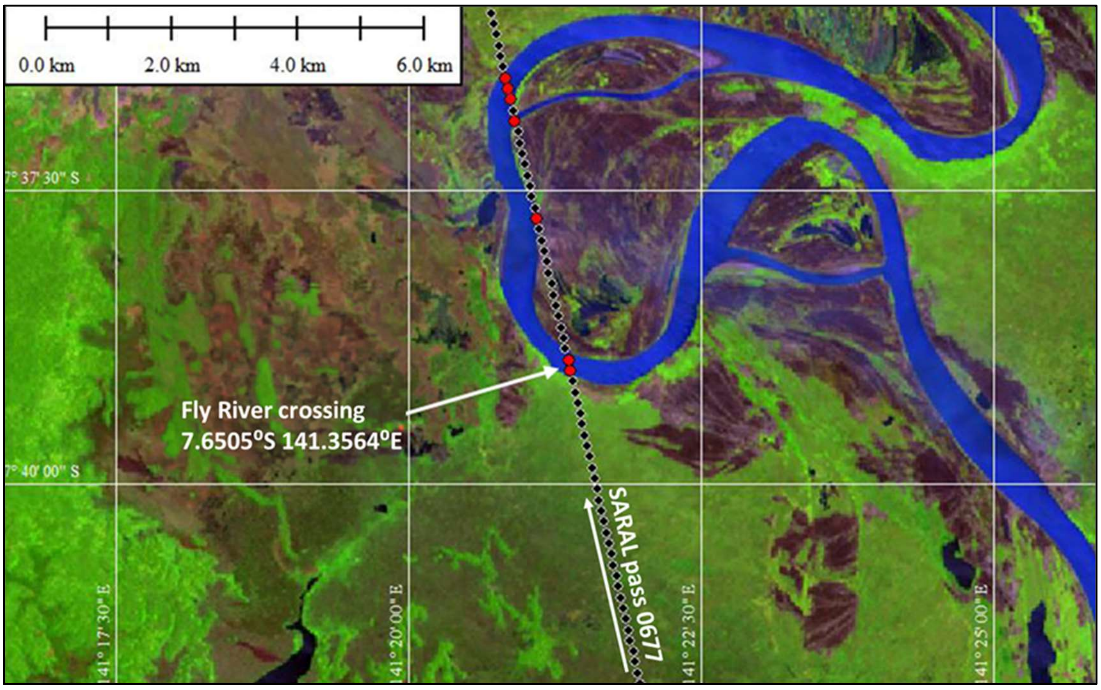

Figure 6-4 SARAL ascending pass 0677 from 20 June 2015. South to north pass over the Fly River floodplain with a crossing of the river at 7.6505ºS 141.3564ºE. The background is a Landsat OLI8 false colour image from September 2015 acquired during an El Niño event. Red dots are waveforms located within the river crossing.

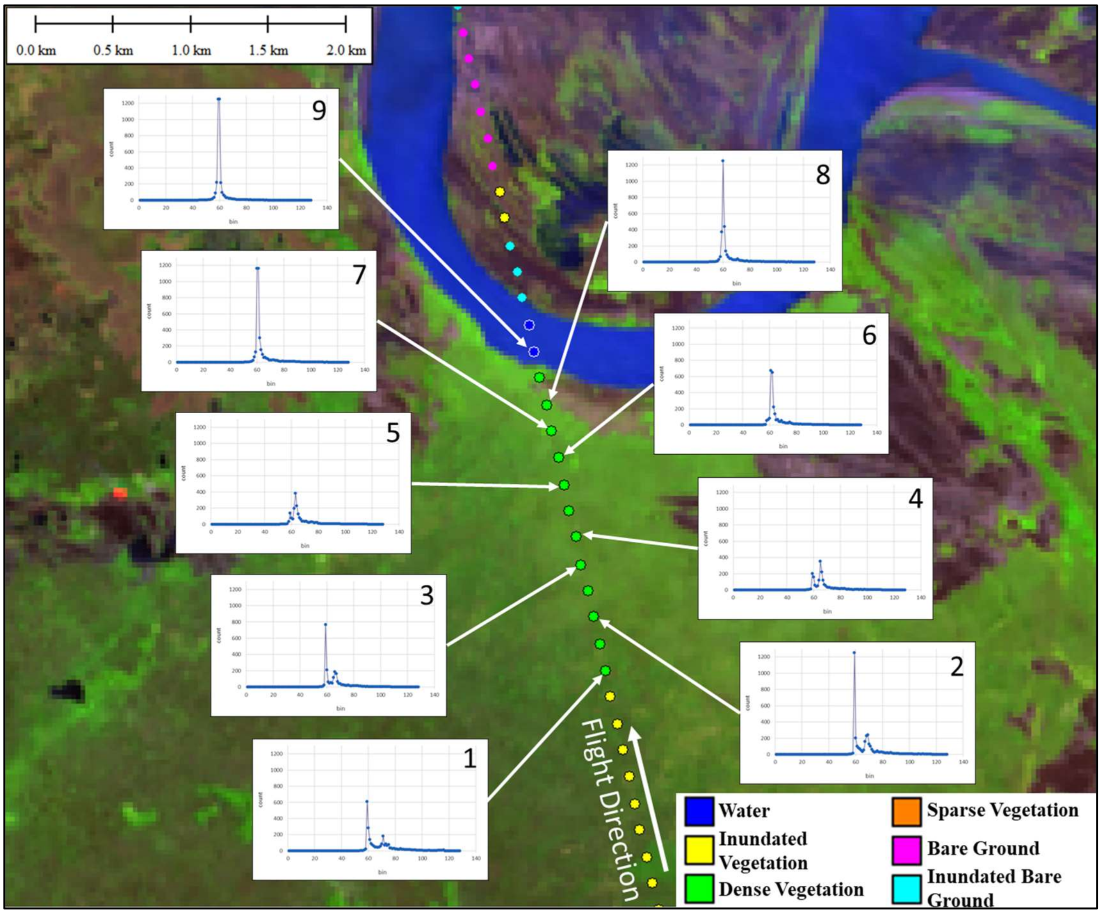

Figure 6-5 Select cycle 24 SARAL/AltiKa waveforms acquired on 20 June 2015. A secondary peak is evident in waveform 1 and this peak increases in intensity through waveforms 2–5 as the satellite tracks towards the Fly River. This peak becomes the only remaining peak by waveform 6 and remains as a quasi-specular return until it becomes a saturated return at the river.

The secondary reflector is evident in the waveform profile of Figure 6-6 with the resulting hooking event being characterised by the hyperbolic shape within the waveform sequence, centred about the dominant reflector. In this case, there are several significant peaks evident leading into the river crossing transitioning to a quasi-specular hooked return.

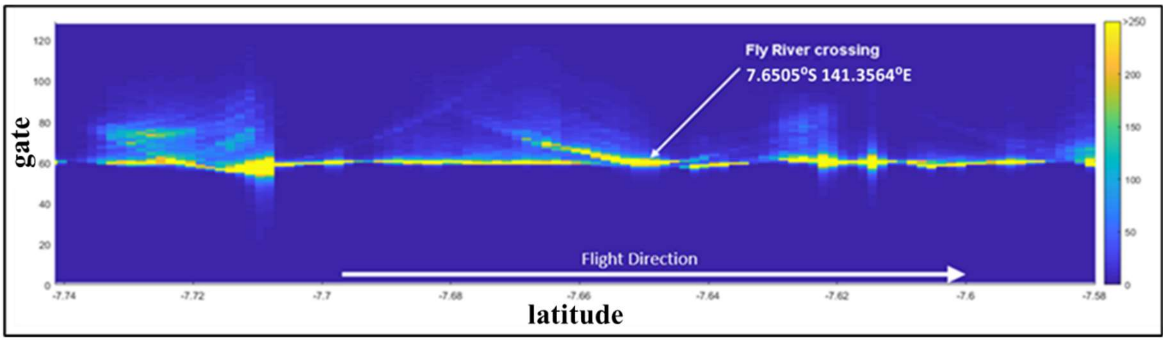

Figure 6-6 The along-track waveform sequence from the same SARAL pass shown in Figure 6-4 with the waveform power stretched to range 0–250 to highlight the hooking hyperbolae within the waveform sequence centred around the river crossing. The arrow at the base of this figure indicates the direction of flight and corresponds to the extent of coverage in Figure 6-4.

The peak linked to the hyperbolic path in Figure 6-6 starts at very low intensity when the satellite is several kilometres from the river and rapidly becomes the dominant peak within the waveform, at which time hooking has effectively commenced.

Figure 6-7 shows the derived along-track altimetric WSE profile following retracking using the Improved Threshold Retracker with the sub-waveform selection process developed in Section 5.2.3 using the maximum power peak within the waveform.

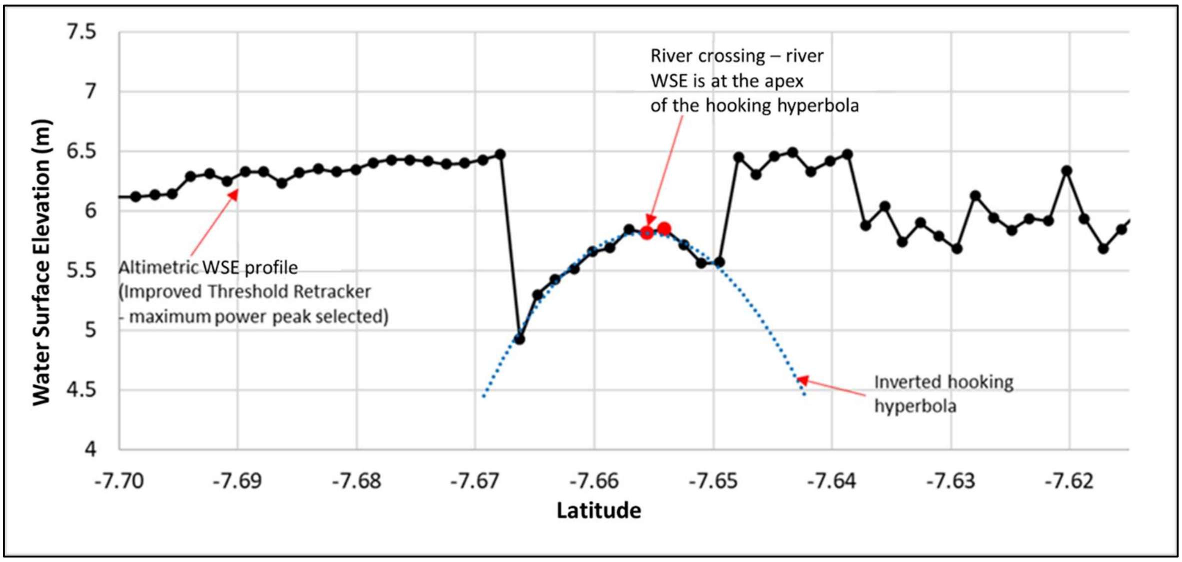

Figure 6-7 The WSE along-track profile from the same SARAL pass shown in Figure 6-4. The waveform data were retracked using the Improved Threshold Retracker with the maximum power peak selected for retracking. This effectively eliminated the low-power nadir return and used the high-power hooked return for WSE definition. The correct WSE is represented by the apex of the hooking hyperbola within the altimetric WSE profile.

This retracking has resulted in an inverted hyperbolic shape within the altimetric WSE profile with the apex of this hyperbola being the valid river WSE. If the first peak is selected, on the basis that it corresponds with the nadir reflection, there is a decrease in the extent of hooking in the execution of the Improved Threshold Retracker. However, the distortion is not eliminated as it is evident in the specular returns closer to the specular reflector where there is essentially no echo in the waveform from nadir. Figure 6-8 shows the results from the Improved Threshold Retracker using the first peak sub-waveform showing a significant reduction in the extent of the distortion. This is an example of hooking that is typical for land–water–land transitions. In many cases, the water component is the only specular reflector in the scene and, as such, is the dominant echo.

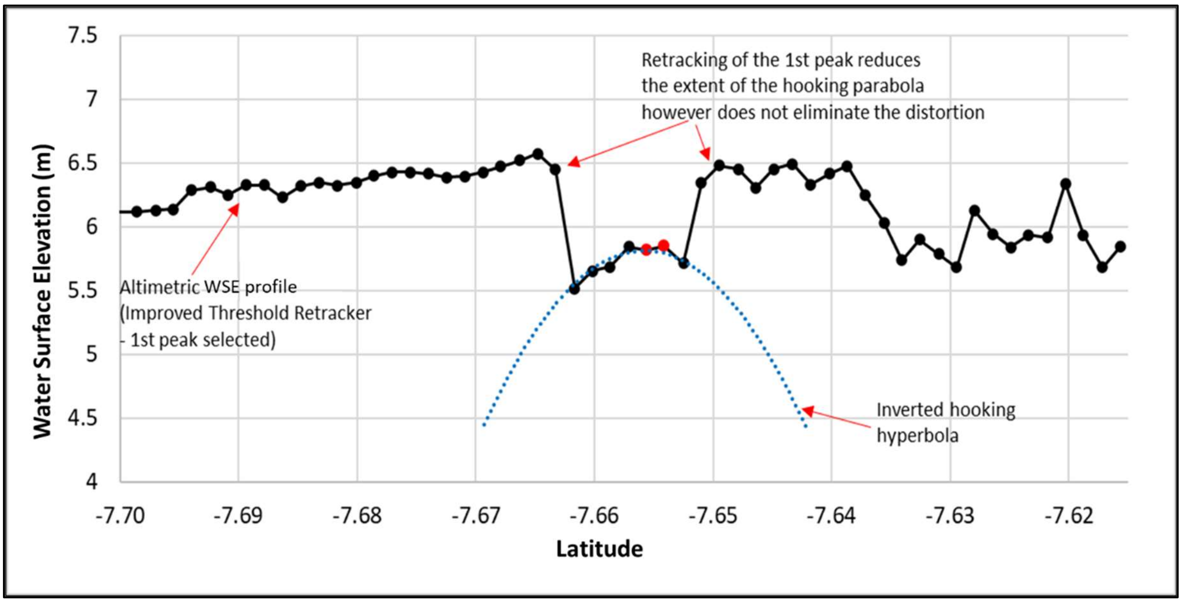

Figure 6-8 The WSE along-track profile from the same SARAL pass shown in Figure 6-4. The waveform data were retracked using the Improved Threshold Retracker with the first peak selected for retracking. While the extent of hooking is reduced compared with retracking using the maximum power peak, the distortion cannot be eliminated from the point where the specular reflector echo becomes quasi-specular with no nadir echo return.

6.1.2.1.2 Land–water transitions for multiple specular reflectors

In the case of multiple specular reflectors within an altimetry footprint, there will likely be a changing hooking location as the satellite passes across the complex wetland or floodplain. Consequently, the classic hyperbolic shape, within both the waveform sequence and the derived altimetric profile, is not evident so the potential to correct for the effect is limited using classical techniques. However, the advantage of a changing hooking location is that the tracking gate is likely to lock onto the closest specular reflector resulting in the magnitude of the error being less than that observed in Section 6.1.2.1.1.

This section contains two examples. The first is where there are numerous potential bright targets and the altimeter is likely to lock onto the closest candidate target. Evidence of hooking within the waveform sequence as well as within the WSE profile will be limited. The second is where part of the zone contains rough water so there is the potential for a hooking signature.

Figure 6-9 is an example of multiple specular reflectors in an altimetry pass. The figure shows select waveforms from an Envisat ascending pass 0677 over the Fly River floodplain acquired on 26 March 2009 during a period of high floodplain inundation.

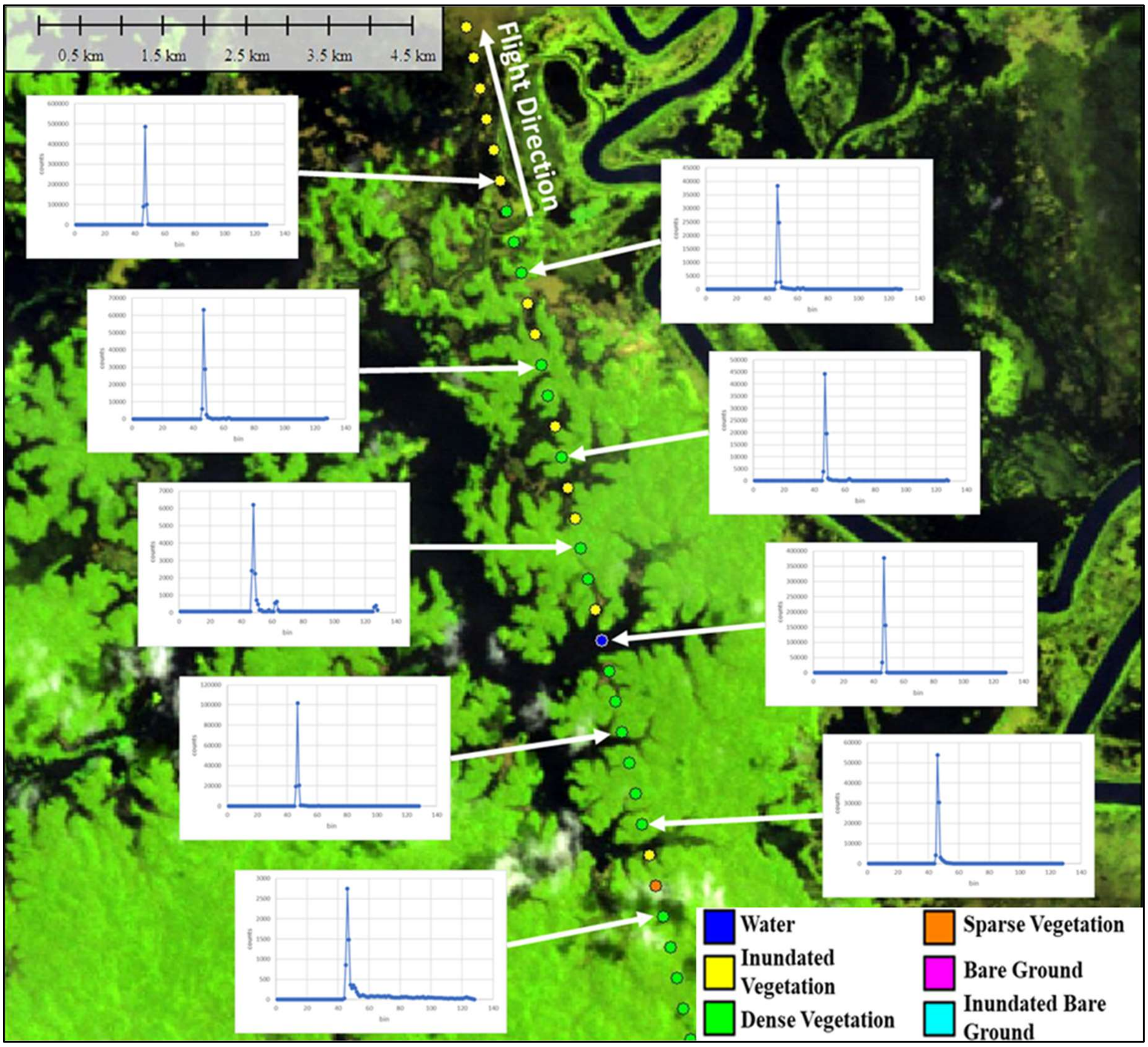

Figure 6-9 Envisat RA-2 waveforms from ascending pass 0677 cycle 102 acquired on 26 March 2009. At the time of the altimetry pass, the floodplain inundation levels were high. The background image is a Landsat TM5 false colour image acquired on 29 March 2009. Hooking has occurred as evidenced by high-powered specular returns over non-inundated sites.

In this case, numerous potential bright targets are evident, and the impact of hooking is unlikely to be resolved. However, the impact on WSE accuracy will be minor as the distance to the specular reflector is likely to be less than the waveform separation distance and the effect will manifest as a minor increase in apparent noise. If the distance is not less than this, then hooking to the same reflector would occur over a sequence of waveforms and a hooking signature in the profiles would be expected.

The pass is adjacent to a blocked-valley lake and a large number of the altimetry nadir footprint classifications are dense forest, with a distance to the nearest water body being less than the along-track waveform separation. All waveforms consist of moderate- to high-powered quasi-specular returns indicating that waveform hooking has occurred. Despite this there is no obvious evidence in the waveform sequence of Figure 6-10 of hooking hyperbolae. With multiple specular reflectors within the sequence it is likely that, while hooking has occurred, it is for a different reflector at each waveform location. While there will be an error due to hooking within the derived WSE profile, the magnitude of the error will manifest as an increase in measurement error rather than as a recognisable systematic hooking signature.

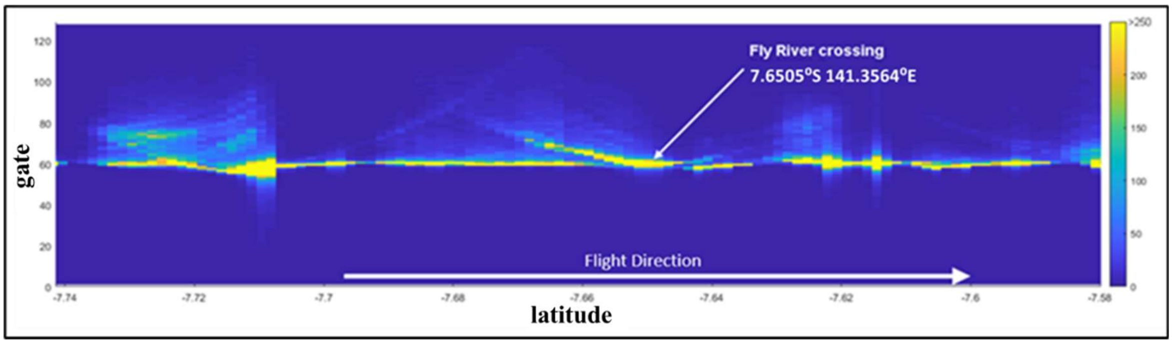

Figure 6-10 The full Envisat RA-2 waveform sequence for the zone covered in Figure 6-9. There is no evidence of hooking hyperbolae within the waveform profile and the majority of waveforms from the headwaters of the blocked-valley lake are characterised by high-powered specular returns.

While there is evidence of a hooking hyperbola leading into the start of the blocked-valley lake system at latitude 7.15ºS, there are no significant systematic effects through the remainder of the sequence other than those that could be attributed to a water level slope between the blocked-valley lake and the Fly River floodplain. The final six waveforms within the sequence are specular returns from the inundated floodplain and have a standard deviation (SD) of ±0.6 cm compared with the SD of the specular returns through the complete sequence of ±4 cm.

The derived altimetric WSE profile for the sequence defined in Figure 6-9 is shown in Figure 6-11.

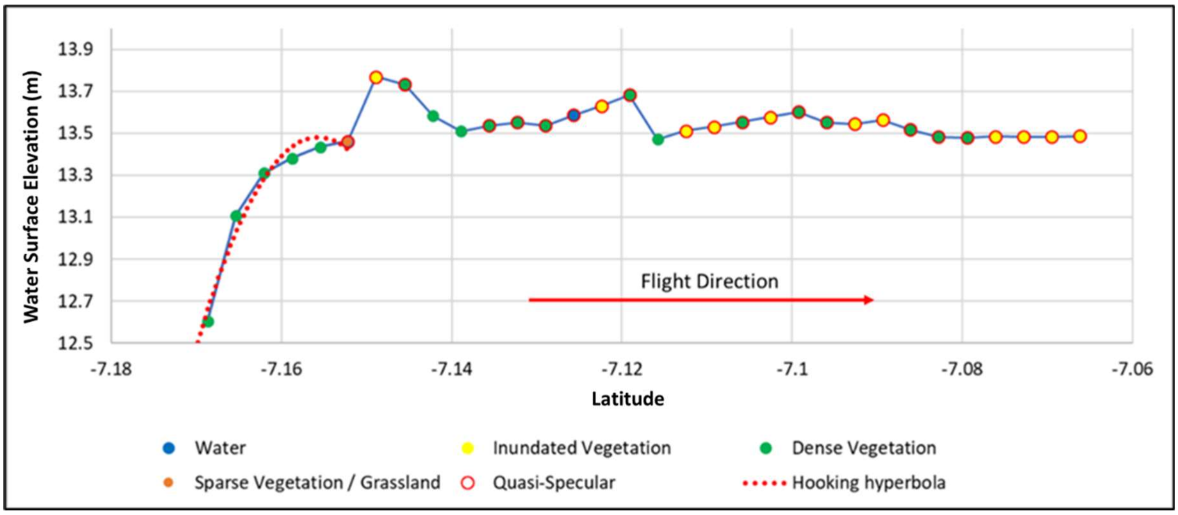

Figure 6-11 The derived altimetric WSE profile for the zone covered in Figure 6-9. The markers on the WSE profile are consistent with those in Figure 6-9 and show the classification of the nadir altimetry footprint. There is evidence of a hooking hyperbola within the profile leading into the headwaters of the blocked-valley lake but there is no readily apparent systematic effect through the remainder of the profile.

Figure 6-12 shows an example where numerous specular reflectors are interspersed with zones of rougher water, creating the potential for a contaminated WSE profile.

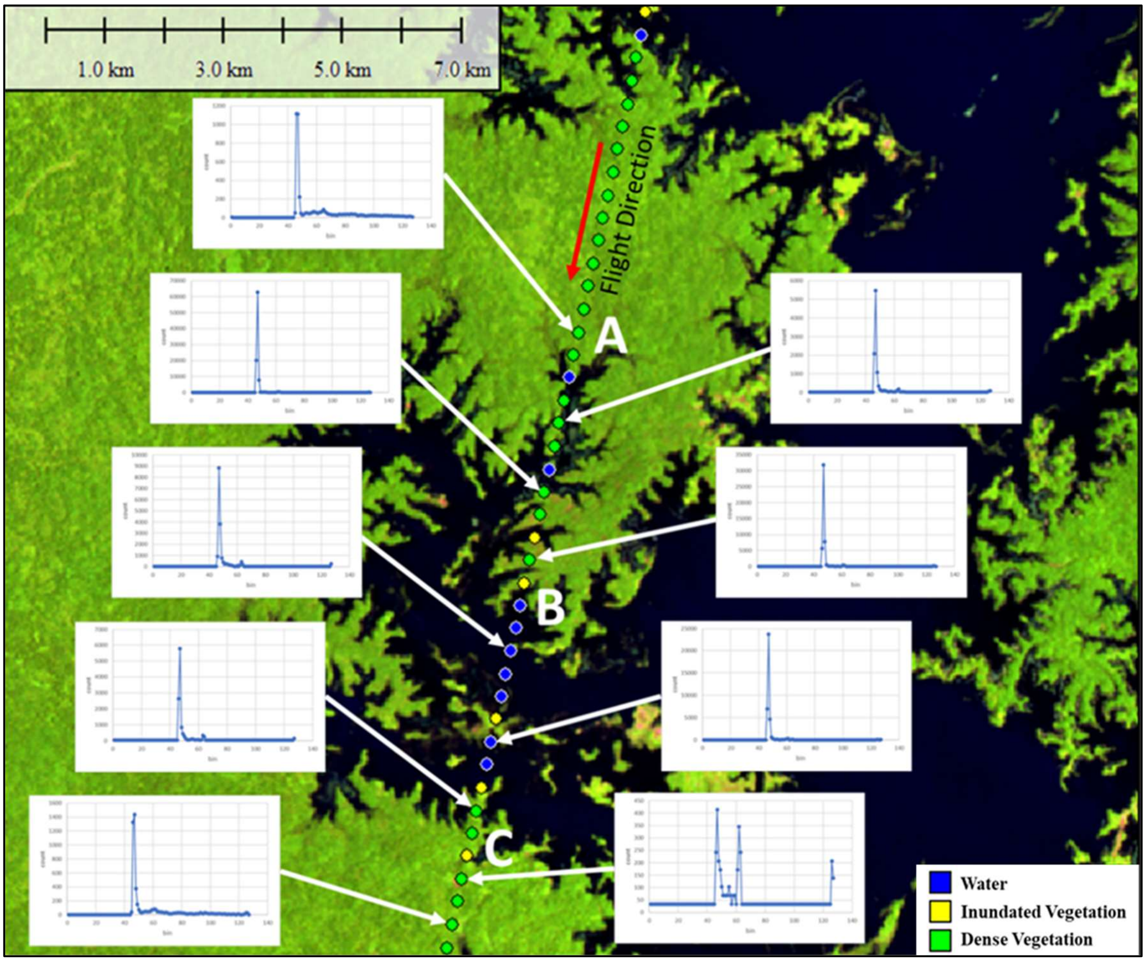

Figure 6-12 Envisat RA-2 select waveforms from descending pass 0004 cycle 102 acquired on 26 April 2011. The background image is a Landsat TM5 false colour image acquired on 12 February 2004 with inundation levels consistent with those of the altimetry pass. Locations A–C identify the main transition zones that will impact waveform shape and magnitude.

In Figure 6-12, a selection of Envisat RA-2 waveforms is plotted. For the zone adjacent to the lake (between A and B in Figure 6-12) the majority of waveforms are quasi-specular, including those with a dense vegetation altimetry footprint. However, in most cases, the distance to the nearest likely calm water location is less than the waveform separation distance. Based on this, while hooking is likely to occur, the magnitude will not be significant with a maximum off-nadir distortion in the zone leading into the main lake crossing estimated to be less than 7 cm. The mix of calm and rough water zones (between B and C in Figure 6-12) is likely to impact the WSE profile with small but systematic hooking biases that will require omission of waveforms from the final waveform sequence to achieve acceptable WSE quality.

The SAR image of Figure 6-13, while not temporally consistent with the altimetric data shown in Figure 6-12, demonstrates the potential for significant water surface roughness over much of the pass, with calm water zones limited to the land–water interface zone and in sheltered inlets.

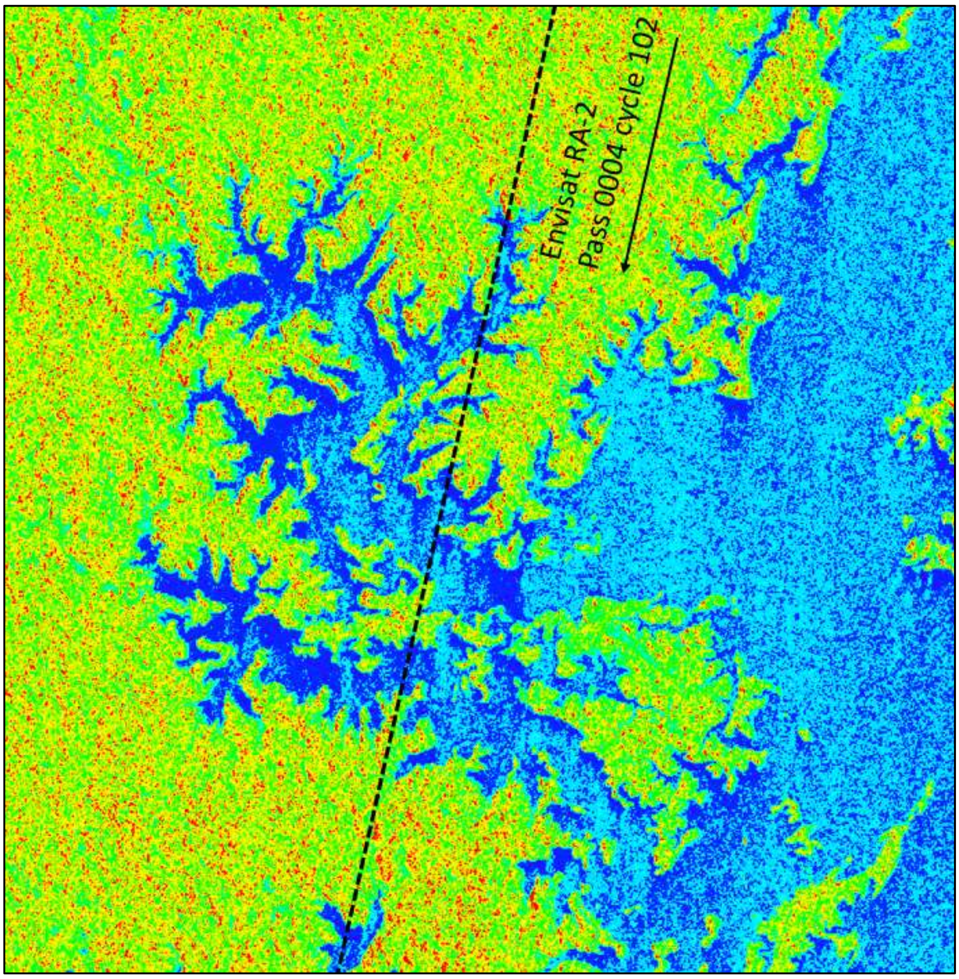

Figure 6-13 The track of the Envisat pass shown in Figure 6-12 as an overlay on a Sentinel-2 SAR image (VV polarisation) over Lake Murray acquired in August 2019. Zones of calm water are shown in dark blue and zones of rough water, characterised by an elevated SAR backscatter coefficient, are light blue.

The waveform sequence of Figure 6-14 shows no evidence of hooking hyperbolae within the waveform profile; however, there is a distinct mix of waveform shape and magnitude evident in the sequence. Locations A–C are shown in Figure 6-12 and identify three distinct zones. Leading into A, the altimeter passes over a zone of dense vegetation with the waveforms being predominantly multi-peaked and likely to be impacted by hooking. Zone A–B passes along the edge of a minor inlet where calm water is likely to dominate and this is reflected in the quasi-specular waveforms with no evidence of significant hooking. Zone B–C contains the main inlet crossing where quasi-specular waveforms result from the land–water interface and lower-powered multi-peak waveforms are acquired of the actual open water zone.

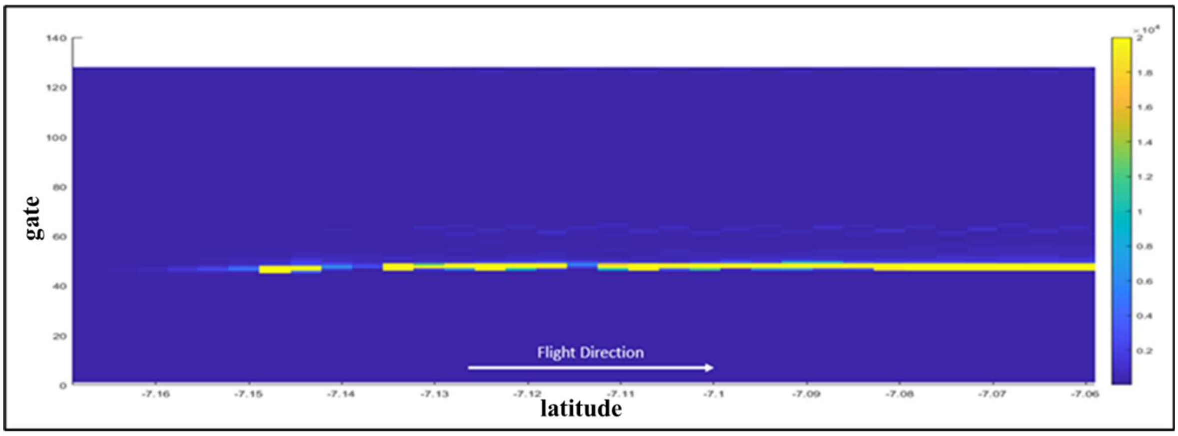

Figure 6-14 The full Envisat RA-2 waveform sequence for the zone covered in Figure 6-12. There is no evidence of hooking hyperbolae within the waveform profile, although the waveforms leading into the lake zone (A) are multi-peaked. There is a relatively even mix of lower-powered multi-peaked waveforms and moderate- to high-powered quasi-specular returns through the remainder of the coverage.

The derived altimetric WSE profile for the zone covered in Figure 6-12 is shown in Figure 6-15. Hooking hyperbolae are seen leading into the lake system but there is no major systematic effect through the remainder of the profile. Minor effects are evident through the crossing of the main water body with small systematic profiles evident at the 10-cm level, which are likely to represent portions of hooking hyperbolae related to bright targets at the land–water interface where calm water would be expected. This is supported by the observation that waveforms located at the centre of the water crossings are multi-peaked and have either hooked to the land–water interface or are contaminated by the adjacent land. The SD of specular returns for the sequence is ±6.2 cm and a result of this magnitude indicates that there is likely to be minor unresolved hooking associated with various bright targets through the sequence.

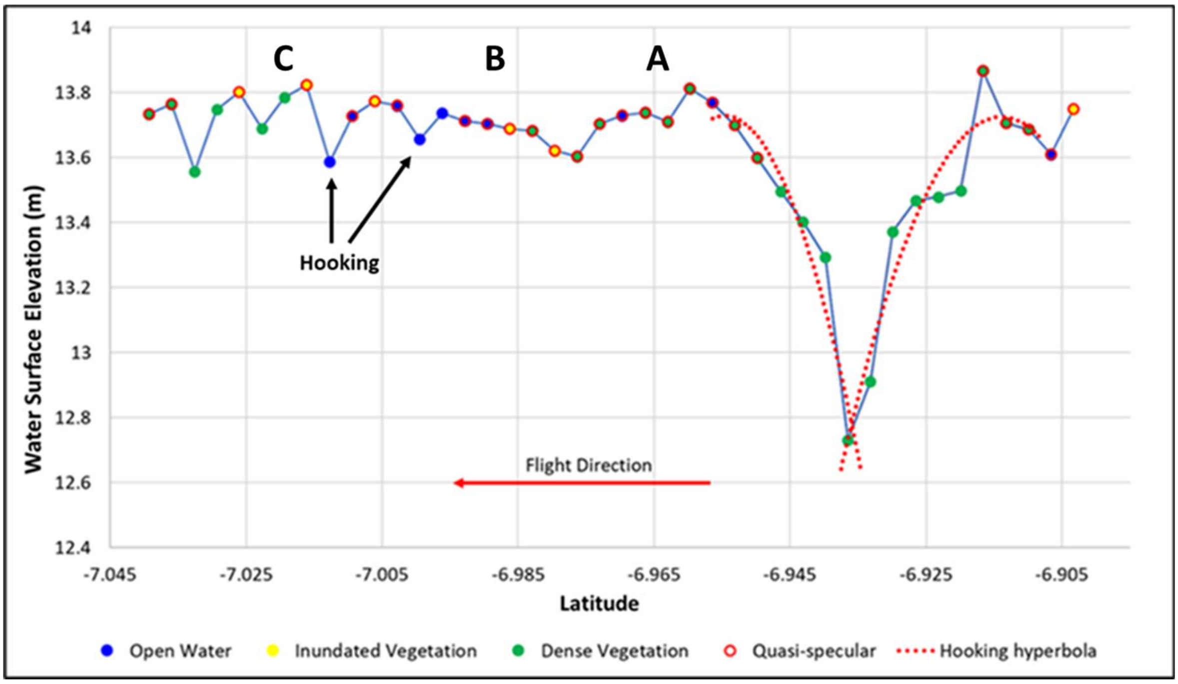

Figure 6-15 The derived altimetric WSE profile for the zone covered in Figure 6-12. The markers on the WSE profile are consistent with those in Figure 6-12 and show the classification of the nadir altimetry footprint. There are two edges of significant hooking hyperbolae leading into the lake system and a mix of minor systematic effects of approximately 10 cm in magnitude through the rest of the sequence. These systematic effects contribute towards a SD of ± 6.2 cm for the WSE estimates located between A and C, as defined in Figure 6-12. Locations of minor hooking at the centre of the water crossings are identified in the figure.

Distortion rectification using the hooking hyperbolae within an altimetric profile to accurately correct for hooking distortion is not always a simple and unambiguous process. Even if there is only a single specular reflector, WSE sequences used to define the hyperbolae can be contaminated by secondary effects that make the definition of the apex subjective. This is illustrated in Figure 6-15 where both WSE sequences that define the hooking hyperbolae leading into the backwater zone of Lake Murray have secondary contamination, particularly evident in the first (northern) sequence.

6.1.2.2 Water transitions

Where the satellite pass is over a water body with both calm and rough water states, hooking can occur in the transition from a body of rough water to a body of calm water or vice versa. The distortion occurs when the satellite passes over the rough water zone, but the on-board tracking system is dominated by off-nadir specular reflectors in the calm water zones within the altimeter footprint.

Wind that affects a body of water will result in a rough water surface, and this will usually occur through the central zones of large lakes or towards the centre of larger rivers, particularly if the wind is opposing the current flow. In zones where there is shielding from wind (e.g. close to the water–land interface) or in zones where aquatic vegetation grows close to the water surface, there is likely to be a dampening of the wind impact and a large reduction in surface roughness compared with open water. It is the edges of these zones that offer a bright source and the potential for off-nadir distortion.

Figure 6-16 shows zones of calm and rough water on the Fly River. This duality of surface roughness over the same water body occurs predominantly where the flow is into the prevailing wind and gives rise to a condition where off-nadir distortion is likely.

Figure 6-16 A photograph taken from the bank of the Fly River with demarcation of a calm water zone located adjacent to the levee and a rough zone at the centre of the 300-m-wide channel where the current is strongest.

Inland water bodies tend to be relatively smooth, and in SAR imagery most of the energy is reflected away from the radar with only slight backscatter towards the radar. Water bodies generally have a dark tonality on radar images, except in the case of wind stress or current increasing the water surface roughness and generating high backscatter (ESA, 2020b).

Figures 6-17 and 6-18 are Sentinel-2 SAR images based on vertical transmit-and-receive (VV) polarisations. Light blue zones identify areas of significant surface roughness and SAR backscatter while dark blue zones define locations of relatively calm water, which are candidate hooking targets for the altimeter. In Figure 6-17 zones of high SAR backscatter on the river are visible in reaches where the flow is into the prevailing wind, predominantly from the south-east. Reaches of the Fly River that flow in a westerly direction are generally calm while easterly draining reaches are characterised by extensive zones of rough water.

Large portions of the water surface of Lake Murray are affected by high SAR backscatter as illustrated in Figure 6-18. Altimetry passes over the lake will be subjected to significant off-nadir distortion as numerous calm water zones are located within protected inlets of the lake.

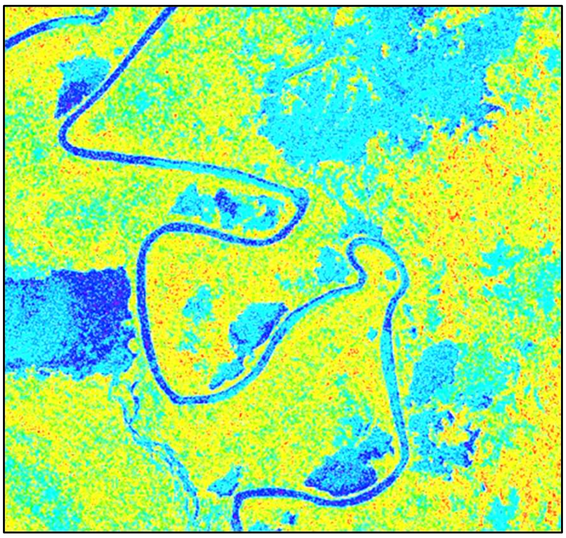

Figure 6-17 Sentinel-2 SAR image (VV polarisation) acquired over the Fly River in August 2019. Zones of calm water are shown as dark blue while zones of rough water with elevated SAR backscatter are in light blue. Where the river flows into the south-east prevailing wind, elevated SAR backscatter is evident.

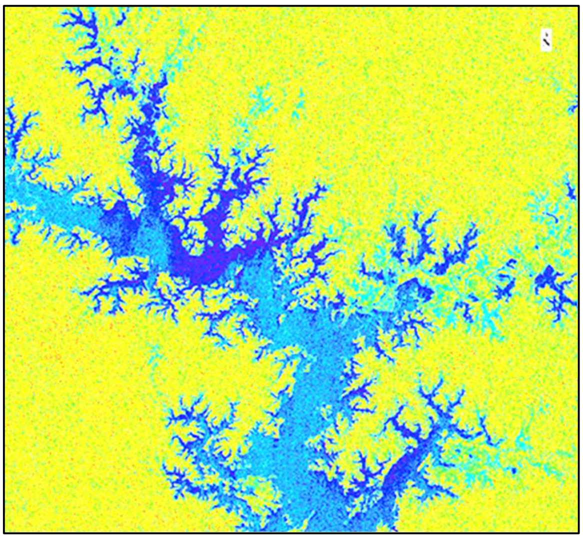

Figure 6-18 Sentinel-2 SAR image (VV polarisation) acquired over Lake Murray in August 2019. Zones of calm water are shown as dark blue while zones of rough water characterised by elevated SAR backscatter are in light blue.

Hooking that occurs in a water transition of the altimeter can be difficult to identify, and methods for the accurate correction of the distortion are limited as the location of the bright source is unknown with numerous possible hooking locations within the altimeter footprint. Without the ability to identify and correct for off-nadir distortion the analysis requires statistical methods to be used to assess the probability of valid heights being derived (Berry, 2006; Dettmering et al., 2016). Using this methodology, waveforms are retained if they have a significant leading edge and sufficient power. However, this means that most waveforms through the central zones of larger rivers and lakes, where surface conditions are likely to be wind affected and consequently rough, are omitted and the WSE is determined from a limited number of quasi-specular returns at the water–land interface.

Figure 6-19 shows a descending Cryosat-2 SIRAL (LRM) pass acquired 13 June 2012 tracking over a 2.5-km section of Lake Murray. The figure identifies the location of specular waveforms that were recorded and the classifications of the altimetry footprints. The majority of waveforms recorded during the water transition are relatively low-power multi-peaked waveforms. Quasi-specular waveforms acquired leading into and from the water crossing will contain a residual hooking distortion as they are not acquired over water. However, the distance to the nearest likely calm water source is less than the waveform separation distance and the distortion error is estimated to be less than 7 cm. As there are numerous calm water sources evident, the distortion is unlikely to have a signature in the derived WSE profile as the hooking location will change as the altimeter passes.

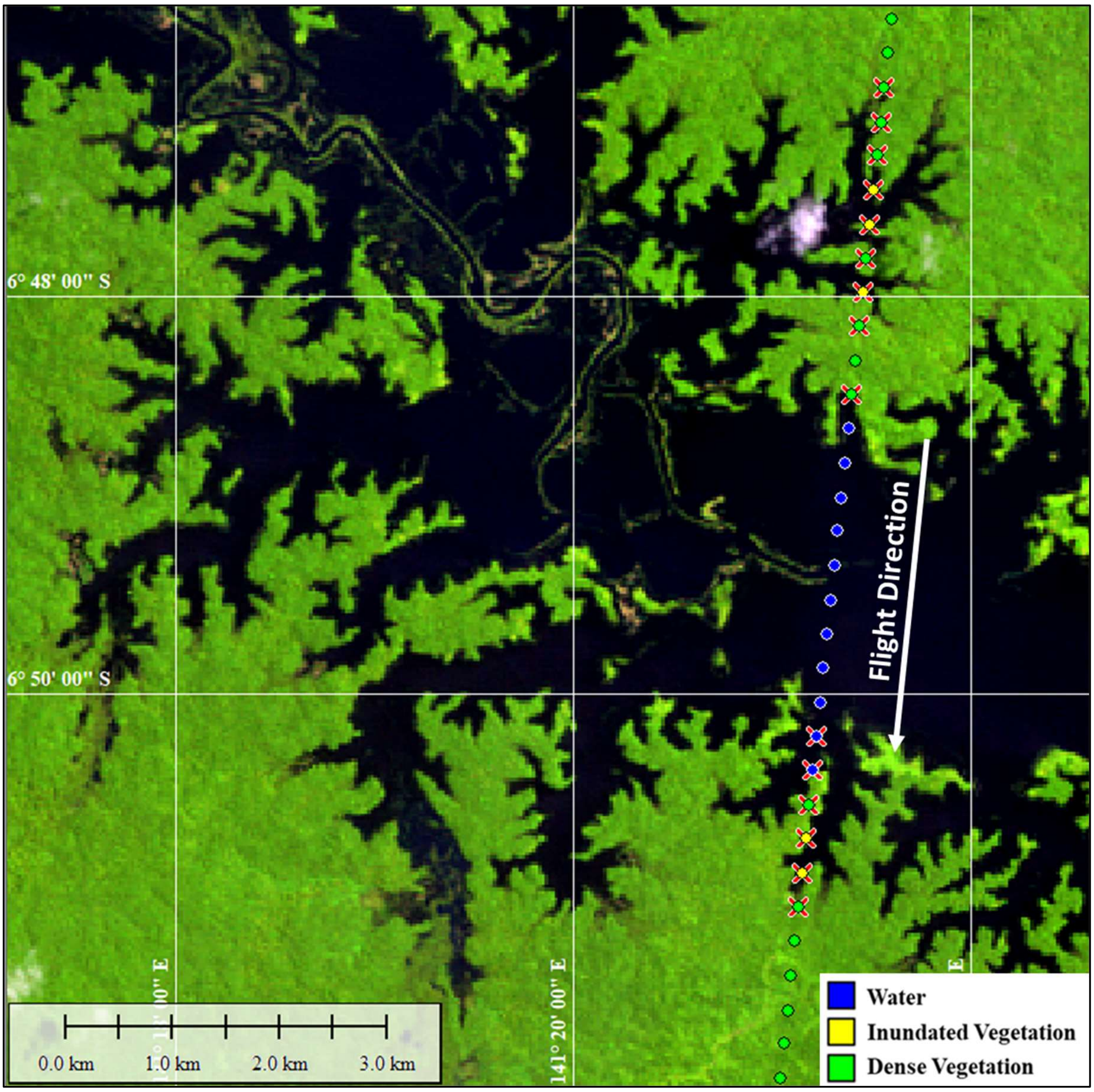

Figure 6-19 Cryosat-2 descending LRM pass over Lake Murray acquired on 13 June 2012 during a period of median inundation. The background image is a false colour Landsat TM5 image acquired on 29 March 2009 during similar inundation levels. Specular returns are highlighted with a red cross.

Figure 6-20 presents the altimetric WSE profile derived for this sequence and shows several hooking events. There is evidence of minor hooking in the land–water transition zones and a relatively significant event in the water transition. The hooking is characterised by two halves of hooking hyperbolae with the altimeter switching from a specular reflector on the northern shoreline of the lake to the southern shoreline at approximately the midpoint of the transition. This water transition event is relatively easy to identify and to rectify using the methodologies detailed in Section 6.1.1 or using the methodology developed in Chapters 4 and 5 whereby predicted WSEs derived from the calm water zones at the edges of the lake are used to select sub-waveforms and identify if there is a nadir water return.

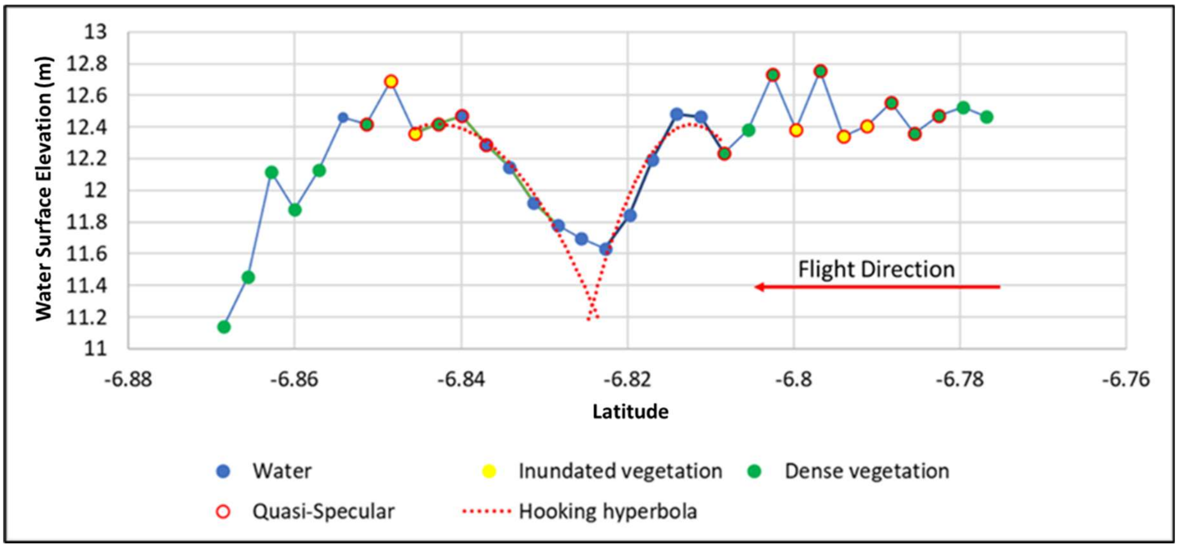

Figure 6-20 The altimetric WSE profile derived for the coverage shown in Figure 6-19. Hooking during the water transition is characterised by two halves of hooking hyperbolae, identified over the open water zones, where the altimeter switched from tracking bright targets on the northern shoreline to bright targets on the southern shoreline at approximately the midpoint of the water transition.

Water transition hooking is typically more complex than the above example, with the impact of hooking difficult to identify and accurately rectify. In the example in Figure 6-21, a Cryosat-2 SIRAL pass with a water transition over an 8-km section of Lake Murray is shown, although the lateral width is significantly less with landforms within 1 km.

As expected, for larger water bodies where the central zones are likely to be impacted by wind, the specular returns leading into the lake become multi-peaked and the backscatter coefficient decreases significantly, although there remains a series of specular returns at the centre of the lake. While it is possible that specular returns over open water are nadir returns, it is unlikely that such an extensive zone of calm water exists at nadir and it is likely that the returns have hooked into small calm water patches on the lake surface or lateral zones of calm water at the land–water interface.

In assessing open water transitions, the derived WSE profile and the magnitude of the backscatter coefficient provide input into the extent of any off-nadir distortion. The WSE profile for this example is shown in Figure 6-22, where waveforms exhibiting a quasi-specular form are highlighted. As the altimeter approaches the lake it passes through a likely calm water zone from 6.916ºS to 6.900ºS. This assessment is based on the waveforms being quasi-specular, having a high backscatter coefficient and being located at the land–water interface. The SD of the five WSE estimates is ±0.5 cm. As the satellite passes over open water the WSE estimates become increasingly noisy through the remainder of the transition; however, the WSE profile contains no evidence of hooking biases.

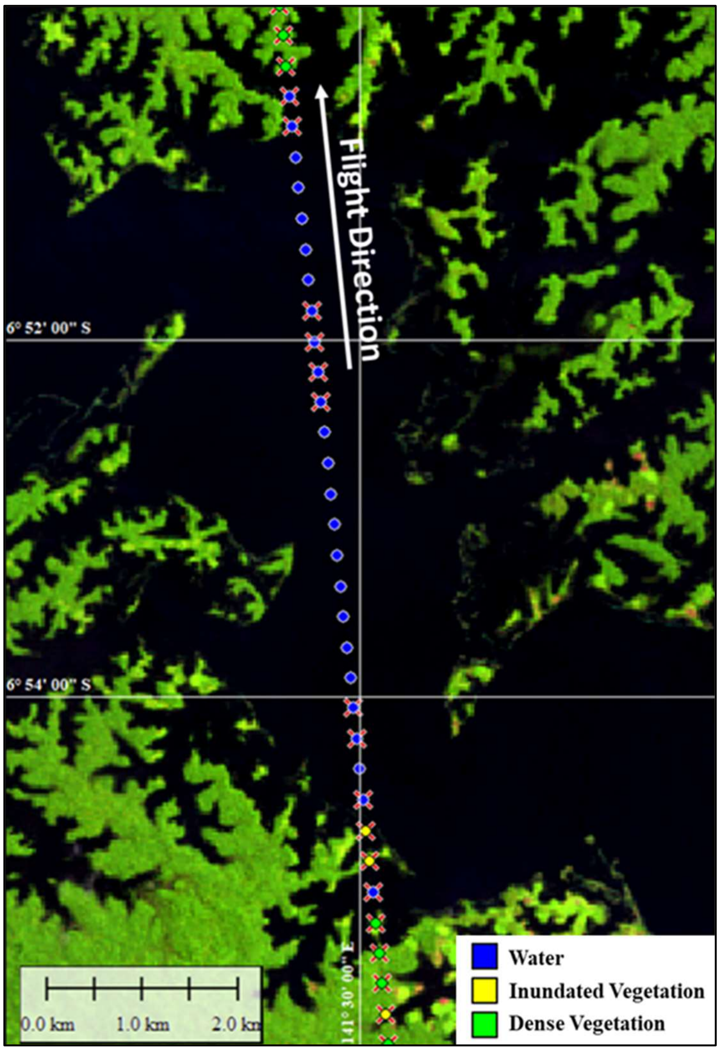

Figure 6-21 Cryosat-2 ascending LRM pass over Lake Murray acquired on 7 March 2011 during a period of high inundation. The background image is a false colour Landsat TM5 image acquired 4 April 2011. Specular returns are highlighted with a red cross.

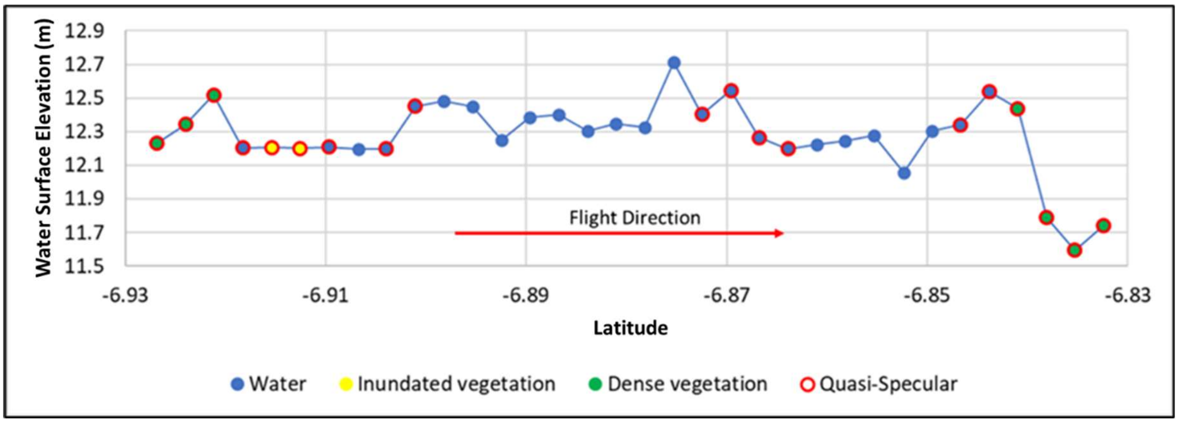

Figure 6-22 The altimetric WSE profile for the coverage shown in Figure 6-21. A quasi-specular specular sequence leading into the lake through a predicted calm water zone demonstrates consistency in derived WSE estimates. Through the open water zones, the derived WSEs exhibit increased noise with no evidence of systematic hooking. Quasi-specular waveforms located towards the centre of the lake likely originate from a small calm water zone in close proximity to the pass.

While there is no evidence of major hooking hyperbolae within the altimetric profile, and no evidence of any hooking to calm water zones at the land water interface, a minor hooking event through the sequence of quasi-specular waveforms located at 6.867ºS has been identified. This hooking is likely due to a small calm water zone along track, identified on the basis of an elevated backscatter coefficient for each waveform and a minor hooking hyperbola within the altimetric WSE profile. While it is atypical for waveforms through open water zones to be quasi-specular unless they have hooked into distant specular reflectors, the above example illustrates that such waveforms require extensive evaluation to confirm whether they have hooked to the calm zones at the land–water interface or are valid nadir returns from calm water zones located mid-lake. Upon rectification of the hooking distortion the resulting SD for the water surface WSE was ± 3 cm with a predicted water surface gradient of 1.2×10^{-5} over the 8-km water transition section of the lake. This was based on retracking of 46% of the available waveforms, with 14 being discarded for failing quality criteria with respect to unresolved hooking and other waveform contamination and one being discarded in the outlier detection phase.

The importance of the backscatter coefficient for deriving quality WSEs over water transitions, where there is little supporting information to be derived from the altimetric footprint classification, is illustrated in the example of Figure 6-23. The lake, covering an area of approximately 25 km^2, is located at the southern end of the study area. At lower-than-average inundation levels, the extent of aquatic vegetation covering the southern half of the lake is evident. The altimetric footprint classification identifies the zone of open water at the northern half of the lake. The altimetry data were retracked using the Threshold Retracker and the resulting WSE and backscatter coefficient profiles are shown in Figure 6-24.

The WSE profile derived using the Threshold Retracker for the coverage is shown in Figure 6-23. Within the lake crossing zone there are two distinct features of the WSE profile. Through the northern open water zone, a drop in the backscatter coefficient is evident, indicating increased surface roughness. There is evidence of characteristic hooking hyperbolae; however, these cannot be used as the apex of the hyperbolae are contaminated by saturated waveforms. Through the southern zone the backscatter coefficient is high, indicating a specular reflecting surface. However, only the waveforms circled in red can be confirmed as being unaffected by waveform saturation and originating from a calm water reflector without significant hooking contamination. The resulting SD of the WSE definition was ± 3.7 cm. This example emphasises the importance of the backscatter coefficient, in conjunction with the altimetric footprint classification, for directing the WATeR retracking process in selection of valid waveforms that contribute to the averaged lake WSE estimate.

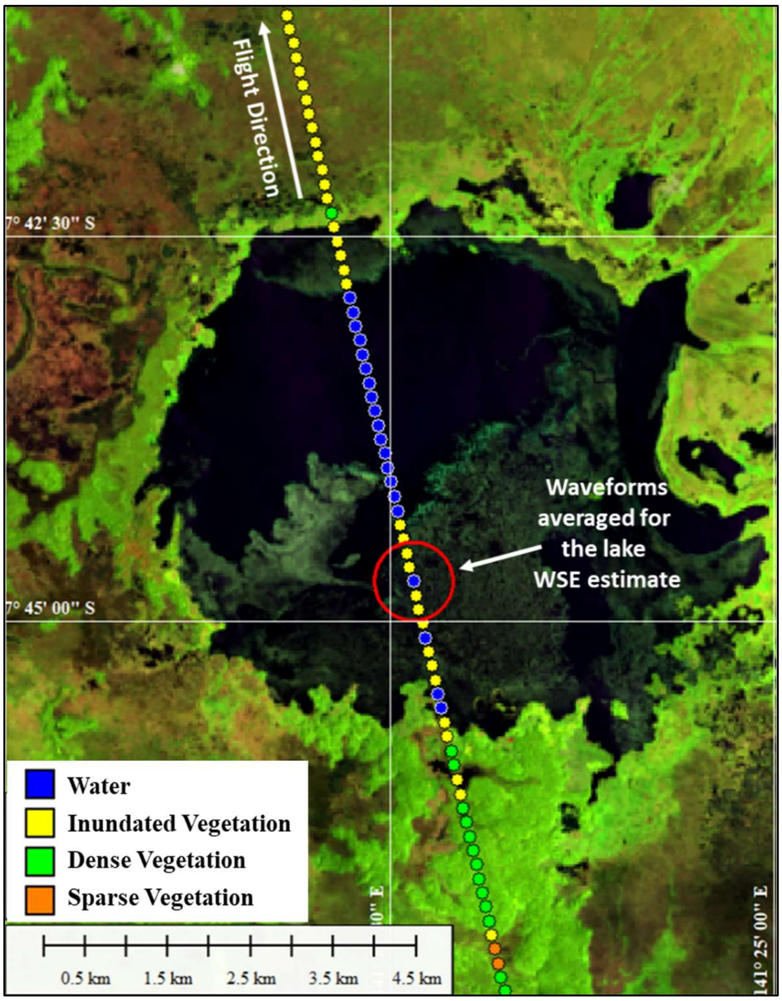

Figure 6-23 SARAL/AltiKa ascending pass 0677 cycle 24 acquired on 20 June 2015. The waveforms identified within the red circle are those that are used by the WATeR altimetry retracking process for the averaged lake WSE. The background image is a Landsat OLI8 false colour image acquired on 25 January 2015.

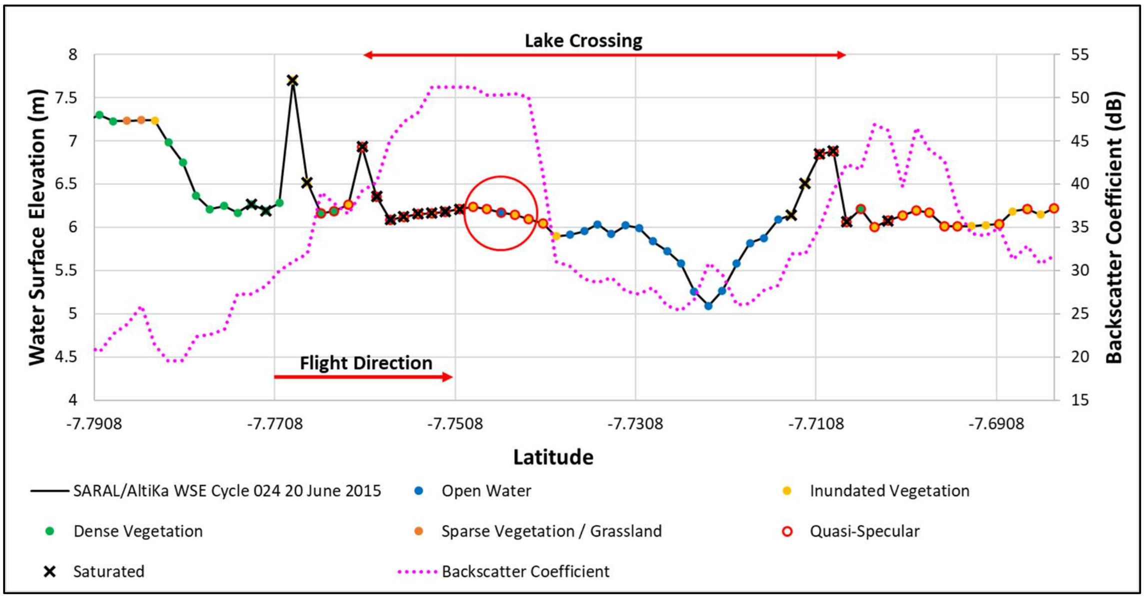

Figure 6-24 The WSE profile derived using the Threshold Retracker for the coverage shown in Figure 6-23. For the lake crossing there are two parts to the WSE profile. The northern zone has a low backscatter coefficient, indicating increased surface roughness, and the southern zone has a high backscatter coefficient, indicating a specular reflecting surface. Only the waveforms circled in red can be confirmed as being unaffected by waveform saturation and originating from a calm water reflector without significant hooking contamination.

In this study, specular waveforms located within open water bodies are retracked and included in the data sequence but are flagged for review. If the derived WSE is consistent with WSEs derived from calm water zones or if hooking is evident, and hooking hyperbolae exist in the WSE sequence so that the distortion can be removed, the waveform is retained. If the WSE cannot be derived in this manner the waveform is omitted from the sequence if the estimated magnitude of the hooking distortion, assuming hooking to the predicted closest calm water location, is likely to degrade the quality of the WSE profile. In the case where there is no clear hooking signature in the altimetric WSE profile to correct for the distortion, as the predicted calm water location is identified by geographical coordinates, it is possible to utilise the range to the bright target in the equations of Section 6.1.1 to determine a WSE for an off-track location. The possibility of using this approach is targeted for future research.

6.2 Waveform saturation

Waveform saturation distortion occurs when there are specular reflectors within the altimetric footprint through a zone of highly variable scattering (Verron et al., 2018) and the antenna gain control loop within the altimeter is not rapid enough to follow the high backscatter shifts that occur leading into a zone of high reflectance. The waveform then saturates the power recording window (Bouzinac, 2010; Zakharova et al., 2015). Of the three altimeters used in this study, only SARAL/AltiKa exhibits waveform saturation distortion over the study area, with occurrences at most calm water targets. Occurrences of waveform saturation have not been observed in either the Envisat RA-2 or Cryosat-2 SIRAL data used in this study. Echo saturation flags are included with the Cryosat-2 SIRAL SGDR data record and have been included in the waveform retracking phase undertaken in this study so that waveform quality can be assessed. However, analysis of the waveform structure and shape is required for Envisat-RA2 and SARAL/AltiKa to determine saturation extent. Waveform saturation occurring when there is a dominant specular reflector within the altimetry footprint typically corrupts what would have been a quasi-specular waveform. Saturation can also occur in multi-peaked waveforms where the first return is saturated but valid secondary peaks follow. The result of waveform saturation in SARAL/AltiKa is that the formation of the saturated peak is terminated at count 1250. The number of gates affected is a function of the strength of the echo returned from the specular reflector. Saturation typically affects one or two gates; however, it has been observed to affect as many as 11 gates. Figure 6-25 is an example of a SARAL/AltiKa saturated waveform comprising a single peak saturated at count 1250 extending over four gates. Figure 6-26 shows a

SARAL/AltiKa saturated multi-peaked waveform comprising an initial peak saturated at count 1250 extending over two gates and a secondary peak terminating at count 1249.

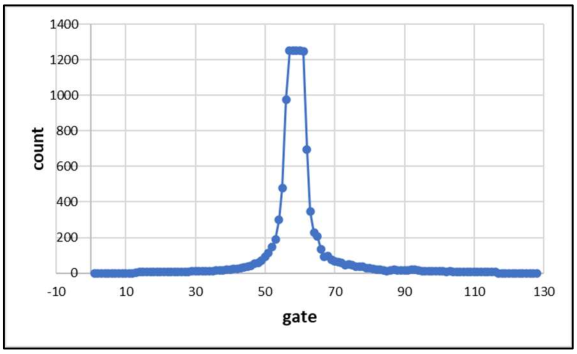

Figure 6-25 A SARAL/AltiKa saturated waveform consisting of a single peak saturated at count 1250 extending over four gates.

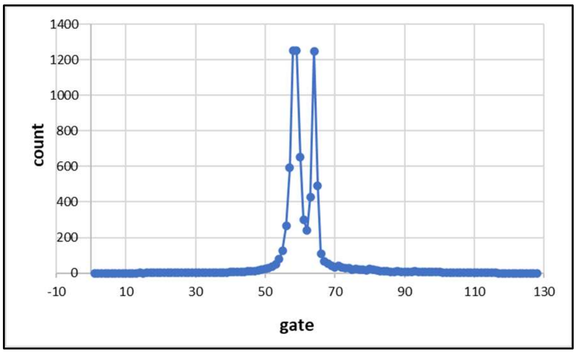

Figure 6-26 A SARAL/AltiKa saturated multi-peaked waveform consisting of an initial peak saturated at count 1250 extending over two gates and a secondary peak terminating at count 1249.

Zakharova et al. (2015) report that approximately 10% of waveforms are lost in sea ice applications but this can reach 20% in some cases. In the 34 SARAL cycles of pass 0677 acquired between April 2013 and June 2016 over the study area, 23% of waveforms contained saturated returns at count 1250. This comprised a significant proportion where only a single gate was impacted, with the overall impacted percentage dropping to 6% if only saturation of two or more gates was considered. Ghosh et al. (2015) adopt a methodology in retracking where waveforms whose count is greater than 1250 are omitted.

An assessment of the impact of saturation was undertaken by processing waveforms using the Threshold Retracker and assessing the derived WSEs compared with return echoes that were specular but not saturated. An example of this is in Figure 6-27 where SARAL cycle 001 from ascending pass 0677 is shown along with the locations of the saturated SARAL/AltiKa waveforms. Saturation occurs near potential specular reflectors where quasi-specular waveforms are typically acquired from other altimeters.

Using the non-saturated specular waveforms as a reference, the difference in derived WSE compared with the saturated waveforms is determined to be a function of the number of gates affected, with the WSE derived from the saturated waveform being greater than that from the reference. The difference from the reference WSE ranges from 0.1 to 0.2 m for two-gate saturation to approximately 0.8 m for four-gate saturation. As there are cases where this correlation is poor, it is likely that additional factors, including possible hooking effects, affect the magnitude of the distortion.

Investigations have been made in this study to reconstruct the waveform by projecting the shape of the leading and trailing edge to an intersection and then reprocessing using the Threshold Retracker; however, this process did not account for the magnitude of distortion required. Because of the magnitude of the observed errors in WSEs derived from the SARAL/AltiKa saturated waveforms, the WATeR retracking methodology adopted in this study omits waveforms with two or more saturated gates from the analysis and flags waveforms with a single saturated gate for review in the statistical validation following retracking. It has been shown in this study that saturated waveforms with a secondary non-saturated peak (as shown in Figure 6-26) can still be used in the sub-waveform selection process and so these waveforms are retained irrespective of extent of the saturated peak.

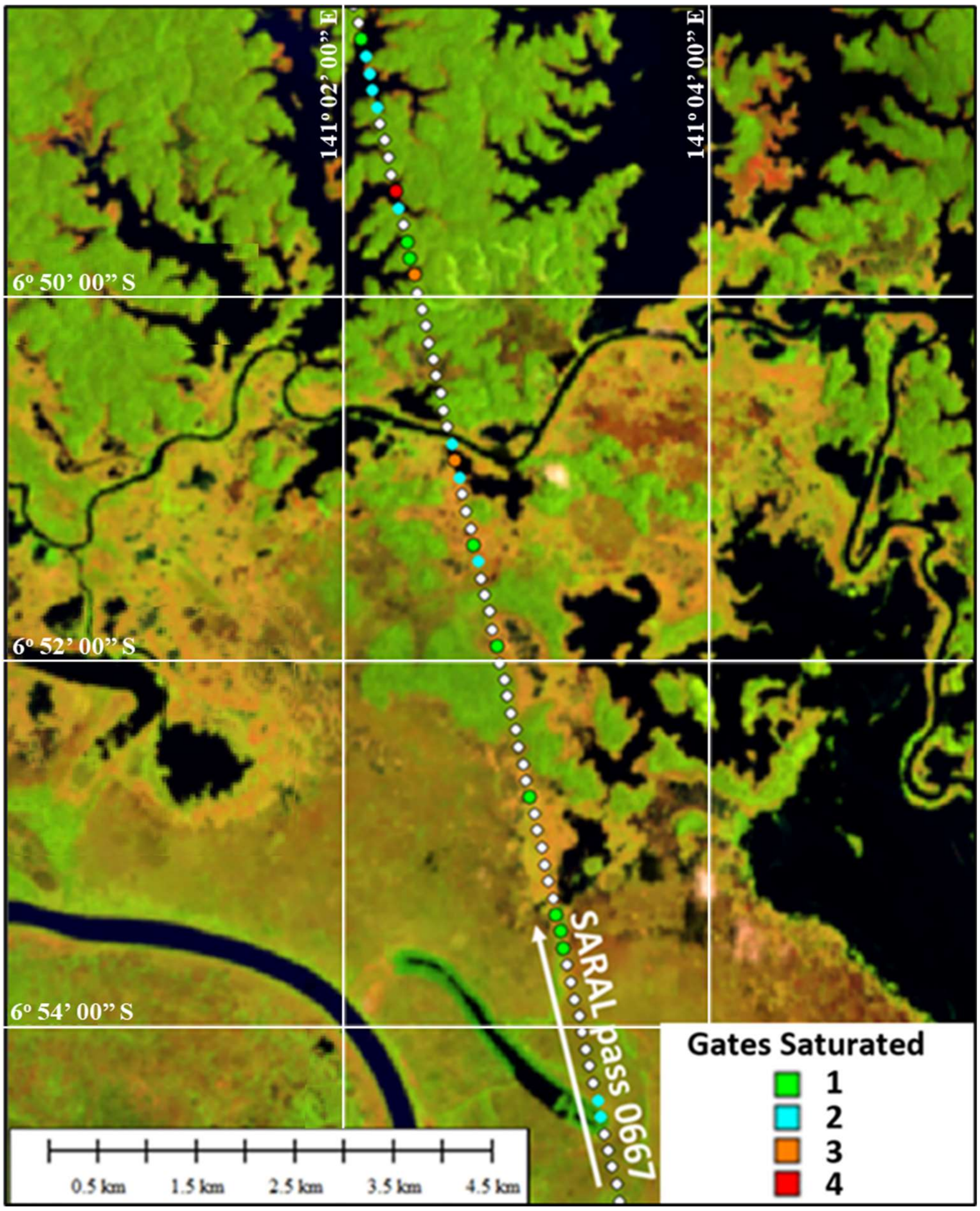

Figure 6-27 SARAL cycle 001 from ascending pass 0677 on 6 April 2013 as an overlay on a Landsat LC8 false colour image acquired in February 2014 under similar inundation conditions. The locations of the saturated SARAL/AltiKa waveforms are highlighted.

Figure 6-28 shows the derived WSE profile from the SARAL cycle 001 altimetry pass, highlighting WSEs derived from saturated waveforms as well as the location of non-saturated quasi-specular waveforms. All saturated waveforms exhibit an increase in WSE compared with adjacent quasi-specular, but unsaturated, waveforms. The WSE increase is not consistent, however, with up to 40-cm difference between waveforms with the same number of saturated gates. It is hypothesised that some saturated waveforms are compounded by other waveform distortions, including hooking distortion, which means this will be a complex distortion to rectify. Waveforms with a single saturated gate can have a derived WSE that is consistent with quasi-specular unsaturated estimates and will be retained in the retracking process but flagged for review in an outlier detection phase.

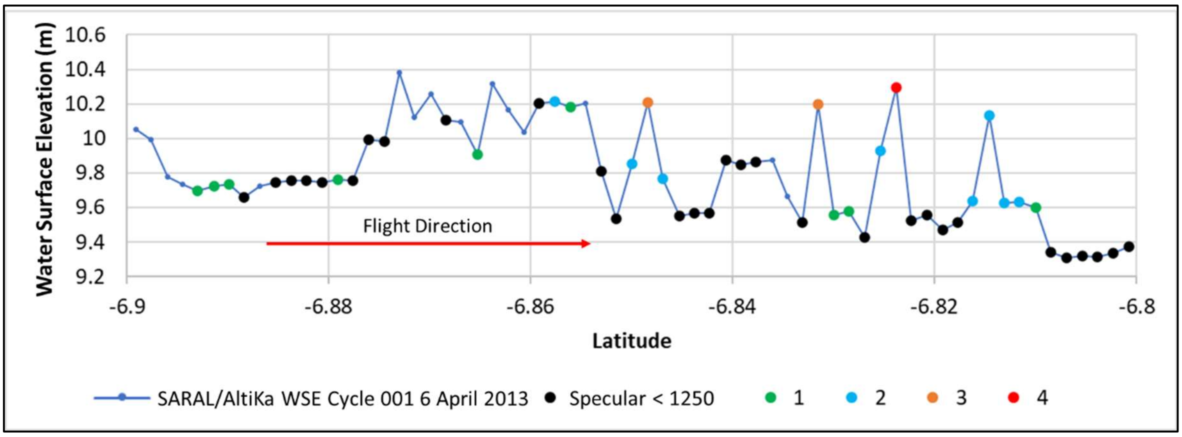

Figure 6-28 The derived WSE profile from the altimetry pass shown in Figure 6-27 highlighting WSEs derived from saturated waveforms as well as the location and WSE of non-saturated specular waveforms. The number of gates affected in the saturated waveforms is also shown.

6.3 Waveform averaging

While waveform averaging is technically not a distortion it manifests as a distortion under certain conditions, particularly for low water level crossing of small water bodies or rivers. Echo averaging for Envisat RA-2, SARAL/AltiKa and Cryosat-2 SIRAL is undertaken at 18 Hz, 40 Hz and 20 Hz respectively. The number of IEs used in each averaged waveform is 100, 96 and 91 with averaging over a distance of approximately 370 m, 170 m and 320 m for Envisat RA-2, SARAL/AltiKa and Cryosat-2 SIRAL respectively. The resulting averaged waveform shape is a not only a convolution of up to 100 IEs; there are contributions from multiple specular reflectors within each IE altimetry footprint. For locations where there is significant terrain slope there is likely to be a blurring of the averaged waveform as a function of the total movement of the range window over the averaging sequence (Roca et al., 2007).

Select bursts of IEs are recorded and transmitted to ground-based receiving stations. This permits comparison between the shape characteristics of the individual waveforms and the resulting averaged waveform and for an assessment of how this averaging impacts the derived WSEs (Berry et al., 2007a; Roca et al., 2007; Berry et al., 2012; Quartly and Passaro, 2014; Abileah et al., 2017). The studies over inland waters were concentrated on quasi-specular waveforms with the aim of understanding biases in the specular echoes (Roca et al., 2007) and how well the averaged waveform reflects the IEs in the averaging window. It was found that a difference of up to 4 cm in the derived WSEs was possible due to the blurring effect within the range window and because the averaging process itself introduces errors in both the position and power of each sample (Roca et al., 2007). Both Berry et al. (2012) and Abileah et al. (2017) found that narrow rivers and lakes were readily identifiable from the IEs. However, using averaged waveforms resulted in identification of such targets being lost in the averaging process. A recommendation for future altimetry missions is to incorporate the ability to recover information at a far higher rate along track so that small inland water targets are not lost (Berry et al., 2007a).

The process by which altimeters generate waveforms can lead to distortion because of under sampling and aliasing (Smith and Scharroo, 2015). Zero padding the digital samples prior to range Fourier transform is reported to reduce the problem. However, access to waveform IEs would eliminate the problem if each echo's complex amplitude were interpolated to double its sampling rate (Smith and Scharroo, 2015).

As IEs are not available over the study area used in this thesis, neither the effect of averaging nor aliasing are directly assessed. While these distortions cannot be effectively rectified from the averaged record, it is important to understand the limitations of averaged waveforms when undertaking waveform retracking and deriving WSEs over inland water bodies.

6.4 Summary

In this chapter, the predominant distortions that impact altimetric waveforms acquired over inland waters are identified and discussed. One of the first waveform distortions to be identified was that introduced by the presence of land within the altimeter footprint, resulting in altimeters having difficulty in retrieving data, particularly over rough terrain (Benveniste and Berry, 2004; Berry et al., 2005a; Berry, 2006). Schwatke et al. (2015b) identified that land contamination within the altimetric waveform could lead to multiple reflections resulting in degraded range quality and potentially unusable data. The study domain for this thesis is characterised by extensive and complex wetland and floodplain environments where the topographic range is relatively small. This flat topography means that there is no significant shadowing of the water body in the altimetric footprint, resulting in less risk in the altimeter losing lock (Boergens et al., 2016). For wetland environments multi-peaked waveforms are still likely when land is evident in the altimetric footprint. However, the correct sub-waveform for retracking can usually be identified via the methodology detailed in Section 5.2.3 using a priori WSE estimates from adjacent waveforms.

Hooking has been recognised as one of the most significant and problematic distortions affecting the altimetry echo (Benveniste and Berry, 2004; Berry, 2006). The magnitude of the hooking distortion is most severe over inland water zones where there is a single dominant off-nadir specular reflector within the altimetric footprint; however, this is also the simplest scenario to rectify. This form of hooking results in a single dominant inverted hyperbolic shape within the retracked WSE profile with the correct WSE being at the apex of the WSE profile. Methods for the identification and rectification of hooking of this nature are documented in numerous publications including Frappart et al. (2006) and Santos da Silva et al. (2010).

Over heterogeneous inland waters there are likely to be multiple specular reflectors within the altimetric footprint with the altimeter switching between off-nadir reflectors with passage across the wetland environment. The magnitude of the hooking distortion is typically less than that of a single off-nadir specular reflector and it is not uncommon for no systematic inverted hyperbolic shape to be evident in the retracked WSE profile. While magnitude is less, the potential for identification of the hooking source and derivation of an uncontaminated WSE is less likely. It is for this reason that the published accuracy of altimetry WSE results for wetland and floodplain environments is significantly lower than those reported in the larger river and lake studies (Frappart et al., 2006; Santos da Silva et al., 2010; Zakharova et al., 2014; Maillard et al., 2015; Villadsen et al., 2016).

The impact of hooking and methodologies for identification and rectification focussed on altimetric acquisitions within complex wetland and floodplain environments have been addressed in this chapter. Altimetry footprint identification methods developed in Chapter 4, along with the WATeR altimetry retracking process developed in Chapter 5, assist with the identification of waveforms that are contaminated by hooking, with either rectification or omission of the waveform as a function of the extent of the estimated hooking distortion. This process leads to improved accuracy in derivation of the resulting WSE time series.

Waveform saturation has been shown to introduce a distortion into the derived WSE time series. Extensive waveform saturation has been observed in SARAL/AltiKa waveforms through zones where bright surface reflectors dominate but this has not been observed in the study area in Envisat RA-2 or Cryosat-2 SIRAL data. While it has been identified that the magnitude of distortion in a derived WSE is correlated with the number of waveform gates affected, it was observed that this is not a linear relationship and additional distortions, such as hooking, have a compounding impact. As such, saturated waveforms are omitted from analyses in this study with a recommendation that additional research be undertaken in this area.

Waveform averaging is technically not a distortion; however, the averaging does affect how representative is the waveform of the altimetric nadir footprint. This is particularly the case where data are acquired at low water levels over a narrow river crossing. IEs over the water surface will be valid but, when averaged with IEs originating from the exposed banks, lead to an averaged waveform for which a valid WSE cannot be accurately extracted. At high water levels, the WSE of the river will approximate that of the adjacent floodplain and so any apparent distortion will be minor.

In this study, systematically elevated WSE estimates compared with the in-situ reference have been observed for estimates derived from the averaged waveform acquired for narrow river crossings under low flow conditions. It is hypothesised that this is related, in part, to the waveform averaging process. In the absence of IE data over the study area, the magnitude of any waveform-averaging distortion has not been quantified for these crossings.

CHAPTER 7: WATeR—RETRACKING VALIDATION AND RESULTS

In this chapter, the results derived from the WATeR retracking methodology for several diverse locations on the Fly River floodplain and over Lake Murray are presented. Where possible, results are compared with data from an in-situ reference for validation of the process. The quality of these in-situ references is estimated and documented so that the altimetry results can be assessed in context.

Retracking validation analysis and comparison with in-situ WSE time series has been undertaken using Envisat and SARAL descending pass 0004 and ascending pass 0677 along with Envisat descending pass 0004 (new orbit). A 369-day repeat cycle Cryosat-2 ascending pass that tracks through the lower-middle Fly floodplain has also been used. The passes used in the validation are shown in Figure 7-1 along with WATeR retracking validation locations.

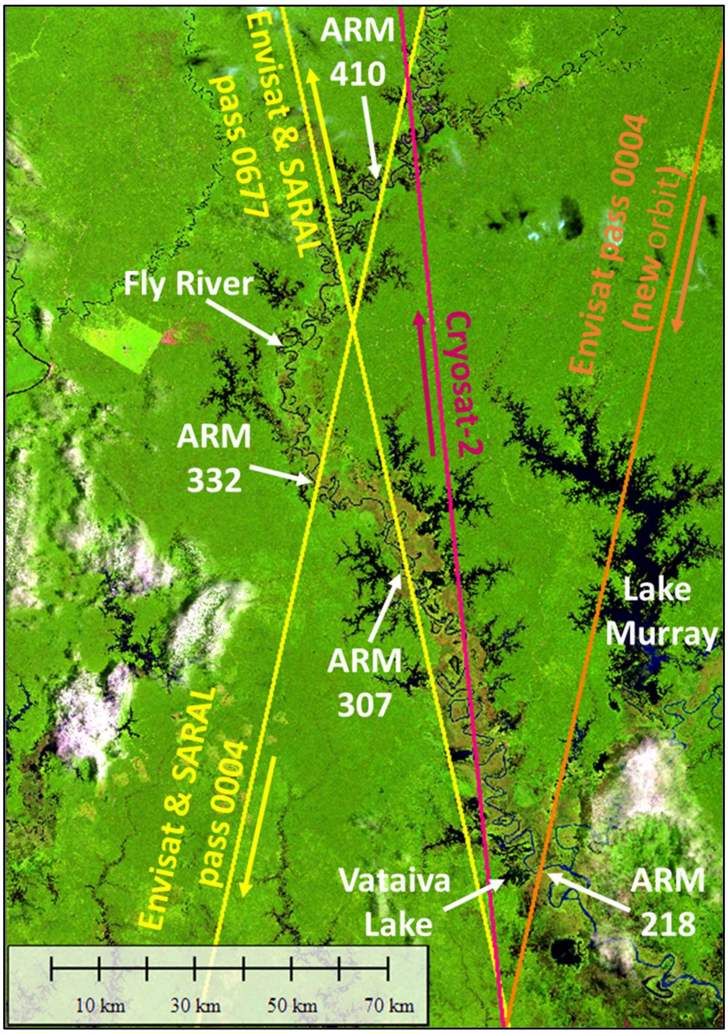

Figure 7-1 Satellite altimeter passes over the study area. Validation is undertaken using Envisat and SARAL passes 0004 and 0677, as well as Envisat pass 0004 (new orbit). WATeR retracking validation sites are ARM218, ARM307, ARM332 and Vataiva Lake. In-situ gauge locations are shown in Figure 3-1.

A key aspect of the retracking methodology is the selection of cloud-free imagery that covers the inundated floodplain within the study area and is representative of the full range of predicted floodplain inundation and river WSE. For this thesis, seven relatively cloud-free Landsat images have been selected with acquisition dates between October 2002 and September 2015. The image acquisition dates have been correlated with the in-situ gauge record for FLY17 at Manda and each image has been assigned a representative inundation range. Figure 7-2 is a plot of the FLY17 river WSE time series covering the period mid-2001 to early 2016. The river level range has been broken into high, median and low flow conditions, as identified in Figure 7-2, with image scenes assigned to the different flow ranges as a function of WSE at the time of capture. The portion of the inundation range defined as extreme low flow is also identified in Figure 7-2. Although other gauges within the network could have been used for this referencing, FLY17 was chosen as it supplies a relatively complete river level record and is located towards the centre of the study area.

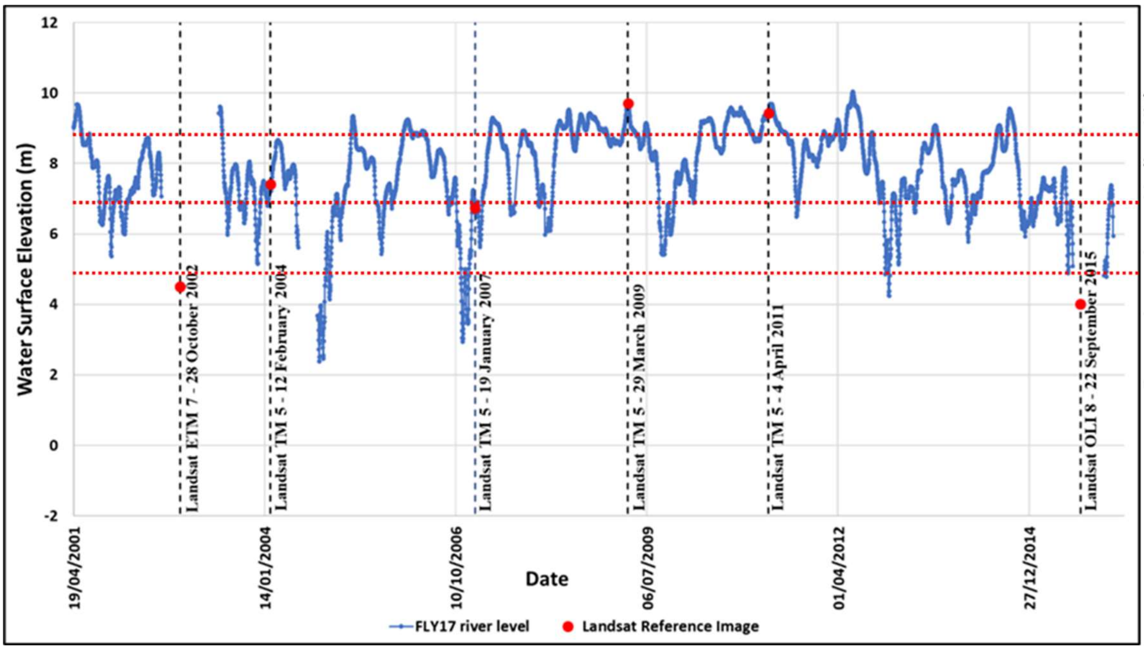

Figure 7-2 Fly river water WSE time series derived from the FLY17 in-situ gauge at Manda, located in the approximate centre of the study area. Relatively cloud-free Landsat images have been identified and their capture date and associated river WSE at the time of capture identified on the plot. The WSE range has been broken into high, median and low flow conditions, as identified by the dotted red lines, with image scenes assigned to the different flow ranges as a function of river level elevation at the time of capture. The plot shows that the majority of the expected inundation range is covered by the imagery. Extreme low flow conditions occur infrequently during extended drier-than-average periods, including during El Niño climatic events.

Table 7-1 documents the Landsat scenes used in the retracking process along with acquisition dates and assigned inundation ranges. The images are radiometrically calibrated and balanced with three-band false colour composite scenes created from the MIR, NIR and red bands.

Table 7-1 Cloud-free Landsat scenes along with acquisition date and assigned inundation range for use in the altimetry footprint classification phase of the WATeR altimetry retracking process. Secondary scenes are used in the event of cloud or cloud shadow detected at the altimetry footprint location.

Satellite	Image	Inundation conditions	FLY17 river level (OHD)	Comments
Landsat OLI8	22 September 2015	Extreme Low	<5 m	El Niño
Landsat ETM7	28 October 2002	Low	5–7 m	
Landsat TM5	19 January 2007	Median	7–9 m	
Landsat TM5	12 February 2004	Median	7–9 m	Secondary
Landsat TM5	29 March 2009	High	>9 m	Pass 0677 and Envisat pass 0004 (new orbit)
Landsat TM5	4 April 2011	High	>9 m	Pass 0004

The false colour image scenes used for altimetry footprint classification in the WATeR altimetry retracking process are shown in Figures 7-3–7-8. Primary scenes have been identified and are used for all classifications, excluding locations where cloud or cloud shadow is evident at the altimetry footprint location, where the secondary image is used. Where there is no a priori estimate of river level the median flow scene, which covers the majority of the inundation period, is used for classification.

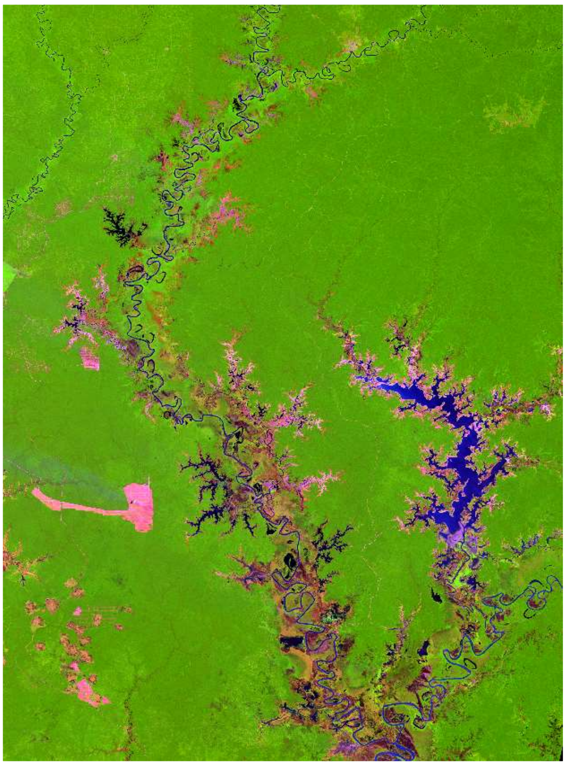

Figure 7-3 Landsat OLI8 22 September 2015—extreme low flow primary footprint classification image (El Niño conditions).

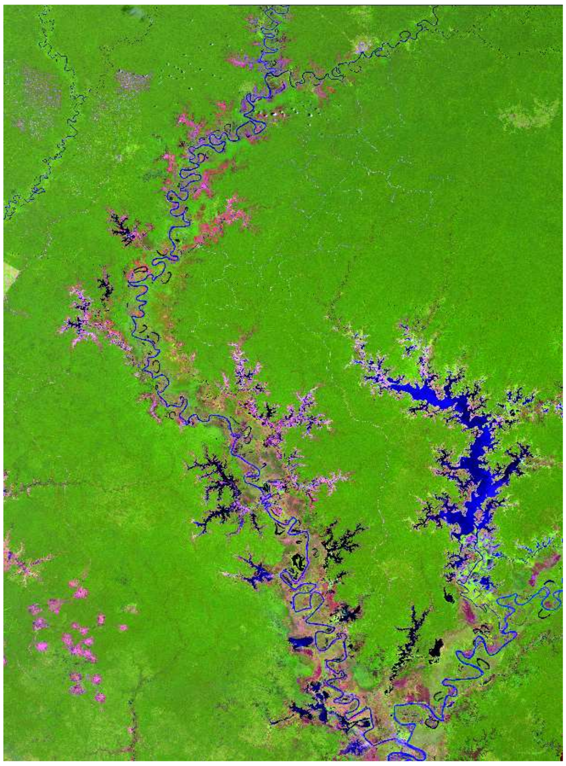

Figure 7-4 Landsat ETM7 28 October 2002—low flow primary footprint classification image.

Figure 7-5 Landsat TM5 19 January 2007—median flow primary footprint classification image.

Figure 7-6 Landsat TM5 19 January 2007—median flow primary footprint classification image.

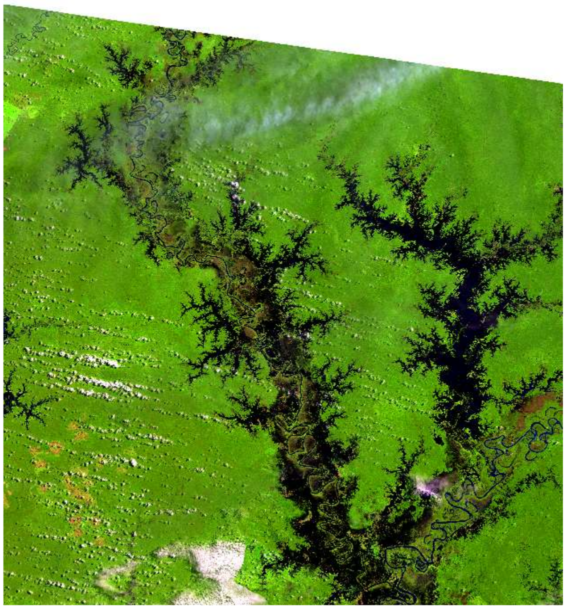

Figure 7-7 Landsat TM5 29 March 2009—Envisat and SARAL pass 0677 and Cryosat-2 high flow footprint classification image.

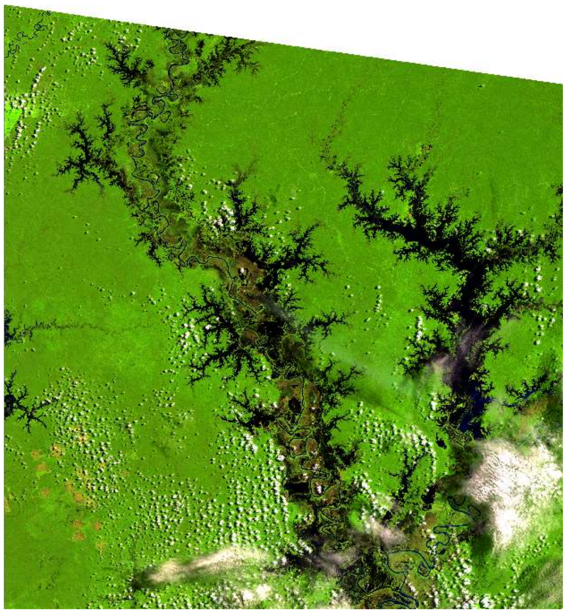

Figure 7-8 Landsat TM5 4 April 2011—Envisat and SARAL pass 0004 and Envisat pass 0004 (new orbit) high flow footprint classification image.

While additional imagery could be added to WATeR's image library to reduce the impact of temporal variability between scenes, this would require sub-scene extraction to ensure cloud-free imagery was available. This could have readily been implemented if the inundation range was not adequately defined by the available image library.

To complement these data, the Fly River in-situ WSE record, as introduced in Section 3.2, has been supplied OTML (1963–2020) and used for the WATeR retracking validation in this chapter. The locations of all gauges in the network are shown in Figure 3-1.

The number of altimetric observations used to derive a WSE is dependent on the location of the altimetric pulses and the size of the water body being assessed. For the purposes of assessing data quality, it is desirable to have multiple observations from which a single WSE is derived. This is implemented in the results derived in this chapter, unless a rigorous outlier detection process dictates otherwise, even if a minor hooking distortion contaminates the results from observations located at the water body limits. The quality of the WSE time series derived in this chapter is examined via an assessment of precision, using the SD of the observations derived from the average WSE estimate and the individual observations, as well as via an assessment of accuracy, where the RMSE between the average WSE and an external reference is derived. The SD is a relative representation of data quality, specifically a measure of the spread of WSE observations about the mean, while the RMSE provides an estimate of quality with respect to an absolute external reference. As a significant number of validation studies presented in this chapter are based on a virtual gauge, a rigorous assessment of virtual gauge accuracy has been undertaken so that the results of the altimetric validation can be assessed in context. The virtual gauge accuracy contains a contribution associated with the distance of the altimetric site from the in-situ site, as well as the estimated in-situ gauge accuracy itself, estimated to be 10 cm (Clews, 2014; OTML, 1963–2020).

Bed aggradation surveys have been undertaken at 105 sites throughout the middle Fly on an annual basis since 1998 as part of OTML's bed aggradation monitoring program (Marshall, 1998–2020). At each site, a cross-section of the river is surveyed, covering the backswamp zone, the levees and the river channel. Sites at ARM410, ARM332, ARM307 and ARM218 are in close proximity to the altimetry crossings used in this study and this facilitates the calibration of virtual WSE gauges at the sites derived from the in-situ gauge network. Surveyed WSEs are used to transform the in-situ gauge and, as the transformation is derived from over 20 measurements, a quality indication of the virtual gauge under the various flow conditions is also derived. The overbank elevation is the elevation at which floodplain inundation occurs; although inundation will result from levee breaches and tributary flow, it is predominantly related to overbank flow. The estimate of overbank elevation derived in these surveys is used in this study as a guide to indicate the possible floodplain inundation extent and consequently the probability of hooking, particularly for river crossings.

7.1 River water surface elevation validation and results

7.1.1 Envisat pass 0004 Fly River crossing—ARM332

Chapter 1 documents the current capabilities for inland WSE measurement from satellite altimetry. Table 1-1 lists the global databases for river and lake WSE, although there are few sites located within the Fly River study area. An exception is the Hydroweb database (http://hydroweb.theia-land.fr/), which includes one site on the Fly River, at 6.854ºS and 140.914ºE. The Envisat RA-2 altimetry data for the period 2002–10 were processed with WSEs derived and published. The resulting Hydroweb WSE time series is shown in Figure 7-9.

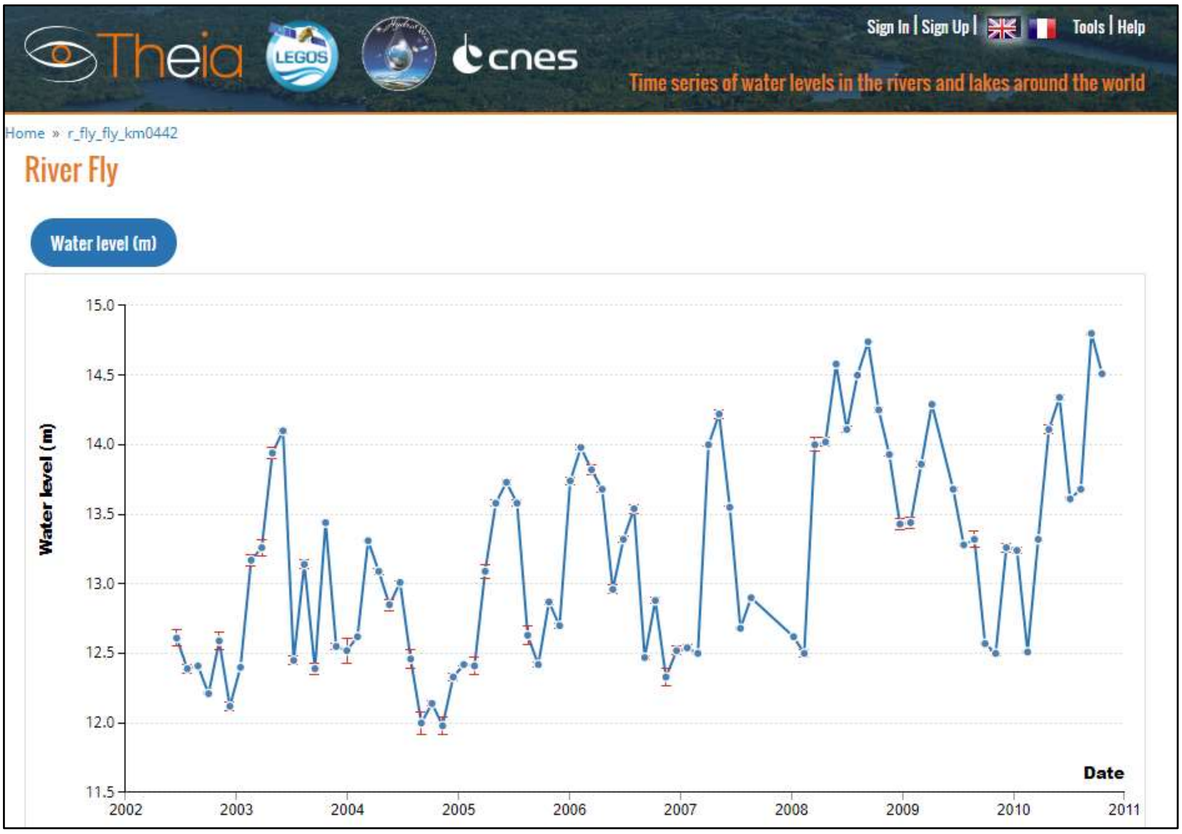

Figure 7-9 Hydroweb WSE time series for the 6.854ºS and 140.914ºE crossing of Envisat pass 0004 of the Fly River (Theia, 2020). The WSE in the plot is the orthometric height relative to the EGM96 geoid.

The Hydroweb retracking methodology is documented in Rosmorduc and Vayre (2020) and is based on the retracking processes defined in Santos da Silva et al. (2010). It consists of a three-stage process of data reading and selection; water level calculation and filtering; and validation and database update. The water level selection process is based primarily on the selection of the most echogenic measurements, typically those where the backscatter coefficient is higher than a pre-set threshold, although that threshold is not identified in the *Hydroweb Product Manual* (Rosmorduc and Vayre, 2020). The selected WSE is then merged into a 'standard year' with filtering against the mean for the site in an iterative process.

Figure 7-10 shows the location of the Envisat descending pass 0004 crossing of the Fly River. The satellite track crosses at a 250-m-wide section of the river, which is at the lower limit for successful retracking of nadir-looking pulse-limited altimetry (Maillard et al., 2015; Boergens et al., 2016). As the orientation of the river at this location is towards the south-east, and in the direction of the prevailing south-east trade winds, rough water is likely to occur through the central portion of the channel under windy conditions.

The satellite altimeter passes in a southerly direction across an extensive floodplain zone that is inundated at high flow and vegetated by grassland and open forest during dryer periods. The floodplain on the southern side is relatively narrow; however, numerous blocked-valley lakes and oxbow water bodies adjacent to the main stem are permanently inundated and would encourage hooking under low flow conditions.

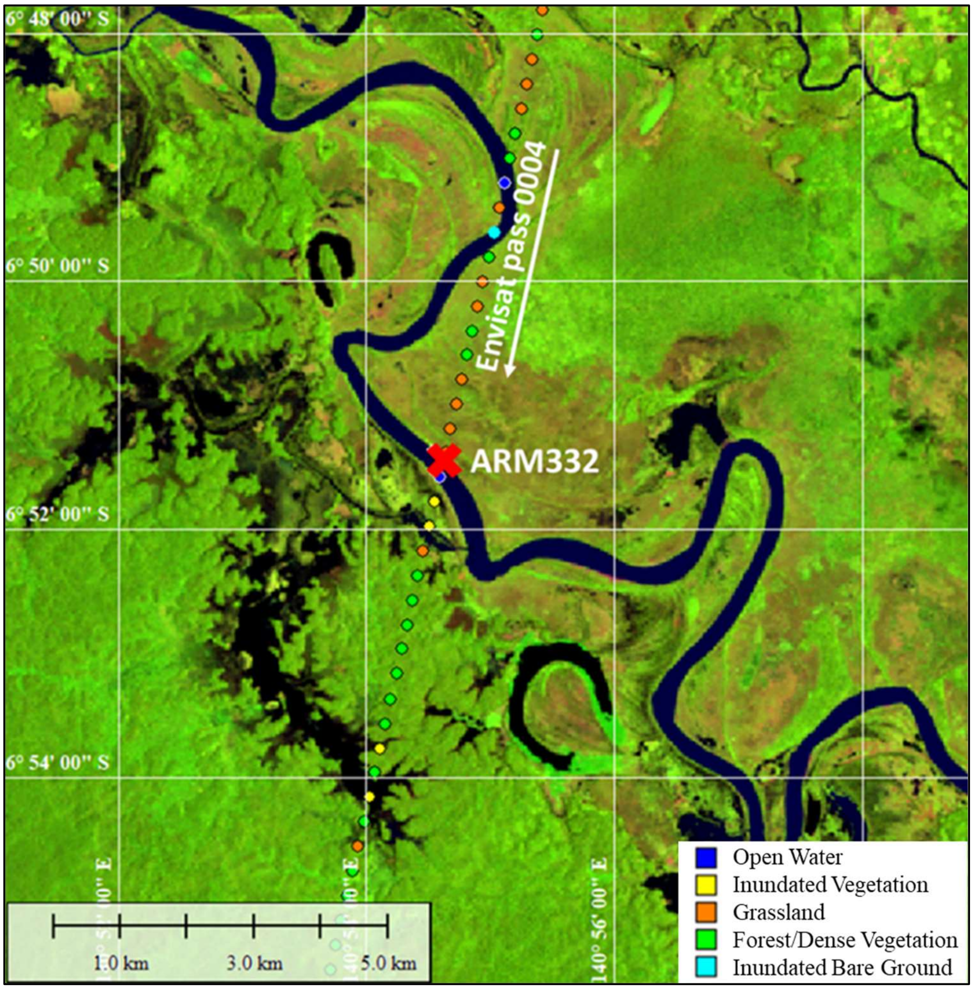

Figure 7-10 The crossing of the Fly River by Envisat descending pass 0004 at 6.854ºS and 140.914ºE, located at ARM332 on the Fly River. The crossing is at a 250-m-wide section of the river with orientation towards the south-east. Displayed is cycle 24 acquired on 3 February 2004 with a Landsat TM5 false colour background image acquired 12 February 2004.

During periods of high river level, the calmer zones at the land–water interface are likely to be specular reflectors and lead to a quasi-specular waveform originating from near nadir. However, during low water periods, if the water is rough, the resulting waveform is likely to be contaminated by surrounding landform and vegetation and the peak corresponding to the water surface of the river, if one exists, is likely to be difficult to identify and extract.

To assess both the Hydroweb altimetry-derived WSE time series and the performance of the WATeR altimetry retracking process, a virtual gauge derived from the FLY17 WSE in-situ gauge has been created at ARM332. The location of the ARM332 virtual gauge is at the Envisat pass 0004 crossing, approximately 62 km upstream of the FLY17 in-situ gauge. There are one major and two minor tributaries to the Fly River located within that reach. The significant upstream distance, and the fact that major tributaries contribute to the flow of the Fly River through the reach, means that a strong linear relationship between the ARM332 virtual gauge and the FLY17 in-situ gauge record is unlikely. This non-linearity manifests as an elevated RMSE derived in the virtual gauge creation process when the FLY17 hydrology record is fitted to discrete ARM332 in-situ WSE measurements. These reference WSE measurements (shown as the red markers in Figure 7-11) have been acquired at ARM332 on an annual basis since 1998 as part of OTML's bed aggradation monitoring program undertaken through the reach (Marshall, 1998–2020) and are used as a calibration in the transformation of the in-situ gauge into a virtual gauge at the crossing site. The FLY17 in-situ WSE record is transformed using the ARM332 annual survey measurements, resulting in the ARM332 virtual gauge shown in Figure 7-11.

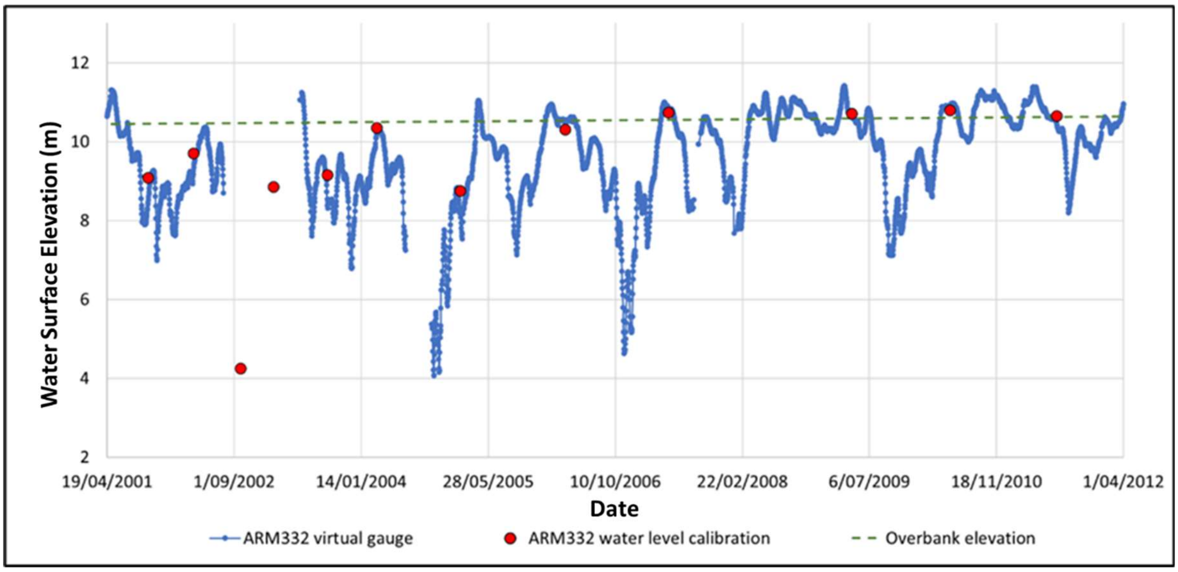

Figure 7-11 Transformation of the FLY17 in-situ gauge WSE time series for the Envisat pass 0004 crossing of the Fly River to create the ARM332 virtual gauge. The transformation is achieved by applying an overall elevation and temporal shift such that the resulting RMSE between the two data sets is minimised. The transformation resulted in an RMSE of 37.6 cm on comparison of the two data sets.

The transformation is achieved by applying an overall elevation and temporal shift such that the resulting RMSE between the two data sets is minimised, and this process resulted in an RMSE of 37.6 cm over the full inundation range and 14.7 cm excluding extreme low water conditions. The majority of differences are less than 20 cm, but several larger differences of 50 cm are evident through the lower inundation range.

The Hydroweb time series was converted to the OHD datum used in this study. This was achieved by using the EGM96 model N to derive an ellipsoidal height, from which an OHD elevation was derived by application of the PNG (Kearsely) N value. The results of the Hydroweb time series along with the ARM332 virtual gauge output are shown in Figure 7-12.

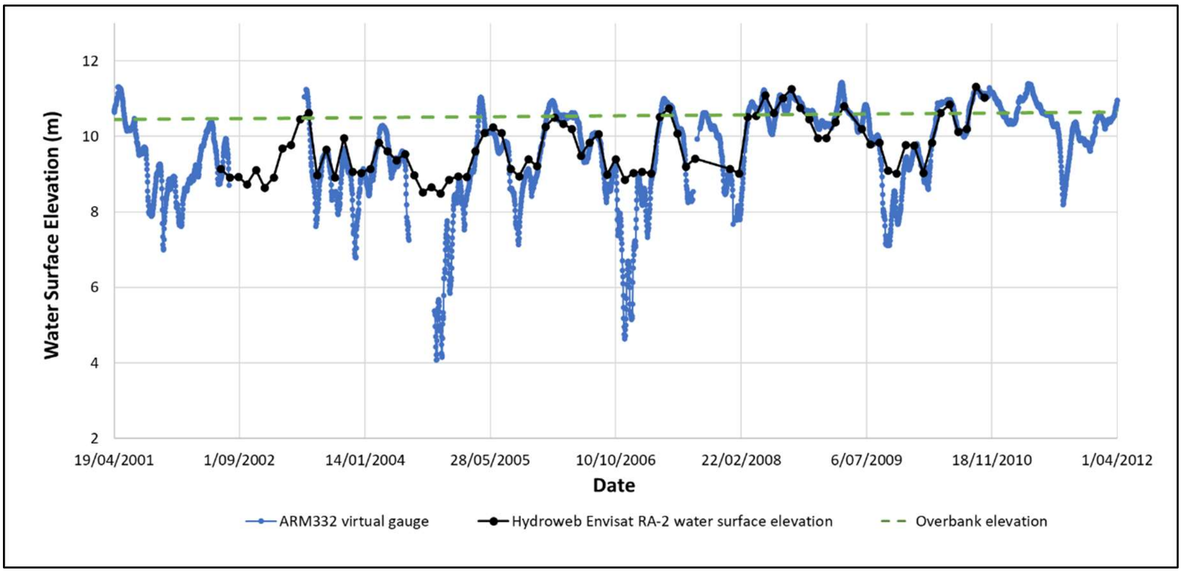

Figure 7-12 The Hydroweb WSE profile derived from Envisat RA-2 at ARM332 on the Fly River along with the ARM332 virtual gauge WSE profile. The approximate overbank elevation is shown as the dashed line.

For WSEs over 10 m the RMSE for the Hydroweb and virtual gauge comparison was 23.7 cm and within the estimated accuracy of the virtual gauge definition. At these elevations, the floodplain would have been inundated and the floodplain WSE would closely approximate the WSE of the river. Returns from the calm water zones during periods of high flow have meant that the methodology employed in the Hydroweb process is ideally suited to the extraction of such time series. For the full WSE time series, however, the RMSE degrades to 142 cm, with differences of 50–100 cm for median and low inundation ranges and up to 500 cm for extreme low flow conditions. In these cases, the adopted Hydroweb methodology is likely to have derived WSE estimates from hooked returns from blocked-valley lakes, oxbow systems or residual water on the floodplain adjacent to the main stem. The use of these returns would have been based on the elevated backscatter coefficient associated with the return from a specular reflector and would have been assigned as a river WSE return in the absence of evidence to the contrary.

Using the WATeR altimetry retracking process developed as part of this study, the same altimetry data as used in the Hydroweb time series were retracked and a WSE time series derived based on the same geoid and datum as used in the Hydroweb transformation. A significant finding was the absence of quasi-specular returns over the main stem for a proportion of the cycles acquired during low water periods. Where available, the quasi-specular returns are used to derive an a priori estimate of WSE. When these returns are not available the process is more complex, with an assessment of waveform shape and structure leading into and away from the river, along with retracking and matching of results of all peaks from adjacent waveforms used to derive the a priori estimate for peak selection in the retracking process. Quasi-specular returns were evident over parts of the floodplain where potential calm water sources were identified. However, these were readily determined to be from floodplain water bodies in the retracking process and not representative of the WSE of the river.

The impact of stage height on the retracking process is illustrated in Figures 7-13 and 7-14, which show passes and waveform shape for high and low inundation conditions.

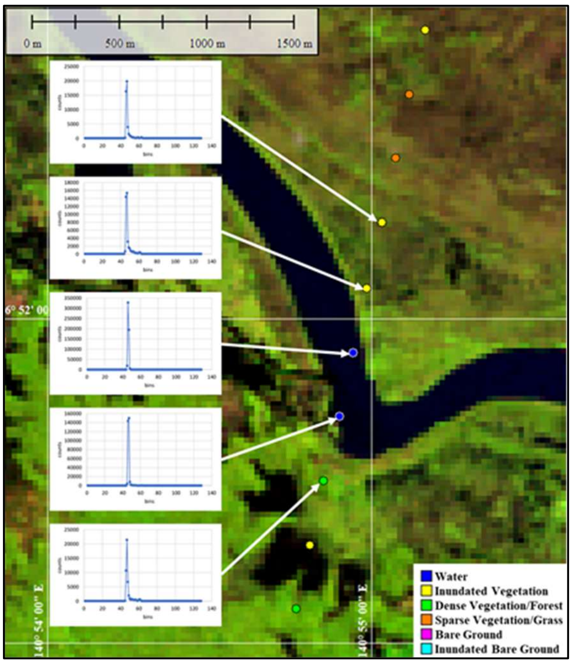

Figure 7-13 Waveform locations for Envisat RA-2 data for descending pass 0004 cycle 46 acquired on 14 March 2006. High-powered quasi-specular waveforms are evident over a zone where river levels are high, and the floodplain inundated.

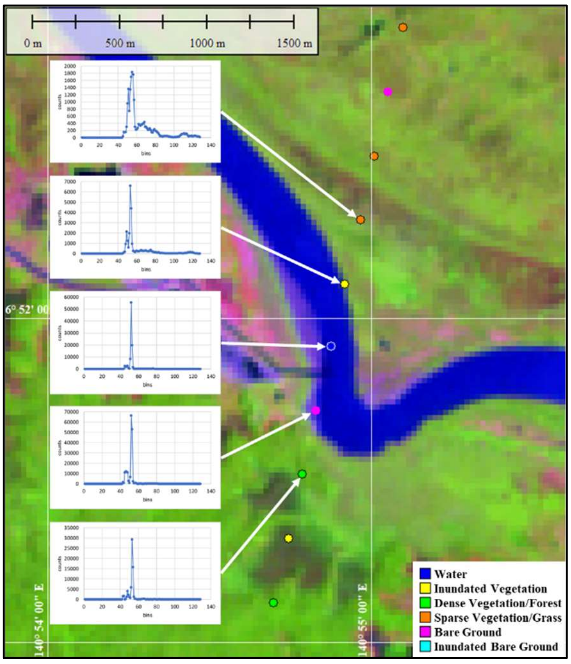

Figure 7-14 Waveform locations for Envisat RA-2 data for descending pass 0004 cycle 32 acquired on 9 November 2004. Multi-peaked waveforms with a dominant peak towards the end of the waveform peak sequence are evident over a zone where river levels were low, and the floodplain exposed.

Figure 7-13 shows the nadir locations for descending pass 0004 on 14 March 2006 and the waveform shape for five waveforms centred at the river crossing. For this cycle, as the river level approximates bank full, the floodplain is expected to be inundated. All waveforms are high-powered and quasi-specular and exhibit a relatively high backscatter coefficient. The waveforms were retracked and returned consistent WSE estimates with a SD of ±6.5 cm and difference of 19.5 cm compared with the virtual gauge.

The waveforms located over the floodplain would have either hooked to the land–water interface at the edge of the river or contained a nadir reflection from floodplain water, and although there was no hooking evident in the elevation profile, the final WSE estimate was derived from the two river returns with the additional observations used to validate and statistically support the process.

Figure 7-14 shows the nadir locations for descending pass 0004 on 9 November 2004 and the waveform shape for five waveforms centred at the river crossing. For this cycle, the river level is within the lower quartile of river stage heights. All waveforms have a multi-peaked shape with the dominant peak being towards the end of the peak sequence. There was no quasi-specular return in the sequence and the backscatter coefficient was low for the floodplain sites and moderate over the river channel. The WATeR altimetry retracking process extracted the third peak for the first waveform and the second peak for the remaining waveforms, and a WSE estimate was derived for each sub-waveform. The SD of the estimates was ±6.7 cm and the difference from the virtual gauge was 27.4 cm. The derived elevation profile exhibited a residual WSE concavity for the floodplain sites, indicating the presence of hooking; however, the final river WSE estimate was derived from observations identified as originating from the main stem.

Waveforms from all Envisat RA-2 crossings of the Fly River at ARM332 were retracked with the location of the waveforms within the main stem identified using the methodology developed in Chapter 4. Waveforms adjacent to the main stem were also included based on the hypothesis that the extent of any hooking bias would be minor because of the relatively short distance to the main channel. Their inclusion permits a statistical review and outlier detection of final results. The SD of the derived WSE time series for all observations was ±7.0 cm with all final WSE estimates derived from at least two observations.

The result of the retracking process for the complete Envisat RA-2 WSE time series is shown in Figure 7-15 along with the ARM332 virtual gauge WSE time series. The WATeR altimetry process performed well at high flow levels with a SD of ±4.9 cm for WSE over

9 m. The WATeR retracking methodology also performed well at median-to-low flow levels, with a SD of ±5.8 cm for WSE of 6–10 m. There was, however, evidence of some decrease in quality under extreme low flow conditions with a SD of ±11.3 cm for WSE below 6 m. This precision degradation is unlikely to be improved with additional retracking investigations as it is related to the contaminated nature of the waveform, including effects of the waveform averaging process where significantly different echoes for individual waveforms are averaged under low flow conditions and where the waveform shape consists of returns dominated by off-nadir reflectors within the footprint. For a narrow river at extreme low flow conditions with the flow in the direction of the prevailing wind, as well as residual calm water reflectors on the floodplain, it is possible that there is no return from the river itself. Despite that possibility, this was not identified through this waveform sequence, with a return from the river identified within each waveform.

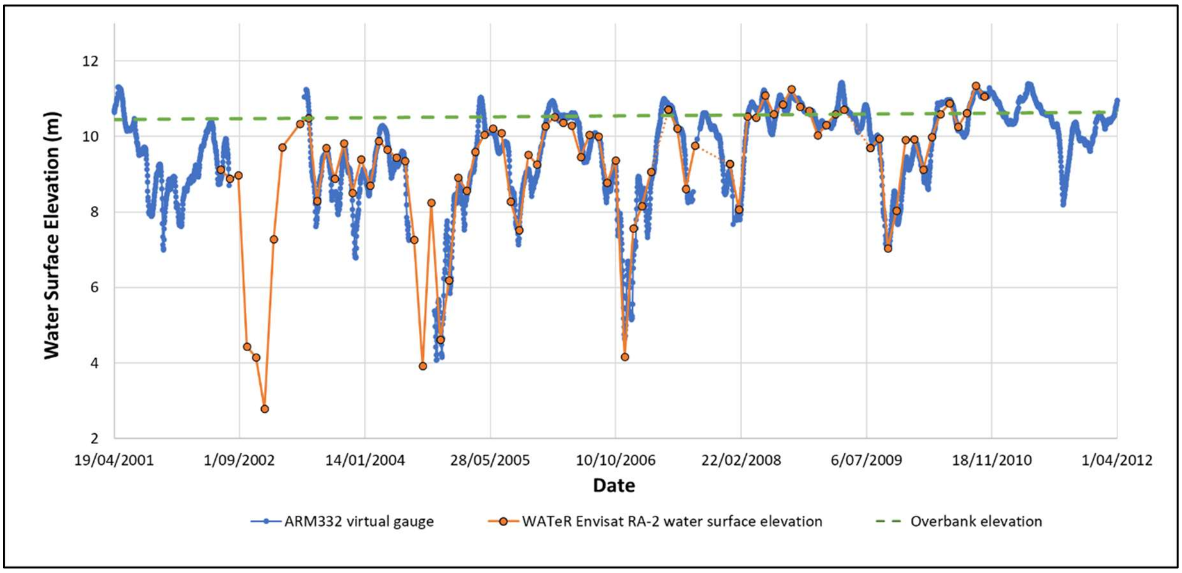

Figure 7-15 The WATeR WSE profile derived from Envisat RA-2 for descending pass 0004 at ARM332 on the Fly River, using the methodology developed for this study along with the ARM332 virtual gauge WSE time series. The approximate overbank elevation is shown as the dashed line.

Under high flow conditions, the WATeR-derived WSEs were consistent with those derived by Hydroweb, but this was not the case for median and low flows with a difference of up to 5.0 m between the two retracking methods for extreme low flows below the 6.0-m level. To validate the derived WSEs, a comparison was made between the WATeR-derived altimetric WSE time series and the ARM332 virtual gauge. For elevations above 10.0 m the RMSE was 27.5 cm and for the median and low flow range of 6.0–10.0 m the RMSE was 36.8 cm, which is consistent with the estimated accuracy of the ARM332 virtual gauge. For WSE below 6.0 m the RMSE increased to 62.7 cm. The overall RMSE for the comparison was

34.2 cm, a fourfold improvement over the Hydroweb results, predominantly as a function of the medium and low flow improvements evident in the WATeR time series.

An El Niño climatic event occurred between 2002 and 2003 and this resulted in a loss of the hydrology record from the majority of OTML's in-situ gauges as the water level dropped below the inlet orifice of the water level sensor. While it was not possible to validate the WATeR-derived altimetric WSEs against the ARM332 virtual gauge during such periods of extreme low flow, the results of the aggradation survey undertaken at the site, where WSE on 26 September 2002 was determined by direct measurement, are used for validation of the altimetric WSE record. Figure 7-16 shows the WSE time series for both Hydroweb and WATeR for the El Niño of 2002. The altimetric observation from 1 October 2002 and the surveyed WSE from 26 September 2002 are highlighted in the figure with the Hydroweb difference being 447.5 cm and the WATeR difference being 18.5 cm. Although the WATeR difference is still significant, it is not unexpected considering the 4-day gap between the survey and altimetry observations.

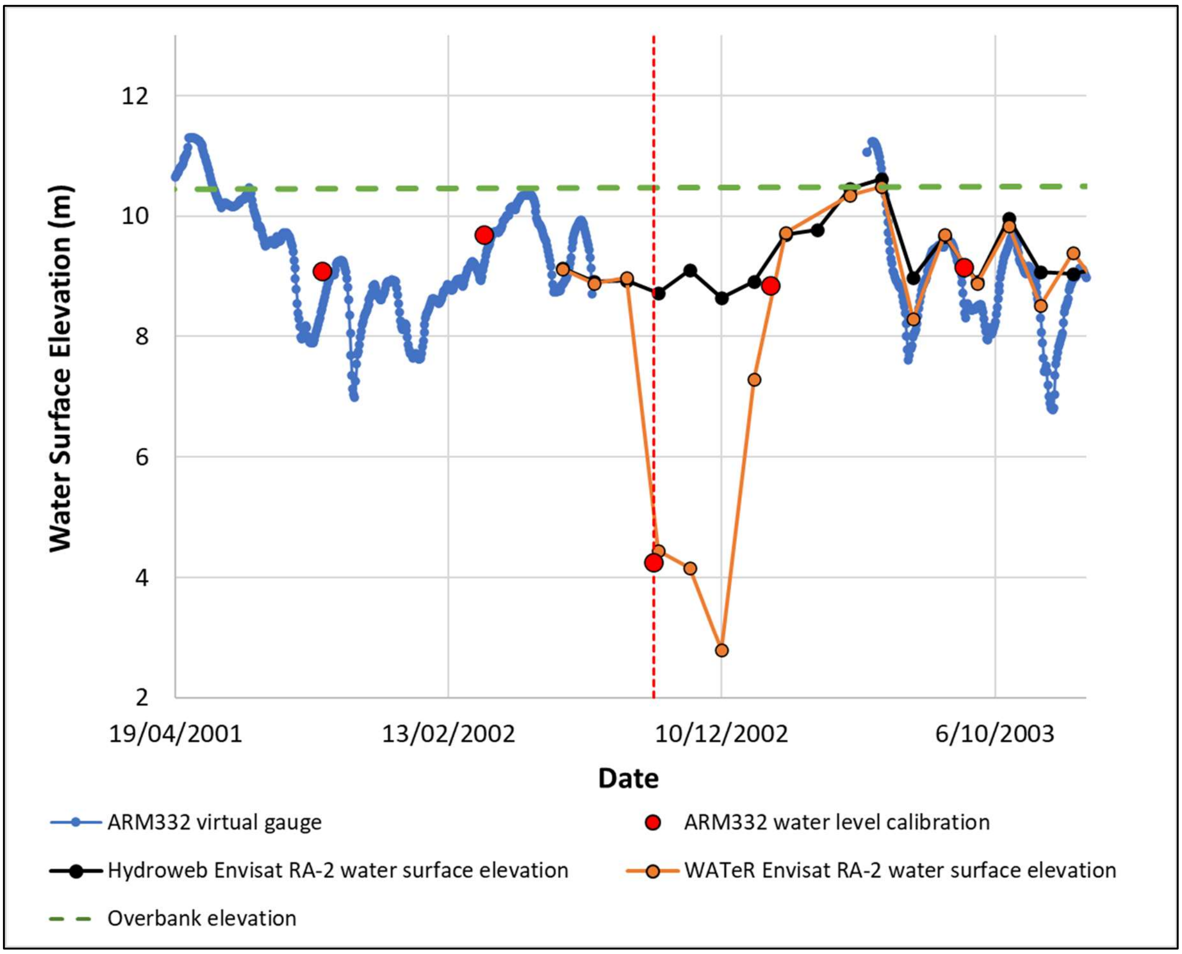

Figure 7-16 WATeR and Hydroweb WSE profiles derived from Envisat RA-2 data for descending pass 0004 at ARM332 for the 2002 El Niño. Relatively good agreement between the surveyed WSE on 26 September 2002 (shown as the vertical red line) and the WATeR altimetric WSE on 1 October 2002 validates the WATeR retracking methodology for low flow conditions.

This result corroborates the WATeR validation results achieved in the comparison with the ARM332 virtual gauge for low water conditions and validates the WATeR retracking process for extreme low flow conditions in the absence of virtual gauge data.

While RMSE results for this site are not exceptional, they are consistent with the documented results of Frappart et al. (2006) and Santos da Silva et al. (2010), as well as the quality estimate derived for the virtual water level record. The quality of the virtual gauge record contributes in large part to the result and an improved estimate would likely result if the in-situ gauge was located within closer proximity to the altimetry crossing. The results presented in this section, however, show significant improvement in the accuracy of derived WSEs compared with WSE estimates available from the Hydroweb global database for the same site and using the same input data. While this level of improvement cannot necessarily be assumed for other sites, the results do demonstrate a significant quality improvement in the retracking process, particularly for low flow conditions.

7.1.2 Envisat and SARAL pass 0677 Fly River crossing—ARM305 to ARM311

A WSE time series has been derived for the combined 14-year altimetry acquisitions from Envisat RA-2 and SARAL/AltiKa for ascending pass 0677. The pass is centred at 7.020°S and 141.085°E, located between ARM305 and ARM311 on the Fly River. Figure 7-17 shows the location of the pass with respect to the Fly River and the location of the crossings at ARM305, ARM309 and ARM311. The figure also shows the location of the in-situ gauge at Manda Village (FLY17) as well as the location of the reference site (FLY16) at ARM307 where the primary virtual gauge is established.

Bed aggradation surveys, including measurement of WSE, have been undertaken annually at both FLY17 and FLY16 since 1998 (Marshall, 1998–2020) and the results are used to derive an estimate of river slope. Through this reach of the Fly River, the measured river gradient is in the order of 2.9×10^{-5}, which is consistent with the gradient reported in Day et al. (2008), although there is evidence of a change in slope as a function of stage height. A gradient of 2.5×10^{-5} is typical at low stage height and 3.2×10^{-5} typical for high stage height; however, there is some variability depending on local catchment rainfall, which can alter tributary backwater impact and have a direct influence on river slope. The gradient difference equates to an elevation difference of 11 cm between FLY17 and the virtual gauge reference site at FLY16 for the expected WSE range and, although this estimate could be built into a variable virtual gauge, the average gradient is used for all inundation states in this study in the virtual gauge creation process.

Although the FLY17 in-situ gauge is only 14 km from the FLY16 reference, the Agu and Kai rivers (with locations shown in Figure 7-17) are both significant tributaries to the Fly River through this reach. The uncertainty associated with their varying discharge to the Fly River and the impact this has on Fly River stage height is likely to limit the accuracy of the virtual gauge established for the altimetry WSE validation.

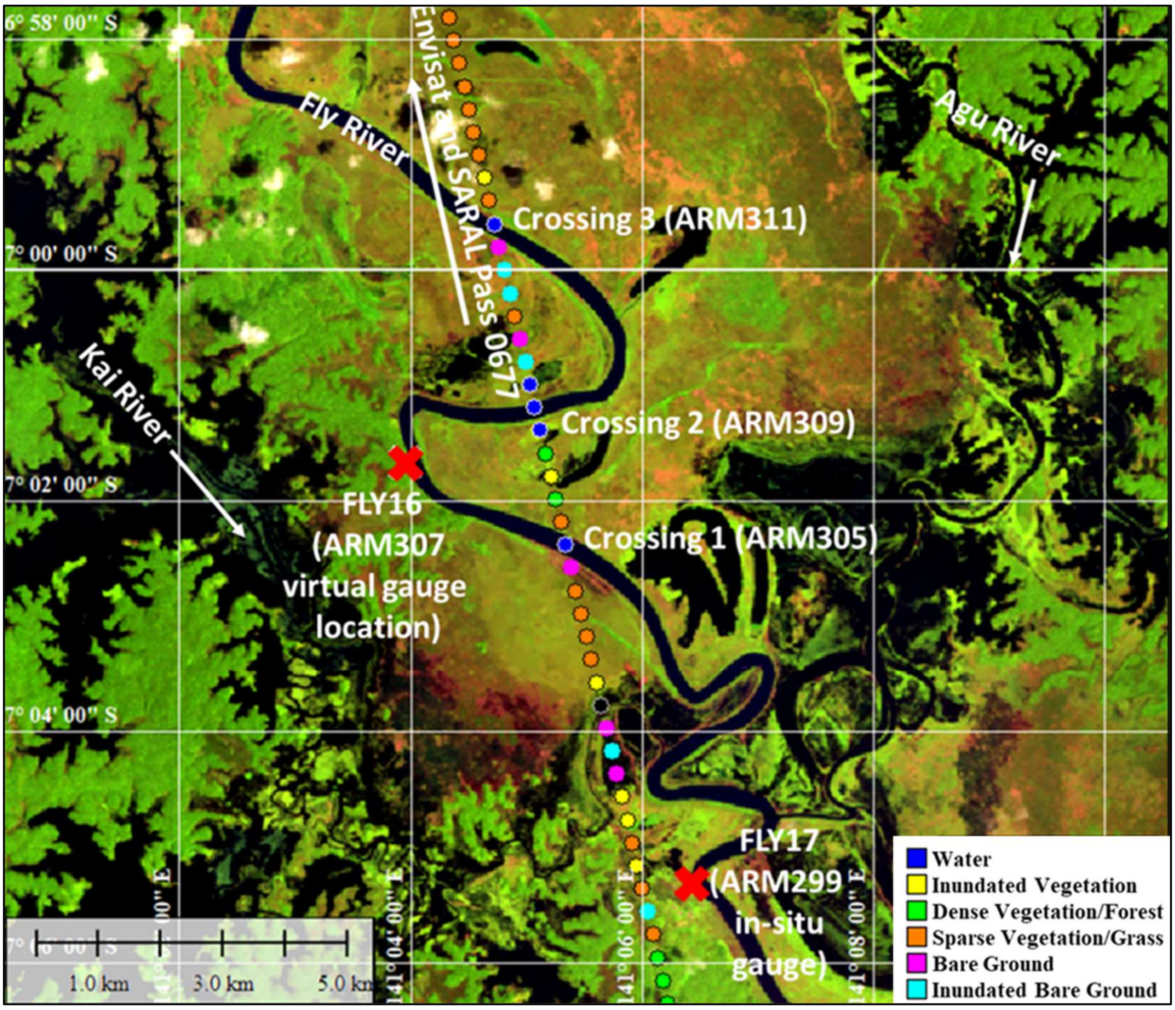

Figure 7-17 Envisat RA-2 and SARAL/AltiKa waveform locations for ascending pass 0677, located between ARM305 and ARM311 on the Fly River. There are three crossings of the river with channel width ranging from 200 to 250 m. The river is oriented towards the south-east for crossings 1 and 3 and to the west for crossing 2. Displayed is cycle 30 acquired on 23 September 2004 with a Landsat TM5 false colour background image acquired 19 January 2007.

Reference WSE measurements have been acquired at FLY16 on an annual basis since 1998 as part of OTML's bed aggradation monitoring program undertaken through the reach (Marshall, 1998–2020) and are used as a calibration in the transformation of the in-situ gauge into a virtual gauge at the site. The transformation of the FLY17 in-situ WSE record for the creation of a virtual gauge at FLY16 is achieved by applying an overall elevation and temporal shift such that the resulting RMSE between the two data sets is minimised. The results from the derived FLY16 virtual gauge are shown in Figure 7-18. The transformation process resulted in an RMSE of 10.0 cm, which is consistent with the uncertainty in river level slope as a function of stage height. Note that additional secondary WSE virtual gauges are derived for each of the actual crossings based on an extrapolation of the average river gradient measured between FLY17 and FLY16.

The altimetric WSEs derived using the WATeR altimetry retracking process are validated against the virtual gauge established from the FLY17 in-situ water level record, for each crossing as well as in internal comparisons for altimetric WSE consistency.

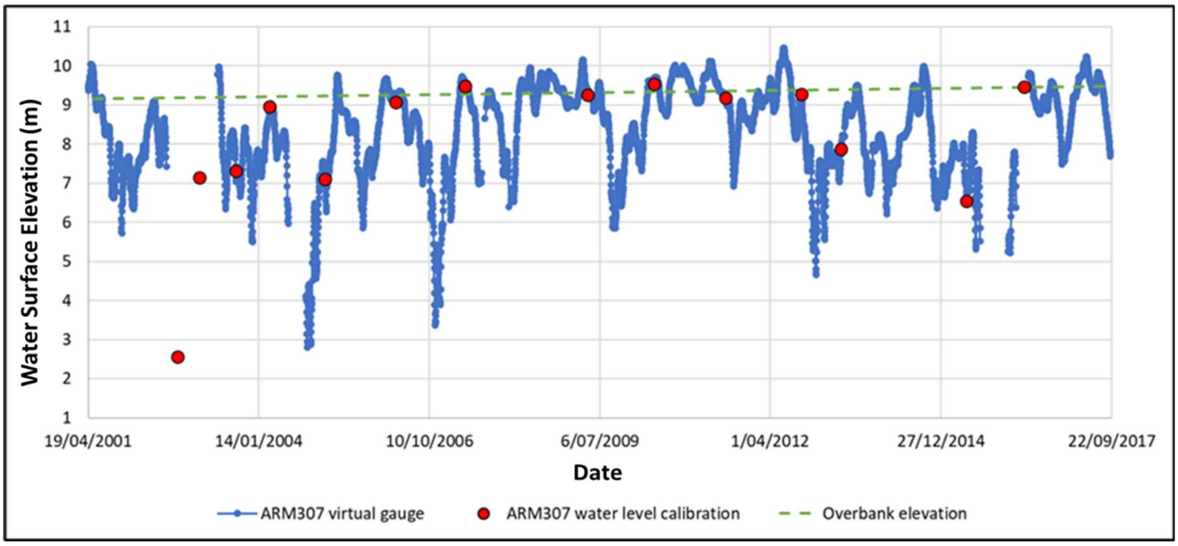

Figure 7-18 Transformation of the FLY17 WSE record from the in-situ gauge at Manda Village for the Envisat pass 0677 crossings of the Fly River between ARM305 to ARM311. The transformation is achieved by applying an overall elevation and temporal shift such that the resulting RMSE between the two data sets is minimised. The transformation resulted in an RMSE of 10.0 cm in a comparison of the two data sets, which is consistent with the estimated uncertainty of the river slope as a function of stage height.

The average river gradient equates to a WSE change of 14 cm between crossings 1 and 2 and 16 cm between crossings 2 and 3. These differences are at the predicted accuracy limits of the derived virtual gauge and are comparable with the expected accuracy of the altimetric WSE estimates. The unique location of the pass with respect to the meandering river facilitates investigations into the use of altimetric WSE estimates for deriving supplementary hydrologic data. For this site, estimates of gradient derived from the in-situ and virtual gauge records will be compared with the derived river gradient from the altimetric WSEs.

While the virtual gauge at ARM307 has been established based on the location of the theoretical track, there is significant lateral variability in track location, particularly for the SARAL passes. While the off-track SARAL/AltiKa data were acquired prior to the satellite moving into its drifting orbit in July 2016 they were acquired when satellite manoeuvrability and orbit maintenance were starting to become an issue (Dibarboure et al., 2018). Figures 7-19 and 7-20 show the cycles for all Envisat RA-2 and SARAL/AltiKa altimetry acquisitions over the crossing at 7.020ºS and 141.085ºE. The 85 Envisat cycles are grouped about the theoretical track with the majority within 250–500 m of the theoretical crossing; however, the full lateral range is approximately 2.5 km and this contributes an additional uncertainty in the validation process of ±4 cm. With the exception of the SARAL cycles that do not cross the Fly River, the majority of SARAL cycles pass within 500–750 m of the theoretical crossing. However, the full lateral range is approximately 3.5 km and this contributes an additional uncertainty in the validation process of ±5 cm as a function of the slope of the river.

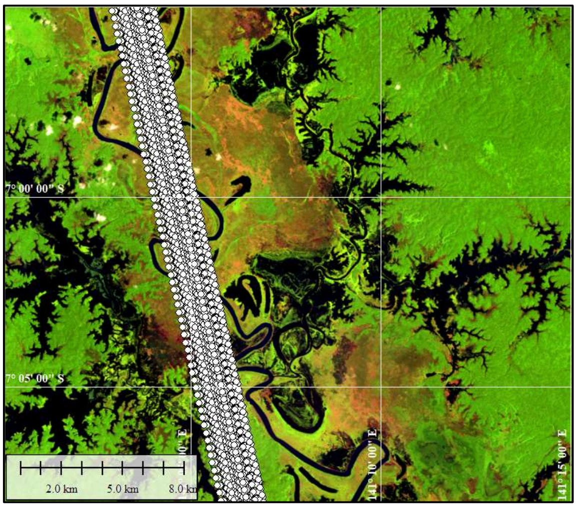

Figure 7-19 Envisat RA-2 cycles from ascending pass 0677 acquired between 11 July 2002 and 7 October 2010.

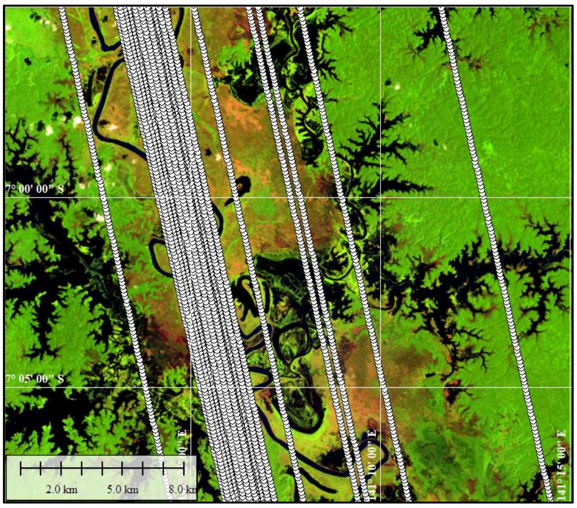

Figure 7-20 SARAL/AltiKa cycles acquired between 6 April 2013 and 30 April 2016. Cycles that drifted from the theoretical track have been omitted.

All waveforms at the river crossing and immediately adjacent to the crossing were retracked using the WATeR altimetry retracking process. The locations of the waveforms within the main stem were identified using the methodology developed in Chapter 4 with adjacent waveforms included in a manner consistent with that adopted in Section 7.1.1. The SD of the derived time series for all observations along with the derived RMSE are detailed for each crossing (cf. Figure 7-17) in Table 7-2.

Table 7-2 SD and RMSE for the Envisat RA-2 and SARAL/AltiKa WSE derived using the WATeR altimetry retracking process for the three crossings of the Fly River of ascending pass 0677.

Altimeter	**Crossing**	**SD (cm)**	**RMSE (cm)**
Envisat RA-2	1	±5.5	11.4
	2	±6.0	10.4
	3	±4.8	12.1
	Average	**±5.4**	**11.3**
SARAL/AltiKa	1	±6.5	13.7
	2	±7.8	10.4
	3	±6.5	16.5
	Average	**±6.9**	**13.5**

Between the three crossings there is little difference in the SD for either the Envisat RA-2 or SARAL/AltiKa WSEs. As a function of the higher PRF for the SARAL/AltiKa altimeter compared with Envisat RA-2, there are approximately double the number of candidate waveforms within the river crossing for SARAL/AltiKa available to extract a valid WSE. It was expected that the SD and possibly the RMSE would be superior for SARAL/AltiKa but Table 7-2 results shows that this is not the case. The reduced quality of the SARAL/AltiKa estimates is due to the waveform saturation issues identified in Section 2.1.2 and detailed in Section 6.2, which significantly limit data availability and interpretation. The river crossings are typical of zones that are likely to be affected by SARAL/AltiKa waveform saturation as they are regions of variable scattering with the likelihood of specular surfaces existing within the altimetric footprint (Verron et al., 2018). This has meant that a significant proportion of single peaked returns that reflect from these specular surfaces are saturated and omitted from analyses, resulting in WSEs of reduced quality derived predominantly from the nadir return sub-waveform of multi-peaked returns. Verron et al. (2018) and Bonnefond et al. (2018) predict improvement in observation of inland water targets from SARAL/AltiKa compared with Ku-band altimeters, based on the characteristics of the instrument including the improved along-track resolution. However, this has not been realised for this site because of limitations associated with waveform saturation.

The RMSE for each crossing has been derived along with an average RMSE for the three crossings. The average RMSE of the Envisat RA-2 cycles is consistent with the accuracy of the virtual gauge and is approximately four times the accuracy of reported WSE definitions over narrow inland river systems and associated wetland environments (Frappart et al., 2006; Santos da Silva et al., 2010; Villadsen et al., 2016; Biancamaria et al., 2017). While both the Envisat RA-2 and SARAL/AltiKa results demonstrate significant quality improvements compared with related studies, the Envisat RA-2 results are approximately 20% superior to those derived from SARAL/AltiKa for this pass.

Evaluation of results between crossings shows a small, but significant, quality improvement in the RMSE of crossing 2 compared with crossings 1 and 3. This is linked to the orientation of the river and the direction of the prevailing wind for these locations. Crossings 1 and 3, for both Envisat RA-2 and SARAL/AltiKa, exhibit an increased incidence of hooking associated with the higher levels of water surface roughness, characterised by a drop in the backscatter coefficient, as the water flows into the prevailing wind. While results are good at high flows, with WSE derived from stable quasi-specular waveforms at calm water locations along the margins of the main channel, the waveform shape at low water levels is typically multi-peaked and this leads to additional uncertainty and inaccuracy in the retracking process. The RMSE results for crossing 2 show a 15% improvement for Envisat RA-2 compared with crossings 1 and 3 and a 50% improvement for SARAL/AltiKa compared with crossings 1 and 3. This illustrates the necessity to be able to identify the state of the water surface, predominantly undertaken by analysis of the backscatter coefficient, but also on the basis of waveform shape and the results of the altimetric footprint classification.

A composite time series has been derived from both the Envisat RA-2 and SARAL/AltiKa cycles from the WSEs derived from the three crossings and is shown in Figure 7-21. The three data sets are corrected for river gradient to the FLY16 reference site and averaged, with an overall SD of ±5.4 and ±6.9 cm for Envisat RA-2 and SARAL/AltiKa respectively. Following comparison with the virtual gauge, the RMSE for the composite WSE from the three crossings was 10.0 cm for Envisat RA-2 and 14.9 cm for SARAL/AltiKa.

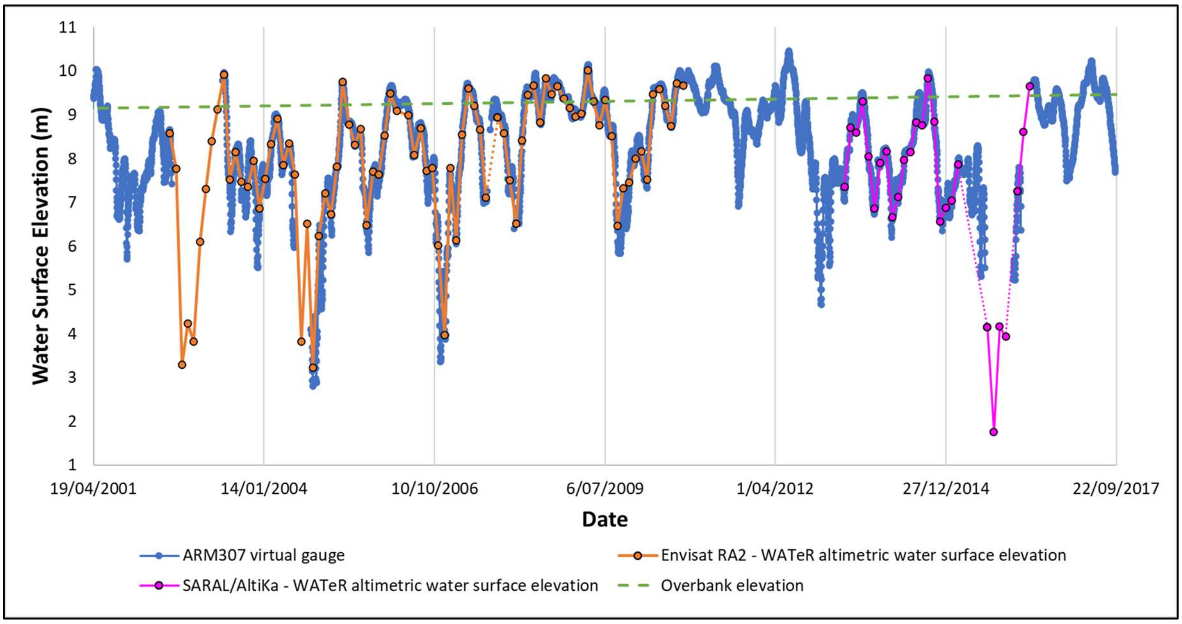

Figure 7-21 The composite WSE time series derived from Envisat RA-2 and SARAL/AltiKa using the WATeR retracking methodology for the 14 years from 2002 to 2016 for the three pass 0677 crossings of the Fly River. The derived RMSE based on comparison with the virtual gauge was 10.0 cm and 14.9 cm for Envisat RA-2 and SARAL/AltiKa respectively. Consistent extraction of valid WSEs at high-to-low flows is demonstrated for both Envisat RA-2 and SARAL/AltiKa. The ability to extract valid WSEs during periods of extreme low water is demonstrated for Envisat RA-2 during the El Niño of 2002 and low water conditions evident in 2004 and 2006 and for SARAL/AltiKa during the El Niño of 2015.

Consistent extraction of valid WSEs at high-to-low flows is demonstrated for both altimeters using the WATeR altimetry retracking process along with the ability to extract valid WSEs during periods of extreme low water, as demonstrated during the El Niño events of 2002 and 2015 as well as the extreme low water conditions evident in 2004 and 2006.

The three crossings are located within a relatively short reach of the river and it is expected that there is a strong linear relationship between the derived WSEs for each site. The overall R has been calculated from comparison of the derived WSEs at all crossings for both Envisat RA-2 and SARAL/AltiKa. For both Envisat RA-2 and SARAL/AltiKa the R was 0.99 confirming high internal precision in the derived WSE estimates, with high correlation between the derived WSE estimates for three separate locations. The relationship of the WSE differences between the three crossing pairs has also been derived, with a moderate R of 0.85 for Envisat RA-2 and 0.83 for SARAL/AltiKa determined.

The river level slope derived from the altimetric WSE differences between the three crossings on the Fly River indicates an average gradient of approximately 2.12×10^{-5} from Envisat RA-2 and 2.77×10^{-5} from SARAL/AltiKa. While these estimates are at the lower end of the river gradient range derived in the virtual gauge validation process, they demonstrate the capability of satellite altimetry-derived WSEs to provide such information. The relationship between the river level slope for the three river crossing pairs was calculated for both Envisat RA-2 and SARAL/AltiKa with the derived R in the moderate range and consistent with that derived for the WSE differences at the three crossings. This result is in agreement with the findings of Santos da Silva et al. (2014) who suggested that the altimetry derived river slope could not always be accurately derived for a relatively flat river surface from altimetric measurements acquired in close proximity to each other. In this study, the result demonstrates that the derived WSEs are at the limit of required accuracy for use in derivation of river slope over relatively short reaches such as those at this site.

7.1.3 Envisat pass 0004 (new orbit) Fly River crossing—ARM218

On 22 October 2010 Envisat moved into a new orbit (AVISO+, 2012) resulting in a shift from that maintained between 1 March 2002 and October 2010. Pass 0004 was originally a descending pass that tracked through the upper half of the Fly River floodplain as shown in Figure 7-1. However, with the shift in orbit it moved to the south, passing in a south-westerly direction over Lake Murray and then crossing the Fly River at Obo. No orbit maintenance was undertaken for the new orbit, with orbit inclination drifting while in this operational phase (Miranda et al., 2010). Envisat only completed 18 cycles in this configuration before communications with the satellite were lost on 8 April 2012 (Blarel et al., 2015). Of the 18 cycles that were completed in this phase of Envisat’s operation, 15 cycles are available for analysis and validation of the WATeR altimetry retracking process. Despite the limited number of available cycles, the data offer the unique advantage that the theoretical location of the track passes directly over the OTML in-situ gauge located at Obo, with all actual cycles passing within 5 km of this location. In addition, the gradient of the river has been verified as being relatively stable over the period of altimetry acquisitions, as determined from the annual aggradation surveys undertaken through the reach, and there are no significant tributaries to the Fly River through the reach to degrade the accuracy of the validation process.

The track of the Envisat pass crosses the Fly River at 7.583ºS and 141.330ºE, slightly downstream of the Obo Station hydrology monitoring site. Figure 7-22 shows the location of the altimetry passes to be used in the validation of the WATeR altimetry retracking process. The initial theoretical location of pass 0004 (new orbit) for Envisat is shown, along with the actual cycle locations and the FLY15 in-situ gauge located at Obo on the Fly River. The river width varies from 250 m at Obo to 350 m at the junction with the Strickland River.

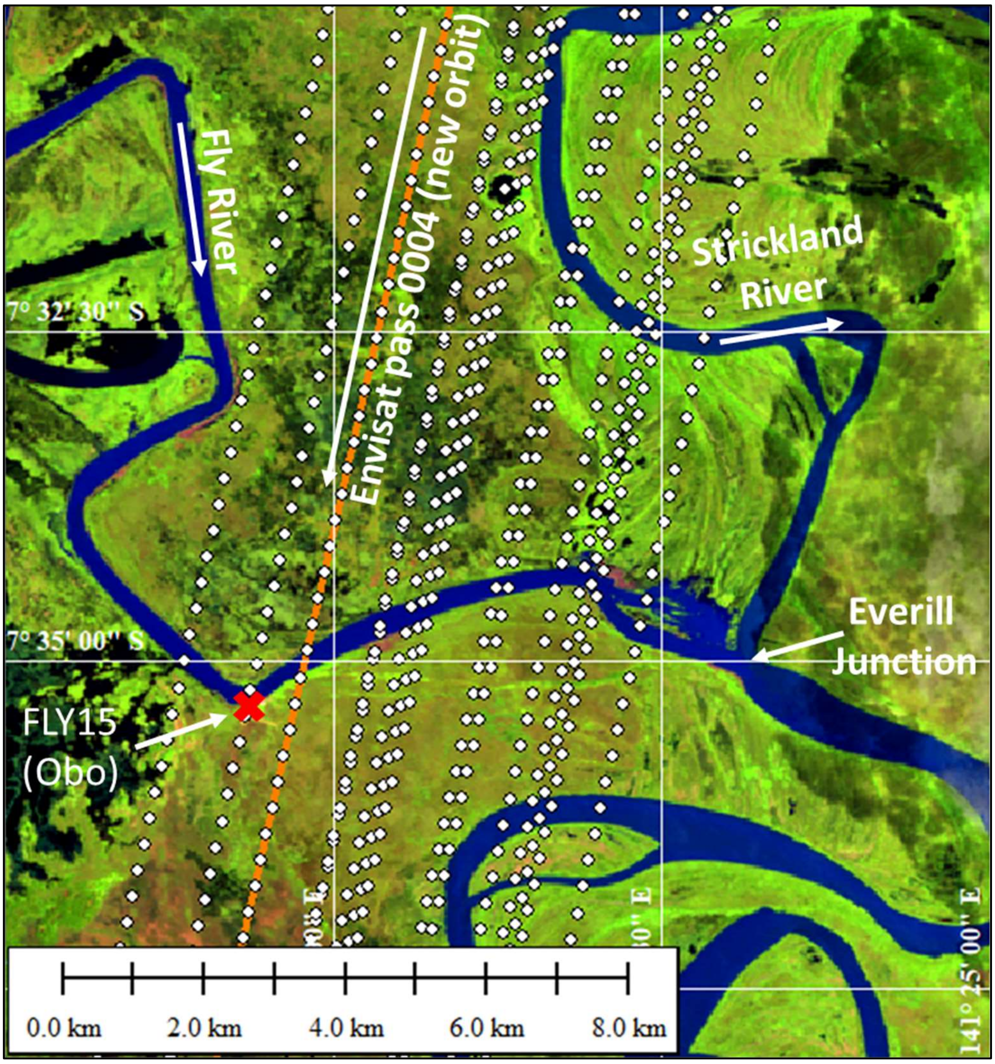

Figure 7-22 Envisat descending pass 0004 crossing the Fly River at 7.583ºS and 141.330ºE located at ARM218 on the Fly River. Cycles acquired between October 2010 and March 2012 are identified, along with the location of the initial theoretical track and the FLY15 in-situ gauge. The background is a Landsat TM5 image acquired 12 February 2004 during a period of median floodplain inundation.

The river slope in the vicinity of the altimetry cycles is relatively constant over time, regardless of stage height, so a variable virtual in-situ gauge has been established to improve the accuracy of the validation process. Because of significant backwater impacts as the Fly River meets the Strickland River at Everill Junction (Pickup and Marshall, 2009), the Fly River flattens significantly, resulting in a relatively stable gradient of 1.0×10^{-5} through this reach. This process results in variable correction applied as a function of distance from the in-situ gauge, ranging from 0 cm in the vicinity of FLY15 through to a reduction by 6 cm approaching the Fly–Strickland junction.

Figure 7-23 is an aerial photograph of Obo Station at ARM218 on the Fly River, acquired on 6 September 2012, which shows the variable water surface roughness as a function of river orientation.

Figure 7-23 An aerial photograph of Obo Station at ARM218 on the Fly River, acquired on 6 September 2012. The roughness of the water surface upstream of Obo Station compared with the downstream zone, where the majority of cycles are located, indicates that there is low likelihood of hooking from locations over the main stem to specular reflectors within the floodplain.

A significant advantage of this site for altimetric validation relates to the orientation of the river for the majority of the cycles. As the river orientation is predominantly easterly, the water surface roughness associated with orientation towards the south-east is less probable. As such the likelihood of hooking from locations over the main stem to specular reflectors within the floodplain waters is reduced.

The FLY15 in-situ gauge WSE record is shown in Figure 7-24 along with the single survey calibration WSE for the validation period. The average overbank elevation indicates that the floodplain is likely to be inundated for a significant proportion of the time. Altimetric data were acquired over the full range of expected stage heights excluding the extreme low water events evident during El Niño climatic conditions.

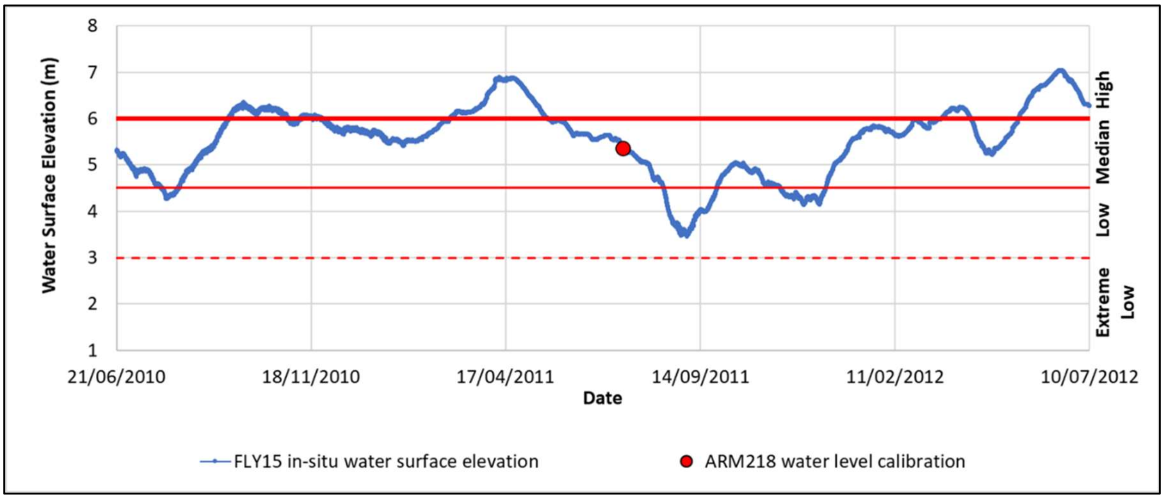

Figure 7-24 The FLY15 in-situ WSE record along with the single survey calibration WSE for the validation period. The average overbank elevation indicates that the floodplain is likely to be inundated for a significant proportion of the time. Altimetric data were acquired over the full range of stage heights excluding the extreme low water events associated with El Niño climatic conditions.

The WATeR altimetry retracking process was used to derive a WSE time series for Envisat RA-2 pass 0004 (new orbit) altimetry crossing of the Fly River at ARM218. These results are shown in Figure 7-25 along with the FLY15 in-situ WSE record.

A minimum of two altimetry observations were selected for each cycle with an overall SD of ±5.1 cm. This result is consistent with the validation results derived for ARM332 and ARM307. The RMSE derived from the comparison of the variable in-situ gauge WSEs and the WATeR derived altimetric WSEs was 8.3 cm. This result is a significant improvement over the validation results from ARM332 and ARM307 and demonstrates the importance of an accurate reference for altimetry WSE validation.

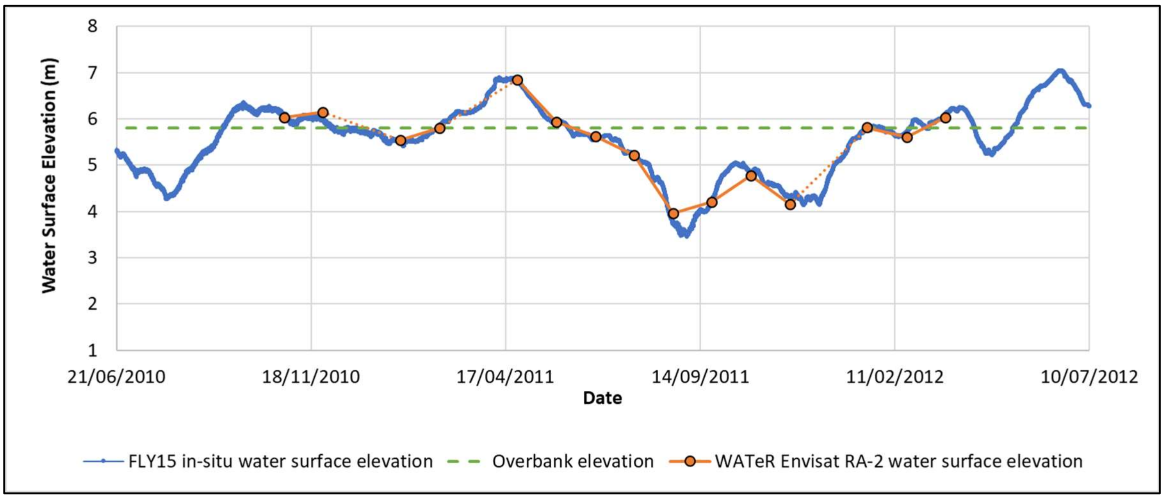

Figure 7-25 The WATeR WSE derived from Envisat RA-2 pass 0004 (new orbit) crossing of the Fly River at ARM218 and the FLY15 in-situ gauge WSE record. The data cover the significantly high water events that were evident in April 2011 as well as relatively low levels that were evident in September 2011.

While the WSE validation RMSE is better than that derived for the upstream locations, the lack of extreme low water measurements along with the relative absence of in-channel hooking has meant that these results may be considered optimistic with a slight degradation expected in the retracking accuracy of waveforms derived from pulse-limited nadir-looking altimeters for passes over narrow rivers under extreme low water conditions. Despite this, these results demonstrate that the WSEs derived using the WATeR altimetry retracking process offer a significant RMSE quality improvement compared with results reported for comparable complex heterogeneous wetland environments (Frappart et al., 2006; Santos da Silva et al., 2010; Jarihani et al., 2013; Maillard et al., 2015; Dettmering et al., 2016; Zakharova et al., 2020) with quality improvements of three to six times demonstrated in this study.

7.1.4 Envisat pass 0004 Fly River crossing—ARM410

In this section, the potential for altimetry-derived WSEs to be used to supplement an existing in-situ gauge network is explored. FLY10 is an in-situ gauge located at ARM435 on the Fly River, immediately downstream of the junction of the Ok Tedi and Fly rivers. The location of FLY10 relative to the Envisat crossing is shown in Figure 7-26.

While the FLY10 gauge has formed an integral part of OTML’s hydrology monitoring program, it was not operational between June 2004 and January 2018 as a result of landowner issues at the gauging site. Envisat descending pass 0004 crosses the Fly River at ARM410, approximately 45 km downstream of the FLY10 gauge, and it is proposed to use the altimetry-derived WSEs from this crossing to augment the FLY10 gauge data.

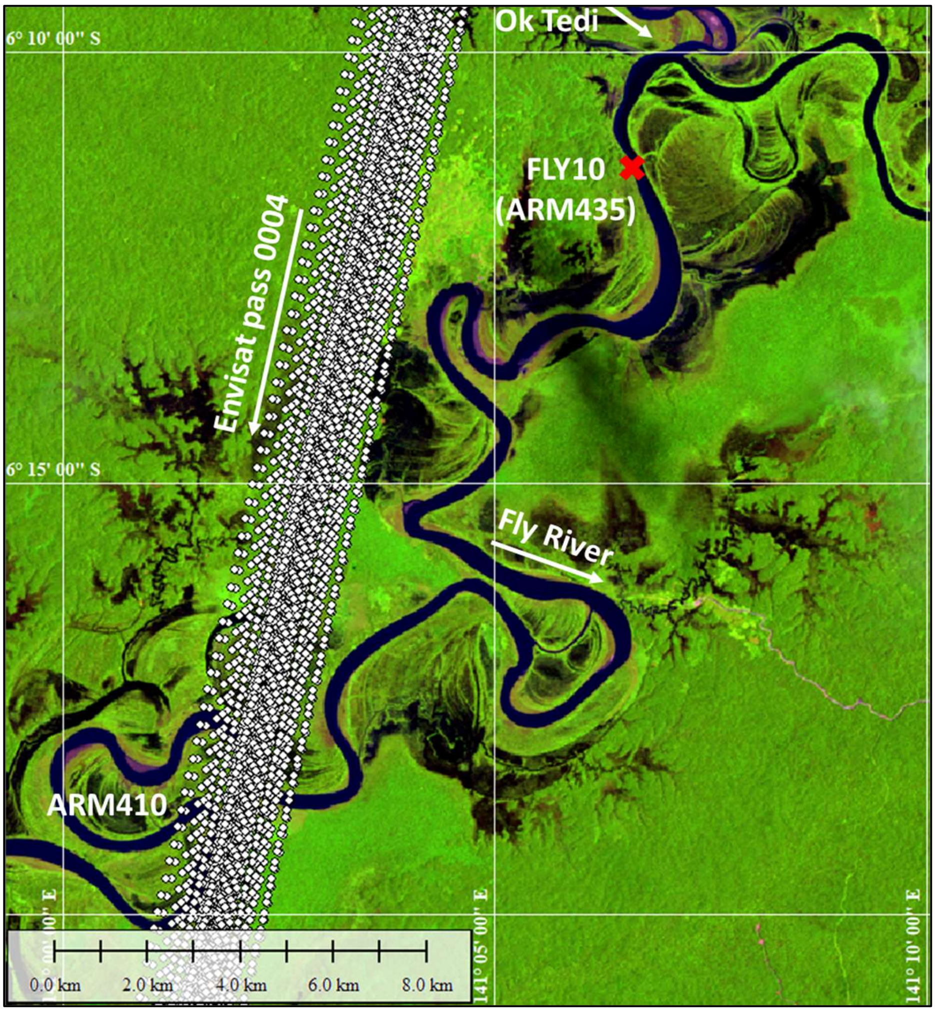

Figure 7-26 Envisat descending pass 0004 crossing the Fly River in the upper reaches of the middle Fly at ARM410 where average river width is 300 m; at the crossing site it drops to around 200–250 m. In-situ gauge FLY10 is located at ARM435, approximately 45 km upstream.

A virtual gauge was derived from the FLY10 hydrologic record and transformed to a virtual gauge using WSE measurements that had been acquired at the ARM410 site on an annual basis since 1998 during the monitoring of bed aggradation change through the reach (Marshall, 1998–2020). Two common observations between the in-situ gauge and survey WSE measurements were used in the transformation of the gauge WSE time series, resulting in an RMSE of 3.3 cm for the comparison between the calibration survey WSE and the derived virtual gauge, although this calibration is not representative of the full inundation range as both calibration estimates were acquired at relatively high river levels. WATeR altimetry retracking was undertaken on the 82 available cycles, with WSEs derived for all available cycles—apart from cycle 15 where significant hooking occurred, and without evidence that any peak within the waveform related to a main stem return, the cycle was excluded. The RMSE for the 10 cycles common to the existing in-situ gauge data was 16.1 cm and the SD from all retracked cycles, with each cycle involving a minimum of two observations, was ±8.6 cm. The SD is higher than that derived from Envisat RA-2 as detailed in Sections 7.1.2 and 7.1.3, probably because of the narrow river and the increased magnitude of unresolved hooking distortion evident in the derived WSEs. A review of the RMSE results for the comparison between the derived altimetric WSEs and the virtual gauge revealed relatively good agreement at higher river levels but a degraded result at lower river levels and during periods of rapid water level change. ARM410 is located in the upper reaches of the middle Fly and the variability in river level through this reach is typically higher than further downstream where backflow from the floodplain tends to dampen any rapid short-term river level fluctuations. The magnitude of the derived RMSE is a function of the increased difficulty in extracting reliable altimetric WSEs at the narrow ARM410 crossing as well as a reflection of the relative inaccuracy of the virtual gauge at lower stage height and when river levels are rapidly changing.

The ARM410 virtual gauge, WSE survey measurements and altimetric WSE time series from Envisat RA-2 descending pass 0004 crossing the Fly River at ARM410 are shown in Figure 7-27.

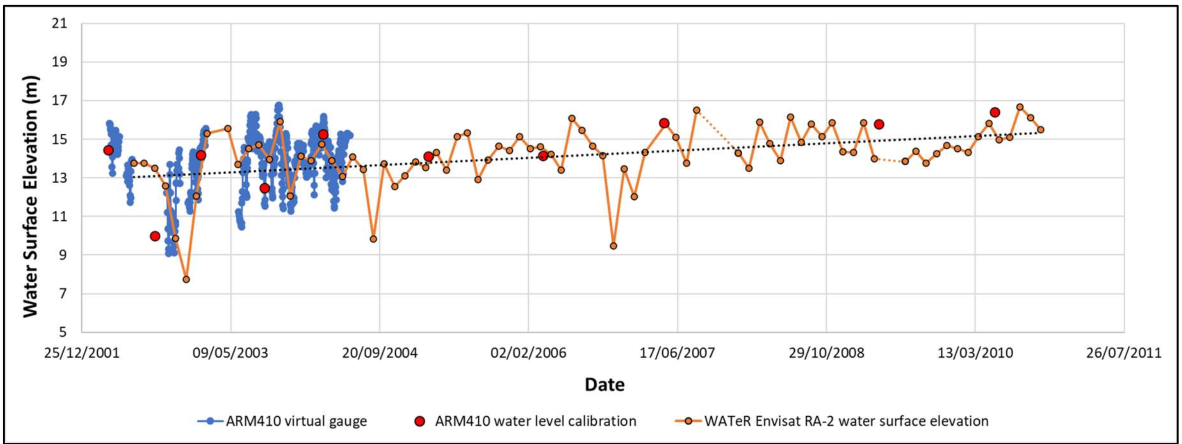

Figure 7-27 The ARM410 virtual gauge, WSE survey measurements and the derived altimetry WSE time series from Envisat RA-2 descending pass 0004 crossing the Fly River at ARM410. While lacking the short-term variability of the in-situ gauge, the altimetry WSE time series successfully identifies the major changes in WSE as well as the average river level rise (black dotted line in the time series) observed between 2000 and 2010. The derived WSE time series also correctly identifies the low water events that occurred in 2002, 2004 and 2006 with WSE time series consistent with those derived in Figures 7-15 and 7-21.

While lacking the short-term variability of the in-situ gauge, due to the repeat period of the altimetry time series, the altimetry WSE time series successfully identifies the average river level rise observed over the period 2000–10 at other Fly River in-situ gauge sites. The derivation of valid WSEs is particularly difficult during extreme low water events. However, the altimetry WSE time series for this site correctly identifies the low water events that occurred in 2002, 2004 and 2006 as identified in the validation investigations undertaken in Sections 7.1.1 and 7.1.2.

7.2 Lake water surface elevation validation and results

7.2.1 Envisat and SARAL pass 0677—Vataiva Lake

Vataiva Lake (cf. Figure 3-3) was introduced in Section 3.3.2 as a location where the potential for creating a virtual floodplain gauge based on an in-situ main stem gauge was assessed. The methodology for the creation of the virtual gauge, covering the period of Envisat RA-2 and SARAL/AltiKa altimetry acquisitions, along with virtual gauge validation was detailed. The RMSE for the difference between the measured and derived water levels at Vataiva Lake was 13.7 cm over the full inundation range and 7.8 cm if periods of extreme low inundation were excluded. Envisat and SARAL ascending pass 0677 tracks over Vataiva Lake and this allows for evaluation of the WATeR altimetry retracking process and validation for lake and wetland environments. While the lake is significant at the scale of the Fly River floodplain, it is considered relatively small, at 12–35 km^2 depending on floodplain inundation extent, compared with those in earlier studies; for example Jarihani et al. (2013), Yi et al. (2013), Schwatke et al. (2015a) and Villadsen et al. (2016).

Although no longer actively maintained, the ESA River & Lake database (ESA, 2012) contains altimetry WSE time series, derived from ERS-2, Envisat RA-2 and Jason-2 altimeters, for some of the world's larger river and lake systems. Several sites are located within the Fly River floodplain and one of these is located at Vataiva Lake. To benchmark the validation of the WATeR altimetry retracking, the River & Lake WSE data have been downloaded, converted to the OHD datum using the method described in Section 3.1, and compared with the derived Vataiva Lake virtual gauge WSE.

The retracking methodology used for the River & Lake WSE time series is documented in Benveniste et al. (2007) and Berry (2009). The retracking process commences with filtering within a River/Lake mask followed by waveform shape analysis and retracking. In this phase, individual waveforms are assessed using tests on waveform shape and power to establish whether the echo has originated from a water reflector. Complex and multi-peaked echoes are discarded. The retracking procedure used varies as a function of echo shape. In the final phase, individual waveforms are combined and averaged to give a single WSE estimate for each cycle (Berry, 2009).

Figures 7-28 and 7-29 show Vataiva Lake, the location of Envisat ascending pass 0677 and the locations of the River & Lake WSE measurements. While all locations are within the same water body at high inundation levels, the lake is segregated at lower levels with connection via a narrow tie channel, so a range of WSEs is possible for the site.

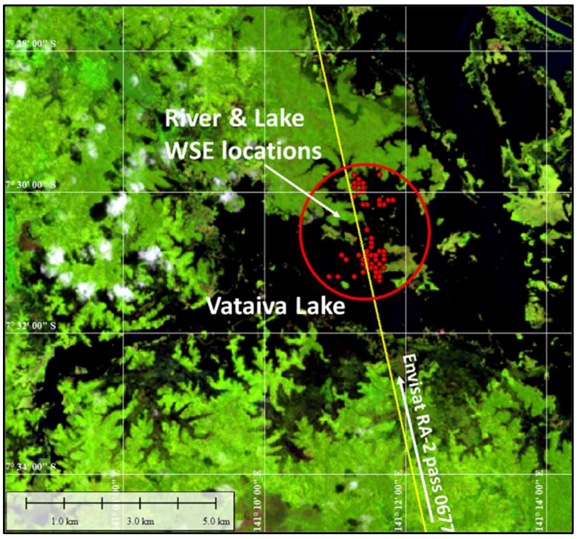

Figure 7-28 Vataiva Lake at high inundation with the location of Envisat pass 0677 and the River & Lake WSE locations. The background image is a false colour Landsat TM5 image captured on 29 March 2009.

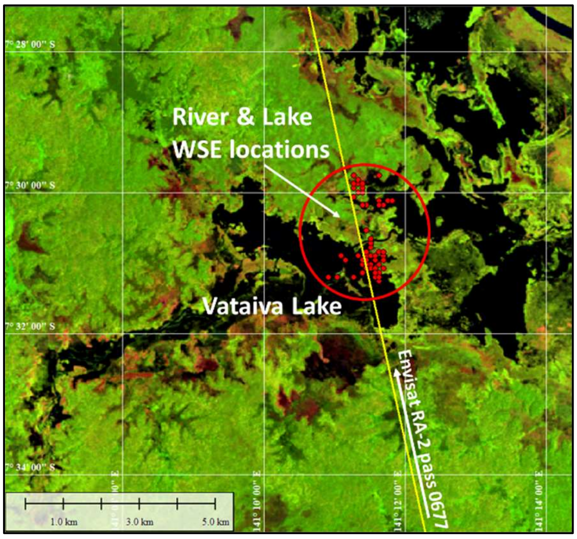

Figure 7-29 Vataiva Lake at median inundation with the location of Envisat pass 0677 and the River & Lake WSE locations. The northern sites of the WSE cluster are within a linked but separate lake system. The background image is a false colour Landsat TM5 image captured on 19 January 2007.

The results of the River & Lake retracking along with the Vataiva Lake virtual gauge WSEs derived from the FLY15 main stem in-situ gauge are shown in Figure 7-30. Of the 85 available Envisat pass 0677 cycles containing a valid SGDR record, 71 were retracked by River & Lake and, of these, 61 had a corresponding WSE in the virtual gauge record for validation. The resulting RMSE for the River & Lake WSE sequence was 35.9 cm. Based on the WSE range definition for FLY15 shown in Figure 7-24, the RMSE for River & Lake WSEs excluding the extreme low inundation range was 22.9 cm and this is a more likely WSE accuracy based on the results of the virtual gauge validation undertaken in Chapter 3, where reduced accuracy at low stage using the Vataiva Lake virtual gauge was expected. The results for low-to-high inundation are consistent with published results for small inland water bodies; for example, in Sulistioadi et al. (2015) where the validation RMSE was 21 cm for a 164 km^2 lake—although this is significantly larger than the 12–35 km^2 Vataiva Lake.

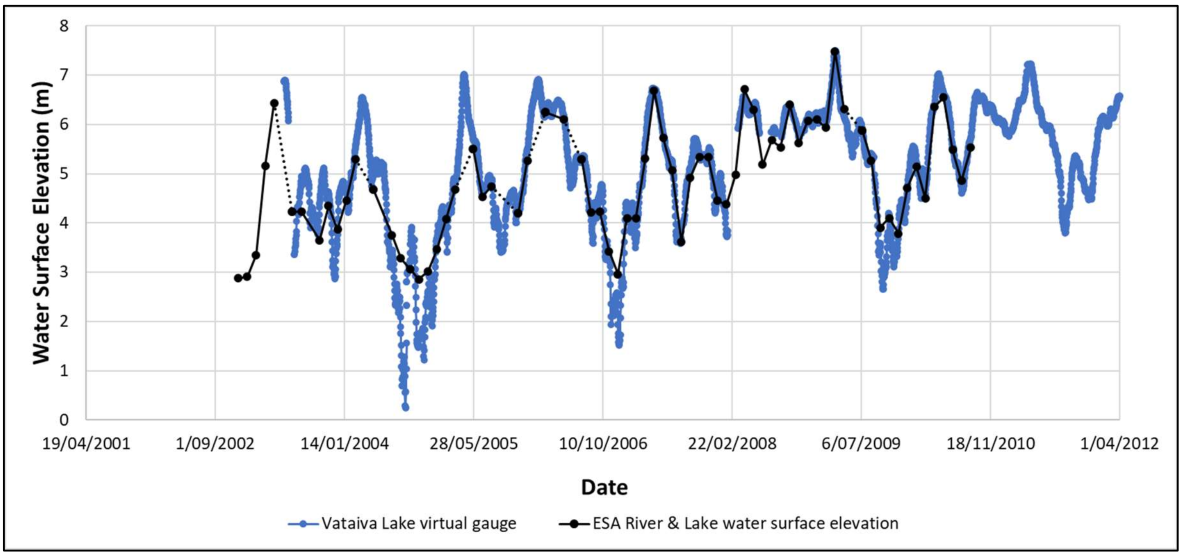

Figure 7-30 The River & Lake WSE profile derived from Envisat RA-2 ascending pass 0677 at Vataiva Lake along with the Vataiva Lake virtual gauge WSE time series, which was derived from the FLY15 main stem in-situ gauge. Dotted lines indicate periods in which cycles were omitted from the River & Lake analysis.

Figures 7-31 and 7-32 show the Envisat and SARAL coverage over Vataiva Lake. The Envisat coverage includes all 85 cycles acquired between July 2002 and October 2010. The SARAL coverage includes 26 cycles acquired between April 2013 and April 2016 with rain-affected and drifting cycles omitted. All available cycles have been retracked using the WATeR altimetry retracking process with the resulting July 2002–April 2016 WSE time series shown in Figure 7-33.

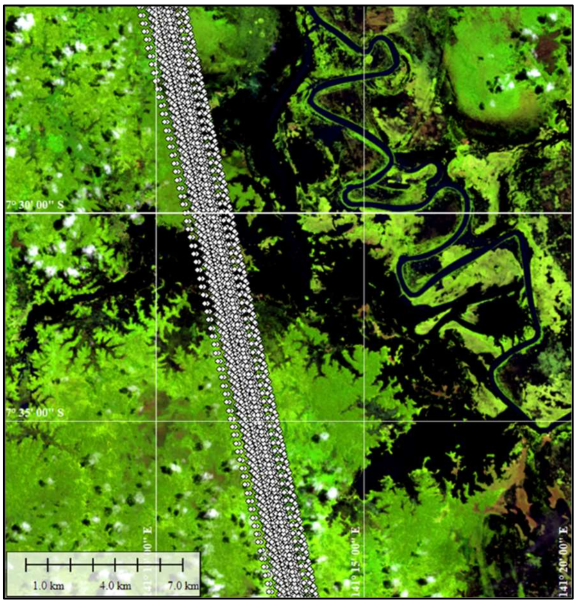

Figure 7-31 Envisat cycles from ascending pass 0677 acquired between 11 July 2002 and 7 October 2010 over Vataiva Lake. All 85 Envisat cycles are processed. The background is an ETM7 false colour image acquired on 28 March 2000 during a period of high floodplain inundation.

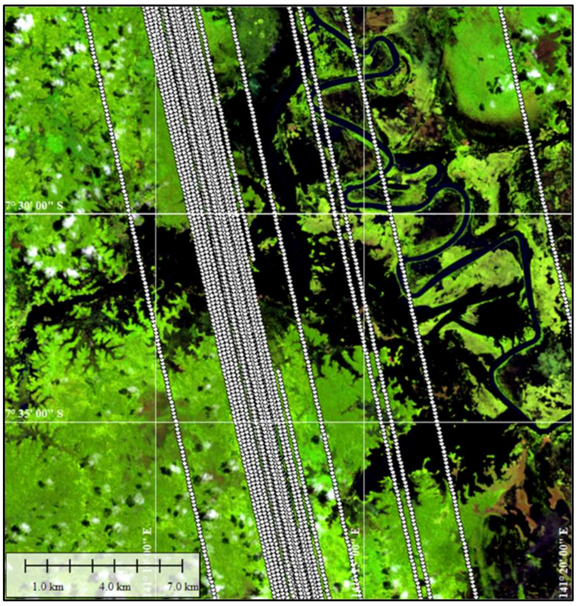

Figure 7-32 SARAL cycles acquired between 6 April 2013 and 30 April 2016. Cycles that drifted from the theoretical track, as well as one rain-affected cycle, have been omitted. A total of 27 cycles are processed in these analyses.

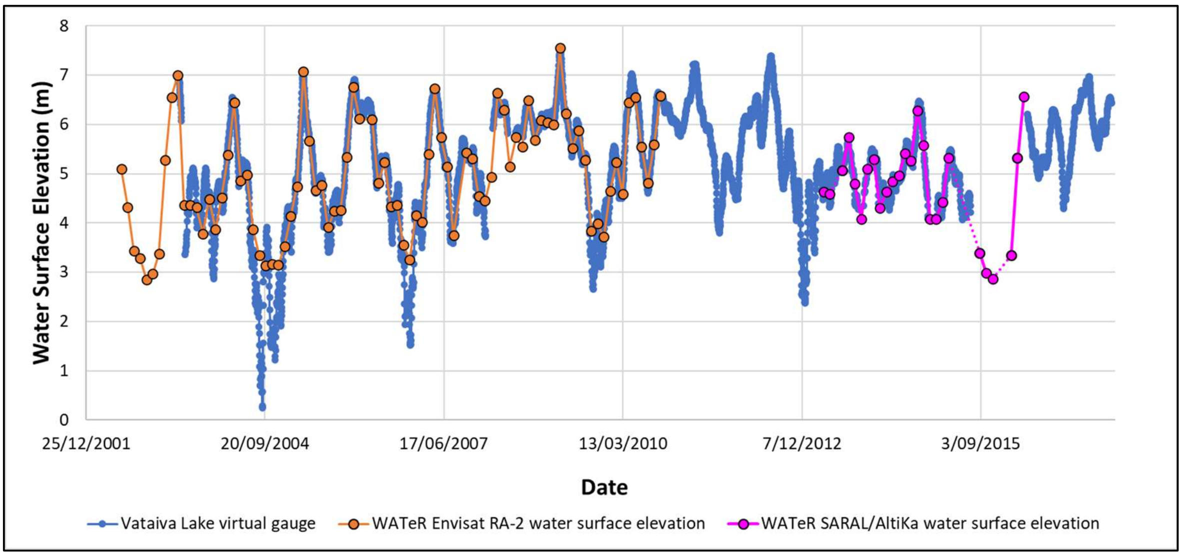

Figure 7-33 The combined Envisat RA-2 and SARAL/AltiKa WSE time series derived using the WATeR altimetry retracking process. The Envisat RA-2 cycles recorded at high water levels from May 2003, April 2004, April 2005 and January 2006, that were omitted from the River & Lake time series, have been retracked in these analyses. Dotted lines indicate cycles where the SARAL/AltiKa altimeter has drifted from the theoretical track and does not pass over Vataiva Lake.

The Envisat RA-2 SD for the sequence acquired between July 2002 and October 2010 was ±6.3 cm and this is consistent with other Envisat RA-2 validation results undertaken in this study. The RMSE for the full 85 waveform sequence was 35.9 cm, which is commensurate with the estimated Vataiva Lake virtual gauge accuracy detailed in Chapter 3 and is the same as the River & Lake-derived RMSE over the same waveform sequence.

The deficiencies in the Vataiva Lake virtual gauge for extreme low flow conditions recorded at FLY15 are confirmed in the WATeR results, with the majority of the significant differences in the RMSE analyses being observed at low WSE. Based on the WSE range for FLY15 defined in Figure 7-24, the RMSE for the WATeR WSEs in the low-to-high inundation range was 19.6 cm, which, although reasonably consistent with the River & Lake result, does constitute a 14% improvement.

The waveform sequence acquired from SARAL/AltiKa between April 2013 and April 2016 resulted in a SD of ±7.1 cm, which is approximately 10% higher than the SD for the Envisat RA-2 results but is consistent with the results from the SARAL/AltiKa river crossings at ARM305 to ARM311 detailed in Table 7-1. The results for this site are shown in Figure 7-33 although validation is not possible for the extreme low water conditions that eventuated during the 2015 El Niño. Validation has been undertaken within the low-to-high inundation range as defined in Figure 7-24.

The RMSE for the comparison between the Vataiva virtual gauge and the retracked WATeR WSEs was 9.3 cm, which provides important validation of the WATeR altimetry retracking process. Although a slightly optimistic result, as validation through extreme low water conditions has not been undertaken, it does constitute a significant improvement from the 50–100 cm RMSE results reported in Frappart et al. (2006), Maillard et al. (2015) and Zakharova et al. (2020), and approaches the altimetry SAR results reported in Nielsen et al. (2015) and Villadsen et al. (2016). The RMSE results for SARAL/AltiKa demonstrate a 30% improvement on the accuracy estimates for the SARAL/AltiKa river crossings at ARM307 documented in Section 7.1.2. At the ARM307 site the impact of saturated waveforms was high and, with removal of these observations, the number of candidate waveforms from which to derive WSEs over a relatively narrow river was limited. At Vataiva Lake, waveform saturation dominated through the very calm water zones at the land–water interface and significant hooking occurred through the rough water zones at the lake centre. Nonetheless, this still left a large number of candidate waveforms from which to derive accurate WSEs.

7.2.2 Envisat pass 0004 (new orbit)—Lake Murray water surface elevation profile

Envisat descending pass 0004 (new orbit) tracks over three inlets of Lake Murray, each zone separated by vegetated land but remaining part of the same larger water body. Figure 7-34 shows the 15 cycles for the period October 2010–March 2012, during which Envisat RA-2 was acquiring altimetry data in its new orbit.

Each cycle was divided into three zones and WSEs were derived using the WATeR altimetry retracking process for each of the lake crossings identified in Figure 7-34. The average SD and average number of observations for each crossing are listed in Table 7-3.

Based on these results, and considering the number of available observations for each cycle, there is scope to implement more stringent outlier detection criteria and to rectify minor unresolved hooking distortion, evident from the residual hooking hyperbola within the WSE profile of some cycles, to further improve the quality of the derived WSE profile.

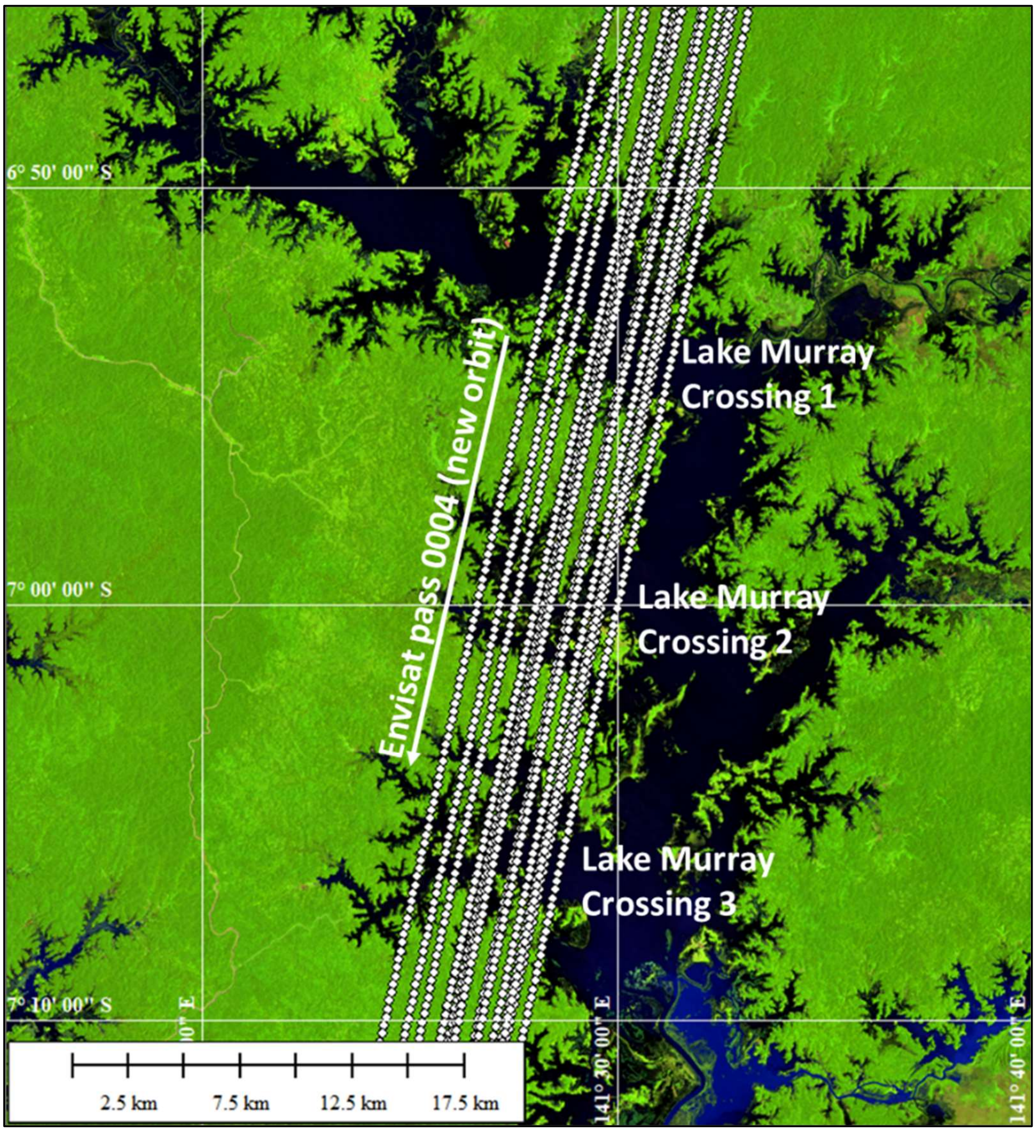

Figure 7-34 Envisat descending pass 0004 (new orbit) crossing over Lake Murray. The satellite passes over three inlets of Lake Murray with the lateral cycle spread being approximately 6 km for the 15 acquired cycles. The background is a Landsat TM5 false colour image acquired on 29 March 2009 during a period of high inundation.

Table 7-3 Average SD and average number of observations derived from the Envisat RA-2 waveforms for the altimetry pass over Lake Murray. Based on the number of available observations for each crossing there is scope to implement more stringent outlier detection methodologies to improve WSE estimates.

Location	**Average SD per cycle (cm)**	**Average number of observations per cycle**
Crossing 1	±3.5	23
Crossing 2	±4.5	18
Crossing 3	±6.1	23
Average	**±4.7**	**21**

Figure 7-35 shows the waveforms used in the WATeR retracking of the 15 Envisat RA-2 cycles over Lake Murray. Measurements were predominantly located through the inundated calm water zones and consisted of both quasi-specular and multi-peaked returns, from which the sub-waveform relating to the nadir return was used to calculate the WSE. Observations over open water zones, where significant hooking with no nadir return within the waveform was evident, were also used with the hooking hyperbola within the derived WSE profile used to rectify the distortion following the process documented in Section 6.1.2.2. Figure 7-36, showing Envisat RA-2 descending pass 0004 (new orbit) cycle 111 acquired on 21 January 2012, is an example of a cycle where this has occurred.

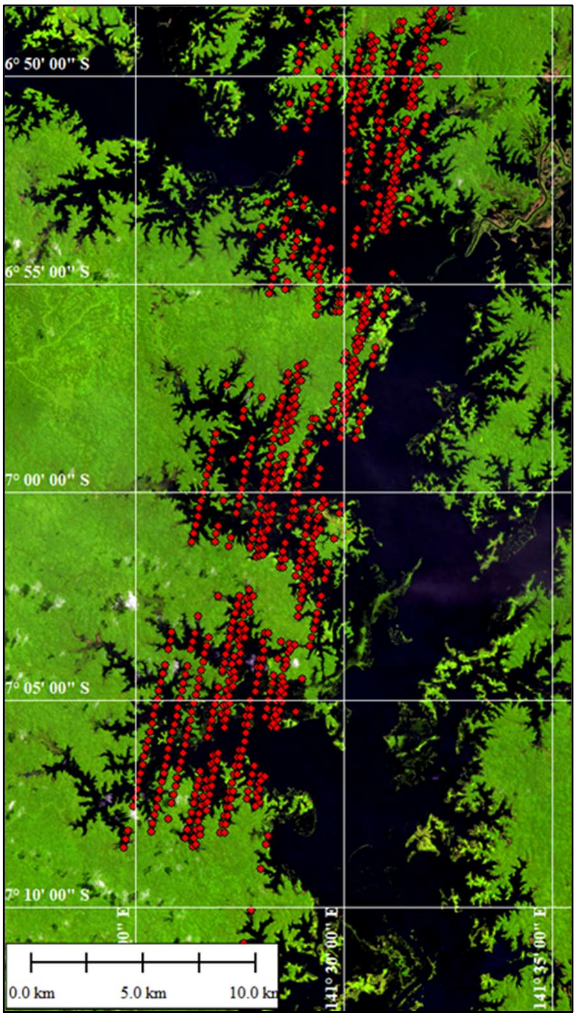

Figure 7-35 Waveform locations (shown as red dots) for the waveforms used in the WATeR altimetry retracking of the 15 Envisat RA-2 cycles over Lake Murray.

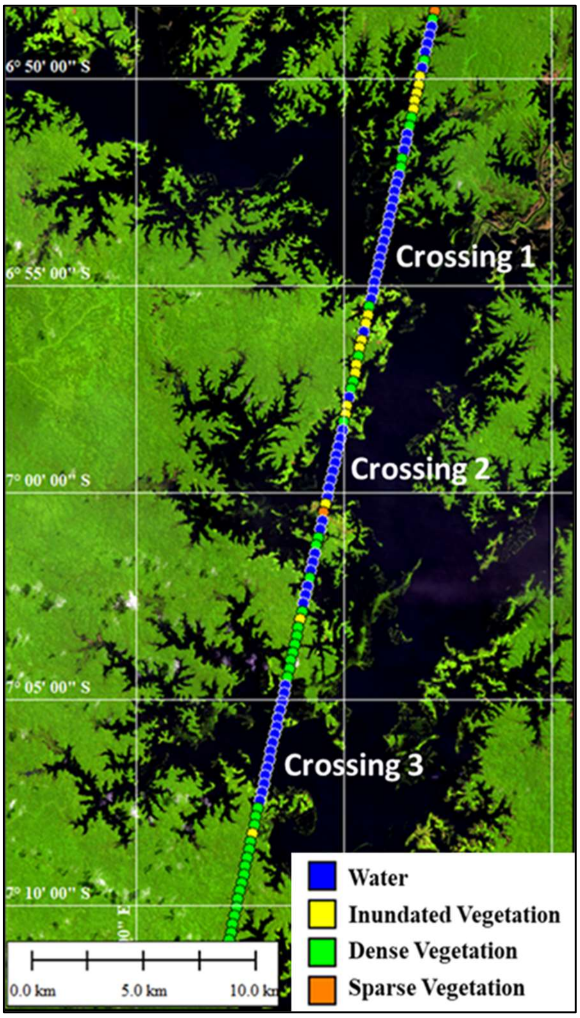

Figure 7-36 Envisat RA-2 descending pass 0004 (new orbit) cycle 111 acquired on 21 January 2012. Altimetry footprint classifications are highlighted.

Figure 7-37 shows the WSE profile derived using the Threshold Retracker for Envisat RA-2 descending pass 0004 (new orbit) cycle 111 acquired on 21 January 2012 over Lake Murray, with significant hooking hyperbolae evident. The hyperbolae were used to derive WSE estimates in the WATeR altimetry retracking process and although the waveform locations within Figure 7-35 are not highlighted, these hooked waveforms contributed to a valid WSE estimate located at the land–water interface.

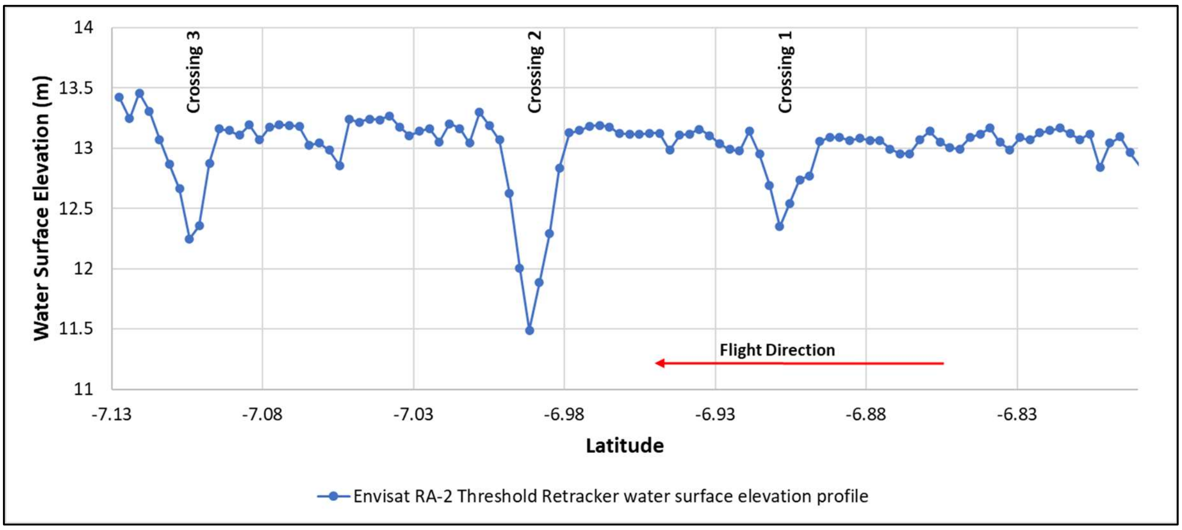

Figure 7-37 WSE profile for Envisat RA-2 descending pass 0004 (new orbit) cycle 111 acquired on 21 January 2012 over Lake Murray. Significant hooking hyperbolae are evident in the WSE profile derived using the Threshold Retracker. The hyperbolae were used to derive WSE estimates in the WATeR altimetry retracking process and, although the waveform locations within Figure 7-35 are not highlighted, these hooked waveforms contributed to a valid WSE estimate located at the land–water interface.

The WATeR altimetry retracking WSEs for all 15 cycles over Lake Murray are shown in Figure 7-38 in the form of a WSE profile.

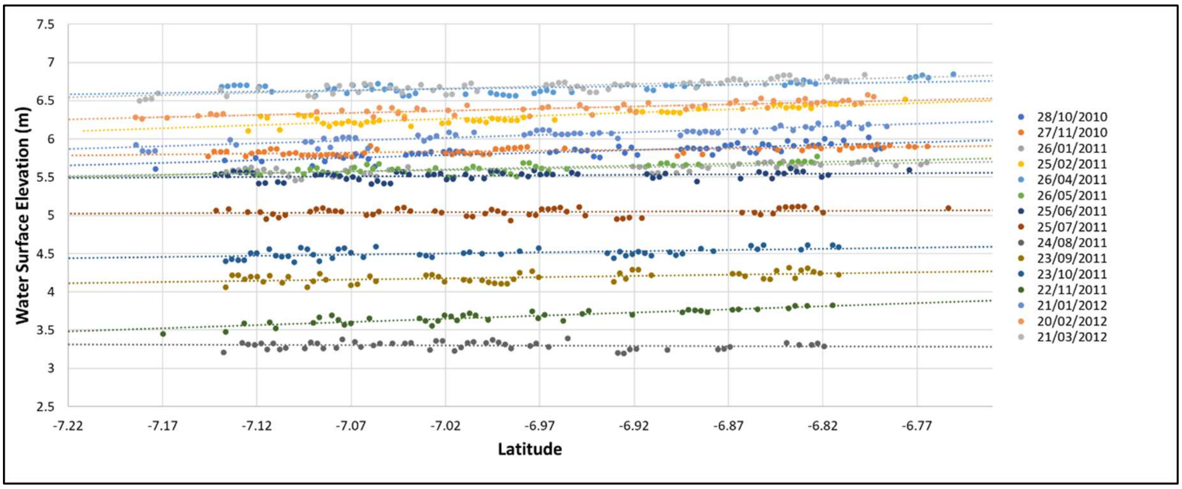

Figure 7-38 WATeR WSE profiles for each of the 15 cycles crossing Lake Murray acquired by Envisat RA-2 on descending pass 0004 (new orbit) between October 2010 and March 2012.

The results show that the lake has a predominant north–south gradient, which is consistent with the normal case of Lake Murray discharging water via the Herbert River into the Strickland River to the south. This gradient will, however, require validation and assessment of the quality of the geoid model used, before the altimetry data are used to monitor water fluxes within the lake.

In this study, the geoid slope over the lake has not been independently verified and so the accuracy of the defined lake gradient cannot be validated. It is noted that the geoid slope differs significantly between EGM96, EGM2008 and the PNG (Kearsley) definitions. The

Gravity field and steady-state Ocean Circulation Explorer (GOCE) satellite measures the earth's gravity field and models the geoid with high accuracy. It has been shown that the conversion of satellite-derived ellipsoid height to orthometric height using the GOCE geoid can be undertaken with 10-15 cm accuracy (Satishkumar et al., 2013) and this would resolve the current inaccuracies in orthometric height determination from the EGM96, EGM2008 and PNG (Kearsley) geoids. Despite the uncertainty with the geoid accuracy, and the associated uncertainty in the derived slope of the lake, this section aims to demonstrate the ability to derive consistent WSE profiles from satellite altimetry with the understanding that a geoid slope correction can be applied in a secondary process if required. The potential variability in lake slope derived from altimetric WSEs is highlighted in Figure 7-39, where WSE profiles were derived from cycle 97 of Envisat RA-2 descending pass 0004 (new orbit) over Lake Murray using the EGM96, PNG (Kearsely) and EGM2008 geoid models. The results show a significant difference in absolute WSE, with estimates using EGM96 and EGM2008 being approximately 1.5–2.0 m higher than those from PNG (Kearsley). The value of this offset is determined in the process of calibrating the altimetric WSE to the in-situ WSE and is applied for any conversion to the selected datum. The slope evident in the WSE profile cannot be rectified in this manner and requires independent calibration for geoid slope verification. For this example, both PNG (Kearsely) and EGM2008 were in close agreement with a geoid slope of 3.3×10^{-6} while there was a reverse slope of 1.5×10^{-5} evident from the EGM96 geoid model.

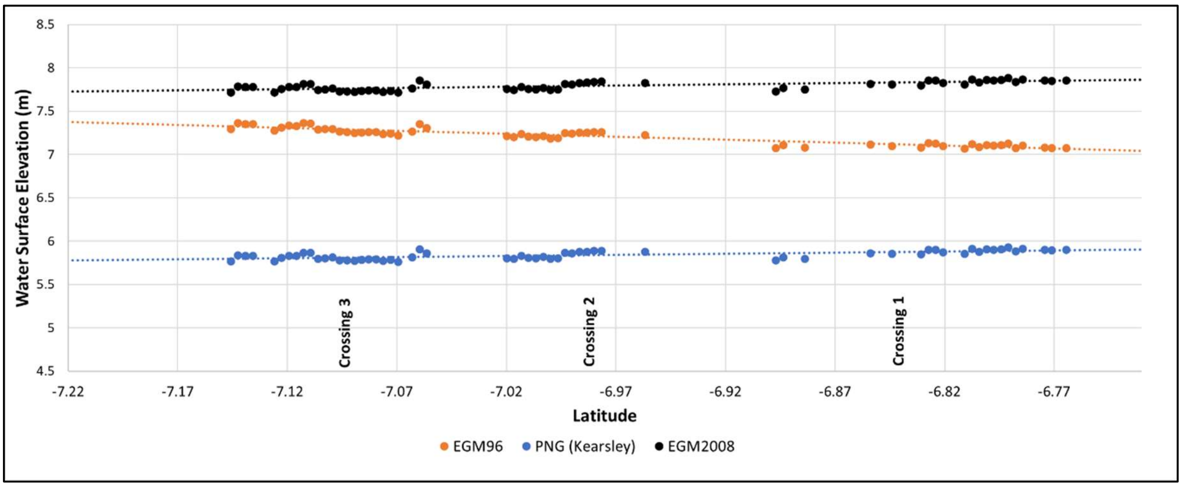

Figure 7-39 WSE profiles for Envisat RA-2 descending pass 0004 (new orbit) for cycle 97 acquired 27 November 2011 over Lake Murray. The WSE record has been derived using geoid models EGM96, PNG (Kearsley) and EGM2008.

For each cycle there is consistency between the WSEs derived at each of the lake crossings and this is supported by the moderate linear fit R of 0.89 for WSEs through the crossings, based on an overall SD of ±4.7 cm per cycle and an average of 54 WSE measurements per cycle.

Figure 7-40 shows the WSE time series for the three crossings of Lake Murray by Envisat RA-2 on descending pass 0004 (new orbit). There is evidence of a high degree of consistency in the observed slope of the lake, as defined by the relatively stable separation of the derived WSEs for each cycle. This offers the potential to detect the timing and magnitude of flow by assessing the change in WSE differences. During the low water period July–October 2011 there is evidence of significant flattening of the lake slope. This is likely due to periodic flow reversal through the Herbert River, as a function of backwater impact from the Strickland River, in conjunction with lower-than-average catchment rainfall during a drier period.

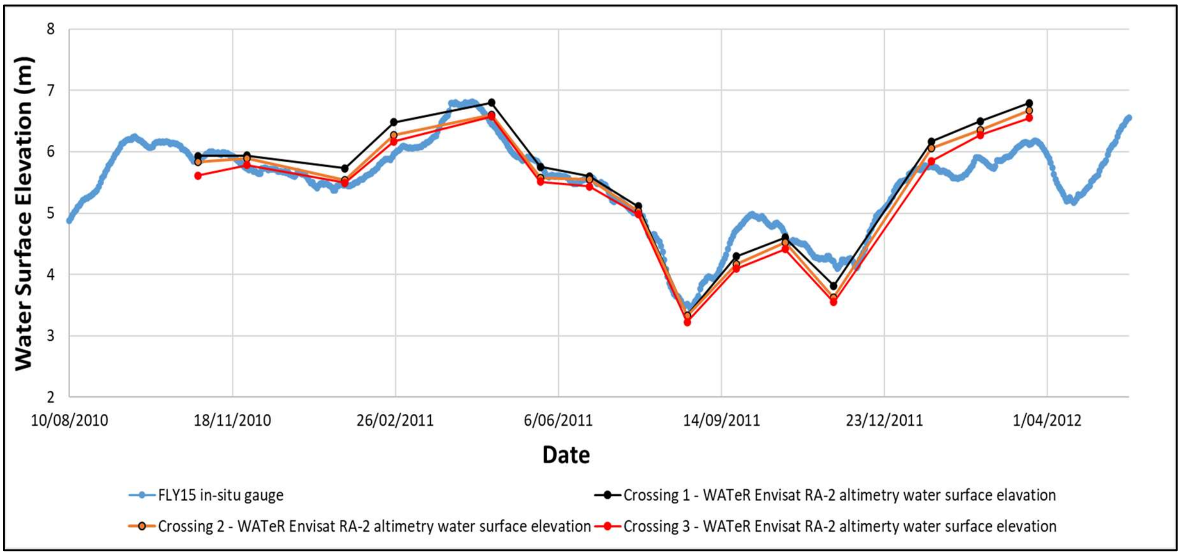

Figure 7-40 The WATeR altimetry WSE time series for the three crossings of Lake Murray acquired by Envisat RA-2 on descending pass 0004 (new orbit). There is evidence of high correlation between the derived WSEs for most cycles and the potential to detect the timing and magnitude of lake fluxes. The FLY15 WSE from the in-situ gauge at Obo shows relatively high correlation with the derived Lake Murray WSE time series; however, it was not used for any retracking validation as no in-situ reference data were available within Lake Murray to derive a reliable virtual gauge.

The FLY15 WSE from the in-situ gauge at Obo demonstrates high correlation with the derived Lake Murray WSE time series; however, it was not used for retracking validation as no in-situ reference data were available in Lake Murray to facilitate the derivation of a reliable virtual gauge.

Becker et al. (2014) demonstrated that floodplain gradients could be derived from the altimetric WSE record. However, Santos da Silva et al. (2014) found that river slopes calculated from altimetric WSEs derived over short distances would likely contain outliers. While the findings of Santos da Silva et al. (2010) are supported by the results from the river gradient studies of Section 7.1.2, the results of this section demonstrate that lake slopes can be reliably derived from altimetric WSEs. Multiple measurements that contribute to an estimate of slope facilitates the detection of outliers, as opposed to a river slope derived from a limited number of discrete measurements, resulting in a more accurate and reliable estimate of lake slope.

7.2.3 Cryosat-2—Fly River floodplain water surface elevation profile

Cryosat-2 SIRAL operates on a 369-day repeat cycle and, while it is not suited to derivation of hydrologic WSE time series for that reason, can be used to derive WSE profiles through a floodplain environment if the pass location is suitable. Such a pass is located in the centre of the Fly River floodplain passing over a multitude of lake, floodplain water bodies and river crossings. The location of this pass with respect to the study area is shown in Figure 7-1. The majority of cycles were within the average inundation range, however there was one cycle acquired during the high inundation period that occurred during the 2011–12 La Niña and one cycle acquired during the extreme low water period that occurred during the 2015–16 El Niño. Figures 7-41 and 7-42 show two cycles of a Cryosat-2 ascending pass (track 10419) acquired at high and low inundation extremes in January 2012 and January 2016 respectively.

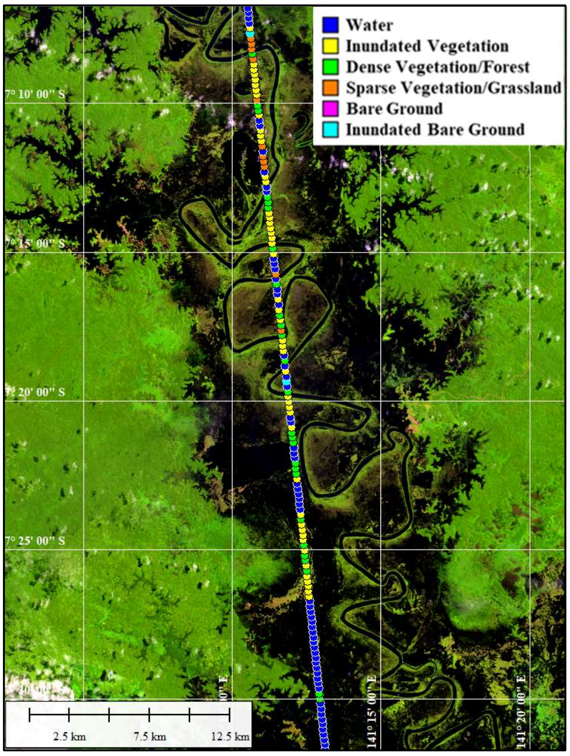

Figure 7-41 Cryosat-2 SIRAL cycle acquired during high floodplain inundation associated with a La Niña wet weather period on 13 January 2012.

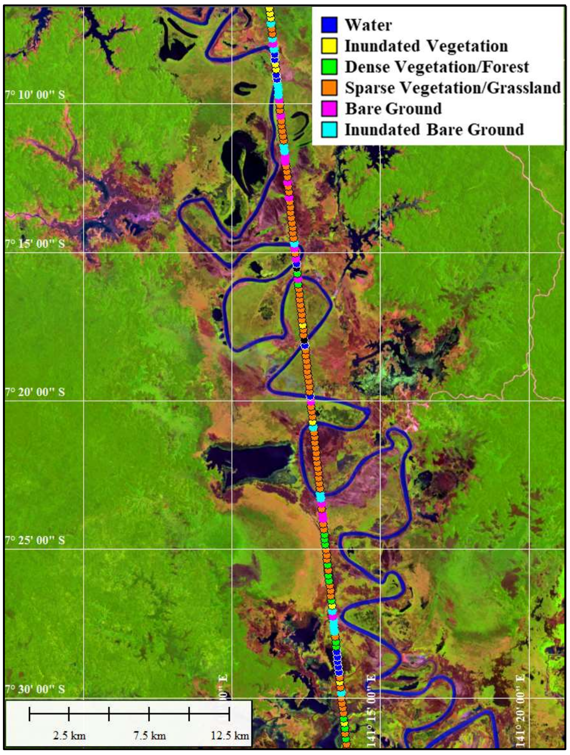

Figure 7-42 Cryosat-2 SIRAL cycle acquired during an El Niño dry weather period on 25 January 2016.

Using the WATeR altimetry retracking process, all cycles from Cryosat-2 SIRAL track 10419, acquired between 2010 and 2020, have been retracked with WSE profiles derived for each cycle through the inundated zones of the Fly River floodplain.

Figure 7-43 shows select WSE estimates, displayed in the form of WSE profiles, covering the full floodplain inundation range. The derived WSE profiles show the magnitude of inundation as well as the extent of water on the floodplain at the various inundation levels.

During the La Niña conditions evident in early 2012, virtually the entire floodplain was inundated, with the only voids in the WSE profile associated with passage over land. This is in contrast with the WSE profile generated during the 2015 El Niño where the only identified water returns were from river crossings and small permanently inundated water bodies.

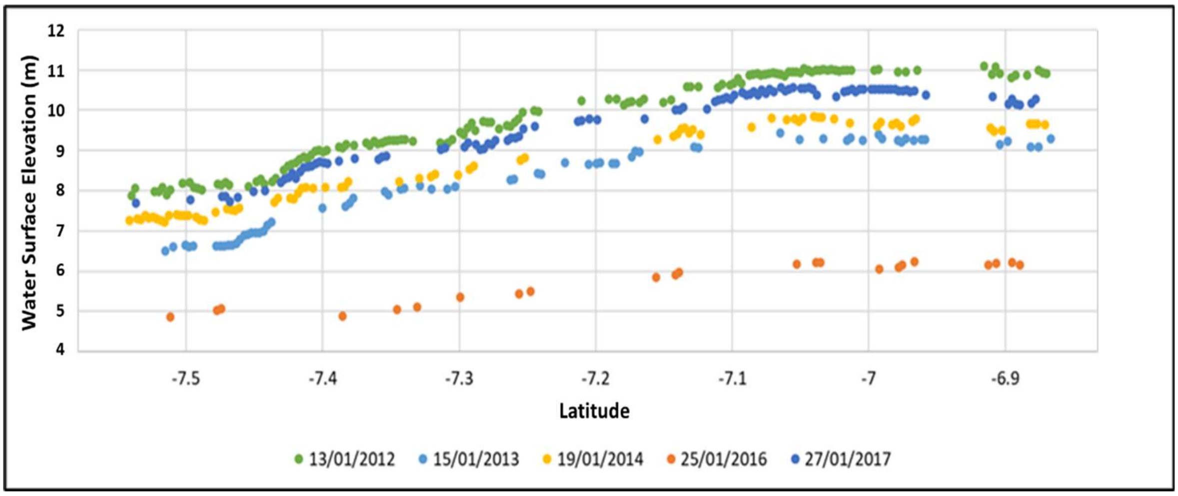

Figure 7-43 Cryosat-2 SIRAL WSE profiles through the Fly River floodplain for data acquired between 2012 and 2017 covering the extremes of the floodplain inundation range.

These analyses provide the greatest complexity in selection of valid WSEs as the process of using results from adjacent waveforms for quality assessment needs to be undertaken with care if the water bodies are separated by land, if the water body is small or if there is a slope to the water surface, for example through the inundated floodplain zone. The complexity in analysis is greatest during periods of low inundation where a limited number of water returns are available and where internal validation is problematic.

Development of robust processes to facilitate the reliable selection of valid WSEs in the creation of WSE profiles and integration of these processes into WATeR are areas for future research and development.

7.3 Summary

In this chapter, WSEs have been derived across a broad range of sites within a heterogeneous floodplain and wetland environment to assess the performance of the WATeR altimetry retracking process developed as part of this thesis. Data acquired by Envisat RA-2 and SARAL/AltiKa pulse-limited nadir-looking altimeters have been used in these validation investigations.

The precision and accuracy of the derived altimetric WSEs have been evaluated. The SD for Envisat RA-2 has consistently been in the range ±5–6 cm for both river WSE and lake WSE investigations, although extended to ±8 cm for the narrow river site at ARM410 in the upper reaches of the middle Fly. SARAL/AltiKa precision was of a slightly poorer quality at ±6–7 cm for both river crossings and lake WSE estimation. The impact of rain and cloud within the footprint of the SARAL/Altika footprint is known to attenuation the altimetry waveform leading to erroneous geophysical parameter estimates (Tournadre et al., 2009) and this, coupled with hooking and saturation, increases the analysis complexity of the SARAL/Altika waveforms for inland water crossings. SARAL/AltiKa waveform saturation was shown to be a significant issue for the relatively narrow river systems, where waveform returns from the main stem were typically saturated and therefore discarded, resulting in a significant reduction in useful waveforms for retracking and an associated increase in WSE uncertainty due to unresolved hooking distortion. Over lakes the issue of saturation was less significant because of a large number of candidate waveforms available for processing, meaning that saturated waveforms could be discarded without significantly affecting WSE estimation.

Accuracy of the WATeR retracking methodology was determined by comparison of the derived WSE with external references—both in-situ gauge WSE time series and discrete survey WSE measurements.

As part of the validation process, and to enable a direct comparison of results being achieved with those derived using alternative published methodologies, the WATeR-derived altimetry WSE estimates at an Envisat RA-2 pass 0004 Fly River crossing were compared with both a virtual in-situ gauge and results from Hydroweb retracking. At high water levels both the WATeR and Hydroweb estimates were in close agreement, with RMSE estimates at the level of the estimated virtual gauge accuracy. At low-to-median river levels the WATeR process proved to have significantly higher accuracy, with a fourfold improvement in RMSE compared with the Hydroweb results, demonstrating the capabilities of WATeR retracking through the lower inundation ranges.

At the Fly River crossings of Envisat and SARAL pass 0677 upstream of Manda, the RMSE for Envisat RA-2 and SARAL/AltiKa was 11.3 and 13.5 cm respectively. At the FLY15 in-situ gauge, where the Envisat pass 0004 (new orbit) crossing was directly overhead, the derived RMSE of 8.3 cm was only slightly higher than the SD. These results constitute a substantial improvement over results documented in related scientific publications as well as results derived in the quality analyses of WSE time series from global databases as undertaken in this study.

In this thesis, a virtual gauge covering the period of altimetry acquisitions for both Envisat RA-2 and SARAL/AltiKa was established at Vataiva Lake to facilitate validation of WATeR retracking accuracy. Based on these data, the RMSE derived for Envisat RA-2 over the low-to-high inundation range was 19.6 cm, and over the full range was 35.9 cm, which was consistent with the estimated virtual floodplain gauge accuracy. For SARAL/AltiKa the RMSE was 9.3 cm; however, while the validation covered the majority of the inundation range it did not include validation under extreme low inundation conditions. The SARAL/AltiKa result was a considerable improvement over the results from the Fly River crossing where adverse waveform saturation impacts were significant.

As additional validation, the retracking undertaken by ESA River & Lake was compared with the results from WATeR as well as the Vataiva Lake virtual gauge. An RMSE of 22.9 cm for the low-to-high inundation range and 35.9 cm over the full range were derived for the River & Lake estimates. These results were consistent with that of WATeR; however, only 71 of the 85 cycles were retracked by River & Lake. The WATeR analysis constituted a 19% quality improvement compared with River & Lake and resulted in WSEs derived over the full 85 cycle sequence.

A summary of the validation results from this chapter is provided in Table 7-4. The internal precision of the derived altimetric WSEs, represented by the SD of the observations; the fit of the derived WSEs to an external reference, represented by the altimetry RMSE; and the associated quality of the derived virtual gauge used to assess the altimetric data, represented by the gauge RMSE are tabulated. *R* values are tabulated for studies where a linear relationship between independent altimetry WSE estimates are available, for example in the definition of the water surface profile of Lake Murray and between the averaged WSE estimates for river crossings at ARM307.

Table 7-4 Summary of derived altimetry WSE quality assessments for river and lake crossings used in the validation of the WATeR altimetry retracking process. The results derived from the Hydroweb and River & Lake global databases for the ARM332 and Vataiva Lake sites and are shown in blue italics.

Location	Altimeter	SD (cm)	Altimeter RMSE (cm)	Gauge RMSE (cm)	R
ARM332	Envisat RA-2	±7.0	34.2 / 27.5 [1]	37.6 / 14.7 [1]	
	Envisat RA-2		*Hydroweb 142.0 / 23.7* [7]	"	
ARM307 Crossing1	Envisat RA-2	±5.5	11.4	10.0	
Crossing 2		±6.0	10.4	"	
Crossing 3		±4.8	12.1	"	
Average		±5.4	11.3	"	0.99 [2] 0.85
Crossing 1	SARAL/AltiKa	±6.5	13.7	"	
Crossing 2		±7.8	10.4	"	
Crossing 3		±6.5	16.5	"	
Average		±6.9	13.5	"	0.99 [2] 0.82
ARM218	Envisat RA-2	±5.1	8.3	0.0 [3]	
ARM410	Envisat RA-2	±8.6	16.1	3.3 [4]	
Vataiva Lake	Envisat RA-2		35.9 / 19.6 [1]	13.7 / 7.8 [1]	
	SARAL/AltiKa	±7.1	9.3 [5]	"	
	Envisat RA-2		*River & Lake 35.9 / 22.9* [8]	"	
Lake Murray Crossing 1	Envisat RA-2	±3.5			
Crossing 2		±4.5			
Crossing 3		±6.1			
Average		±4.7			0.89 [6]

Notes:

1. The first RMSE value tabled is for the full inundation range; the second excludes periods of extreme low water.
2. The first *R* value tabled is for the comparison between the WSEs for each cycle; the second is for the comparison between the derived river gradients for each cycle.
3. Envisat Pass 0004 (new orbit) tracked over the FLY15 gauge so no virtual gauge was created using available survey data.
4. The RMSE for the generation of the virtual gauge at ARM410 is derived from two median-to-high water survey calibration WSE readings.
5. The WSEs derived from the SARAL/AltiKa data at Vataiva Lake did not cover a period of extreme low water.
6. The *R* for the Lake Murray crossing is derived from the linear fit of the derived WSEs within the elevation profile.

7. Hydroweb - The first RMSE value is for the full inundation range; the second covers median to high flow conditions.
8. River & Lake – The River & Lake results are derived from WSEs for 71 of the 85 available cycles compared to the WATeR results which were derived from all available cycles.

The summary of validation results in Table 7-4 shows that there is a correlation between the RMSE of the derived altimetric WSEs and the quality of the virtual gauge. The establishment of quality virtual gauges is difficult to achieve if the virtual gauge location is at a significant distance from the in-situ gauge or if there is variable inundation between the two sites. Despite this, the validation undertaken in this chapter has successfully demonstrated the capabilities of the WATeR altimetric retracking process with significant improvements in retracking accuracy demonstrated over a range of heterogeneous inland water zones. This is particularly evident in the results from ARM218 where direct comparison could be made to an in-situ reference, resulting in a four to five times accuracy improvement compared with that reported and published for comparable complex wetland and floodplain environments (e.g. Frappart et al., 2006; Santos da Silva et al., 2010; Villadsen et al., 2016).

The estimation of accurate altimetry WSE has been shown to be most complex and challenging for the crossing of relatively narrow rivers under low flow conditions. The results of the validation detailed in Table 7-4 show a difference in WSE accuracy for low-to-high flow conditions compared with that for the full inundation range. While this can be attributed in part to virtual gauge accuracy, as discussed above, there will also be a component linked to the echo averaging process as discussed in Section 6.3. There is the potential for an elevated WSE estimate derived under extreme low flow conditions as a result of a shortened satellite-to-average-reflecting-surface range, which is derived from the averaging of the IEs acquired over both the inundated channel and the adjoining exposed bank landforms. This effect on the derived WSEs is recognised in the results for low water acquisitions in this study.

Additional studies have been undertaken to derive WSE over large open water systems, where hooking is known to be a significant issue, and in the derivation of WSE estimates to complement in-situ gauge data, derived from narrow river crossings where hooking distortion and ambiguity in WSE source identification are known issues. While no validation was undertaken for these studies, they demonstrate the capabilities of the WATeR altimetry retracking process to derive a wide range of data for hydrologic studies.

CHAPTER 8: CONCLUSION AND RECOMMENDATIONS

The pressure that population change, human impact and climate change are having on the allocation of, and access to, water creates the increasing need to monitor the world's water resources. The use of satellite radar altimetry for WSE time series measurement to augment the existing hydrology in-situ gauge network has been actively developed and researched over the past two decades. Many of these developments have been derived for pulse-limited nadir-looking altimeters; while these have been used successfully for ocean studies, they have had limited application over inland waters with most activities being related to research. The reason for this is twofold: first, the sparse spatial and low temporal coverage of the altimetry data, which limits hydrological applications; and second, the waveform contamination that occurs as a function of the varying terrain, vegetation and variable water states within the altimeter footprint for the majority of inland water locations. This contamination means that estimation of accurate WSEs is difficult, with achieved accuracy being at least an order of magnitude worse than that achieved over ocean environments and often worse than this for complex wetland and floodplain environments (Frappart et al., 2006; Villadsen et al., 2016). While the magnitude of this contamination is mitigated, but not eliminated, in currently operational SAR-based altimetry systems, a need was identified to develop methods that facilitate extraction of significantly improved WSE time series from archived data and support analysis of the data from currently operational altimeters into the future.

In this study, the performance of three of the pulse-limited nadir-looking satellite altimeters that have operated within the past two decades has been analysed. A study area within the Fly River floodplain of PNG was selected as it contained a significant variety of inland water types that would facilitate the development of flexible analysis methods. Few studies for complex wetland and floodplain environments such as this have been documented. While most satellite altimetry studies over inland waters have concentrated on larger river and lake systems, this research develops strategies and analysis methodologies targeted at genuine heterogeneous environments. Envisat RA-2, SARAL/AltiKa and Cryosat-2 SIRAL (LRM) altimetry missions were selected as their orbits offered extensive coverage of the Fly River floodplain and passed sufficiently close to the existing in-situ gauge network such that validation of any developed analysis methodology could be undertaken.

8.1 Research results

8.1.1 Altimetry footprint landform classification

It is recognised that the largest source of error for inland water altimetry is related to hooking (Benveniste and Berry, 2004; Berry, 2006), a distortion introduced into the derived WSE where specular reflectors within the echo footprint can lead to an off-nadir distortion (Santos da Silva et al., 2010). If not detected, this distortion will result in an over-estimate of the satellite-to-nadir range and an incorrect WSE estimate. In this study, it was identified that improved knowledge of the nature of the altimeter footprint was required to support the selection of waveform retracking methods and to guide any waveform analysis decisions that were implemented.

A flexible method for the accurate and automated assessment of the inundation status of an altimetry footprint and definition of the extent of vegetation cover was developed. The method integrates image analysis techniques with data from the altimetry retracking process to facilitate automated decision making to guide the retracking process. Satellite images are selected that represent the full range of inundation conditions expected over the floodplain. The imagery used in this study consisted of multispectral Landsat imagery, from which MIR, NIR and red bands are extracted, as well as Envisat and Sentinel-1 SAR imagery based on HH and VV polarisations. The acquisition dates are correlated with the in-situ gauge record and, for this study, imagery at low, median and high inundation conditions selected. Remote sensing techniques are then used to identify waveforms reflected from a water surface and to classify the nature of the nadir footprint of the altimetric echo. In this study, the classes used consisted of open water, inundated vegetation, dense forest, sparse forest/grassland, bare ground and inundated bare ground categories.

While classification of the nadir footprint of the altimetry echo can be undertaken successfully and robustly, there are cases where the nadir point is not the actual reflector for which the altimetric range is derived. Quasi-specular returns received from a non-inundated nadir footprint would indicate some degree of hooking. Additional image analysis to detect the nearest water source to nadir gives an estimate of the degree of hooking. This has meant that for every waveform, the proximity to water and the spatial extent of that water body is known, and this facilitates an automated decision making capability within the waveform retracking process. In conjunction with other measures, including waveform shape and backscatter coefficient magnitude, the classification of the nadir altimetry footprint has been used to assist in the identification, and in some cases rectification, of off-nadir distortion robustly and autonomously.

This method represents a significant improvement over the approach using classical waveform shape analysis or water body masking. For large flat floodplains and their associated river systems, the proposed image analysis methodology offers improved accuracy of selection of inundated sites. The process also offers potential for the inclusion of quality flags for directing additional investigation in which exposed or vegetated ground is identified at nadir for waveforms that demonstrate the classical shape of a calm water return so that the impact of any hooking distortion can be minimised.

8.1.2 Sub-waveform selection for the Improved Threshold Retracker

The Improved Threshold Retracker is an empirical retracker developed by Hwang et al. (2006) and based on the Threshold Retracker developed by Davis (1997). These retrackers are extensively used in inland water altimetry studies where the waveform shape of the altimetry echo does not conform to the Brown–Hayne form of typical ocean waveform returns. The Improved Threshold Retracker facilitates the retracking of complex multi-peaked waveforms by predicting the peak that relates to the nadir water body; effectively trims the waveform of secondary peaks leading into and from the selected peak; and then utilises conventional retracking to derive the leading edge, the corresponding retracked range and ultimately the WSE estimate relating to the sub-waveform.

The sub-waveform selection methodologies proposed by Hwang et al. (2006) have been further enhanced in this study where an a priori estimate of the WSE is derived from neighbouring quasi-specular waveforms that have been identified as having a calm water nadir footprint. While proximity improves the accuracy of the a priori estimate, it has been shown to be an effective method of sub-waveform selection from relatively large distances. The a priori WSE estimate, along with an analysis of the power differences between waveforms as proposed by Hwang et al. (2006), Bao et al. (2008) and Lee et al. (2008), are then used to identify and extract the sub-waveform. An additional improvement implemented in this study relates to the determination of the extent of the sub-waveform. Existing methods use a fixed number of gates either side of the selected peak; however, in this study, the sub-waveform extends from the troughs either side of the selected peak, meaning that the sub-waveform is less likely to be contaminated by returns from secondary off-nadir reflectors within the echo footprint.

8.1.3 Waveform Adaptive Threshold Retracker

The WATeR altimetry retracking process has been developed in this study to optimise the autonomous extraction of accurate water level time series from a variety of inland water targets. While incorporating the basic functionality of the Improved Threshold Retracker, WATeR utilises a range of ancillary information regarding waveform shape as well as external inputs, such as altimetry footprint classification, to guide the retracking process. In the manner of an expert system, following selection of processing criteria options, WATeR will undertake the remainder of the retracking process in a predominantly autonomous manner.

WATeR performs an initial pass of all waveforms in the sequence and, for each waveform, determines the retracked WSE using the standard Threshold Retracker as well as extracting a range of parameters related to waveform shape and structure. These parameters are then incorporated in a second pass that retracks the waveform based on either the full waveform or a sub-waveform, as a function of predictions undertaken following the first iteration. Different retracking processes have been developed for the various nadir footprint classifications, as these classes control the methods used to identify and rectify hooking distortion, the sub-waveform retracking method that is utilised and the process flow that is adopted for each waveform. Waveforms are automatically removed from the retracking process if they do not meet select conformance criteria. Some waveforms will retain a residual error from unresolved distortions, and these are flagged for rectification in a secondary process.

The proposed retracking process constitutes a deconstruction of the altimetry waveform and a micro-scale analysis of the impact of the receiving environment on the waveform structure. While aiming for an autonomous process, currently some facets require secondary intervention, such as statistical analysis of the WSE time series including outlier detection and the resolution of unresolved hooking distortions following the second iteration.

8.1.4 Waveform hooking

This study has confirmed that the most significant distortion affecting the echo return for wetland and floodplain environments is related to hooking. For a single off-nadir specular reflector, methodologies exist to resolve the hooking distortion; for example, those of Santos da Silva et al. (2010), Maillard et al. (2015) and Boergens et al. (2016) where a hyperbolic shape within a retracked WSE profile is used to estimate a single WSE located at the apex of the hyperbolic feature. In a wetland environment, there are likely to be numerous specular reflectors within the altimetry footprint and so, rather than an inverted hyperbolic shape resulting within the WSE profile, it appears to have increased variance, with little systematic pattern, as the hooking location varies with the passage of the altimeter over the wetland. In this study, methods have been developed that facilitate the detection of hooking; the waveform peak related to nadir return in the case of multi-peaked waveforms; and the location of the nearest calm water source to a quasi-specular return that has hooked to an off-nadir specular reflector. While there is some rectification of hooked waveforms, and some waveforms that have hooked are retained if the distortion is estimated to be minor, most waveforms that are identified are omitted from the waveform sequence if the magnitude and origin of the hooking are unknown. For wetland environments this is a significant advancement as it was likely to be unidentified hooked waveforms that contributed to the significant accuracy degradation over complex wetland and floodplain environments compared with altimetry studies over larger inland waters (Frappart et al., 2006; Santos da Silva et al., 2010; Zakharova et al., 2014; Maillard et al., 2015; Zakharova et al., 2020). Based on the results of this study, it is likely that additional rectification of waveforms subject to minor hooking will not significantly improve overall WSE accuracy. In addition, it is likely that a proportion of waveforms included in the WSE time series calculations contain no nadir signature, particularly for narrow river crossings, and this remains a residual error within the calculated altimetric WSE error budget.

8.1.5 Waveform saturation

The impact of SARAL/AltiKa waveform saturation on the derived WSE time series has been identified along with the correlation between distortion magnitude and the number of waveform gates affected. In this study, distortion magnitude ranged from 10 to 20 cm for two-peak saturation to approximately 80 cm for four-peak saturation. There are cases where this correlation is poor, so there are likely additional factors, including hooking distortion as well as rain and cloud effects, that influence the magnitude of the observed distortion. The saturation distortion manifests as an increase to the derived WSE while the hooking distortion manifests as a decrease to the WSE. There will be cases where both distortions occur within a waveform and this will result in the overall error reducing to some extent, however the magnitude of this has not been quantified in this study.

Investigations have been undertaken in this study to reconstruct the saturated waveform by projecting the shape of the leading and trailing edge to an intersection and then reprocessing using the Threshold Retracker; however, this process did not account for the magnitude of distortion observed. Because of the magnitude of the observed errors in derived elevations from the SARAL/AltiKa saturated waveforms, the WATeR retracking methodology adopted in this study omits waveforms with two or more saturated gates from the analysis and flags waveforms with a single saturated gate for review in the statistical validation following retracking. It has been shown in this study that saturated waveforms with a secondary non-saturated peak can still be used in the sub-waveform selection process, and they are retained regardless of the extent of the saturated peak.

8.2 Results from the WATeR altimetry retracking process

In this study, WSEs have been derived across a broad range of sites within a heterogeneous floodplain and wetland environment to assess the performance of the WATeR altimetry retracking process developed as part of this thesis. Results have been derived from Envisat RA-2 and SARAL/AltiKa pulse-limited nadir-looking altimeters and, although Cryosat-2 SIRAL data have been used in the investigations for the thesis, these data have not been used in the validation assessment because of the 369-day repeat period that has limited the statistical assessment potential of Cryosat-2 SIRAL results.

In this study, both the precision and accuracy of the derived WSEs have been evaluated. The assessment of precision has been undertaken using the SD of the observations. The SD for Envisat RA-2 has consistently been in the range ±5–6 cm for both river and lake WSE investigations although it increased to ±8 cm for the narrow river site at ARM410 in the upper reaches of the middle Fly. SARAL/AltiKa precision was of slightly poorer quality, at ±6–±7 cm for both river and lake WSE estimation. SARAL/AltiKa waveform saturation was shown to be a significant issue for relatively narrow river systems where waveform returns from the river were often saturated and therefore discarded. This resulted in a significant reduction in useful waveforms for retracking and an associated increase in WSE uncertainty associated with unresolved hooking distortion in a portion of the remaining waveforms. Over lakes, the issue of saturation was less significant because of a large number of candidate waveforms available for processing, meaning that saturated waveforms could be discarded without significantly adversely affecting WSE estimation. Waveform saturation is not the only reason for the lower accuracy of the SARAL/Altika WSE accuracy compared to that of Envisat RA-2 with waveform distortion resulting from cloud or rain within the Ka-band altimetric footprint known to result in the derivation of erroneous geophysical parameters.

Accuracy of the WATeR retracking methodology was determined via comparison of derived WSEs with an external reference—either in-situ gauge WSE time series or discrete survey WSE measurements. The derived RMSE from the comparison of the altimetry-derived WSE and the external reference was understandably larger than the SD estimate as it was contained an uncertainty contribution from both of the input sources. To correctly assess the derived RMSE estimates, considerable work has been undertaken to estimate the quality of the external references used in the validation process, primarily by direct comparison with survey WSE observation of higher accuracy than that of both the altimetry and in-situ gauge WSE time series.

As part of the validation process, and to derive a direct comparison of results being achieved using alternative external retracking methodologies, the WATeR-derived altimetry WSE estimates at an Envisat RA-2 pass 0004 Fly River crossing were compared with both a virtual in-situ gauge and the results from Hydroweb retracking. At high river levels, the WATeR and Hydroweb estimates were consistent, with RMSE estimates at the level of the estimated virtual gauge accuracy. At median-to-low water levels, the WATeR process proved to be of significantly higher accuracy with a fourfold improvement in RMSE compared with the Hydroweb results, predominantly as a function of the median and low flow improvements evident in the WATeR altimetry WSE time series. This study has highlighted the relative difficulty in extracting accurate WSEs at low water levels, in contrast to the relative ease at higher water levels; however the results of this study have demonstrated the ability of the WATeR altimetry retracking process to effectively undertake these analyses.

At the Fly River crossings of Envisat RA-2 and SARAL/AltiKa pass 0677 upstream of Manda, the RMSE for Envisat RA-2 and SARAL/AltiKa was 11.3 and 13.5 cm respectively. At the FLY15 in-situ gauge where the Envisat RA-2 pass 0004 (new orbit) crossing was directly overhead, the derived RMSE of 8.3 cm was only slightly higher than the SD. These results constitute a substantial improvement over results documented in related scientific publications as well as results derived in the quality analyses of WSE time series from global databases as undertaken in this study.

The validation of WATeR altimetric WSE accuracy for lake and off-river water body sites has been limited because of the absence of in-situ gauges within the floodplain that are required for quality assessment to be undertaken effectively. A significant effort has been directed at establishing a floodplain gauge that will facilitate validation of the altimetry WSE estimates over a heterogeneous lake region within the Fly River floodplain. A virtual gauge, covering the period of altimetry acquisitions for both Envisat RA-2 and SARAL/AltiKa, was established at Vataiva Lake to facilitate validation of WATeR retracking accuracy, predominantly for median-to-high inundation levels. Based on these data the RMSE derived for Envisat RA-2 over the low-to-high inundation range was 19.6 cm, and over the full range including extreme low-water events was 35.9 cm, which was consistent with the estimated virtual floodplain gauge accuracy over the same range. Over the 3-year period between April 2013 and April 2016, the SARAL/AltiKa WSE RMSE derived from the comparison of the altimetric WSEs and the virtual gauge was 9.3 cm. Although there was a significant El Niño during 2015, there was no in-situ WSE record for this period and so the derived RMSE does not include any contribution for extreme low water events. The SARAL/AltiKa result was, however, a considerable improvement over the results from the Fly River crossing where waveform saturation was significant. As additional validation at this site, the retracking undertaken by River & Lake was compared with the results from WATeR as well as the Vataiva virtual gauge. An RMSE of 22.9 cm for the low-to-high inundation range and 35.9 cm over the full range was derived for the River & Lake estimates. This result was consistent with that of WATeR; however, only 61 of the 85 cycles were retracked in the River & Lake data. In the WATeR analyses, WSEs were derived for the full 85 cycle sequence with an associated 14% quality improvement compared with the River & Lake analyses.

Additional studies have been undertaken to derive WSEs over large open water systems, where hooking is known to be a significant issue, and in the derivation of WSE estimates to complement in-situ gauge data, derived from narrow river crossings where hooking distortion and ambiguity in identification of the dominant reflector within the waveform are known issues. While no validation was undertaken for these studies, the internal assessment of quality demonstrates the capability of the WATeR altimetry retracking process to derive a wide range of data suitable for hydrological studies.

In a large and complex floodplain and wetland system it can be difficult to demonstrate the capability and accuracy of WSE estimation methodologies because of logistical constraints on the generation of reliable and accurate in-situ data for validation. For this study, a select range of in-situ data sources has facilitated the verification of the capability of the developed WATeR retracking methodology, and this has been illustrated over a range of inland water types within a heterogeneous wetland and floodplain environment. The estimation of WSE time series from conventional pulse-limited nadir-looking altimeters using the WATeR altimetry retracking processes has been demonstrated in this thesis with results showing a substantial validated accuracy improvement compared with published results over similar inland water environments.

8.3 Recommendations for future research

The evolution of research in satellite altimetry and the development of analysis methods, particularly for the extraction of WSE over inland waters, has been a gradual process with numerous small steps, particularly in the field of waveform retracking, over the past two decades. In this thesis, additional steps have been added to improve the overall process; however, other key areas have been identified as requiring additional investigation. These areas have been evaluated in part in this thesis and the requirements in terms of future understanding have been documented. The areas that have been identified do, however, require targeted investigation to derive specific solutions to the problems identified.

a) Waveform saturation has been demonstrated to be a significant problem in the extraction of accurate WSE over heterogeneous inland waters, particularly where water levels are low and there are competing specular surfaces within the altimetric footprint. SARAL/AltiKa, in particular, has been shown to regularly suffer from waveform saturation and, although not identified in either Envisat RA-2 or Cryosat-2 SIRAL data in this study, this has been reported in data derived from other pulse-limited nadir-looking altimeters. In this study, the existence of saturation within a waveform has been identified, the number of gates within the waveform that are impacted extracted and the contribution to the WSE error budget estimated. While this study identifies the correlation between the number of gates impacted and the magnitude of the saturation distortion error, it has not progressed the analysis such that the saturated waveform can be rectified and accurately retracked, but flags the waveform to be excluded from WSE determination. Where there are multiple candidate waveforms available for the derivation of a WSE—for example, over larger lakes or inland water bodies—the exclusion of saturated waveforms has little impact. However, for measurement over narrow rivers where there is a limited number of candidate waveforms for WSE determination, the exclusion of saturated waveforms can potentially result in no waveforms being available for the site. A future research activity would involve a targeted study of the relationship between the number of gates within a waveform impacted by saturation, the magnitude of the saturation distortion on the WSE and the compounding impact of both hooking distortion and rain or cloud attenuation. The aim would be to develop a process to understand the impacting distortions, estimate distortion magnitude and rectify the waveform such that accurate retracking and WSE estimation could be undertaken.

b) The aim of measurement of WSE time series for an inland water body or at a narrow river crossing is to have several WSE measurements contributing to each entry in the final time series. The inclusion of multiple estimates will generally result in a more accurate final WSE value, unless the return is related to off-nadir secondary reflectors within the echo footprint, and this enables calculation of measurement precision and for simple outlier detection strategies to be undertaken. This is not the case for the measurement of WSE profiles where each observation needs to be classed as an independent node in the WSE sequence. For larger inland water bodies or lakes, the water surface gradient will be small enough so that it can be ignored for a sequence of three to four waveforms and these observations could be processed in a manner similar to that adopted for WSE time series. In floodplain and wetland environments there is likely to be a significant gradient in the predominant direction of river flow, as well as a significant number of smaller water bodies and river tributaries that can potentially have different WSEs. In these cases, each WSE estimate needs to be kept as a discrete measurement; however, this reduces the ability to derive quality assessments for the observations. While WSEs could simply be consolidated if the derived height agreed with estimates from neighbouring returns, this does not necessarily facilitate the ability to derive separate WSEs for each floodplain water body covered within the profile. The image analysis processes developed in this thesis have been used to assist with echo footprint classification in the generation of WSE profiles, but additional research is required to improve the process and methodology for selecting WSEs that are estimated to be returns from the same water body and therefore consolidated. This will require the development of methods using image analysis, as well as waveform shape and echo return characteristics, so that waveforms can be selected for consolidation if appropriate.

c) In this study, the retracking processes utilised have resulted in a significant improvement in the accuracy of WSE measurement compared with that reported for similar environments (e.g. Frappart et al., 2006; Jarihani et al., 2013; Zakharova et al., 2014; Maillard et al., 2015), where accuracies range from 50 to 100 cm for wetland and similar complex environments. While accuracies reported in this study are relatively consistent across the whole inundation range for lakes and off-river water bodies, there is considerable variation in reported accuracy for rivers, and particularly for narrow crossings. This additional uncertainty is likely related to the accuracy of the virtual gauge required to validate the altimetry WSE; however, it is also likely that there is a component related to waveform contamination, possibly in the waveform averaging process, where the water return is biased by landform on either side of a deep river channel. Improved virtual gauge accuracy, with associated quality assessment, will facilitate the targeted assessment of waveform structure that exists for low flow conditions with the aim of improving the retracking process for this portion of the inundation range, and to consequently improve the quality of the derived WSE time series.

d) This study has confirmed that the most significant distortion affecting the echo return for wetland and floodplain environments is related to hooking. Although a significant advancement in this study relates to the accurate detection of waveforms subject to hooking, there is uncertainty regarding the benefit of pursuing rectification of waveforms subject to minor hooking. Additional research using the identified nearest calm water source as the hooking location and development of off-nadir retracking methodologies such that WSEs can be derived for these cases is recommended. If the derived WSEs are consistent with other estimates within the WSE sequence they could be used in the final analyses rather than being discarded. It is likely that a proportion of waveforms included in the WSE time series calculations contain no nadir signature, particularly for narrow river crossings under low flow conditions. These waveforms will contain some residual hooking distortion and measures to identify such waveforms and estimate their impact on WSE accuracy requires investigation.

e) The research has focussed on the altimetric data generated from the Envisat RA-2, SARAL/AltiKa and Cryosat-2 SIRAL (LRM) altimeters however, the processes developed in this research can be readily applied in the retracking of data from other pulse-limited nadir-looking satellite altimeters. Retracking altimetric data from Jason-2 and ERS-2 would mean that accurate and continuous WSE time series dating back to 1995 could be created. If Topex/Poseidon and ERS-1 data were also retracked then the time series would span back to 1992. Some of these data are likely to be unsuitable due to acquisition issues over land, however the retracking methods developed in this research offer the potential to identify corrupt data and to optimise the extraction of reliable WSE time series. Future work is planned to verify the suitability of the research for other pulse-limited nadir looking altimeters and to formulate altimeter specific retracking guidelines if required.

Over the past decade the focus in altimeter design has been to incorporate SAR techniques that give high along-track resolution over relatively flat surfaces. The magnitude of the hooking distortion is significantly reduced in SAR altimeters due to the greatly reduced size of the altimetry footprint compared to conventional pulse-limited nadir-looking altimeters. Despite this there is scope to apply the methods detailed in this research to data derived from SAR altimeters, resulting in improved accuracy and reliability in the derived WSE time series or other hydrologic data products. Sentinel-3 offers scope to further enhance capabilities by linking the output of the SAR altimetry with the onboard Ocean and Land Colour Imager (OLCI) such that the altimetry waveform and waveform footprint classification can be undertaken without needing to consider temporal offset issues. The performance of Sentinel-3 SAR altimetry over the Fly River floodplain will also be processed, concentrating on relative narrow crossings of the Fly River, in order to document the performance of SAR altimetry compared to pulse-limited nadir looking altimetry, to assess the magnitude of hooking distortions within SAR altimetric data and to assess the benefits of using the WaTER retracking methodology in retracking data from SAR altimeters.

f) In 2021 the SWOT mission, which is designed to make the first global high-resolution survey of the Earth's water surface and measure how water bodies change over time, is due for launch. The developments in this thesis offer the potential for assisting with SWOT validation studies (Chen et al., 2018), particularly those planned for wetland and floodplain environments. Simard (2017) notes that SWOT's capabilities and limitations in coastal wetlands remain to be assessed as these are complex systems characterised by a mosaic of various vegetation types covering the water surface and are interspersed with numerous rivers and channels of different sizes. With the changes predicted to impact the Fly River floodplain over the next 50 years (Pickup and Marshall, 2009; Pickup and Marshall, 2019) the SWOT mission offers the opportunity for altimetry studies to be undertaken, potentially as part of a validation program within the Asia/Pacific region, and to generate data that will improve understanding of human impact on wetland environments into the future.

8.4 Proposed scientific exploitation of the altimetric data

This research facilitates the extraction of reliable and accurate long-term data from satellite altimeters relating to water level changes in a complex wetland environment. The research has particular significance for the Fly River floodplain where anthropogenic factors are likely to be the primary driver for accelerated change to the floodplain inundation regime. Although climate change will be a factor, the dominant effect will be the inundation changes that are predicted to occur over the next 50 years due to riverbed aggradation associated with mining. Bed aggradation is predicted to lead to significantly increased floodplain inundation levels well past mine closure. There will be an increasing need to monitor water level change through the Fly River floodplain to support local communities with information regarding changes to inundation that could lead to potential impacts on their communities and subsistence livelihood.

With this research, there is now the capability to derive long term historical WSE time series dating back to 1992. While this does not pre-date mining operations it does coincide with the first observed impacts within the Fly River floodplain. Although there are several in-situ gauges on the main stem, the WSE time series from these gauges is incomplete and this research has demonstrated the potential to accurately derive WSE time series to complement the in-situ record, particularly during periods of low river level where the main stem gauges have routinely failed.

For portions of the floodplain that are covered by the satellite track, the research demonstrates the capability to accurately discriminate individual water body entities and to derive separate WSE estimates for these water bodies. Rather than relying on one or two isolated main-stem gauges, the research facilitates the creation of multiple long-term virtual gauges covering a wide range of water bodies within the floodplain. This offers the potential to accurately quantify changes to floodplain inundation levels as well as derive floodplain fluxes, allowing for the prediction of potential change to vegetation communities and to land that is used for settlement as well as hunting and gathering.

Significant research is currently undertaken by OTML to model sediment transport as well as floodplain inundation within the middle Fly floodplain. An immediate application of the results of this research will focus on the calibration of the model outputs to improve the quality of inundation predictions.

With a transition to SAR altimetry into the future, the impact of hooking is predicted to decrease but is not likely to be negated. This research offers the potential for the retracking of SAR altimetric data using a methodology consistent with that used for the conventional pulse-limited nadir looking altimetric data. The ability to accurately identify and discriminate the various water bodies will continue and this means that future WSE time series can be generated with the same rigour as the conventional altimeter data sets from the past that have been retracked using the WATeR methodology. Following OTML mine closure it is unlikely that in-situ hydrological monitoring will continue within the Fly River floodplain. Remote monitoring of hydrological change, based on reliable altimetric processing, in the post-mine closure period when inundation levels are predicted to continue increasing, is a significant potential application of this research.

In addition to WSE time series, this research facilitates the generation of WSE profiles across the floodplain. With the resolution of geoid uncertainties, potentially through the use of GOCE based geoid data, water surface gradients and therefore water flow paths can be measured. Floodplain flow characteristics are important in determining the passage of water, and hence sediment, throughout the floodplain and the derivation of WSE profiles from altimetric data will assist with the assessment of environmental impacts of these sediments.

A wetland environment is typically relatively flat and there exists the need to have accurate WSE observations to be able to interpret change and understand system hydrology. The historical accuracies of altimetric time series derived over wetland environments have been reported to be in the order of 50 cm and this would not allow for the interpretation of hydrological processes for the Fly River which has an average gradient in the order of 3.2×10^{-5}. Based on the results of this research, altimetric WSE time series and profiles can now be derived with accuracy and reliability compatible with the assessment of Fly River hydrological processes. This facilitates the creation of long term historical data sets at multiple sites throughout the floodplain with updates into the future that facilitate a range of hydrologic monitoring and modelling activities within the Fly River catchment.

While the above activities specifically target immediate applications within the Fly River floodplain, the research can be readily applied to varied metrology applications at other inland water sites to improve the quality, reliability and abundance of historical and future WSE data at a wide range of sites across the globe.

REFERENCES

Abazu, I., Md Din, A. H. & Omar, K. 2017. Mean dynamic topography over Peninsular Malaysian seas using multimission satellite altimetry. *Journal of Applied Remote Sensing,* 11(2), 1-16. doi:10.1117/1.JRS.11.026017

Abileah, R., Scozzari, A. & Vignudelli, S. 2017. Envisat RA-2 individual echoes: a unique dataset for a better understanding of inland water altimetry potentialities. *Remote Sensing,* 9, 605-627. doi:10.3390/rs9060605

Abileah, R., Vignudeli, S. & Scozzari, A. 2014. The near-specular altimeter waveforms of small inland water bodies. European Space Agency, *8th Coastal Altimetry Workshop*, 23–24 October 2014, Lake Constance, Germany, 32pp.

Amarouche, L., Thibaut, P., Zanife, O. Z., Dumont, J. P., Vincent, P. & Steunou, N. 2004. Improving the Jason-1 ground retracking to better account for attitude effects. *Marine Geodesy,* 27, 171-197. doi:10.1080/01490410490465210

Andersen, O. B. & Scharroo, R. 2011. Range and geophysical corrections in coastal regions: and implications for mean sea surface determination. *In:* VIGNUDELLI, S., KOSTIANOY, A. G., CIPOLLINI, P. & BENVENISTE, J. (eds.) *Coastal altimetry,* Springer, Berlin, Heidelberg, 103-145. doi:10.1007/978-3-642-12796-0_5

AVISO+. 2012. *CNES AVISO+ Envisat* [Online]. CNES AVISO+. Available: https://www.aviso.altimetry.fr/en/missions/past-missions/envisat.html [Accessed 31 May 2020].

AVISO+. 2019. *CNES AVISO+ - Satellite altimetry history* [Online]. CNES AVISO+. Available: https://www.aviso.altimetry.fr/en/techniques/altimetry/history.html [Accessed 17 June 2020].

AVISO+. 2020. *CNES AVISO+ Envisat instruments* [Online]. CNES AVISO+. Available: https://www.aviso.altimetry.fr/fr/missions/missions-passees/envisat/instruments.html [Accessed 13 March 2020].

Bamber, J. L. 1994. Ice sheet altimeter processing scheme. *International Journal of Remote Sensing,* 15, 925-938. doi:10.1080/01431169408954125

Bao, L., Lu, Y. & Wang, Y. 2008. Improved retracking algorithm for oceanic altimeter waveforms. *Progress in Natural Science,* 19, 195-203. doi:10.1016/j.pnsc.2008.06.017

Baup, F., Frappart, F. & Maubant, J. 2014. Combining high-resolution satellite images and altimetry to estimate the volume of small lakes. *Hydrology & Earth System Sciences,* 18(5), 2007-2020. doi:10.5194/hess-18-2007-2014

Becker, M., Santos da Silva, J., Calmant, S., Robinet, V., linguet, L. & Seyler, F. 2014. Water level fluctuations in the Congo Basin derived from ENVISAT satellite altimetry. *Remote Sensing*, 6(10), 9340-9359. doi:10.3390/rs6109340

Benveniste, J. 2011. Radar altimetry: past, present and future. *In:* VIGNUDELLI, S., KOSTIANOY, A. G., CIPOLLINI, P. & BENVENISTE, J. (eds.) *Coastal altimetry,* Springer, Berlin, Heidelberg, 3-17. doi:10.1007/978-3-642-12796-0_1

Benveniste, J. & Berry, P. A. M. 2004. Monitoring river and lake levels from space. *ESA Bulletin 117,* 7pp. [Online]. European Space Agency. Available: http://www.esa.int/esapub/bulletin/bullet117/chapter5_bul117.pdf [Accessed 17 June 2020].

Benveniste, J., Berry, P. A. M., Milagro, M. & Serpe, D. 2007. River and lake level data from radar altimetry in support of the Tiger Initiative. European Space Agency, *2nd Space for Hydrology Workshop*, 12–14 November 2007, Geneva, Switzerland, 5pp.

Benveniste, J., Roca, M., Levrini, G., Vincent, P., Baker, S., Zanife, O. Z., Zelli, C. & Bombaci, O. 2001. The Radar Altimetry Mission: RA-2, MWR, DORIS and LRR. *ESA Bulletin 106,* 10pp. [Online]. European Space Agency. Available: https://www.esa.int/esapub/bulletin/bullet106/bul106_5.pdf [Accessed 17 June 2020].

Berry, P. A. M. 2006. Two decades of inland water monitoring using satellite radar altimetry. European Space Agency/Centre National d'Etudes Spatiales, *Proceedings of the Symposium on 15 years of progress in radar altimetry,* 13-18 March 2006, Venice, Italy, 8pp.

Berry, P. A. M. 2009. ENVISAT-Jason2 exploitation river and lake product handbook., 19pp. [Online]. European Space Agency/De Montfort University. Available: http://altimetry.esa.int/riverlake/info/documents.html [Accessed 18 July 2020].

Berry, P. A. M., Freeman, J. A., Rogers, C. & Benveniste, J. 2007a. Global analysis of Envisat RA-2 burst mode echo sequences. *IEEE Transactions on Geoscience & Remote Sensing,* 45, 2869–2874. doi:10.1109/TGRS.2007.902280

Berry, P. A. M., Garlick, J. D., Freeman, J. A. & Mathers, E. L. 2005. Global inland water monitoring from multi-mission altimetry. *Geophysical Research Letters,* 32, 4pp. doi:10.1029/2005GL022814

Berry, P. A. M., Smith, R. G., Freeman, J. A. & Attwood, L. 2007b. Global analysis of Jason-1 over inland water. European Space Agency, *2nd Space for Hydrology Workshop,* 12-14 November 2007, Geneva, Switzerland, 5pp.

Berry, P. A. M., Smith, R. G., Salloway, M. K. & Benveniste, J. 2012. Global analysis of EnviSat burst echoes over inland water. *IEEE Transactions on Geoscience & Remote Sensing,* 50, 1980–1985. doi:10.1109/TGRS.2011.2170695

Biancamaria, S., Frappart, F., Leleu, A. S., Marieu, V., Blumstein, D., Desjonquères, J. D., Boy, F., Sottolichio, A. & Valle-Levinson, A. 2017. Satellite radar altimetry water elevations performance over a 200m wide river: evaluation over the Garonne River. *Advances in Space Research,* 59, 128–146. doi:10.1016/j.asr.2016.10.008

Biancamaria, S., Hossain, F. & Lettenmaier, D. 2011. Forecasting transboundary river water elevations from space. *Geophysical Research Letters,* 38, 5pp. doi:10.1029/2011GL047290

Biancamaria, S., Lettenmaier, D. P. & Pavelsky, T. M. 2016. The SWOT mission and its capabilities for land hydrology. *Surveys in Geophysics,* 37, 307–337. doi:10.1007/s10712-015-9346-y

Blarel, F., Frappart, F., Legrésy, B., Blumstein, D., Rémy, F., Fatras, C., Mougin, E., Papa, F., Prigent, C., Niño, F., Borderies, P., Biancamaria, S. & Calmant, S. 2015. Altimetry backscattering signatures at Ku and S bands over land and ice sheets. SPIE Remote Sensing, *Remote Sensing for Agriculture, Ecosystems, and Hydrology XVII*, 22-25 September 2015, Toulouse, France, 7pp.

Boergens, E., Dettmering, D., Schwatke, C. & Seitz, F. 2016. Treating the hooking effect in satellite altimetry data: a case study along the Mekong River and its tributaries. *Remote Sensing,* 8, 91-112. doi:10.3390/rs8020091

Bonnefond, P., Verron, J., Aublanc, J., Babu, K. N., Bergé-Nguyen, M., Cancet, M., Chaudhary, A., Crétaux, J.-F., Frappart, F., Haines, B. J., Laurain, O., Ollivier, A., Poisson, J.-C., Prandi, P., Sharma, R., Thibaut, P. & Watson, C. 2018. The benefits of the Ka-band as evidenced from the SARAL/AltiKa altimetric mission: quality assessment and unique characteristics of AltiKa data. *Remote Sensing,* 10, 83-108. doi:10.3390/rs10010083

Bosch, W., Dettmering, D. & Schwatke, C. 2014. Multi-mission cross-calibration of satellite altimeters: constructing a long-term data record for global and regional sea level change studies. *Remote Sensing,* 6, 2255–2281. doi:10.3390/rs6032255

Bouzinac, C. 2010. *Cryosat product handbook* [Online]. European Space Agency. Available: https://earth.esa.int/documents/10174/125272/CryoSat_Product_Handbook [Accessed 30 June 2020], 150pp.

Bronner, E., Guillot, A. & Picot, N. 2016. *SARAL/Altika products handbook*. Centre National d'Etudes Spatiales/Indian Space Research Organisation, CNES Ref. SALP-MU-M-OP-15984-CN, 76pp.

Brown, G. 1977. The average impulse response of a rough surface and its applications. *IEEE Transactions on Antennas & Propagation,* 25, 67–74. doi:10.1109/TAP.1977.1141536

Cai, X. & Wei, J. 2009. Wetland hydrologic application of satellite altimetry—a case study in the Poyang Lake watershed. *Progress in Natural Science,* 19, 1781-1787. doi:10.1016/j.pnsc.2009.07.004

Calmant, S., Seyler, F. & Cretaux, J. 2009. Monitoring continental surface waters by satellite altimetry. *Surveys in Geophysics,* 29, 247-269. doi:10.1007/s10712-008-9051-1

Chelton, D. B., Ries, J. C., Haines, B. J., Fu, L. L. & Callahan, P. S. 2001. Satellite altimetry, 1-131. *In:* FU, L.-L. & CAZENAVE, A. (eds.) *Satellite Altimetry and Earth Sciences: A Handbook of Techniques and Applications,* San Diego, California, USA, Academic Press. doi:10.1016/S0074-6142(01)80146-7

Chen, C., Desai, S., Picot, N., Fu, L. L., Morrow, R., Pavelsky, T. & Cretaux, J. 2018. *SWOT calibration/validation plan*. NASA/Jet Propulsion Laboratory/California Institute of Technology, California, USA. NASA Report JPL D-75724, 152pp.

Clews, P. 2014. Personal communication, email 2 July 2014, *OTML in-situ gauge accuracy.*

Connor, L. N., Laxon, S. W., Ridout, A. L., Krabill, W. B. & McAdoo, D. C. 2009. Comparison of Envisat radar and airborne laser altimeter measurements over Arctic sea ice. *Remote Sensing of Environment,* 113, 563–570. doi:10.1016/j.rse.2008.10.015

Coss, S., Durand, M., Yi, Y., Jia, Y., Guo, Q., Tuozzolo, S., Shum, C. K., Allen, G. H., Calmant, S. & Pavelsky, T. 2020. Global River Radar Altimetry Time Series (GRRATS): new river elevation earth science data records for the hydrologic community. *Earth System Science Data,* 12, 137–150. doi:10.5194/essd-12-137-2020

Crétaux, J. F. & Birkett, C. M. 2006. Lake studies from satellite radar altimetry. *Comptes Rendus Geoscience,* 338, 1098–1112. doi:10.1016/j.crte.2006.08.002

Crétaux, J. F., Jelinski, W., Calmant, S., Kouraev, A., Vuglinski, V., Bergé-Nguyen, M., Gennero, M. C., Nino, F., Abarca Del Rio, R., Cazenave, A. & Maisongrande, P. 2011. SOLS: a lake database to monitor in the near real time water level and storage variations from remote sensing data. *Advances in Space Research,* 47, 1497–1507. doi:10.1016/j.asr.2011.01.004

Davies, H. 2020. *Introduction to FAN language and utilities FAN Version 2.0* [Online]. UniData Data Services and Tools for Geoscience. Available: https://www.unidata.ucar.edu/software/netcdf/fan_utils.html [Accessed 31 June 2020].

Davis, C. H. 1997. A robust threshold retracking algorithm for measuring ice-sheet surface elevation change from satellite radar altimeters. *IEEE Transactions on Geoscience & Remote Sensing,* 35, 974–979. doi:10.1109/36.602540

Day, G., Dietrich, W. E., Rowland, J. C. & Marshall, A. 2008. The depositional web on the floodplain of the Fly River, Papua New Guinea. *Journal of Geophysical Research (Earth Surface),* 113, 19pp. doi:10.1029/2006JF000622

Deng, X. & Featherstone, W. E. 2006. A coastal retracking system for satellite radar altimeter waveforms: application to ERS-2 around Australia. *Journal of Geophysical Research,* 111, 16pp. doi:10.1029/2005JC003039

Deng, X., Featherstone, W. E., Hwang, C. & Berry, P. A. M. 2002. Estimation of contamination of ERS-2 and POSEIDON satellite radar altimetry close to the coasts of Australia. *Marine Geodesy,* 25, 249–271. doi:10.1080/01490410214990

Desai, S., S., C., Ganguly, D., Chauhan, P., Lele, P. D. & James, M. E. 2015. Waveform classification and water-land transition over the Brahmaputra River using SARAL/AltiKa & Jason-2 altimeter. *Journal of the Indian Society of Remote Sensing,* 43, 475-486. doi:10.1007/s12524-014-0428-y

Desportes, C., Obligis, E. & Eymard, L. 2007. On the Wet Tropospheric Correction for Altimetry in Coastal Regions. Geoscience and Remote Sensing, IEEE Transactions on, 45, 2139-2149. doi:10.1109/TGRS.2006.888967

Dettmering, D., Schwatke, C., Boergens, E. & Seitz, F. 2016. Potential of ENVISAT radar altimetry for water level monitoring in the Pantanal Wetland. *Remote Sensing,* 8, 596.

Dibarboure, G., Lamy, A., Pujol, M.-I. & Jettou, G. 2018. The drifting phase of SARAL: securing stable ocean mesoscale sampling with an unmaintained decaying altitude. *Remote Sensing,* 10, 1051-1071. doi:10.3390/rs10071051

Dubey, A. K., Gupta, P. K., Dutta, S. & Singh, R. P. 2015. An improved methodology to estimate river stage and discharge using Jason-2 satellite data. *Journal of Hydrology,* 529, 1776–1787. doi:10.1016/j.jhydrol.2015.08.009

ESA. 2012. *River & lake* [Online]. European Space Agency. Available: http://altimetry.esa.int/riverlake/shared/main.html [Accessed 27 July 2020].

ESA. 2014. *RA2/MWR products user guide* [Online]. European Space Agency. Available: http://envisat.esa.int/handbooks/ra2-mwr/CNTR1.html [Accessed 22 June 2020 2016].

ESA. 2020a. *CryoSat-2 (Earth Explorer Opportunity Mission-2)* [Online]. European Space Agency. Available: https://directory.eoportal.org/web/eoportal/satellite-missions/c-missions/cryosat-2#references [Accessed 13 March 2020].

ESA. 2020b. *Parameters affecting radar backscatter* [Online]. European Space Agency. Available: https://earth.esa.int/web/guest/missions/esa-operational-eo-missions/ers/instruments/sar/applications/radar-courses/content-2/-/asset_publisher/qIBc6NYRXfnG/content/radar-course-2-parameters-affecting-radar-backscatter [Accessed 25th May 2020].

ESA. 2020c. *Sentinel-3* [Online]. European Space Agency. Available: https://sentinels.copernicus.eu/web/sentinel/missions/sentinel-3 [Accessed 17 June 2020].

ezilonMaps. 2009. *Map of Papua New Guinea and Papua New Guinea details maps* [Online]. ezilon Maps. Available: https://www.ezilon.com/maps/oceania/papua-new-guinea-road-maps.html [Accessed 25 May 2020].

Fenoglio-Marc, L., Fehlau, M., Ferri, L., Becker, M., Gao, Y. & Vignudelli, S. 2010. Coastal Sea Surface Heights from Improved Altimeter Data in the Mediterranean Sea. In: MERTIKAS, P. (ed.) *Gravity, Geoid and Earth Observation .International Association of Geodesy Symposia*, Berlin, Heidelberg: Springer Verlag, 253-261. doi:10.1007/978-3-642-10634-7_33

Frappart, F., Calmant, S., Cauhope, M., Seyler, F. & Cazenave, A. 2006. Preliminary results of ENVISAT RA-2 derived water levels validation over the Amazon Basin. *Remote Sensing of Environment,* 100, 252–264. doi:10.1016/j.rse.2005.10.027

Frappart, F., Cazenave, A., Seyler, F. & Calmant, S. 2005. Comparison of the Envisat waveform retrackers over inland waters. European Space Agency, *Proceedings of the 2004 Envisat & ERS Symposium*, 6-10 September 2004*,* Salzburg Austria. ESA (Special Publication) SP-572, 8pp.

Freeman, J. A. & Berry, P. A. M. 2006. A New Approach to Retracking Ocean and Coastal Zone Multi-Mission Altimetry.European Space Agency, *Symposium on 15 Years of Progress in Radar Altimetry*, 13-18 March 2006, Venice, Italy, 4pp.

Fu, L. L. & Cazenave, A. 2000. Satellite Altimetry and Earth Sciences: A Handbook of Techniques and Applications, San Diego, California, USA, Academic Press, 1-463. doi:10.1016/S0074-6142(01)80146

Gao, Q., Makhoul, E., Escorihuela, M. J., Zribi, M., Seguí, P. Q., García, P. & Roca, M. 2019. Analysis of retrackers' performances and water level retrieval over the Ebro River Basin using Sentinel-3. *Remote Sensing,* 11, 718-742. doi:10.3390/rs11060718

Gautschi, W. 2010. The spiral of Theodorus, numerical analysis, and special functions. *Journal of Computational & Applied Mathematics,* 235, 1042–1052. doi:10.1016/j.cam.2009.11.054

Ghosh, S., Thakur, P. K., Garg, V., Nandy, S., Aggarwal, S., Saha, S. K., Sharma, R. & Bhattacharyya, S. 2015. SARAL/AltiKa waveform analysis to monitor inland water levels: a case study of Maithon Reservoir, Jharkhand, India. *Marine Geodesy,* 38, 597–613. doi:10.1080/01490419.2015.1039680

Gomez-Enri, J., Vignudeli, S., Quartly, G., Gommenginger, C., Cipollini, P., Challenor, P. G. & Benveniste, J. 2010. Modeling Envisat RA-2 waveforms in the coastal zone: case study of calm water contamination. *IEEE GRSL Geoscience & Remote Sensing Letters,* 7, 474-478. doi:10.1109/LGRS.2009.2039193

Gommenginger, C., Thibaut, P., Fenoglio-Marc, L., Quartly, G., Deng, X., Gomez-Enri, J. & Gao, Y. 2010. Retracking altimeter waveforms near the coasts. *In:* VIGNUDELI, S., KOSTIANOY, A. G., CIPOLLINI, P. & BENVENISTE, J. (eds.) *Coastal altimetry.* Springer, Berlin, Heidelberg, 61-101. doi:10.1007/978-3-642-12796-0_4

Guinle, T., Verron, J., Bonnefond, P. & Arunan, S. 2016. [Saral] A new phase with a drifting orbit [Online]. AVISO+. Available: https://www.aviso.altimetry.fr/en/news/front-page-news/news-detail.html?tx_ttnews%5Btt_news%5D=1990&cHash=722c44244fb3d915aa9e915e398c2961 [Accessed 20 June 2020].

Hayne, G. 1980. Radar altimeter mean return waveforms from near-normal-incidence ocean surface scattering. *IEEE Transactions on Antennas & Propagation,* 28, 687–692. doi:10.1109/TAP.1980.1142398

Henry, J.-B., Chastanet, P., Fellah, K. & Desnos, Y.-L. 2003. ENVISAT multipolarised data for flood mapping. *IGARSS 2003, 2003 IEEE International Geoscience and Remote Sensing Symposium Proceedings*, 21-25 July 2003, Toulouse, France, 2, 1136-1138, doi:10.1109/IGARSS.2003.1294036

Hwang, C., Jinyun, G., Deng, X., Hsu, H.-Y. & Liu, Y. 2006. Coastal gravity anomalies from retracked Geosat/GM altimetry: improvement, limitation and the role of airborne gravity data. *Journal of Geodesy,* 80, 204–216. doi:10.1007/s00190-006-0052-x

Idris, N. H. & Deng, X. 2012. The retracking technique on multi-peak and quasi-specular waveforms for Jason-1 and Jason-2 missions near the coast. *Marine Geodesy,* 35, 217–237. doi:10.1080/01490419.2012.718679

Jarihani, A. A., Callow, J. N., Johansen, K. & Gouweleeuw, B. 2013. Evaluation of multiple satellite altimetry data for studying inland water bodies and river floods. *Journal of Hydrology,* 505, 78–90. doi:10.1016/j.jhydrol.2013.09.010

JAXA. 2011. ALOS AW3D 30 metre DSM [Online]. Japan Aerospace Exploration Agency. Available: https://www.eorc.jaxa.jp/ALOS/en/aw3d/index_e.htm [Accessed 10 May 2020].

Jinyun, G., Gao, Y., Xiao-Tao, C. & Hwang, C. 2010. Optimized threshold algorithm of envisat waveform retracking over coastal sea. *Chinese Journal of Geophysics,* 53, 231–239. doi:10.1002/cjg2.1490

Khajeh, S., Jazireeyan, I. & Ardalan, A. A. 2014. Applying satellite altimetry to wetland water levels monitoring (case study: Louisiana Wetland). *Geoscience & Remote Sensing Letters, IEEE,* 11, 4pp. doi:10.1109/LGRS.2013.2295831

Kirby, J. M., Van Dijk, A. I. J. M., Mainuddin, M., Peña-Arancibia, J., Guerschman, J.-P., Liu, Y., Marvanek, S., McJannet, D. L., Paydar, Z., McVicar, T. R., van Niel, T. G. & Li, L. T. 2008. *River water balance accounts across the Murray–Darling Basin, 1990–2006*, CSIRO, 28pp.

Kuo, C.-Y. & Kao, H.-C. 2011. Retracked Jason-2 altimetry over small water bodies: case study of Bajhang River, Taiwan. *Marine Geodesy,* 34, 382–392. doi:10.1080/01490419.2011.584830

Laxon, S. 1994. Sea ice altimeter processing scheme at the EODC. *International Journal of Remote Sensing,* 15, 915-924. doi:10.1080/01431169408954124

Lee, H., Shum, C. K., Yi, Y., Braun, A. & Kuo, C.-Y. 2008. Laurentia crustal motion observed using TOPEX/POSEIDON radar altimetry over land. *Journal of Geodynamics,* 46, 182–193. doi:10.1016/j.jog.2008.05.001

Legresy, B., Papa, F., Remy, F., Vinay, G., van den Bosch, M. & Zanife, O.-Z. 2005. ENVISAT radar altimeter measurements over continental surfaces and ice caps using the ICE-2 retracking algorithm. *Remote Sensing of Environment,* 95, 150–163. doi:10.1016/j.rse.2004.11.018

Liebe, J. R., van de Giesen, N., Andreini, M. S., Steenhuis, T. S. & Walter, M. T. 2008. Suitability and limitations of ENVISAT ASAR for monitoring small reservoirs in semiarid area. *IEEE Transactions on Geoscience & Remote Sensing,* 47, 1536-1547. doi:10.1109/TGRS.2008.2004805

Lu, Z., Kim, J.-W., Lee, H., Shum, C. K., Duan, J., Ibaraki, M., Akyilmaz, O. & Read, C.-H. 2009. Helmand River hydrologic studies using ALOS PALSAR InSAR and ENVISAT altimetry. *Marine Geodesy,* 32, 320–333. doi:10.1080/01490410903094833

Maillard, P., Bercher, N. & Calmant, S. 2015. New processing approaches on the retrieval of water levels in Envisat and SARAL radar altimetry over rivers: a case study of the São Francisco River, Brazil. *Remote Sensing of Environment,* 156, 226–241. doi:10.1016/j.rse.2014.09.027

Mantovani, P.-L. (ed.) 2015a. *CRYOSAT L1B products specification format*. Advanced Computer Systems, report CS-RS-ACS-GS-5106, issue 6.4, 114pp.

Mantovani, P.-L. (ed.) 2015b. *CRYOSAT L2 products format specification*. Advanced Computer Systems, report CS-RS-ACS-GS-5123, issue 4.5, 98pp.

Marshall, A. R. 1998–2020. *River Bed Aggradation Database*. Ok Tedi Mining Limited, Environment Department, Industrial Sites & Water Management.

Marshall, A. R. 1999. *Lower Ok Tedi and Middle Fly, estimate of current vegetation dieback, classification of floodplain vegetation and prediction of maximum potential dieback extent*. Report to Ok Tedi Mining.

Marshall, A. R. & Deng, X. 2016. Image analysis for altimetry waveform selection over heterogeneous inland waters. *IEEE GRSL Geoscience & Remote Sensing Letters,* 13, 5pp. doi:10.1109/LGRS.2016.2575068

Martin, T., Brenner, A., Zwally, H. & Bindschadler, R. 1983. Analysis and retracking of continental ice sheet radar altimeter waveforms. *Journal of Geophysical Research Atmospheres,* 88, 1609-1616. doi:10.1029/JC088iC03p01608

Mayer, V., Sneeuw, N. & Tourian, M. J. 2014. *Cryosat-2 for hydrological purposes, data processing, visualization and analysis*, 26-28 March 2014, Geoinformatics 2014 of GfGI eV and GiN eV, Hamburg, Germany, 7pp.

McFeeters, S. K. 1996. The use of the Normalised Difference Water Index (NDWI) in the delineation of open water features. *International Journal of Remote Sensing,* 17, 1425-1433. doi:10.1080/01431169608948714

Michailovsky, C. I., McEnnis, S., Berry, P. A. M., Smith, R. & Bauer-Gottwein, P. 2012. River monitoring from satellite radar altimetry in the Zambezi River basin. *Hydrology & Earth System Sciences,* 16, 2181–2192. doi:10.5194/hess-16-2181-2012

Milton, D., Yarrao, M., Fry, G. & Tenakanai, C. 2005. Response of barramundi, Lates calcarifer, populations in the Fly River, Papua New Guinea to mining, fishing and climate-related perturbation. *Marine & Freshwater Research,* 56, 969-981. doi:10.1071/MF04278

Miranda, N., Duesmann, B., Pinol, M., Giudici, D. & D'Aria, D. 2010. Impact of the Envisat Mission Extension on SAR data. *ESA Technical Note* [Online]. Available: https://earth.esa.int/web/eoportal/satellite-missions/e/envisat [Accessed 30 September 2020].

Nielsen, K., Stenseng, L., Andersen, O. B., Villadsen, H. & Knudsen, P. 2015. Validation of CryoSat-2 SAR mode based lake levels. *Remote Sensing of Environment,* 171, 162–170. doi:10.1016/j.rse.2015.10.023

Nuth, V., Pulliam, J. & Wilson, C. 2002. Migration of radar altimeter waveform data. *Geophysical Research Letters,* 29, 4pp. doi:10.1029/2001GL014015

Observing Systems Capability Analysis and Review. 2020. *Satellite: HY-2A* [Online]. Observing Systems Capability Analysis and Review Tool, World Meterological Organization. Available: https://www.wmo-sat.info/oscar/satellites/view/176 [Accessed 22 June 2020].

Osborne, P. L., Kyle, J. H. & Abramski, M. S. 1987. Effects of seasonal water level changes on the chemical and biological limnology of Lake Murray, Papua New Guinea. *Marine & Freshwater Research,* 38, 397–408. doi:10.1071/MF9870397

OTML 1963–2020. *OTML Hydrology Database*. Ok Tedi Mining Limited, Environment Department, Industrial Sites & Water Management.

OTML. 2020. *Mine Closure; Ok Tedi Mining Limited has a comprehensive Mine Closure Plan for what happens after the mine closes in 2025* [Online]. Available: https://oktedi.com/who-we-are/our-history/mine-closure/ [Accessed 25 February 2020].

Passaro, M., Cipollini, P., Vignudeli, S., Quartly, G. & Snaith, H. 2014a. ALES: a multi-mission adaptive subwaveform retracker for coastal and open ocean altimetry. *Remote Sensing of Environment,* 145, 173–189. doi:10.1016/j.rse.2014.02.008

Peng, F. & Deng, X. 2018. A new retracking technique for brown peaky altimetric waveforms. *Marine Geodesy,* 41, 99–125. doi:10.1080/01490419.2017.1381656

Pickup, G. & Marshall, A. 2019. *Mapping floodplain inundation from Sentinel and Palsar Synthetic Aperture Radar*. Report to Ok Tedi Mining.

Pickup, G. & Marshall, A. R. 2009. Geomorphology, hydrology, and climate of the Fly River system. *In:* BOLTON, B. R. (ed.) *The Fly River Papua New Guinea, environmental studies in an impacted tropical river system,* Elsevier, Amsterdam, The Netherlands, 3-49. doi:10.1016/S1571-9197(08)00420-5

PNG 2013. *National Population and Housing Census 2011—final figures*. National Statistical Office, Port Moresby, Papua New Guinea.

Physical Oceanography Distributed Active Archive Center 2019. *Altimetric data information: missions* [Online]. NASA Earth Science Data and Information System (ESDIS). Available: https://podaac.jpl.nasa.gov/Altimetric_Data_Information/Missions [Accessed 17 June 2020].

Quartly, G. 2010. Hyperbolic retracker: removing bright target artefacts from altimetric waveform data. European Space Agency, *ESA Living Planet Symposium,* 28 June-2 July 2010, Bergen, Norway, 6pp.

Quartly, G. & Passaro, M. 2014. Initial examination of AltiKa's individual echoes. *Marine Geodesy,* 38, 73-85. doi:10.1080/01490419.2014.984882

Resti, A., Benveniste, J., Roca, M. & Levrini, G. 1999. The Envisat radar altimeter system (RA-2). *ESA Bulletin* [Online], 98. Available: http://www.esa.int/esapub/bulletin/bullet98/RESTI.PDF [Accessed 17 June 2020].

Roca, M., Martinez, D., & Reche, M. 2007. The RA-2 individual echoes processing description and some scientific results. *Proceedings of the 2007 IEEE International Geoscience and Remote Sensing Symposium*, 23–28 July 2007, 3541–3546. doi:10.1109/IGARSS.2007.4423610

Roca, M., Laxon, S. & Zelli, C. 2009. The EnviSat RA-2 instrument design and tracking performance. *IEEE Transactions on Geoscience & Remote Sensing,* 47, 3489–3506. doi:10.1109/TGRS.2009.2020793

Rosmorduc, V., Benveniste, J., Dinardo, S., Lauret, O., Maheu, C., Milagro, M., Picot, N., Escola, R., Garcia-Mondejar, A., Schrama, E., Ambrozio, A., Terra-Homen, M. & Restano, M. 2018. *Radar altimetry tutorial*. (B Benveniste , J. & Picot, N. [eds.]) [Online]. European Space Agency/Centre National d'Etudes Spatiales. Available: http://www.altimetry.info [Accessed 2 June 2020].

Rosmorduc, V. & Vayre, M. 2020. *Hydroweb product user manual* [Online]. Theia Land Data Centre. Available: https://theia.sedoo.fr/wp-content-theia/uploads/sites/2/2020/04/Handbook_Hydroweb-V2.0-1.pdf [Accessed 30 June 2020].

Santos da Silva, J., Calmant, S., Seyler, F., Filho, O. C. R., Cochonneau, G. & Mansur, W. J. 2010. Water levels in the Amazon basin derived from the ERS 2 and ENVISAT radar altimetry missions. *Remote Sensing of Environment,* 114, 2160–2181. doi:10.1016/j.rse.2010.04.020

Santos da Silva, J., Calmant, S., Seyler, F., Moreira, D. M., Oliveira, D. & Monteiro, A. 2014. Radar altimetry aids managing gauge networks. *Water Resources Management,* 28, 587–603. doi:10.1007/s11269-013-0484-z

Santos Da Silva, J., Seyler, F., Calmant, S., Filho, F. C. R., Roux, E., Araújo, A. A. M. & Guyot, J. L. 2012. Water level dynamics of Amazon wetlands at the watershed scale by satellite altimetry. *International Journal of Remote Sensing,* 33, 3323–3353. doi:10.1080/01431161.2010.531914

Sarmiento, S. E. & Khan, S. 2010. Spatial–temporal variability of Great Slave Lake levels from satellite altimetry. *IEEE Geoscience & Remote Sensing Letters,* 7, 426–429.

Satishkumar, B., Muralikrishnan, S., Narendran, J., Venkataraman, V. R. & Dadhwal, V. K. 2013. Bias-corrected GOCE geoid for the generation of high-resolution digital terrain model. Current Science, 104, 940-943. doi:10.1007/s00190-010-0395-l. 6

Schneider, R., Godiksen, P. N., Villadsen, H., Madsen, H. & Bauer-Gottwein, P. 2017. Application of CryoSat-2 altimetry data for river analysis and modelling. *Hydrology & Earth System Sciences,* 21, 751–764. doi:10.5194/hess-21-751-2017

Schwatke, C., Dettmering, D., Börgens, E. & Bosch, W. 2015a. Potential of SARAL/AltiKa for inland water applications. *Marine Geodesy,* 38, 626–643. doi:10.1080/01490419.2015.1008710

Schwatke, C., Dettmering, D., Bosch, W. & Seitz, F. 2015b. DAHITI—an innovative approach for estimating water level time series over inland waters using multi-mission satellite altimetry. *Hydrology & Earth System Sciences,* 19, 20. doi:10.5194/hess-19-4345-2015

Simard, M. 2017. *Understanding SWOT measurements in coastal wetlands* [Online]. NASA Jet Propulsion Laboratory. Available: https://swot.odyseallc.net/project-simard.htm [Accessed 18 August 2020].

Smith, R. & Berry, P. A. M. 2007. Contribution to wetland monitoring of multi-mission satellite radar altimetry. European Space Agency, *Hydrospace07*,12-14 November, Geneva, Switzerland, 5pp.

Smith, W. H. F. & Scharroo, R. 2015. Waveform aliasing in satellite radar altimetry. *IEEE Transactions on Geoscience & Remote Sensing,* 53, 1671-1682. doi:10.1109/TGRS.2014.2331193

Snaith, H. 2011. *ENVISAT coastal altimetry product handbook* (2.0.1 ed.). European Space Agency report reference ENVI-DTEX-EOPS-TN-09-0006 [Online]. European Space Agency. Available: https://www.yumpu.com/en/document/read/37738534/envisat-coastal-altimetry-product-handbook-coastalt [Accessed 2 June 2020].

Soussi, B. 2011. *Envisat altimetry level 2 user manual* [Online]. European Space Agency. Available: https://earth.esa.int/pub/ESA_DOC/ENVISAT/RA2-MWR/PH_light_1rev4_ESA.pdf [Accessed 22 June 2020].

Stanaway, R. 2008. A dynamic datum for PNG—improving PNG94. *42nd Association of Surveyors PNG Congress*, 9-12 July 2008, The Association of Surveyors of Papua New Guinea, Port Moresby, PNG, 9pp. [Online]. Available: http://www.aspng.org/techinfo.htm [Accessed 5 May 2020].

Stanaway, R. 2012. *Geodetic survey—North Fly District, Papua New Guinea*. Quickclose Pty Ltd. Report to Horizon Oil/Talisman Energy.

Steunou, N., Desjonquères, J. D., Picot, N., Sengenes, P., Noubel, J. & Poisson, J. C. 2015. AltiKa altimeter: instrument description and in flight performance. *Marine Geodesy,* 38, 22–42. doi:10.1080/01490419.2014.988835

Sulistioadi, Y. B., Tseng, K.-H., Shum, C. K., Hidayat, H., Sumaryono, M., Suhardiman, A., Setiawan, F. & Sunarso, S. 2015. Satellite radar altimetry for monitoring small rivers and lakes in Indonesia. *Hydrology & Earth System Sciences,* 19, 341-359. doi:10.5194/hess-19-341-2015

Swales, S. 2001. *Fish and fisheries of the Fly River, Papua New Guinea: population changes associated with natural and anthropogenic factors and lessons to be learned* [Online]. Pacific Environment Portal. Available: https://pacific-data.sprep.org/dataset/species [Accessed 31 August 2020].

Tarpanelli, A. & Benveniste, J. 2019. On the potential of altimetry and optical sensors for monitoring and forecasting river discharge and extreme flood events. *In:* MAGGIONI, V. & MASSARI, C. (eds.) *Extreme hydroclimatic events and multivariate hazards in a changing environment.* Elsevier, Amsterdam, The Netherlands, 267-287. doi:10.1016/B978-0-12-814899-0.00011-0

Theia. 2020. *Hydroweb—time series of water levels in the rivers and lakes around the world* [Online]. Available: http://hydroweb.theia-land.fr/hydroweb/view/R_FLY_FLY_KM0442?lang=en&basin=Fly&river=Fly [Accessed 17 July 2020].

Tourian, M., J. 2012. *Controls on satellite altimetry over inland water surfaces for hydrological purposes.* Institute of Geodesy, Universitat Stuttgart, Germany, 58pp.

Tourian, M. J., Sneeuw, N. & Bárdossy, A. 2009. Controls on satellite altimetry over non-ocean surfaces for hydrological purposes. *EGU General Assembly 2009.* 19-24 April 2009, Vienna, Austria.

Tournadre, J. 2007. Signature of lighthouses, ships, and small islands in altimeter waveforms. *Journal of Atmospheric & Oceanic Technology,* 24, 1143–1149. doi:10.1175/JTECH2030.1

Tournadre, J., Lambin, J. & Steunou, N. 2009. Cloud and Rain Effects on AltiKa/SARAL Ka-Band Radar Altimeter-Part I: Modeling and Mean Annual Data Availability. *IEEE Transactions on Geoscience and Remote Sensing.*, 47, 1806-1817. doi: 10.1109/TGRS.2008.2010130

Tournadre, J., Poisson, J. C., Steunou, N. & Picard, B. 2015. Validation of AltiKa matching pursuit rain flag. *Marine Geodesy,* 38, 107–123. doi:10.1080/01490419.2014.1001048

Troitskaya, Y. I., Rybushkina, G. V., Soustova, I. A., Balandina, G. N., Lebedev, S. A., Kostianoy, A. G., Panyutin, A. A. & Filizola, N. 2012. Satellite altimetry of inland water bodies. *Water Resources,* 39, 184-199. doi:10.1134/S009780781202008X

United Nations Department of Economic and Social Affairs. 2019. *World population prospects 2019* [Online]. United Nations–DESA/Population Division. Available: https://population.un.org/wpp/ [Accessed 25 August 2020].

United Nations Water. 2019. *Water and climate change* [Online]. United Nations–UN Water. Available: https://www.unwater.org/water-facts/climate-change/ [Accessed 25 August 2020].

USGS. 2020. *Landsat missions* [Online]. Available: https://www.usgs.gov/land-resources/nli/landsat [Accessed 20/05/2020].

Verron, J., Bonnefond, P., Andersen, O. B., Ardhuin, F., Bergé-Nguyen, M., Bhowmick, S., Blumstein, D., Boy, F., Brodeau, L., Crétaux, J.-F., Dabat, M. L., Dibarboure, G., Fleury, S., Garnier, F., Gourdeau, L., Marks, K., Queruel, N., Sandwell, D., Smith, W. H. F. & Zaron, E. D. 2020. The SARAL/AltiKa mission: a step forward to the future of altimetry. *Advances in Space Research*, 66(9), 2075-2274. doi:10.1016/j.asr.2020.01.030

Verron, J., Bonnefond, P., Aouf, L., Birol, F., Bhowmick, S., Calmant, S., Conchy, T., Cretaux, J., Gerald, D., Dubey, A., Yannice, F., Guerreiro, K., Gupta, P., Hamon, M., Jebri, F., Kumar, R., Morrow, R., Pascual, A., Pujol, I. & Vergara, O. 2018. The benefits of the Ka-band as evidenced from the SARAL/AltiKa altimetric mission: scientific applications. *Remote Sensing,* 10, 83-108. doi:10.3390/rs10020163

Verron, J., Sengenes, P., Lambin, J., Noubel, J., Steunou, N., Guillot, A., Picot, N., Coutin-Faye, S., Sharma, R., Gairola, R., Murthy, D., Richman, J., Griffin, D., Pascual, A., Rémy, F. & Gupta, P. 2015. The SARAL/AltiKa altimetry satellite mission. *Marine Geodesy,* 38, 2–21. doi:10.1080/01490419.2014.1000471

Vignudelli, S., Scozzari, A., Abileah, R., Gómez-Enri, J., Benveniste, J. & Cipollini, P. 2019. Water surface elevation in coastal and inland waters using satellite radar altimetry. *In:* MAGGIONI, V. & MASSARI, C. (eds.) *Extreme hydroclimatic events and multivariate hazards in a changing environment.* Elsevier, Amsterdam, The Netherlands, 87-127. doi:10.1016/B978-0-12-814899-0.00004-3

Villadsen, H., Andersen, O. B., Stenseng, L., Nielsen, K. & Knudsen, P. 2014. Cryosat-2 altimetry for river level monitoring—evaluation in the Ganges–Brahmaputra river basin. *Remote Sensing of Environment*, 168,80-89. doi:10.1016/j.rse.2015.05.025

Villadsen, H., Deng, X., Andersen, O. B., Stenseng, L., Nielsen, K. & Knudsen, P. 2016. Improved inland water levels from SAR altimetry using novel empirical and physical retrackers. *Journal of Hydrology,* 537, 234–247. doi:10.1016/j.jhydrol.2016.03.051

Watling, D., Wood, S., Gresham, P., Carew-Reid, J., Kula, G. & Douglas.J. 1995. *The Fly River catchment Papua New Guinea: a regional environmental assessment.* IUCN/PNG Environment and Conservation , 88pp. [Online]. Available: https://portals.iucn.org/library/node/6969 [Accessed 21 May 2020].

Weier, J. & Herring, D. 2015. *Measuring vegetation (NDVI and EVI)* [Online]. NASA Earth Observatory. Available: http://earthobservatory.nasa.gov/Features/MeasuringVegetation/ [Accessed 13 December 2019].

Wingham, D. J., Francis, C. R., Baker, S., Bouzinac, C., Brockley, D., Cullen, R., de Chateau-Thierry, P., Laxon, S. W., Mallow, U., Mavrocordatos, C., Phalippou, L., Ratier, G., Rey, L., Rostan, F., Viau, P. & Wallis, D. W. 2006. CryoSat: a mission to determine the fluctuations in Earth's land and marine ice fields. *Advances in Space Research,* 37, 841–871. doi: 10.1016/j.asr.2005.07.027

Wingham, D. J., Rapley, C. G. & Griffiths, H. 1986. New techniques in satellite altimeter tracking systems. *IGARSS 86, Proceedings of the International Geoscience and Remote Sensing Symposium,* 8 September 1986, Zurich, Switzerland, ESA SP-254, 1339-1344.

Wingham, D. J., Rapley, C. G. & Morley, J. 1993. Improved resolution ice sheet mapping with satellite radar altimeters. *Eos Transactions American Geophysical Union,* 74, 113–116. doi:10.1029/93EO00962

Yang, Y., Hwang, C., Hsu, H.-J., Dongchen, E. & Wang, H. 2012. A subwaveform threshold retracker for ERS-1 altimetry: a case study in the Antarctic Ocean. *Computers & Geosciences,* 41, 88–98. doi:10.1016/j.cageo.2011.08.017

Yi, Y., Kouraev, A. V., Shum, C. K., Vuglinsky, V. S., Crétaux, J.-F. & Calmant, S. 2013. The performance of altimeter waveform retrackers at Lake Baikal. *Terrestrial, Atmospheric & Oceanic Sciences,* 24, 513–519. doi:10.3319/TAO.2012.10.09.01(TibXS)

Zakharova, E., Fleury, S., Guerreiro, K., Willmes, S., Rémy, F., Kouraev, A. & Heinemann, G. 2015. Sea ice leads detection using SARAL/AltiKa altimeter. *Marine Geodesy,* 38, 522-533. doi: 10.1080/01490419.2015.1019655

Zakharova, E., Nielsen, K., Kamenev, G. & Kouraev, A. 2020. River discharge estimation from radar altimetry: assessment of satellite performance, river scales and methods. *Journal of Hydrology,* 583, 17pp. doi:10.1016/j.jhydrol.2020.124561

Zakharova, E. A., Kouraev, A. V., Rémy, F., Zemtsov, V. A. & Kirpotin, S. N. 2014. Seasonal variability of the Western Siberia wetlands from satellite radar altimetry. *Journal of Hydrology,* 512, 366–378. doi:10.1016/j.jhydrol.2014.03.002

Zhang, M. 2009. *Satellite radar altimetry for inland hydrologic studies.* Ohio State University, Ohio State University, Geodetic Science and Surveying. Report. no. 491, 89pp.

Zhang, S. & Sandwell, D. T. 2017. Retracking of SARAL/AltiKa radar altimetry waveforms for optimal gravity field recovery. *Marine Geodesy,* 40, 40–56. doi:10.1080/01490419.2016.1265032